A Study of Atomic and Molecular Species in Low Temperature Plasmas Close to Divertor-like Materials

Thesis submitted in accordance with the requirements of the University of Liverpool for the degree of Doctor in Philosophy by

Ella Fox-Widdows

March 2022

Abstract

A deeper understanding of the basic plasma processes in low temperature plasmas is essential to the success of future commercial fusion machines. Atomic and molecular processes are key to the successful handling of power in tokamaks and plasma detachment is vital to limit the fluxes of particles and heat to divertor surfaces. However, the processes that influence divertor detachment are currently not fully understood.

In this thesis, an investigation into the behaviour of atoms and molecules in both fusion and non-fusion plasmas is presented. The aim of these studies is to characterise the trends in atomic and molecular emission in low temperature plasmas in order to improve the understanding of atoms and molecules relevant to fusion machines and push the field of fusion towards economic viability. Achievement of this objective will allow for a significant improvement in the accuracy of predictive simulation codes used to model plasmas in future fusion devices.

In the first study, the inductively coupled plasma discharge source at the University of Liverpool will be utilised to characterise the plasma emission and plasma parameters for varying discharge conditions. Langmuir probes are employed to identify the trends in electron temperature and electron density and show decreasing electron temperatures and increasing electron densities for increasing discharge pressure and RF power. The observed trends in both electron properties and emission are attributed to known plasma mechanisms in ICP discharges, such as changes in collisional paths lengths with pressure, and changes in the dominant power coupling from capacitive to inductive mode.

The second study focuses on an investigation into the effects of divertor-like samples on plasma conditions. These measurements highlight the differences in plasma conditions in the presence of three different samples, carbon, tungsten and nanostructured tungsten, and conclude that the carbon sample has a significant effect on both the atomic and molecular emission. These measurements show an increase in the Balmer emission at higher sample temperatures by a factor of 3 and the carbon sample is also shown to influence the distribution of molecular states as seen through spectroscopy measurements of the hydrogen Fulcher band. These results show that plasma-material interactions play a significant role in low temperature plasmas and motivates future studies into the chemical processes influencing the observed trends in both atomic and molecular emission.

In the third study, trends in the emission measurements collected in the MAST-U

divertor are presented. Distinct differences can be seen in the emission of the D_α, Fulcher band, CD band and the ratio of the Balmer n=6/5 lines, for varying divertor configurations and plasma conditions. The cooler detached plasmas are indicated by a reduction in the Fulcher band emission close to the divertor tiles, while the D_α emission profiles are seen to peak close to the divertor targets in the attached divertor state. An analysis of the key trends in these emission profiles in both the conventional and Super-X divertor are discussed along with the key processes that dominate in these regions.

The final study describes the development of a 0D collisional-radiative model. Benchmarking with the 0D Yacora model and comparison with experimental measurements collected in the ICP plasma source show good agreement with the CR model and demonstrate the capability of this model to extract useful information from low temperature plasmas.

Acknowledgements

I would like to first thank my PhD supervisor, Dr Mark Bowden, for his kind and continued support and guidance throughout my PhD project, across time zones and during a global pandemic. I am grateful for this opportunity to learn a range of new skills and grow as a researcher and I am very thankful for his support and advice throughout my studies.

To Mark Burnley, for the hundreds of hours of technical support, words of encouragement and friendship, I am more than grateful. Thank you to Gareth Blacoe, Dave Donaghy, Lindsey Clarke, Alison Goodyear, Jill Anson and the staff in the Electrical Engineering and Electronics department for all their support. I would also like to thank Marcus Law, for always checking in on me, Mike Barnes, for passing on his knowledge of inductively coupled plasmas, and Peter Ryan for his encouragement and Langmuir probes expertise.

Thank you to the University of Liverpool and the Fusion CDT programme for providing me with the opportunity to pursue my passion and for facilitating a number of dear friendships over the last few years. Thanks also go to EPSRC for funding this studentship.

From my time spent in Tokyo, I would like to express my sincere thanks to Professor Kazuo Hoshino and Professor Akiyoshi Hatayama for hosting me in the plasma group and for their mentorship. I am very thankful for the support of Ryoko Tatsumi and Yuka Tsubotani who supported me endlessly during my time at Keio University and beyond, through conversations about collisional-radiative models, tennis matches and baseball games, karaoke, hanami and lunchtime trips to 7-eleven.

To Kevin Verhaegh and Nick Osborne at the Culham Centre for Fusion Energy, thank you for your advice and guidance through the MAST-U collaboration and for the very helpful conversations about atomic and molecular emission.

Finally, I would like to say a huge thank you to Cai, my parents, Anita and Ian, my brother, Gabriel, and my friends for their love and unfaltering confidence in me, through the highs and lows of the last few years and beyond.

Contents

Abstract **1**

Acknowledgements **3**

Contents **6**

List of Figures **14**

List of Tables **15**

1 Introduction **17**
1.1 Fusion energy and the tokamak 18
1.1.1 Plasmas and their properties 21
1.1.2 Plasma conditions for fusion 23
1.1.3 Divertors and the power exhaust problem 26
1.1.4 The MAST-U tokamak 30
1.2 Atoms and molecules in low temperature plasmas 32
1.3 The role of laboratory experiments in understanding the exhaust problem in tokamaks 33
1.4 Thesis objectives 34
1.5 Thesis outline 36

2 Low Temperature Edge Plasmas and Divertor Physics **37**
2.1 Low pressure plasma discharges 37
2.1.1 Inductively coupled plasmas 39
2.2 Low temperature regions of fusion plasmas 43
2.2.1 Divertor plasmas and divertor detachment 44
2.3 Plasma-surface interactions in low temperature plasmas 48
2.4 Atoms and molecules in low temperature plasmas 52
2.4.1 Collisional-radiative models 53
2.4.2 Diagnosing atoms and molecules in low temperature plasmas 58

2.5 Summary 62

3 Experimental Apparatus and Diagnostic Techniques 64
3.1 The Inductively coupled radio frequency plasma source 64
3.1.1 Discharge plasma rig set up 65
3.1.2 Bespoke sample heater 67
3.1.3 Diagnostic measurement positions 68
3.2 Optical emission spectroscopy 69
3.2.1 Experimental setup 69
3.2.2 Data acquisition 72
3.2.3 Analysis of emission data 73
3.3 Langmuir probes 77
3.3.1 Probe construction 77
3.3.2 Data acquisition 79
3.3.3 Implementing probe theory and extracting plasma parameters 81
3.4 Summary 87

4 Characterisation of a Low Temperature Hydrogen Plasma in an Inductively Coupled Plasma Discharge Source 88
4.1 Introduction 88
4.2 Range of measurements 89
4.3 Characterisation of electron properties 90
4.3.1 Electron properties for varying pressure and power 90
4.3.2 Interpretation of electron property measurements 92
4.3.3 Comparison with published ICP research 94
4.3.4 Conclusions about available regimes 96
4.4 Measurements of atomic and molecular emission 97
4.4.1 Emission results for varying pressure and power 98
4.4.2 Analysis of Balmer line emission for varying discharge conditions . . 100
4.4.3 Analysis of Fulcher band emission for varying discharge conditions . 101
4.4.4 Interpretation of atomic and molecular emission measurements . . . 104
4.5 Summary 108

5 A Study of Low Temperature Plasma Conditions Close to Divertor-like Materials 111
5.1 Introduction 111
5.2 Range of conditions utilised 112
5.3 Measurements of electron properties 115
5.3.1 Electron properties for varying power, pressure and sample temperature 115
5.3.2 Interpretation of trends in plasma parameters close to samples . . . 121

5.4 Measurements of atomic and molecular emission close to sample surfaces . . 123
5.4.1 Emission results close to material surfaces for varying pressure, power and sample temperature 124
5.4.2 Analysis of Balmer line emission for varying discharge and material conditions 134
5.4.3 Analysis of Fulcher band emission for varying discharge and material conditions 136
5.4.4 Interpretation of emission measurements close to the samples 137
5.5 Summary 142

6 Emission Measurements in the MAST-U Divertor 145
6.1 Introduction 145
6.2 Range of measurements and experimental set up 146
6.3 Atomic and molecular emission in the MAST-U divertor 150
6.3.1 Emission measurements for varying divertor conditions and configurations 151
6.3.2 Analysis of Fulcher band emission for varying divertor conditions . . 160
6.3.3 Interpretation of emission measurements 161
6.4 Summary 165

7 The Development of a Zero-Dimensional Collisional-Radiative Model 167
7.1 Research aims 168
7.2 Model structure 169
7.3 Development of the collisional-radiative model 169
7.3.1 The inclusion of molecular species 170
7.3.2 Emission intensity calculation 172
7.3.3 Wall recycling coefficient 174
7.4 Benchmarking with the Yacora CR model 176
7.5 Comparison with experimental data 177
7.6 Summary 178

8 Conclusions and Future Work 181
8.1 Conclusions 181
8.2 Suggestions for future work 184
8.3 Outlook 185

References 186

List of Figures

1.1 Fusion cross-sections as a function of incident particle kinetic energy. From this it can be seen that the D-T reaction has the highest cross-section compared with other reactions, making it a favourable reaction to utilise in fusion experiments. Copied from [3]. 19
1.2 The progress made over the last 50 years by a variety of tokamaks around the world to achieve energy breakeven and fusion ignition through increasing values of $nT\tau_e$. Copied from [13]. 24
1.3 Schematic overview of (a) a conventional tokamak and (b) a stellarator device to illustrated the difference in shape and magnetic coil structure. Copied from [16]. 25
1.4 The experimental set up of an inertial confinement fusion reaction using a gold hohlraum, indicating the laser beams and fuel capsule. Copied from [22]. 26
1.5 A comparison of the divertor geometric configurations available in the MAST-U tokamak. The black lines show the the shape of the divertor region, the blue lines indicate the magnetic field lines throughout the divertor, with the field lines in the Super-X configuration extending furthest into the divertor leg, and the red lines indicate the last closed flux surface. Adapted from [23]. 27
1.6 A poloidal cross-section of a conventional tokamak, showing the key features of the tokamak plasma. Copied from [24]. 28
1.7 A comparison of the cross-section of a conventional versus a spherical tokamak with reference to the aspect ratio, A, and elongation, κ. Copied from [34]. 30
1.8 Schematic of the main components of the MAST-U upgrade tokamak. Copied from [38]. 31

2.1 A range of different plasmas characterised by their temperature and plasma density. Copied from [47]. 38

2.2 Schematic representation of the electromagnetic fields created inside the ICP chamber by applying RF power to the planar coil through the dielectric window. Copied from [51]. 40
2.3 (a) The ICP capacitive E-mode in which the coil E field dominates in the plasma bulk. (b) An induced electric field and corresponding ring current generated in the skin layer in the inductive H-mode. Adapted from [62]. . . 42
2.4 Poloidal cross-section of a single-null tokamak plasma, highlighting the divertor region, separatrix and X-point. Copied from [67]. 45
2.5 A schematic of the key processes and temperature and density profiles within a detached divertor plasma. Copied from [41]. 47
2.6 The behaviour of hydrocarbon molecules and key atomic and molecular processes within the plasma divertor region. Copied from [101]. 50
2.7 A micrograph image of the tungsten nanostructures formed through helium bombardment. Copied from [104]. 51
2.8 The first four Balmer emission lines of hydrogen and their corresponding wavelengths. 59
2.9 A plot of the potential curves, vibrational energy levels and wave functions for some of the states of H_2. Copied from [101]. 60
2.10 An example spectra of the Fulcher band of H_2. Indicated are an example of lines within the P-, Q- and R-branches of the vibrational transitions. Copied from [130]. 61

3.1 Schematic of the University of Liverpool inductively coupled plasma discharge source, highlighting the position of the RF matching unit, induction coil, and ports in relation to the centre of the chamber. 65
3.2 A horizontal cross-section of the ICP chamber to show the diagnostic ports, positions of the “bulk” plasma measurements and sample heater position. . 68
3.3 A horizontal cross-section of the ICP rig to show the diagnostic ports, measurement positions and sample heater position with the edge plasma probe. 69
3.4 A horizontal cross-section of the ICP rig to show the four lines of sight used in emission measurements close to the material samples. LOS1, the closest line of sight to the sample, is 2.175 cm away from the sample surface, and the subsequent lines of sight are separated by 1 cm. 70
3.5 A full hydrogen spectra collected in the UoL discharge plasma rig for a discharge pressure of 10 Pa and RF input power of 300 W. The H_α, H_β, H_γ lines and Fulcher band are indicated. Collected using the Ocean Optics spectrometer. 71
3.6 An example Gaussian fit to a H_α line collected using the Horiba FHR1000 spectrometer. The raw data and best fit are indicated. 74

3.7 An example Boltzmann plot collected in the ICP discharge plasma at 10 Pa and 300 W using the Horiba FHR1000 spectrometer. The data points are calculated using the intensity and wavelength of the Q-branch (1-1) band with respect to rotational energy, $F_V(J)$. 76
3.8 (a) The dimensions and shape of the "bulk" Langmuir probe. (b) The dimensions and shape of the "edge" Langmuir probe. 79
3.9 A schematic of the Langmuir probe ramp circuit utilised to bias the probe in diagnostic measurements. The circuit is comprised of a ramp generator used to supply a sawtooth waveform to the probe, and both a voltage probe and differential amplifier in order to measure the current and voltage simultaneously. 80
3.10 An ideal IV characteristic indicating the electron and ion saturation regions, the transition region and the plasma and floating potentials. Adapted from [140]. 81

4.1 Electron temperature and electron density for varying discharge pressure at a constant power of 100 W collected using a Langmuir probe in the centre of the chamber. 91
4.2 Electron temperature and electron density for varying RF power at a constant pressure of 10 Pa collected using a Langmuir probe in the centre of the chamber. 92
4.3 Mean free path for elastic electron-hydrogen molecule collisions for varying pressure at 500 K. Cross-sections used in mean free path calculations taken from [152]. 94
4.4 A plot of electron density and electron temperature for varying discharge pressure at a constant input power of 520 W. Taken from [154]. 95
4.5 Electron temperature and density for varying pressure at a constant power of 100 W. A copy of Figure 4.1 to highlight the three available regimes, (i) low pressure below 4 Pa (ii) intermediate pressures between 4 - 7 Pa and (iii) high pressures above 7 Pa. 97
4.6 H_α, H_β and H_γ line intensity for varying discharge pressure for a fixed power of 100 W. 99
4.7 H_α, H_β and H_γ line intensity for varying RF power at a fixed pressure of 10 Pa. 100
4.8 Fulcher band spectra Collected in the centre of the ICP chamber at a constant pressure of 10 Pa and power of 300 W. 101
4.9 Fulcher band Q1 (0-0), (1-1) and (2-2) line intensity for varying pressure at a fixed RF power of 100 W. 102
4.10 Fulcher band Q1 (0-0), (1-1) and (2-2) line intensity for varying power at a discharge pressure of 10 Pa. 102

4.11 The ratio of the H_γ to H_α line intensities for varying pressure at a constant RF power of 100 W. 103
4.12 The ratio of H_γ to H_α line intensities for varying power at a constant pressure of 10 Pa. 104
4.13 Boltzmann plot and rotational temperatures for 1, 5 and 10 Pa at a constant power of 100 W calculated using the Q-branch (0-0) band. 105
4.14 Boltzmann plot and rotational temperatures for 10, 50, 100 and 300 W at a constant pressure of 10 Pa calculated using the Q-branch (0-0) band. . . . 106

5.1 A repeat of Figure 3.3 to show the horizontal cross-section of the ICP rig to highlight the diagnostic ports, measurement positions and sample heater position with the edge plasma probe. 114
5.2 Electron temperature and density measurements for varying pressure with carbon, tungsten and nanostructured tungsten samples inserted into the plasma at a constant power of 100 W and sample temperature of 100C. Measured in the centre of the chamber using the "bulk" Langmuir probe. . 116
5.3 Electron temperature and density measurements for varying power with carbon, tungsten and nanostructured tungsten samples inserted into the plasma at a constant pressure of 10 Pa and sample temperature of 100C. Measured in the centre of the chamber using the "bulk" Langmuir probe. . 117
5.4 Electron temperature measurements for varying sample temperature with carbon, tungsten and nanostructured tungsten samples inserted into the plasma at a constant pressure of 10 Pa and RF power of 100 W. Measured in the centre of the chamber using the "bulk" Langmuir probe. 118
5.5 Electron density measurements for varying sample temperature with carbon, tungsten and nanostructured tungsten samples inserted into the plasma at a constant pressure of 10 Pa and RF power of 100 W. Measured in the centre of the chamber using the "bulk" Langmuir probe. 119
5.6 Electron temperature measurements for varying sample temperature with carbon, tungsten and nanostructured tungsten samples inserted into the plasma at a constant pressure of 10 Pa and RF power of 100 W. Measured close to the surface of the sample using the "edge" Langmuir probe. 120
5.7 Electron density measurements for varying sample temperature with carbon, tungsten and nanostructured tungsten samples inserted into the plasma at a constant pressure of 10 Pa and RF power of 100 W. Measured close to the surface of the sample using the "edge" Langmuir probe. 121
5.8 A repeat of Figure 3.4 to show the horizontal cross-section of the ICP rig and highlight the four lines of sight used in emission measurements close to the material sample. LOS1, the closest line of sight to the sample, is 2.175 cm away from the sample surface, and the subsequent lines of sight are separated by 1 cm. 123

5.9 H_α, H_β and H_γ line intensities for varying pressure with a carbon sample inserted into the plasma at a constant power of 100 W and sample temperature of 100C using LOS1, the line of sight closest to the sample. . . 125
5.10 H_α, H_β and H_γ line intensities for varying pressure with a tungsten sample inserted into the plasma at a constant power of 100 W and sample temperature 100C using LOS1, the line of sight closest to the sample. . . . 126
5.11 H_α, H_β and H_γ line intensities for varying pressure with a nanostructured tungsten sample inserted into the plasma at a constant power of 100 W and sample temperature 100C using LOS1, the line of sight closest to the sample.127
5.12 H_α line intensity for varying pressure with carbon, tungsten and nanostructured tungsten samples inserted into the plasma at a constant power of 100 W and sample temperature 100C using LOS1, the line of sight closest to the sample. 127
5.13 H_α, H_β and H_γ line intensities for varying power with a carbon sample inserted into the plasma at a constant pressure of 10 Pa and sample temperature 100C using LOS1, the line of sight closest to the sample. . . . 128
5.14 H_α, H_β and H_γ line intensities for varying power with a smooth tungsten sample inserted into the plasma at a constant pressure of 10 Pa and sample temperature 100C using LOS1, the line of sight closest to the sample. . . . 128
5.15 H_α, H_β and H_γ line intensities for varying power with a nanostructured tungsten sample inserted into the plasma at a constant pressure of 10 Pa and sample temperature 100C using LOS1, the line of sight closest to the sample. 129
5.16 H_α line intensity for varying power with carbon, tungsten and nanostructured tungsten samples inserted into the plasma at a constant pressure of 10 Pa and sample temperature 100C using LOS1, the line of sight closest to the sample. 129
5.17 H_α, H_β and H_γ line intensities for varying sample temperature with a carbon sample inserted into the plasma at a constant pressure of 10 Pa and RF power of 100W using LOS1, the line of sight closest to the sample. 130
5.18 H_α, H_β and H_γ line intensities for varying sample temperature with a smooth tungsten sample inserted into the plasma at a constant pressure of 10 Pa and RF power of 100W using LOS1, the line of sight closest to the sample. 131
5.19 H_α, H_β and H_γ line intensities for varying sample temperature with a nanostructured tungsten sample inserted into the plasma at a constant pressure of 10 Pa and RF power of 100W using LOS1, the line of sight closest to the sample. 131

5.20 H_α line intensity for varying sample temperature with carbon, tungsten and nanostructured tungsten samples inserted into the plasma at a constant pressure of 10 Pa and RF power of 100 W using LOS1, the line of sight closest to the sample. 132
5.21 Heat map of the H_α intensity for varying line of sight and sample temperature with a carbon sample inserted in the plasma. The gas pressure is fixed at 10 Pa and RF power at 100 W. 133
5.22 Heat map of the H_α intensity for varying line of sight and sample temperature with a smooth sample inserted in the plasma. The gas pressure is fixed at 10 Pa and RF power at 100 W. 133
5.23 Heat map of the H_α intensity for varying line of sight and sample temperature with a nanostructured sample inserted in the plasma. The gas pressure is fixed at 10 Pa and RF power at 100 W. 134
5.24 Fulcher band spectra in the presence of the carbon sample using LOS1, the line of sight closest to the sample. Collected at a constant pressure of 10 Pa, power of 300 W and sample temperature of 100C. 135
5.25 Fulcher band spectra in the presence of the smooth tungsten sample using LOS1, the line of sight closest to the sample. Collected at a constant pressure of 10 Pa, power of 300 W and sample temperature of 100C. 136
5.26 Fulcher band spectra in the presence of the nanostructured tungsten sample using LOS1, the line of sight closest to the sample. Collected at a constant pressure of 10 Pa, power of 300 W and sample temperature of 100C. 137
5.27 Hydrogen spectra in the presence of the carbon sample using LOS1, the line of sight closest to the sample. Collected at a constant pressure of 10 Pa, power of 300 W and sample temperature of 100C. Carbon emission lines are emphasised with the red dashed lines. 138
5.28 Hydrogen spectra in the presence of the smooth tungsten sample using LOS1, the line of sight closest to the sample. Collected at a constant pressure of 10 Pa, power of 300 W and sample temperature of 100C. Tungsten emission lines are emphasised with the red dashed lines. 138
5.29 The ratio of the H_γ to H_α line intensities with all three samples for varying gas pressure at a constant RF power of 100 W and sample temperature of 100C. 139
5.30 The ratio of the H_γ to H_α line intensities with all three samples for varying RF power at a constant pressure of 10 Pa and sample temperature of 100C. 139
5.31 The ratio of the H_γ to H_α line intensities with all three samples for varying sample temperature at a constant pressure of 10 Pa and RF power of 100 W.140
5.32 Boltzmann plot and rotational temperatures at constant pressure of 10 Pa, power of 300 W and sample temperature 1000C in the presence of a carbon, smooth tungsten and nanostructured tungsten sample. Boltzmann plot calculated using the Q-branch (1-1) band. 140

6.1 A detailed schematic of the MAST-U tokamak with annotations highlighting the divertor tiles, poloidal coils and structure of the machine. Copied from [155] 147
6.2 A schematic of the line of sight configuration through the MAST-U divertor region connected to the DMS system. Fibre 1 is close to the divertor surface at tile 5, and fibre 20 approaches the entrance of the divertor. Fibre 13 intersects tiles 2 and 3. Taken from the MAST Users page. 149
6.3 A comparison of the conventional and Super-X divertor configurations utilised in the MAST-U tokamak divertor. The magnetic field lines can be seen to extend further into the leg of the Super-X divertor when compared with the conventional configuration. Taken from the MAST Users page. . . 150
6.4 Emission data for each fibre as a function of time for shot number 45243. (a) shows the D_α emission profile, (b) shows the Fulcher band profile, (c) corresponds to the CD band emission and (d) to the n=6/5 Balmer line ratio.152
6.5 Emission data for each fibre as a function of time for shot number 45247. (a) shows the D_α emission profile, (b) shows the Fulcher band profile, (c) corresponds to the CD band emission and (d) to the n=6/5 Balmer line ratio.153
6.6 Emission data for each fibre as a function of time for shot number 45371. (a) shows the D_α emission profile, (b) shows the Fulcher band profile, (c) corresponds to the CD band emission and (d) to the n=6/5 Balmer line ratio.155
6.7 Emission data for each fibre as a function of time for shot number 45372. (a) shows the D_α emission profile, (b) shows the Fulcher band profile, (c) corresponds to the CD band emission and (d) to the n=6/5 Balmer line ratio.156
6.8 Emission data for each fibre as a function of time for shot number 45376. (a) shows the D_α emission profile, (b) shows the Fulcher band profile, (c) corresponds to the CD band emission and (d) to the n=6/5 Balmer line ratio.157
6.9 Emission data for each fibre as a function of time for shot number 45377. (a) shows the D_α emission profile, (b) shows the Fulcher band profile, (c) corresponds to the CD band emission and (d) to the n=6/5 Balmer line ratio.159
6.10 Boltzmann plot and rotational temperature calculated using the (0-0) Q-branch lines of the high resolution Fulcher band measured in shot 45068 with a conventional divertor configuration. 160
6.11 Boltzmann plot and rotational temperature calculated using the (0-0) Q-branch lines of the high resolution Fulcher band measured in shot 45244 with a Super-X divertor configuration. 162
6.12 Boltzmann plot and rotational temperature calculated using the (0-0) Q-branch lines of the high resolution Fulcher band measured in shot 45248 with a conventional divertor configuration. 163

7.1 Flowchart highlighting the structure of the model in order to calculate the rate equations for each species. 170

7.2 The development of the reaction rates for the loss reactions of H_3^+ over time. 173
7.3 Densities of all the species included in the model over time until steady-state convergence. 174
7.4 The density of the H_2 vibrational species, v=0-12, over time. 175
7.5 Emission intensity against wavelength plot for the Balmer series outputted by the CR model with the intensity plotted on a log scale. 176
7.6 Benchmarking of the ratio of the H_γ to H_α intensities for varying electron density outputted by the Keio CR 0D model and the Yacora 0D model. . . 178
7.7 Comparison of the ratio of the experimental H_γ to H_α intensities for varying electron density with the outputted CR model ratio. 179

List of Tables

3.1 Overview of the specifications of the spectroscopic diagnostic equipment utilised in experiments in the University of Liverpool ICP discharge source. 72

3.2 Positions of the spectral lines corresponding to the Q-branch (0-0), (1-1) and (2-2) bands of the hydrogen molecular Fulcher band. (Wavelengths in nm.) 76

5.1 A description of the key properties of the three materials utilised in measurements close to divertor-like samples. 113

6.1 Description of the MAST-U shot numbers utilised in this research. 148

7.1 Reactions for hydrogen atoms and molecules previously added to the 0D collisional-radiative model. 171

7.2 Reactions for hydrogen atoms and molecules that were added to the 0D collisional-radiative model through the development of the code. 172

Chapter 1

Introduction

With the ever increasing global population and looming climate crisis, there is a growing demand for clean, sustainable and secure sources of energy. By 2040, there will be a 30 percent increase in global energy demand as economies and populations grow [1], which is only predicted to increase further into the second half of the decade. Clean, green sources of energy will be necessary to mitigate the impacts of climate change, and nuclear fusion is predicted to be an important component of a carbon-free future energy mix. Fusion energy could also be useful as a supply of low-carbon baseline, continuous, reliable energy, to fill the gaps where intermittent renewable energy sources, such as solar and wind power, are not operational.

Current research into fusion energy systems is focused on reactors that contain very high temperature plasmas, heated to extreme temperatures to enable the fusion of hydrogen isotopes. The research in this thesis consists of several linked studies that are aimed at understanding the low temperature plasma conditions that exist at the edge of fusion machines. This research uses laboratory-based discharge plasmas to generate conditions that are similar in many respects to those found near the walls and surfaces in fusion machines. While small laboratory discharges cannot replicate these conditions exactly, the same physical processes can be investigated, and the laboratory environment enables plasma control and diagnostic access which is not readily available for fusion machines. The understanding gained in these controlled conditions can then be used to help interpret the results of studies of fusion systems. This thesis uses this approach, with the bulk of the work being carried out using a laboratory discharge at the University of Liverpool, together with experimental and modelling studies carried out with collaborators at the

UK's Culham Centre for Fusion Energy, and Keio University in Japan.

The main research topics covered in this thesis are: (i) Optical emission spectroscopy and Langmuir probe measurements in an inductively coupled hydrogen plasma, (ii) Emission and plasma parameter measurements in front of divertor-like materials for varying surface temperature and structure in an ICP device, (iii) Analysis of emission measurements in the MAST-U divertor for varying plasma conditions and divertor configurations, (iv) Collisional-radiative modelling and the importance of atomic and molecular behaviour in low temperature plasmas. This chapter aims to provide an introduction to these research objectives and introduce the key topics that underpin this thesis. These objectives are then outlined in further detail at the end of this chapter in Section 1.4 with an outline of this thesis presented in Section 1.5.

1.1 Fusion energy and the tokamak

Due to the environmental impact and finite supply of fossil fuels on Earth, alternative clean, green and sustainable methods of creating electricity, including nuclear fusion, have been explored. Nuclear fusion reactions have a higher energy density than nuclear fission [2], and there is inherently no risk of nuclear meltdown using fusion machines. Fusion energy is therefore often seen as favourable when comparing the two forms of nuclear energy generation. Fusion energy has the potential to provide a clean, unlimited energy source for future generations and revolutionise the energy industry. Since the origin of fusion energy research over 70 years ago, producing energy for commercial use has been the ultimate goal of fusion scientists. This research has prompted a search for the optimum plasma and reactor material conditions to push towards commercial power production with longer machine lifetimes.

Fusion is the process in which light nuclei fuse together to produce a heavier particle, releasing energy due to the change in mass via $E = mc^2$. For a small change in mass, a significant amount of energy is released from fusion reactions and as such is an energy dense form of energy production. Fusion in the Sun occurs through the fusion of two hydrogen nuclei to produce a helium nucleus. The Sun's large gravitational forces confine the species in order for the energetic nuclei to overcome the repulsive electrostatic forces and fuse. The most attractive candidate for fusion on Earth is the fusion of two isotopes of hydrogen, deuterium (D) and tritium (T). Figure 1.1 shows the cross-sections for the most favourable fusion reactions, with the D-T reaction having the lowest threshold and largest

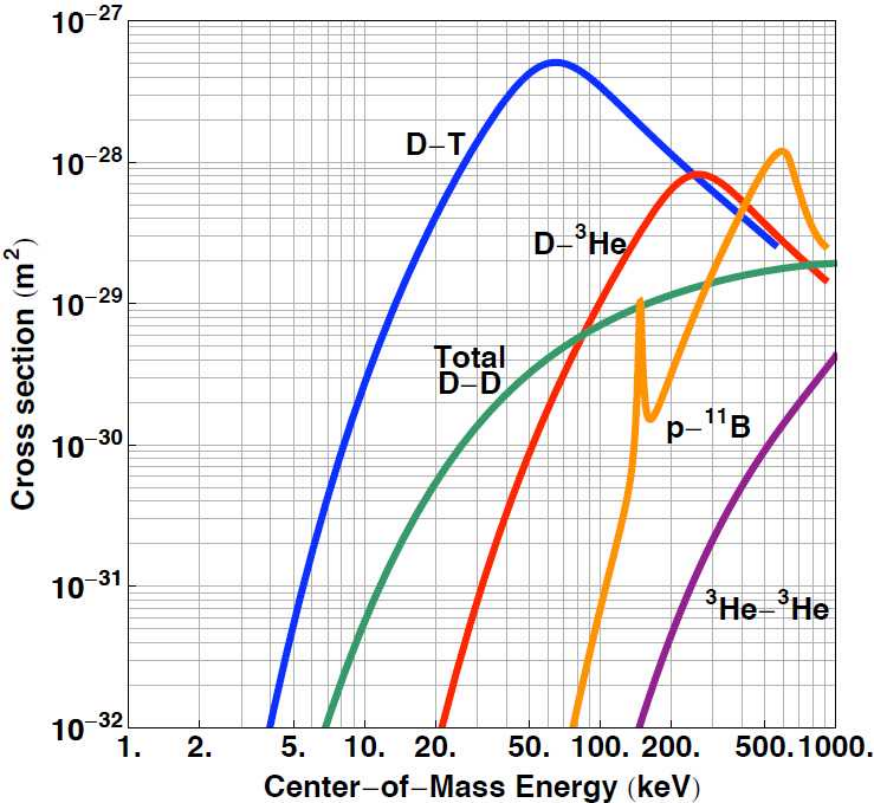

Figure 1.1: Fusion cross-sections as a function of incident particle kinetic energy. From this it can be seen that the D-T reaction has the highest cross-section compared with other reactions, making it a favourable reaction to utilise in fusion experiments. Copied from [3].

magnitude over a wide range of energy. This higher reaction cross-section implies that for achievable temperatures on Earth, there would be more fusion reactions per second, and therefore would result in a higher power output. For these reasons, D-T fusion is the target of nearly all current fusion research.

The products of the D-T reaction are a helium-4 nuclei and a neutron via the process:

$$\begin{aligned} {}^2_1\mathrm{D} + {}^3_1\mathrm{T} &\rightarrow {}^4_2\mathrm{He} + {}^1_0\mathrm{n} \\ \mathrm{Q} &= 17.6\ \mathrm{MeV} \end{aligned} \tag{1.1}$$

where Q is the energy released from nuclear mass conversion. The neutron generated in

this reaction has an energy of 14.1 MeV. The energy from this neutron will be used to generate electricity in practical fusion machines, via the heating of water in order to drive a steam turbine. The remaining energy from the reaction is carried by the helium nucleus and will be used to sustain the fusion plasma itself.

Deuterium is abundant on Earth, with deuterium atoms making up 0.0156 percent of the naturally occurring hydrogen in oceans [4] and therefore is readily accessible with an almost inexhaustible supply. Tritium however is an unstable isotope of hydrogen, with a half-life of 12.3 years and only occurs in trace quantities in nature. Tritium can be generated in fission reactors [5] but as these reactors shut down, fusion plants will need to be tritium self-sufficient and the tritium fuel cycle will need to be replenished. Tritium is intended to be bred on site using lithium-coated 'breeder blanket' modules which will surround the vacuum vessel of the fusion power plant. The lithium in the breeder blankets will then be utilised to breed the tritium fusion fuel through the following reaction,

$$\begin{aligned} {}^{6}_{3}\mathrm{Li} + {}^{1}_{0}\mathrm{n} \rightarrow {}^{4}_{2}\mathrm{He} + {}^{3}_{1}\mathrm{T} \\ \mathrm{Q} = 4.8\ \mathrm{MeV} \end{aligned} \tag{1.2}$$

where the neutron here is the same neutron produced through the D-T reaction described in Equation 1.1.

Breeding tritium from lithium has the potential to provide an almost limitless supply of fusion fuel. Lithium is also an abundant resource on Earth with known reserves available to supply 5000 years of fuel for tritium breeding in fusion machines, with an additional 35 million years worth of lithium to be extracted from seawater [6].

Temperatures and densities in fusion machines must be sufficiently high in order for the fusion fuel (e.g deuterium and tritium nuclei) to overcome the repulsive electrostatic forces and combine via the process of nuclear fusion. Typical core plasma temperatures required for this, for example in the Joint European Torus, are up to 200 million degrees Celsius, over 10 times the temperatures found at the centre of the Sun. Under these hot dense conditions, the fusion fuel becomes ionised and forms a plasma, introducing a variety of complex physics challenges including plasma confinement, instabilities and plasma-surface interactions. Therefore to fully understand and optimise the conditions in fusion machines for commercial fusion, it is vital to study plasma physics.

1.1.1 Plasmas and their properties

The fundamental science of plasma physics has been studied since the first half of the nineteenth century [7] and is outlined in a number of publications [8,9]. In this introduction, a brief description and definition of the plasma state is given to provide the building blocks for research into nuclear fusion.

The fourth state of matter, "plasma", exists when atoms from a gas are stripped of their electrons due to extreme heating or strong electromagnetic fields. This then results in a "soup" of electrons, ions and nuclei in the form of an ionised or partially-ionised gas, consequently named plasma from the Ancient Greek $\pi\lambda\acute{\alpha}\sigma\mu\alpha$ meaning "to mold". However not all ionised gases are plasmas. For an ionised gas to qualify as a plasma, three conditions should be met. The first condition states that for an ionised gas to be a plasma, it must maintain quasineutrality. Quasineutrality defines the net neutral charge of a plasma, despite the existence of local electric fields at smaller scales [8]. The condition that a plasma is quasineutral indicates that it can be treated as globally electrically neutral and the ion density, n_i can be assumed to be equal to the electron density, n_e, such that,

$$n_i \approx n_e \tag{1.3}$$

The Debye length, λ_D, is a characteristic length which describes the scale at which electric fields in plasmas are shielded by mobile charge carriers (e.g electrons and ions). Outside of a Debye sphere, i.e a volume with radius λ_D, any electric potentials are screened and so quasineutrality is maintained. This length is derived from the solution to Poisson's equation for a potential in the presence of an external charge and is given by the following relationship between the plasma density, n and the electron temperature, T_e,

$$\lambda_D = \left(\frac{\epsilon_0 k T_e}{n e^2}\right)^{\frac{1}{2}} \tag{1.4}$$

If λ_D is much less than the size of the system, L,

$$\lambda_D \ll L \tag{1.5}$$

then any net charge can be shielded over a small region and so the plasma can be considered quasineutral. However on the scale of λ_D, this is not the case and electromagnetic forces still exist.

In addition to quasineutrality, plasmas must also exhibit 'collective behaviour' as a result of the long range electromagnetic interactions between the plasma particles [10]. This implies the number of particles N_D, in the Debye sphere (shielding volume) must be large enough to shield the net charge, and so in a sphere of radius λ_D, must satisfy:

$$N_D = \frac{4}{3}\pi n \lambda_D^3 \ggg 1 \tag{1.6}$$

The final condition describes the collisions within a ionised gas. If the charged particles in an ionised gas collide with neutral atoms frequently, hydrodynamic forces dominate over the electromagnetic forces and so do not display plasma characteristics. For a gas to behave like a plasma, the relationship between the plasma oscillation frequency, ω, and the mean time between collisions with neutral atoms, τ, must satisfy the following condition.

$$\omega\tau > 1 \tag{1.7}$$

If an ionised gas satisfies conditions 1.5-1.7, it is a plasma.

As the most abundant form of matter in the universe, common plasmas include the Aurora Borealis, lightning and neon lights. Since plasmas are ionised, high temperatures are required to preserve the level of ionisation needed to sustain them. The level of ionisation of a plasma can be determined using the Saha equation. This equation gives the total ionisation of a gas at thermal equilibrium by comparing the density of ionised atoms, n_i, and neutral atoms, n_n, through the relationship below [8],

$$\frac{n_i}{n_n} \approx 2.4 \times 10^{21} \frac{T^{\frac{3}{2}}}{n_i} e^{\frac{-U_i}{kT}} \tag{1.8}$$

Recombination of the electrons and ions in a plasma will occur at cooler temperatures and results in the plasma returning to a gaseous state. This is an important process to consider when studying low temperature plasmas. In this thesis, there will be a focus on studying atomic and molecular processes relevant to low temperature edge plasmas as current predictive codes for modelling low temperature plasmas are unsuccessful in a few vital areas. A plethora of processes, including recombination, will be investigated in this research to study the trends in plasma parameters and emission for varying plasma conditions in order to improve the accuracy of these plasma models.

1.1.2 Plasma conditions for fusion

Significantly high temperatures and densities are required to ignite and sustain nuclear fusion reactions. To define this ignition condition, the Lawson criteria, or 'fusion triple product' describes the relationship between three important plasma quantities that influence the probability of ignition. These quantities are the plasma temperature, T, which indicates the energy of the plasma species, the plasma density, n, which indicates how many nuclei are available to react with each other, and the confinement time, τ_E, which indicates the time that the reaction partners are close enough to each other for fusion to take place. For ignition, this triple product must satisfy the following condition:

$$nT\tau_E > 2 \times 10^{21} \text{ keVm}^{-3}\text{s} \tag{1.9}$$

For the types of fusion plasmas that are being developed for power systems, the combination of conditions to satisfy the Lawson criteria are such that the temperature should be in the range 10-20 keV, values of n should be in the range 10^{20} m^{-3} with a value of τ_E around a few seconds [11].

Over the past few decades, significant progress has been made by international fusion experiments to satisfy the Lawson criteria. The ITER project, alongside many private fusion companies, hope to achieve energy breakeven within the next couple of decades, before a demonstration power plant, DEMO, is constructed. Figure 1.2 shows the progression of the triple product since the 1970s. The data points are labelled with the acronym of the research machine where that value was obtained. The required conditions for ignition are in the top right of the figure, where the value expected for ITER, currently under construction, is shown. The record for energy released from fusion is currently held by the Joint European Torus (JET) tokamak, with 16 MW of fusion power generated for an input power of 24 MW (Q=0.67) [12]. Q is defined as the ratio of the energy produced from fusion reactions to the energy injected into a fusion machine to ignite a plasma and sustain fusion reactions. For Q $>$ 1, energy breakeven is achieved.

The most advanced fusion approaches utilise toroidal magnetic fields to confine plasmas in donut-shaped chambers called "tokamaks". This approach is called Magnetic Confinement Fusion (MCF), with designs for these fusion machines consisting of a combination of toroidal and poloidal magnetic coils to confine the fusion plasma. However, other designs exist including spherical "cored-apple" shaped tokamaks that utilise smaller aspect ratios resulting in higher plasma pressure and magnetic field efficiency and therefore

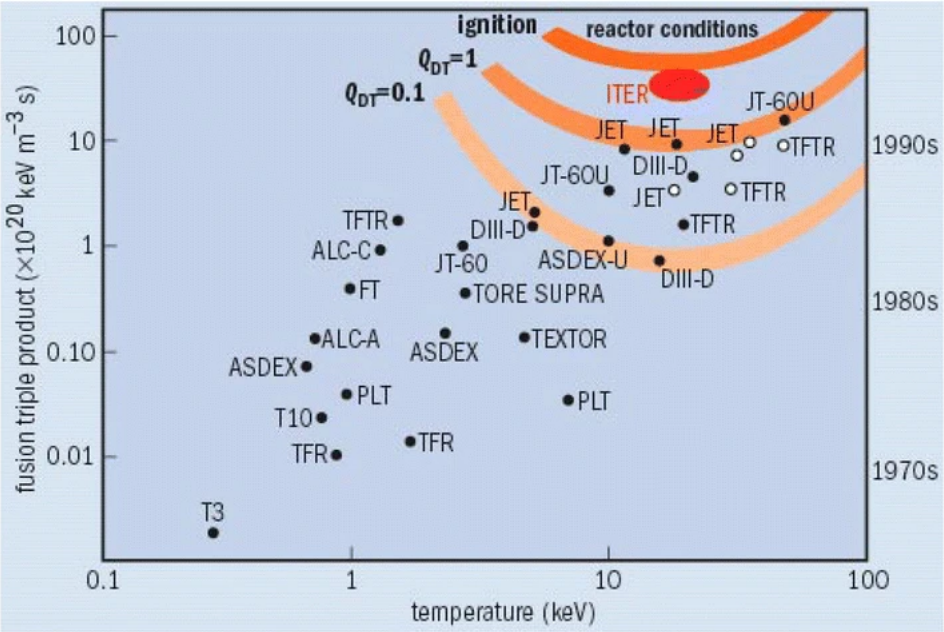

Figure 1.2: The progress made over the last 50 years by a variety of tokamaks around the world to achieve energy breakeven and fusion ignition through increasing values of $nT\tau_e$. Copied from [13].

improved stability [14], or more complex geometries of magnets utilised in the design of stellarators. A schematic comparing the shape of a conventional tokamak and a stellarator can be seen in Figure 1.3.

In MCF, the high energy neutron produced through the reaction shown in Equation 1.1, which is not contained by the magnetic fields, collides with the reactor walls and transfers it's energy to the machine materials. This energy is then used to heat water circulating through the tokamak walls to drive a steam turbine and generate electricity with no greenhouse gas emission. The stable helium nucleus is pumped out of the chamber after creation and so is quickly removed from the fusion fuel-cycle. By the end of the 1950s, the first tokamak utilising magnetic fields, T-1 [15], began operation and in the following decades the United Kingdom, the United States, Russia, France, Germany and Japan had produced functioning fusion machines for use in MCF research.

Another candidate for plasma confinement utilised for nuclear fusion is the use of high power lasers for Inertial Confinement Fusion (ICF). ICF uses energy from high powered lasers to compress pellets of fuel to high enough densities and temperatures to achieve

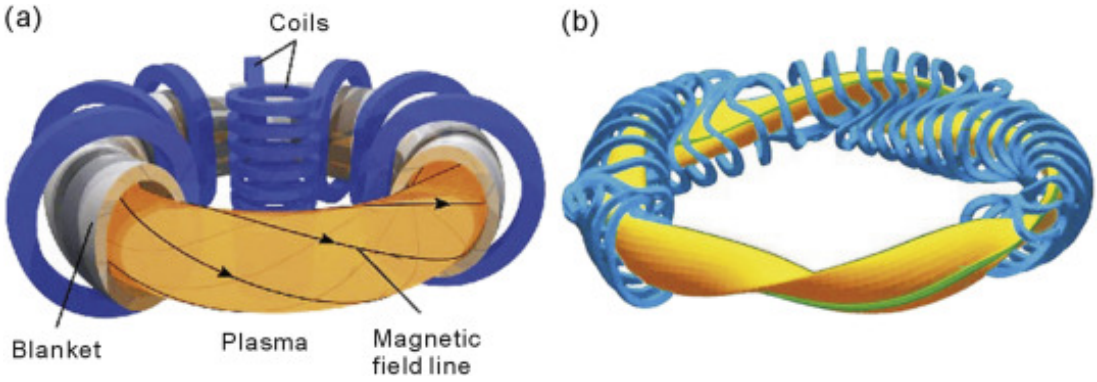

Figure 1.3: Schematic overview of (a) a conventional tokamak and (b) a stellarator device to illustrated the difference in shape and magnetic coil structure. Copied from [16].

fusion ignition. A laser beam heats the outer layer of the fuel pellet, causing it to explode. An opposite force compresses the fuel and shock waves with sufficient power can heat the fuel to high enough temperatures for fusion to occur. ICF experiments often incorporate the use of a gold cavity, a hohlraum, to radiate X-rays onto the pellet of fuel and heat up the outer layer, as seen in Figure 1.4.

ICF experiments conducted in facilities, such as The National Ignition Facility (NIF) in California, aim to produce fusion reactions with enough electrical energy to generate a viable amount for commercial use, (around 500 MW of electrical power [17]). Recent successful experiments at NIF achieved 1.3 MJ of output energy, around 70 percent of the energy delivered to the fuel capsule by the laser, and future experiments plan to bring this closer to breakeven. There also exist a variety of novel approaches to nuclear fusion employed by private fusion companies worldwide, including non-thermal hydrogen-boron fusion [18], magnetic-pinch configurations [19], and magnetised target fusion [20]. Currently there are over thirty private fusion companies worldwide aiming to demonstrate energy breakeven and build commercial fusion power plants [21] adopting a range of confinement techniques, including MCF and ICF.

The focus of the research in this thesis is on magnetically confined fusion (MCF), and research in this area is carried out worldwide using a number of medium- and large-sized tokamaks. Some past and present systems have already been referred to in Figure 1.2, which showed the historical progress of fusion towards ignition.

Large MCF experiments that utilise the “conventional” ring-donut shaped design

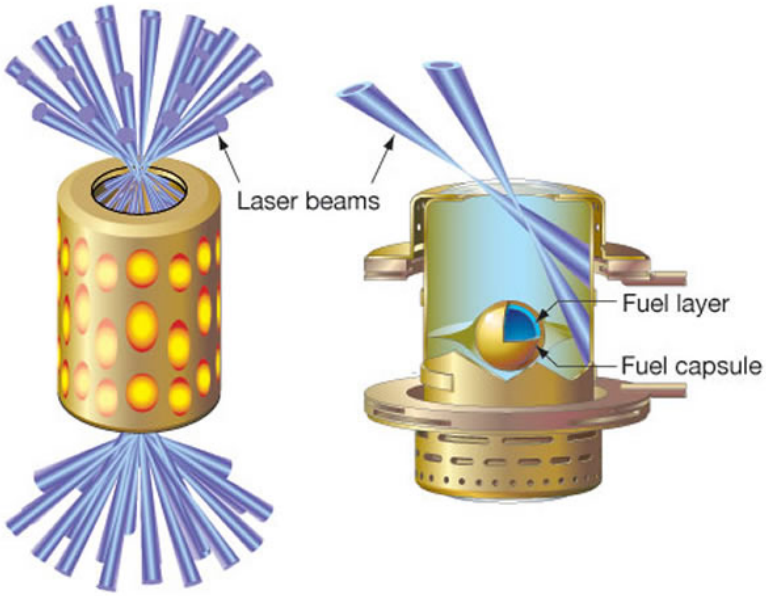

Figure 1.4: The experimental set up of an inertial confinement fusion reaction using a gold hohlraum, indicating the laser beams and fuel capsule. Copied from [22].

include the Joint European Torus (JET) tokamak based at the Culham Centre for Fusion Energy (CCFE), in Oxfordshire, UK, the Japan Torus-60 Super Advanced (JT60-SA) in Naka, Japan, and ITER, a large international collaborative fusion project located in the South of France. Successful examples of medium-sized tokamaks include the Mega Ampere Spherical Tokamak Upgrade (MAST-U), also housed at CCFE in Oxfordshire, the Tokamak à Configuration Variable (TCV) tokamak in Lausanne, Switzerland and the Axially Symmetric Divertor Experiment Upgrade (ASDEX-U) at the Max Planck Institute for Plasma Physics, Garching.

This thesis will centre on an investigation of low temperature plasmas relevant to MCF machines, specifically the power exhaust "divertor" region of tokamaks. The aim of this research is to investigate the behaviour of atoms and molecules in these regions to allow for a better understanding of the processes that can improve the power handling in tokamaks.

1.1.3 Divertors and the power exhaust problem

As magnetic confinement is not perfect in tokamaks, a dedicated exhaust region that is magnetically separated from the core plasma is required to handle power leaks from

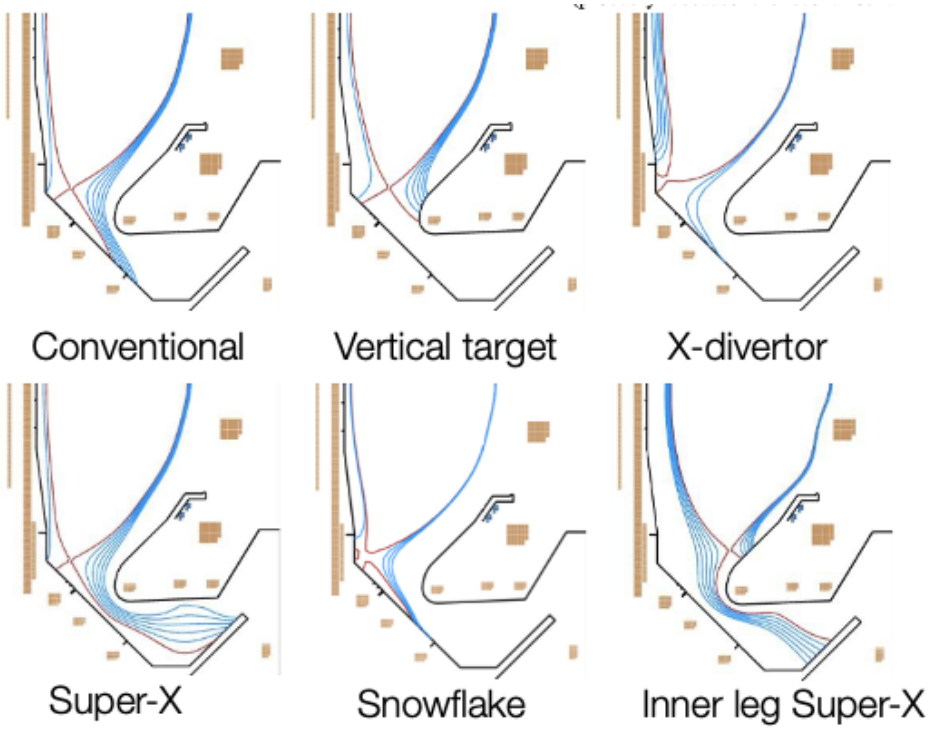

Figure 1.5: A comparison of the divertor geometric configurations available in the MAST-U tokamak. The black lines show the the shape of the divertor region, the blue lines indicate the magnetic field lines throughout the divertor, with the field lines in the Super-X configuration extending furthest into the divertor leg, and the red lines indicate the last closed flux surface. Adapted from [23].

the core plasma and prevent contamination of the fusion fuel. To handle the leakage of heat and particles into the tokamak scrape-off layer, an exhaust system is designed. The tokamak power exhaust, or divertor, is typically located at the base of the fusion reactor vessel (illustrated in the tokamak schematic in Figure 1.6) and is an extractor for heat and impurities created by fusion reactions. The divertor region is formed by "diverting" the magnetic field with a magnetic null, or X-point, also shown in Figure 1.6. Impurities from the plasma facing materials within the vessel are extracted by the electrodynamical divertor by an E $\times$ B force, limiting damage to the vessel materials from neutronic and energetic loads while also reducing the level of contamination in the core plasma.

Tokamak divertors are required to handle high heat fluxes, as high energy particles flow into the divertor and hit strike points on the divertor plates. It is predicted that

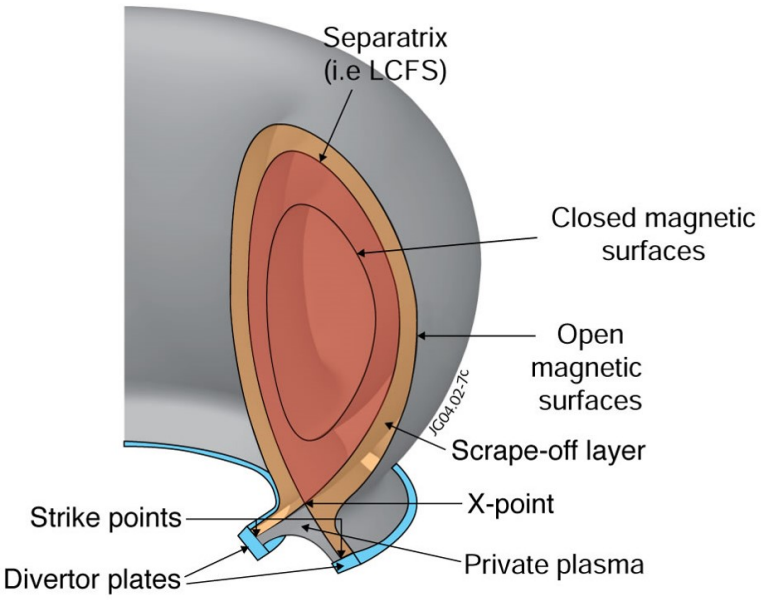

Figure 1.6: A poloidal cross-section of a conventional tokamak, showing the key features of the tokamak plasma. Copied from [24].

without any mitigation, a heat flux of 400 MWm^{-2} will be incident on the divertor targets of the ITER reactor [25]. However the tolerable engineering limit of the tungsten divertor tiles is < 10 MWm^{-2} [26], and therefore it is vital that methods of reducing this heat flux be implemented. One method currently under investigation is the use of divertor detachment to reduce the power flux to the divertor plates. High radiated power fractions by impurity seeding and detachment are required to limit the heat and particle fluxes to the material surfaces. Control, characterisation and understanding of divertor detachment with significant power fluxes to the divertor are crucial for the sound extrapolation of results from present-day tokamaks such as ASDEX Upgrade and JET to future reactors like DEMO via ITER.

Plasma detachment in tokamak divertors is defined as the state in which the divertor plasma is "detached", or separated, from the divertor tiles by cooler neutral gas with the primary goal to dissipate energy before high heat fluxes strike divertor materials. This can be achieved via neutral pumping into the divertor region or through manipulating the gradients of temperature and density throughout the divertor region in order to stimulate increased levels of plasma recombination. Large pressure gradients are observed parallel

to the magnetic field which results in a reduction in the power fluxes reaching the divertor surfaces. The processes that influence divertor detachment will be discussed in a subsequent section and will be important for this research project.

By changing the magnetic geometry within the divertor, the high energy load can be managed by increasing the target area. The power flux can then be spread over a larger surface area, reducing the damage to the divertor tiles. A critical review on the effects of varying magnetic geometry on detachment and the exhaust of power and particles can be seen in [27]. Advanced magnetic geometries have been designed for use in ITER and the Mega Ampère Spherical Tokamak Upgrade (MAST-U) device, including the Super-X and snowflake divertor geometries [28] which can be seen in Figure 1.5, where they are compared with the conventional divertor design. These geometries have been extensively studied and compared [29] to understand the effects on the target parameters. By integrating these geometric solutions into the designs for ITER divertors, the power flux to the plates can be reduced by a factor of 100, key for the sustainable economic operation of future fusion machines.

For the successful operation of ITER and future fusion devices, divertor plasma detachment will be essential to control and reduce particle and heat fluxes to divertor materials to below their material limits of 10 MWm^{-2}. A deeper understanding of the detachment process is needed to inform predictive modelling codes and enable greater control of the tokamak power exhaust.

For detachment to be realised, neutral gas should be retained in the divertor region which can be achieved by neutral gas pumping [30]. The heat load is then spread over a larger surface area as the energy from the plasma particles is lost via radiation through interactions in the detached region. This allows for cooling of the exhaust plasma to around 1 eV [31], before impacting with divertor surfaces, minimising the heat flux to the materials to below the maximum allowed flux of 10 MWm^{-2}. Due to the advantages of utilising a detached regime for the power exhaust and divertor materials, many scientists are aiming to fully understand how to initiate detachment, and how different effects such as edge localised modes and plasma impurities influence the detached region at the plasma edge [32, 33]. The physics of divertor detachment will be discussed further in Chapter 2. The processes that trigger detachment are not fully understood despite over 30 years of research aiming to quantify detachment onset in divertors. There is currently significant gaps in predictive modelling codes to outline the key atomic and molecular processes that influence detachment specifically in relation to varying divertor configurations and plasma

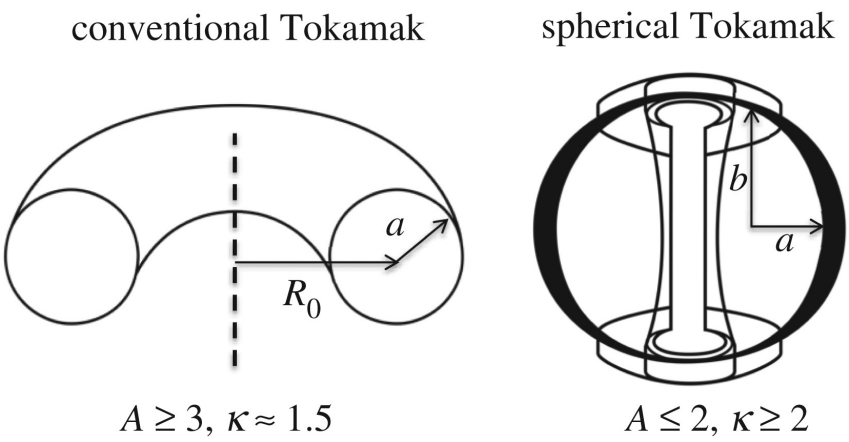

Figure 1.7: A comparison of the cross-section of a conventional versus a spherical tokamak with reference to the aspect ratio, A, and elongation, κ. Copied from [34].

facing component materials.

1.1.4 The MAST-U tokamak

The Mega Ampère Spherical Tokamak Upgrade (MAST-U) is a spherical tokamak located at the Culham Centre for Fusion Energy (CCFE) in Abingdon, Oxfordshire. A spherical tokamak is so called due to the more spherical shape of the plasma when compared with the flatter donut torus shape observed in conventional tokamaks. A comparison of the cross-section of conventional and spherical tokamaks can be seen in Figure 1.7, where the aspect ratio, A, and elongation, κ, are defined as:

$$A = \frac{R_0}{a}$$
$$\kappa = \frac{b}{a}$$

where A is the aspect ratio, the ratio of the major radius, R_0, to the minor radius, a. The elongation, κ, is the ratio the height of the plasma measured from the midplane, b, to the minor radius, a.

A diagram of the MAST-U tokamak can be seen in Figure 1.8. The MAST-U tokamak has a major radius, R_0, of 0.85 m and minor radius of, a, 0.65 m [35], slightly smaller that it's neighbour, the JET tokamak, which has major and minor radii of 2.96 m and

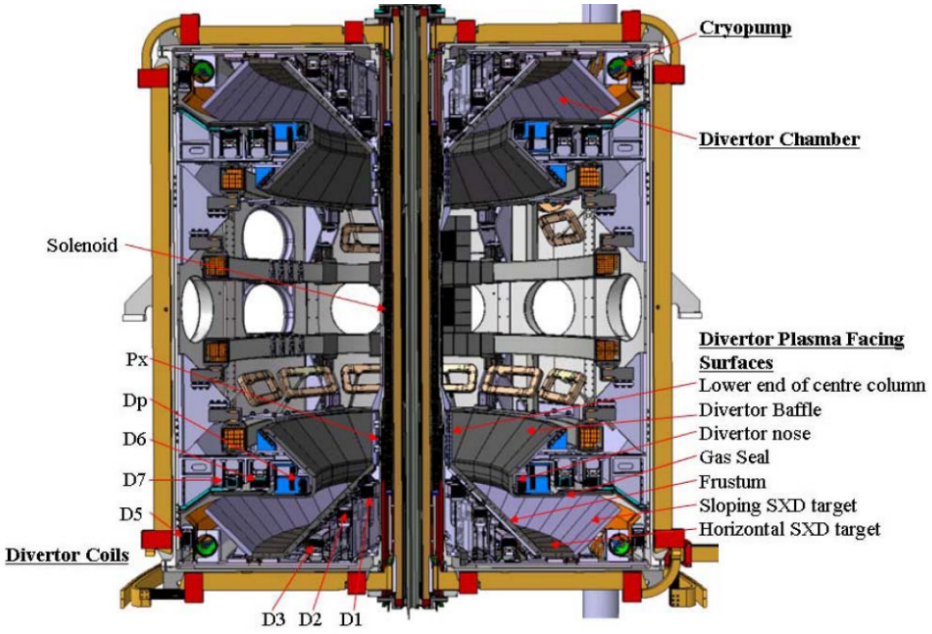

Figure 1.8: Schematic of the main components of the MAST-U upgrade tokamak. Copied from [38].

1.25 m respectively [36]. In MAST-U, graphite is used for the first wall and divertor tile material due to the excellent mechanical and thermal properties of carbon and carbon composites [37]. The research at MAST-U centres on studying the advantages of spherical tighter aspect ratio tokamaks over conventional toroidal tokamaks and the effects of advanced divertor configurations on the power exhaust, specifically focusing on the onset of detachment and the effects of detachment on reducing damage to the plasma facing components.

In 2021 the upgrade of the MAST tokamak was completed, which included the modification of the exhaust system to allow for alternative divertor configurations, such as the Super-X divertor. The first MAST-U experimental campaigns concluded in Autumn 2021 and many of the experimental shots aimed to quantify the extent to which alternative divertor configurations and neutral gas pumping regimes affect the degree of detachment in the divertor region, alongside measuring the flux of heat and particles to the divertor tiles. During this campaign, experimental measurements in the Super-X divertor demonstrated a tenfold reduction in the flux of heat to the divertor tiles [39]. This result is crucial as it successfully demonstrates that varying the divertor configuration to extend the target area

results in a significantly reduced heat flux to within material limits. This will subsequently reduce the level of damage to reactor materials, increasing the lifetime of these materials and push towards economically viable commercial fusion.

Plasma emission in the low temperature region of the MAST-U divertor will be investigated in this thesis. Knowledge of low temperature plasmas will be used to study the molecular properties of the gas discharges as they interact with the divertor plates. In Chapter 6 of this thesis, results from a collaborative research project looking at the behaviour of atoms and molecules in the MAST-U tokamak will be detailed. This work focuses on investigating how the emission from atoms and molecules varies with different plasma conditions and divertor configurations in MAST-U, with a focus on the effects of divertor detachment on trends in the plasma emission.

1.2 Atoms and molecules in low temperature plasmas

The low temperature plasmas that exist in the divertors of MCF reactors have significant populations of atomic and molecular species, as well as charged particles originating from the core plasma. While atomic and molecular processes have been studied extensively in non-fusion plasma research, there is still a need to understand how these processes influence the behaviour of the plasma in divertors.

A suite of diagnostic techniques can be utilised to investigate atoms and molecules in low temperature plasmas. Two powerful techniques, and the focus of this research, are optical emission spectroscopy, which allows for a characterisation of the composition of a plasma via atomic and molecular emission, and Langmuir probes, useful for diagnosing densities, temperatures and other plasma properties in low temperature plasmas.

The high densities and low temperatures found in divertor plasmas are characterised by the balance of a number of important atomic and molecular processes. Momentum exchange and particle transport in these plasmas can be influenced by many processes including, ionisation, recombination, mutual neutralisation, elastic scattering and resonant charge transfer among hydrogen ions, atoms, and molecules. As the key atomic and molecular processes relevant to divertor plasmas are currently poorly understood in models, the aim of this research is to investigate, both experimentally and computationally through the use of a collisional-radiative model, the most important processes in tokamak divertor plasmas. The gaps in these models and a review of existing research in these fields will be outlined in Chapter 2 and more information will be presented on the key atomic and

molecular processes which will be the focus of this research.

Collisional-radiative (CR) models are predominantly utilised to study the distribution of atoms and molecules over their excited states. Through the use of these models, the population densities of the excited states of atoms and molecules in a plasma can be determined by solving a set of steady-state rate balance equations. By analysing the model outputs, the interplay between different atomic and molecular processes can be studied and the most important processes identified. This outcome is beneficial when applied to the study of atoms and molecules in low temperature plasmas (e.g in tokamak divertors), as by combining data from experimental emission measurements and information of the key processes from CR models, a deeper understanding can be gained of the interplay between atomic and molecular processes (e.g plasma volume recombination) and detached regions of tokamak divertors. A detailed description of the structure of collisional-radiative models and a review of existing models can be found in Chapter 2.

1.3 The role of laboratory experiments in understanding the exhaust problem in tokamaks

Although a considerable number of both public and private fusion laboratories exist worldwide that focus on diagnosing plasmas relevant to magnetic confinement fusion, the complex geometry of tokamaks can limit the diagnostic access to ports or specific regions of interest. Additionally, bids for time in experimental campaigns on large fusion experiments are competitive, making it difficult to complete investigations on specific plasma behaviour or access certain conditions. To solve these issues, it can be useful to support tokamak research with the use of basic experiments in laboratory plasmas in order to recreate specific conditions and provide further understanding of key processes in tokamak plasmas.

Complimentary laboratory studies in discharge plasmas can be utilised to diagnose plasma parameters and the behaviour of atoms and molecules in chambers that are more easily accessible and on a smaller scale. The focus of these studies can then hone in on specific gaps in knowledge in order to improve databases and predictive modelling. By using discharge plasmas, such as the inductively coupled plasma discharge source used in this study, an exploration of the key processes in low temperature plasmas can be completed which might be inaccessible in large tokamaks.

There exist many examples of research studies which demonstrate the benefits of

utilising laboratory experiments to validate or invalidate theoretical plasma models, discover unexpected results that might not have been accessible in larger machines, and provide physical insight into phenomena, as discussed in [40].

Linear plasma devices, such as NAGDIS-II, PISCES-B, GAMMA-10 and MAGNUM PSI, can be used to study plasma-material interactions, plasma detachment and the effect of gas pumping on the evolution of detachment [41–44]. Discharge plasmas can be utilised to study the behaviour of ions in fusion reactions and caesium-free alternatives of negative ion sources for power injection into tokamaks [45, 46]. Inductively coupled plasmas (ICPs) and other low temperature discharge plasma sources can also be utilised to replicate specific conditions in edge plasmas of tokamaks. Low temperatures of a few eV and lower densities compared with linear plasma devices can be employed to reproduce low temperature plasma conditions found in tokamak divertor regions. The availability of these conditions in ICP devices can then allow for a study of plasma parameter trends with increased diagnostic accessibility and specific control of the discharge conditions and consequently the plasma parameters.

The work presented in the first two research chapters of this thesis will centre on diagnostic studies of atoms and molecules close to divertor-like surfaces in an inductively coupled plasma discharge source at the University of Liverpool. The ICP device is useful as a test bed to gather experimental data of plasma emission and plasma parameters for a range of conditions. By varying RF power, gas discharge pressure and also surface material and temperature of three different samples, trends in the emission, temperature and density can be studied. These measurements in low temperature discharge plasmas will be compared to experimental emission data from the MAST-U divertor in order to link the key processes in both fusion and non-fusion low temperature plasmas.

1.4 Thesis objectives

The aim of this research is to improve the understanding of partially ionised plasmas close to divertor surfaces, with the specific goal of improving the treatment of atomic and molecular species in divertor modelling codes. Achievement of this aim will have significant impact on the accuracy of predictive simulation codes used for ITER and post-ITER devices. This goal will be achieved by investigating molecular properties of H_2 and D_2 discharges in contact with divertor relevant surfaces.

A combination of fusion and non-fusion low temperature hydrogen plasma research

techniques will be employed to identify key physical processes both in the plasma volume and close to divertor surfaces. Optical emission spectroscopy will be utilised to study the plasma emission close to divertor materials and identify trends in atomic and molecular behaviour important to provide the experimental knowledge for predictive modelling codes of plasma detachment.

In this research, an inductively coupled discharge plasma at the University of Liverpool will be investigated to understand the behaviour of atoms and molecules in partially ionised hydrogen plasmas. Divertor-like samples will be submerged in the ICP via a bespoke sample heater, and the plasma and surface conditions will be varied to enable a study of the effects of these samples on the plasma emission.

The main research objectives of this work are to:

1. Understand the degree to which local plasma conditions such as gas temperature and density influence plasma properties both in the immediate vicinity of the surface and further into the plasma volume
2. Understand the degree to which surface properties (intrinsic material properties and surface conditions) influence molecular properties in the vicinity of a divertor-like surface
3. Investigate how changes in the material and plasma properties are reflected in the plasma emission, focusing on Balmer line (atomic) and Fulcher band (molecular) emission
4. Quantify how the degree of detachment/non-detachment of the plasma incident on the surface and the condition of the surface itself is reflected in the properties of the partially ionised plasma near the surface

To achieve these objectives, the aims of this research were to:

(i) Implement diagnostic techniques to extract information about the plasma emission and plasma parameters of a low temperature inductively coupled plasma

(ii) Utilise emission-based diagnostic techniques to investigate low temperature plasma-surface interactions relevant for divertor regions in fusion tokamaks

(iii) Compare experimental emission data with a 0D collisional-radiative model in order to quantify key atomic and molecular processes

1.5 Thesis outline

This thesis is organised into eight chapters. The first chapter aims to outline the key topics relevant to this thesis, present the aims and objectives of this research, and provide a structure to the following seven chapters. Chapter 2 will present a review of the existing research on both low temperature fusion and discharge plasmas, the importance of atomic and molecular processes in low temperature plasmas and diagnostic techniques utilised to study atoms and molecules. The main aim of Chapter 2 is to outline the motivation of this research and situate this work into the existing research field. Chapter 3 will outline the experimental set up of the diagnostic measurements that underpin this research. In this chapter, a description of the inductively coupled plasma at the University of Liverpool will be presented alongside a description of the diagnostic theory used to analyse the measurements that underpin this thesis. Throughout the following three chapters, experimental results will be presented from research carried out both in the inductively coupled plasma discharge source at the University of Liverpool, and in the MAST-U tokamak divertor, with the aim of characterising the behaviour of atoms and molecules in low temperature edge plasmas. Chapter 7 centres on a computational research collaboration at Keio University, in which the extension of a 0D collisional-radiative model is presented in order to characterise the key processes in low temperature plasmas. Conclusions on the research presented in Chapters 4-7 and suggestions for future work are summarised in Chapter 8.

Chapter 2

Low Temperature Edge Plasmas and Divertor Physics

The focus of this chapter will be to introduce the motivation of this research and situate this thesis in context with previous work within the wider research fields. A discussion of relevant research in the surrounding fields will be presented, including low temperature plasmas in both tokamaks and low pressure discharge plasmas, atomic and molecular processes in edge plasmas, diagnostic techniques and collisional-radiative models.

This chapter is composed of four sections and aims to provide a basis for the motivation behind the research presented in this thesis. The first section will outline the existing research into low temperature discharge plasmas at low pressures, specifically highlighting the use of inductively coupled plasmas. Section 2.2 will discuss low temperature regions of fusion machines and the power exhaust problem. The key areas of plasma-surface interactions will be outlined in Section 2.3 followed by a discussion on the behaviour of atoms and molecules in low temperature plasmas and the main methods of investigating these behaviours via the use of computational modelling and experimental diagnostic research.

2.1 Low pressure plasma discharges

A gas discharge is a laboratory plasma, formed by supplying enough electrical energy to ionise neutral gas. In its simplest form, the plasma is created by applying a potential difference between two electrodes. The potential difference accelerates electrons, and the

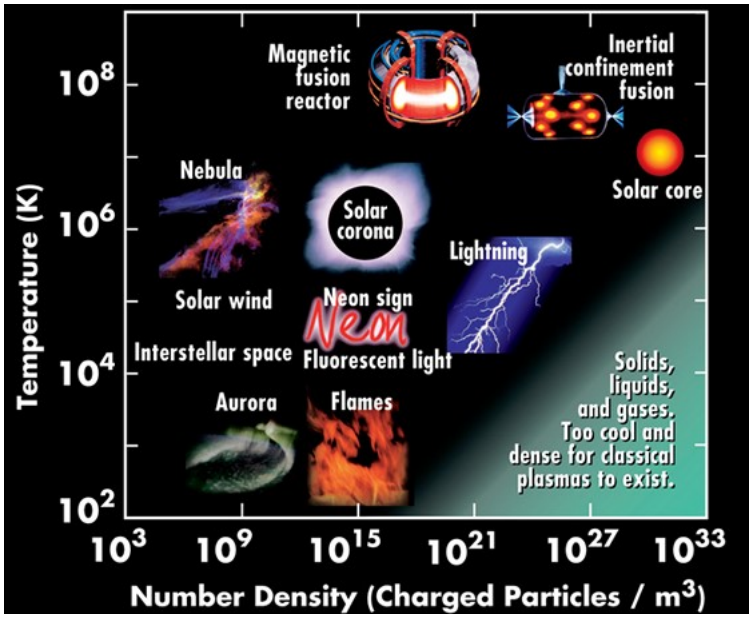

Figure 2.1: A range of different plasmas characterised by their temperature and plasma density. Copied from [47].

subsequent collisions of energetic electrons with background gas species results in the ionisation of the particles in the gas. If the electric field is strong enough, the ionisation can be sufficiently strong for a plasma to form, and the neutral gas becomes a conducting medium.

Figure 2.1 shows different types of plasmas, plotted according to their plasma density and temperature. Fusion plasmas are shown near the top of the figure, reflecting the moderate to high density and high temperatures associated with the core plasma where fusion occurs. Low temperature laboratory plasmas are located close to the centre of the figure, represented by the neon sign. This region of slightly lower density and much lower temperature is also characteristic of the edge regions of magnetically confined fusion reactors.

Low pressure plasma discharges make use of vacuum pumps and vacuum chambers in order to achieve pressures below atmospheric pressure. These low pressures are particularly useful in applications such as thin film depositions from sputtering, semiconductor etching and manufacturing of liquid crystal displays (LCDs) [48]. This is due to the longer mean free paths at low pressures, which enables a large energy distribution and therefore a

plethora of important plasma interactions are achievable.

Low pressure plasmas can be generated through a variety of different methods, including microwave plasmas, hollow cathode arc plasmas, magnetrons, dc glow discharges and radio frequency (RF) plasmas. The focus of this research will be on inductively coupled RF plasmas. A review of the existing research on low pressure RF discharges can be seen in [49, 50].

Capacitively coupled and inductively coupled plasmas (CCP and ICP) are plasma discharges which utilise radio frequency power to ignite a plasma. For a typical CCP source, one of two electrodes is connected to the RF power supply, and the other is grounded, similar to a capacitor in an electric circuit. For the diagnostic measurements presented in this thesis, an ICP discharge source is utilised in order to study the behaviour of hydrogen atoms and molecules in low temperature plasmas.

2.1.1 Inductively coupled plasmas

An inductively coupled plasma is a type of plasma discharge source in which the plasma is generated via electromagnetic induction of radio frequency waves. ICPs are typically used in plasma processing and utilise RF currents passed through an induction coil which creates a magnetic field in the chamber. This magnetic field induces a RF current in the discharge gas, resulting in plasma ignition. As the induction coil is separated from the plasma chamber by a dielectric window, ICP plasmas are relatively free of contamination. However capacitively coupled plasmas (CCPs) utilise electrodes which are submerged in the chamber and so are exposed to chemical species in plasmas.

ICP devices have been studied for over a century [51], however since the early 1990s the development of low pressure ICP sources has been a keen area of research for semiconductor manufacturing. ICPs are useful for a variety of applications due to their good uniformity, the ability to easily control their plasma densities and temperatures and their low contamination from sputtering. These properties also make ICPs suitable as a test bed for low temperature edge plasma diagnostic measurements, as the plasma properties can be controlled over a wide range of conditions.

Current research using ICPs focuses on semiconductor etching, atomic emission spectroscopy and mass spectrometry. Semiconductor etching is a very large industry that utilise reactive etching in order to remove material that is deposited on wafers of semiconducting material. High energy ions generated by a low pressure inductively coupled

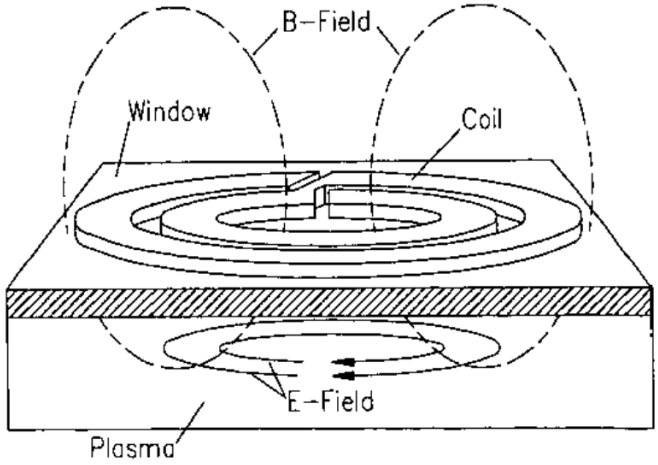

Figure 2.2: Schematic representation of the electromagnetic fields created inside the ICP chamber by applying RF power to the planar coil through the dielectric window. Copied from [51].

plasma can be used to react with the wafers and form etched patterns [52]. Inductively coupled plasmas are also used to detect chemical elements in food and wine by the use of atomic emission spectroscopy [53].

For fusion energy, ICPs can be used to simulate the low temperature regions found in divertors in order to provide further diagnostic information about the plasma behaviour that may be inaccessible in tokamaks. ICPs are also utilised to study negative hydrogen ion sources for the development of neutral beam injection systems for future fusion devices such as ITER and DEMO, e.g in the BATMAN negative ion source [54–57].

In an ICP discharge source, the dominant energy absorption mechanism is collisional/Joule heating, as electrons are accelerated by an inductive field created in the plasma volume. Figure 2.2 shows the arrangement for a planar ICP, in which an exterior planar coil generates a time dependent electric field in the chamber. Electrons in the volume are accelerated by this field, E, and then collide with neutral gas species. The Joule heating power, P_j, is formulated as,

$$P_j = e n_e \mu_e E^2 \tag{2.1}$$

where e is the electron charge, n_e is the electron density and μ_e is the electron mobility [48].

Electrons are also heated via a collisionless process through anomalous skin effects within the skin depth. The skin depth is a thin layer close to the induction coil in which the alternating current flows. If the electron mean free path is larger than this skin depth, electrons in this region close to the dielectric window interact with the oscillating RF sheaths and gain energy through stochastic heating [58].

The skin depth thickness, δ, is related to the spatial decay constant of electromagnetic waves in a plasma, α, by,

$$\delta = \frac{1}{\alpha} \tag{2.2}$$

Where α is formulated as [59],

$$\alpha = -\frac{\omega}{c}\mathrm{Im}\kappa_p^{1/2} \tag{2.3}$$

and the relative plasma dielectric constant, κ_p, is defined as,

$$\kappa_p = 1 - \frac{\omega_{pe}^2}{\omega(\omega - j\nu_m)} \approx -\frac{\omega_{pe}^2}{\omega^2(1 - j\nu_m/\omega)} \tag{2.4}$$

where ω is the frequency of the electromagnetic waves, ω_{pe} is the plasma frequency and ν_m is the elastic collision frequency.

In an ICP discharge, the frequency of the RF waves is typically lower than ω_{pe} which results in the attenuation of the waves by electrons within the skin depth.

When ω_{pe} is much larger than ν_m, Equation 2.3 becomes,

$$\alpha = \frac{\omega_{pe}}{c} \equiv \frac{1}{\delta_p} \tag{2.5}$$

and thus the collisionless skin depth, δ_p can be written as,

$$\delta_p = \frac{c}{\omega_{pe}} \tag{2.6}$$

However for $\nu_m \gg \omega$, Equation 2.3 becomes:

$$\alpha = \frac{1}{\sqrt{2}}\frac{\omega_{pe}}{c}\left(\frac{\omega}{\nu_m}\right)^{\frac{1}{2}} \equiv \frac{1}{\delta_c} \tag{2.7}$$

where δ_c, the collisional skin depth becomes,

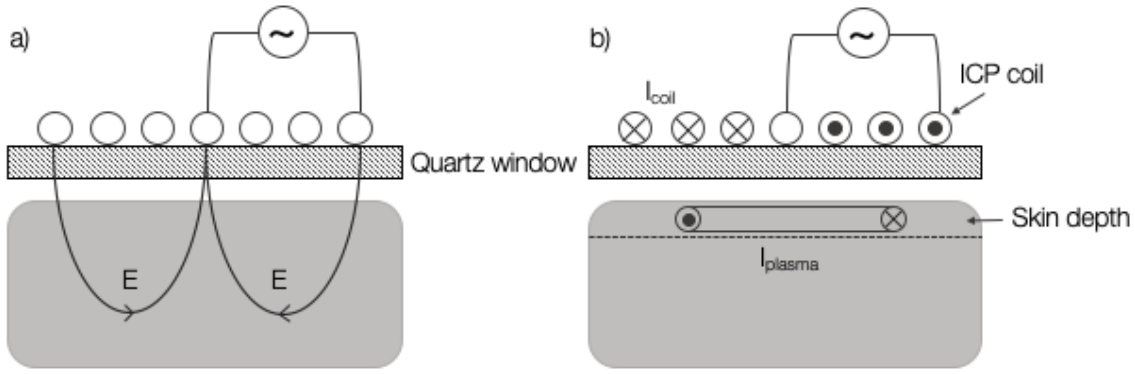

Figure 2.3: (a) The ICP capacitive E-mode in which the coil E field dominates in the plasma bulk. (b) An induced electric field and corresponding ring current generated in the skin layer in the inductive H-mode. Adapted from [62].

$$\delta_c = \delta_p \left(\frac{2\nu_m}{\omega} \right)^{\frac{1}{2}} \tag{2.8}$$

A third regime also exists to describe the anomalous skin depth, δ_e, [60, 61]. In this regime, the interaction time of the skin layer with the electrons is much less than the time period of the RF oscillations and the neutral collision frequency.

An interesting phenomenon in ICP discharge plasmas is the E to H transition. This describes the two modes of ICP discharges from the 'E' electrostatic low density mode in which axial acceleration dominates, to 'H' electromagnetic high-density mode where azimuthal acceleration dominates. This is also described as a transition from capacitive to inductive power coupling.

Figure 2.3 shows the dominance of the electric field from the ICP coil in the E-mode compared with the induced electric field and corresponding current within the skin layer in the H-mode. The capacitive E-mode is characterised by much larger plasma potentials and bigger sheaths close to the coil. Research into the relationship between capacitive coupling and inductive coupling in low pressure discharge plasmas is ongoing. In general, a discharge plasma can be defined as inductively coupled if the generation of a high-density plasma is achieved by an inductive structure in a Faraday shielded chamber. As mentioned previously, CCP discharges suffer from sputtering due to the large RF potentials created

between the inductive coil and the plasma, and so the degree of capacitive power coupling affects the level of contamination in the plasma.

At lower RF input powers, the dominant power coupling mechanism is electrostatic capacitive coupling between the plasma and the coil. This regime can be characterised by lower densities, higher plasma potentials and less plasma emission resulting in a weaker glow. For increasing input power, the transition from E mode to H mode will occur and the emission from the plasma will suddenly increase, resulting in a brighter glow from the plasma. The plasma density is much greater in H mode compared to E mode and so this transition can be utilised to achieve a wide range of plasma densities across these two modes.

2.2 Low temperature regions of fusion plasmas

Tokamak plasmas are characterised by two distinct regions, the core plasma and the edge plasma. The hot core plasma confined by the magnetic field, reaches temperatures O(keV) with plasma densities $O(10^{20}$ m$^{-3})$ [63]. In contrast, temperatures in the cooler edge plasma are magnitudes lower, typically O(eV), with densities $O(10^{18}$ m$^{-3})$ [64]. Due to the drastic differences in the core and edge plasmas of tokamaks, it is necessary to develop different approaches to diagnosing and understanding the plasmas in these regions.

The core and edge plasmas are separated by the separatrix, or last-closed-flux surface (LCFS). The separatrix is defined as the boundary between open and closed field lines in a tokamak where there is a transition from toroidal confinement to a region where magnetic field lines intersect with materials. The scrape-off layer (SOL) describes the region with open field lines, outside of the separatrix and terminating at material surfaces of the plasma facing components. The separatrix, SOL and divertor region can be seen in Figure 2.4.

The edge plasmas in the SOL region of tokamaks absorb the majority of the exhaust from the core plasma, consisting of heat and particles, and transport this along the open field lines to the divertor targets. The core particles enter the SOL and are diverted via parallel transport to the exhaust region where they interact with divertor surfaces. This region is of key interest to the studies of power handling in tokamaks, and in order to manage the high fluxes to divertor surfaces, the key mechanisms that influence divertor detachment must be understood.

Leading on from the successful results from experiments at the Joint European Torus [65, 66], the International Thermonuclear Experimental Reactor (ITER) in the south of

France, aims to demonstrate fusion energy breakeven. However the power fluxes from fusion reactions in ITER are predicted to exceed tolerable material limits of divertor tiles and so it is clear that the issue of power handling, divertor materials and divertor detachment are paramount for the success of commercial fusion.

Edge localised modes, or ELMs, are a type of plasma instability that can disrupt the fusion plasma and cause a loss of confinement. Typically ELMs occur at the edge of the fusion machines and can result in significantly high heat loads on the plasma facing components. Since ELMs introduce large power pulses into tokamaks, the power handling of divertors is a difficult problem for fusion scientists and extensive experimental and theoretical research is required. Many international research facilities focus on divertor power handling and plasma stability to reduce the damage to the plasma facing components and obtain high fusion performance in future reactors. Poloidal divertors are the principal way of controlling the particle and heat fluxes from the plasma and this section will outline the current status of the research into low temperature fusion plasmas in divertor regions.

If plasma conditions in tokamak edge plasmas can be created that can reduce the power and particle flux to divertor tiles, successful fusion power plants will be within reach. One way of reducing the flux to the divertor surfaces is detachment, which induces a barrier of neutral atoms and molecules between hot plasma particles allowing for the reduction in the level of erosion and other forms of material damage to the divertor surfaces.

2.2.1 Divertor plasmas and divertor detachment

The main confinement fields in a tokamak are created by large toroidal field coils that surround the plasma. These fields generate the closed magnetic surfaces that confine the hot core plasma and keep it separated from the chamber walls. As discussed in Chapter 1, plasma confinement is not perfect and there is a need to control the exhaust from the core plasma in tokamaks. This is achieved by using additional poloidal field coils to modify the field structure at the top and/or bottom of the plasma, to create the divertor structures of the type shown in Figure 2.4. This magnetic field configuration separates impurities from the core plasma through impurity screening in the scrape-off layer and allows for the removal of unwanted particles and energy. An overview of divertor plasma physics can be seen in [64]. In this section, a summary of the key takeaways from divertor research and detachment will be presented.

Modelling of divertor plasmas is extremely challenging as diagnostic access to tokamak

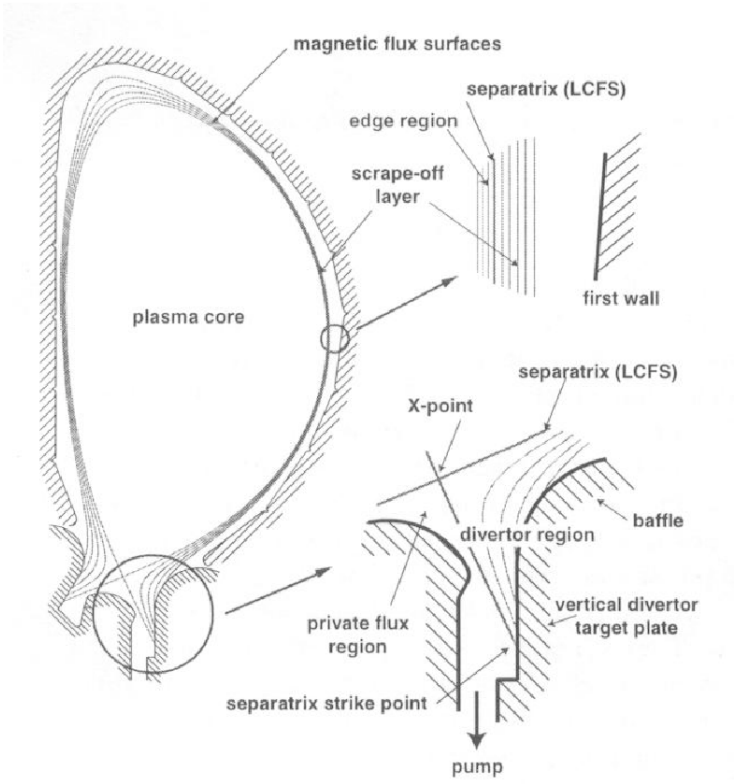

Figure 2.4: Poloidal cross-section of a single-null tokamak plasma, highlighting the divertor region, separatrix and X-point. Copied from [67].

divertors has historically been limited and hence it has been difficult to validate the results of any modelling that has been done. The understanding of atomic and molecular behaviour in low temperature fusion plasmas is still poor, and further investigations of the key processes are necessary to improve divertor plasma modelling. Fusion codes such as EIRENE [68] and SOLPS [69], include the most relevant plasma-surface interaction processes, however there are still a range of key species and reactions that are not currently considered in these codes and so experimental research into diagnosing atoms and molecules is useful to develop comprehensive models.

Divertor geometry has significant effects on tokamak power exhaust and the feasibility of divertor detachment. At the Culham Centre for Fusion Energy, the MAST-U tokamak is utilised to study the effects of alternative divertor configurations on the power exhaust region [70, 71]. This work shows how advanced geometrical configurations, e.g the Super-X

configuration, can provide improved power handling and plasma confinement within MAST-U by studying the effect of volumetric power losses on target fluxes and how neutral species in the divertor region effect core confinement.

The Tokamak à Configuration Variable tokamak (TCV), in Switzerland, was designed to study the exhaust and confinement of fusion power via complex heating and shaping capabilities. Research on the TCV tokamak also utilises diagnostic systems and control hardware to study plasma detachment and divertor physics in order to optimise power handling in tokamaks. This research will then be used in designs of future experiments for the ITER project and future fusion machines on the road to prototype fusion power plants, such as DEMO [72].

The detached plasma state is an important regime for the successful power handling of future fusion devices with higher output powers. Divertor detachment results in a significant reduction in the particle and heat loads to divertor targets to within tolerable material limits, alongside minimising erosion of divertor surfaces through sputtering, and has been studied experimentally in fusion machines [73–77]. Lower electron temperatures present in edge tokamak plasmas result in the recombination of the plasma particles which in turn decreases the flux of heat and particle to material surfaces, limits the material damage via sputtering and ultimately increases the lifetime of the plasma facing components [78, 79].

In these low temperature edge plasmas, clouds of neutral atoms and molecules form close to the divertor surface, separating the core plasma from the divertor tile resulting in the plasma becoming "detached" from the divertor tiles. Detachment is induced by a chain of both atomic and molecular processes and so by utilising diagnostic techniques, the key processes can be identified in order to characterise the conditions required for detachment.

In order to stimulate divertor detachment, neutral gas is pumped into the divertor region through impurity seeding. This reduces the heat load onto the targets as the energy from the core plasma is lost through collisions and radiation, spreading the flux of power over larger surface areas. This regime has demonstrated a significant mitigation of the steady-state heat and particle flux to divertor tiles in a number of MCF devices [80–84].

Detached plasmas are characterised by very low temperatures ($T_e < 3$ eV) with distinct layers of recombination and ionisation. Detachment requires power, particle and momentum loss through collisions and reactions. A schematic of these processes close to the divertor plate, along with the density and temperature profiles as the exhaust plasma moves from the core region to the divertor tile can be seen in Figure 2.5. Ionisation sources and

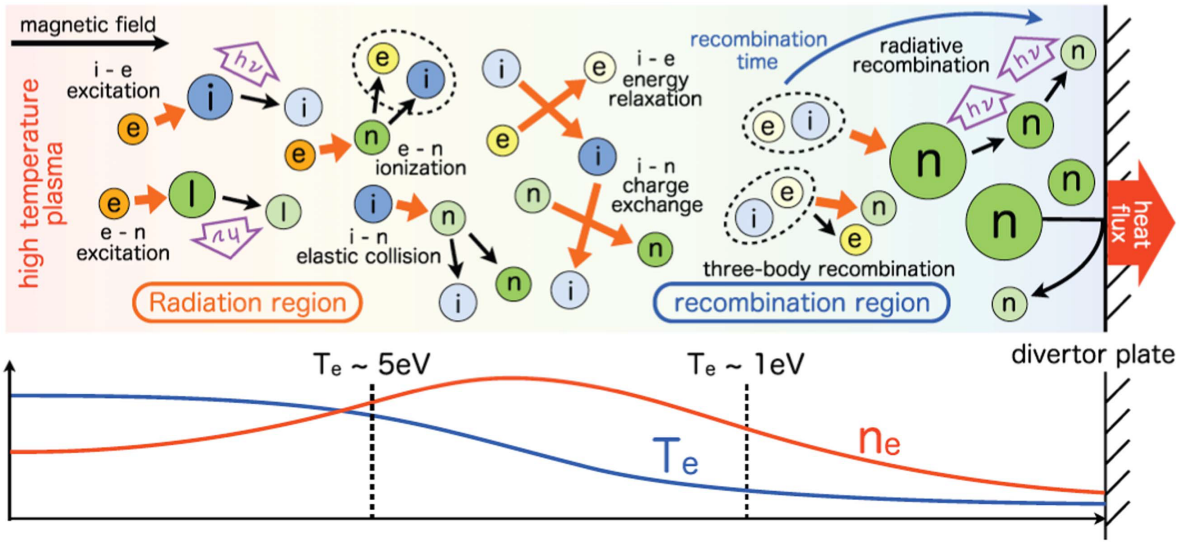

Figure 2.5: A schematic of the key processes and temperature and density profiles within a detached divertor plasma. Copied from [41].

sinks play a large role in achieving detachment and hydrogen molecules play an important part in influencing the degree of ionisation in divertor plasmas. Research into key processes, such as Molecular Assisted Recombination (MAR), provide useful information about the vibrational states of molecules in divertor regions.

Experiments at ASDEX-U at the Institute for Plasma Physics, Garching, utilise the injection of neon and deuterium gas to achieve complete detachment of the divertor while simultaneously preserving high core confinement by enhancing radiative losses using the injection of such impurities [85]. These experiments and similar research aims to characterise how divertor detachment is influence by the transport of heat and particles along magnetic field lines as well as the triggers for detachment onset [78].

The DIII-D tokamak in San Diego operates using continuous gas puffing to achieve high confinement (H-mode) plasmas [84]. The research at DIII-D aims to study the distributions of temperature and density in both the SOL and divertor region in order to generate a low temperature, low density region close to divertor surfaces. This then results in high density regions upstream of the divertor surfaces, observed in a variety of experiments by researchers at the Plasma Science and Fusion Center at the Massachusetts Institute of Technology [86]. This redistribution of density and temperature in the divertor region is a result of plasma detachment, characterised at the Fusion Research Center at the Georgia

Institute of Technology, Atlanta [87].

Researchers in the Applied Physics and Physico Informatics at Keio University [88] are studying MAR in detached regions of fusion plasmas to realise the detached plasma state. This research uses a 0D model to study how MAR and the detached state that comes as a result of this process is affected by ELM heat pulses. However there is still a lot of work to be done to frame this within a fusion context and fully understand how collisional-radiative processes influence detachment. This project will aim to investigate collisional-radiative processes and the extent to which emission measurements can be used to quantify levels of detachment in order to bridge the gap in the understanding of atoms and molecules in low temperature plasmas.

The geometry of the divertor plates can influence the likelihood of plasma detachment and make it easier to attain. Many fusion scientists and engineers have modelled divertor geometry to enable the improvement of power handling. Research at the DIII-D tokamak [89] has centred on the effects of divertor geometry on detached regions of tokamaks and have found that impurity transport codes can predict how levels of impurities in divertor plasmas can reduce the degree of detachment, therefore different divertor geometries should be employed to control impurity transport and power exhaust properties in order to increase the likelihood of detachment.

2.3 Plasma-surface interactions in low temperature plasmas

In the exhaust edge plasma region of fusion machines, heat and particles interact with tokamak plasma facing components (PFC), such as wall and divertor materials. These plasma-surface interactions can result in damage to the materials and processes such as sputtering and erosion can reduce the lifetime of the reactor components [90–92]. It is therefore very important to fully understand the key plasma-surface interaction mechanisms in low temperature plasmas in order to reduce the damage to PFCs and increase the lifetime of fusion materials, in doing so increasing the economic viability of steady-state fusion power plants.

Divertor detachment is characterised by low temperature, low density plasma conditions close to divertor surfaces. Plasma particles close to divertor tiles can interact with the surfaces via atomic and molecular processes. The subsequent reactions can lead to recycling of core or surface species, re-radiation of energy from the divertor surfaces, hybrid molecule generation from hydrogen isotopes and divertor surface species. Divertor surfaces are also

expected to be micro- or nano-structured, however the effect of these structures on plasma properties are currently not understood. These features are considered to be relevant to the successful operation of tokamak divertors, but despite the recently improved diagnostic access to divertor regions on MAST-U and ASDEX-U, the information that can be gained from experimental measurements is limited.

High fluxes of particles in tokamaks lead to increased rates of erosion and deposition of reactor materials. Eroded materials are then deposited throughout the machine and can contaminate the core plasma. Contamination of the core plasma by impurities from PFC materials can have an effect on the degree of confinement in the core and plasma detachment in the edge region. By studying the effect of different fusion relevant material impurities, e.g carbon and nanostructured tungsten, on the onset of divertor detachment, information on the mechanisms to reduce the damage to the PFCs without sacrificing plasma confinement can be gained.

High densities of hydrogen molecules in edge plasmas are a result of the hydrogen ions originating in the core plasma impacting divertor surfaces. These ions are absorbed by the divertor tiles and then subsequently desorbed, contributing to the detached region close to the divertor plates. Therefore it is clear that molecular hydrogen species play an important role in detachment and power handling.

Carbon, beryllium and tungsten are typically used for plasma facing materials. Carbon is used as the divertor tile material in the MAST-U tokamak due to it's high sublimation temperature, thermal-shock resistance and low atomic number [67]. Graphite is utilised as the material for the JET first wall, in TCV, and in the National Spherical Torus Experiment (NSTX) [93].

Tungsten is utilised as a plasma-facing component in many tokamaks due to it's high atomic number, high melting point and low sputtering yield. Tungsten is used for JET divertor [94], the ASDEX-U first wall [95], and will be used for the ITER divertor tiles. However under neutron irradiation, hydrogen and helium bubbles can form on tungsten surfaces and cause material swelling [96], alongside a loss of ductility with high heat loads.

Beryllium will be employed to cover the first wall of the ITER main chamber. Beryllium has a low atomic number and low radiation yield, which ensures low contamination of the core plasma. However the low melting point of beryllium limits the use of this material in the divertor where power loads can exceed 20 MWm^{-2} during transient events [97].

For machines utilising carbon divertor plates, hydrocarbon molecules can be produced through chemical sputtering. Figure 2.6 illustrates the main molecular processes

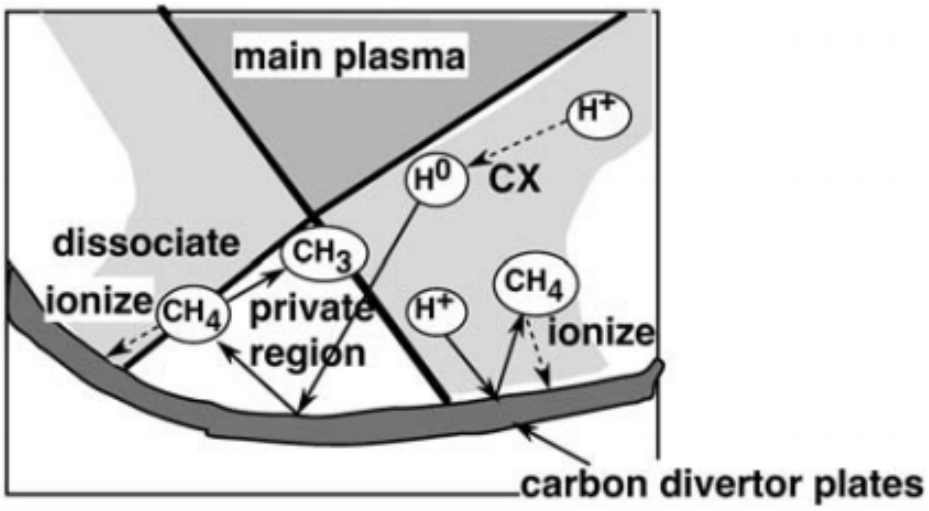

Figure 2.6: The behaviour of hydrocarbon molecules and key atomic and molecular processes within the plasma divertor region. Copied from [101].

influencing hydrocarbons in plasma divertors. These hydrocarbon molecules play a key role in radiative losses and contamination from impurities and can be ionised close to divertor surfaces. These ionised molecules can then be transported back to the divertor surfaces via parallel magnetic field lines or upstream, resulting in core plasma contamination. Amorphous carbon films can be formed through plasma-surface interaction processes [98, 99], and research at the Max Planck Institute of Plasma Physics aims to characterise the interplay of hydrogen and carbon molecules [100].

Erosion yields vary significantly for different plasma-facing materials. For the high-Z materials, such as tungsten, erosion yields are much less than low-Z PFC yields of graphite [101]. However graphite is still an appealing material for PFCs in tokamaks due to it's excellent thermal properties. The choice of PFC material also influences the properties of the plasma, as erosion from the wall materials can lead to impurities penetrating into the centre of the chamber. This has two negative implications for fusion performance. Firstly, radiation from impurity species in edge plasmas can alter plasma temperatures and pressure gradients, which can negatively impact plasma stability and H-mode confinement. Secondly, impurities reaching the plasma core dilute the fusion fuel which leads to a reduction in the fusion power output. PFCs should be chosen so as to reduce these negative effects from the transport of impurities into both the core and edge regions.

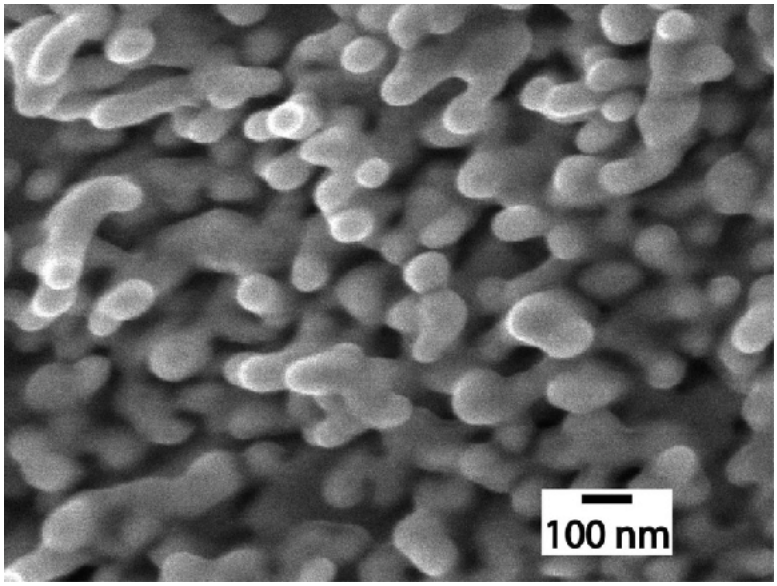

Figure 2.7: A micrograph image of the tungsten nanostructures formed through helium bombardment. Copied from [104].

Nanostructured tungsten, or "fuzzy" tungsten, is a phenomena produced through high fluences of light ions (e.g hydrogen or helium) which causes irradiation of hot tungsten surfaces. These structures are comprised of a number of interlocking tendrils, with diameters around 50 nm [102], as seen in Figure 2.7. Depending on the plasma and surface conditions, these tendrils can form layers of "fuzz" up to several μm thick [103].

Tungsten will be used as a plasma facing component in the divertors of a number of future fusion devices, such as ITER. As helium is a by-product of D-T fusion reactions (seen in Equation 1.1), a deeper understanding of these nanostructures is required to ensure the successful control of the power exhaust in future machines. There are a number of advantages to using nanostructured tungsten as a PFC, including reduced deuterium retention and sputtering yield, however the relationship between nanostructured materials and low temperature edge plasmas is not fully known.

In this research, samples of carbon, tungsten and nanostructured tungsten, materials used for plasma facing components in fusion reactors, will be inserted into the edge plasma region of the ICP discharge plasma. The trends in the plasma emission and plasma parameters for varying sample material, temperature and texture will be studied and form the work presented in Chapter 5.

2.4 Atoms and molecules in low temperature plasmas

In low temperature plasmas the level of ionisation is much lower, resulting in increased densities of neutral atoms and molecules. Hydrogen molecules play a key role in edge plasmas as a sink of ions and since many molecular processes result in excited hydrogen atoms, hydrogen emission can be impacted by both atomic and molecular processes.

Atomic and molecular processes are currently underestimated in numerical simulations (e.g SOLPS), and are not fully accounted for in the analysis of spectroscopic measurements. The importance of molecule-ion processes in low temperature plasmas has been studied computationally [105] and these interactions along with a host of additional processes and species have been added to plasma modelling codes [106,107]. Despite these improvements to predictive models, there are still considerable aspects of divertor plasmas and divertor detachment that are poorly understood.

The onset of plasma detachment is driven by atomic and molecular processes through particle, power and momentum balances. These balances are impacted by plasma-molecule interactions through either collisions or reactions between the plasma and molecular species. Collisions between the plasma and molecular hydrogen lead to a transfer of power and momentum from the plasma to molecules and can lead to the excitation of molecular hydrogen resulting in increased molecular emission. Reactions between the plasma and molecular species can also result in an increased number of excited species leading to hydrogenic line emission and impact particle and momentum balances through volume recombination (i.e ion-electron recombination and molecular assisted recombination) and ionisation.

Molecular assisted recombination (MAR) describes the contribution of vibrationally excited molecules towards volume recombination through the following chain of reactions,

$$\underbrace{H_2(v) + e^- \rightarrow H^- + H}_{\text{Dissociative attachment}} \quad \text{followed by} \quad \underbrace{H^- + H^+ \rightarrow H + H^*}_{\text{Mutual neutralisation}} \tag{2.9}$$

or,

$$\underbrace{H_2(v) + H^+ \rightarrow H_2^+ + H}_{\text{Ion conversion}} \quad \text{followed by} \quad \underbrace{H_2^+ + e^- \rightarrow H + H^*}_{\text{Dissociative recombination}} \tag{2.10}$$

Recombination is very important in detached plasmas but these processes are not very well understood experimentally. There is a need for both experimental and computational investigations to characterise detached plasmas. Research by Verhaegh et al [108] utilises spectroscopy to investigate the particle and power balances in the TCV divertor. Through this work, a reduction in the ion target current influences a suite of molecular processes relevant to the onset of detachment, including recombination (momentum and ion sinks) in the divertor plasma.

Elastic collisions between molecules and plasma particles results in a loss of momentum. This causes the molecular species to heat up from a kinetic energy conversion, exciting the molecules and resulting in molecular Fulcher band emission. This momentum loss may impact the onset of detachment, but is not thoroughly understood. Quantifying this loss in relation to other radiative losses in edge plasmas would allow for a deeper understanding of the role of plasma-molecule interactions in divertor detachment.

Hydrogen and deuterium atoms are often treated as one species and so H CR models can provide an insight into the behaviour of deuterium in fusion plasmas [101]. However this is not the case for molecules, as the energy levels of the vibrational and rotational states of molecular H and D differ significantly. Rate coefficients and vibrational states have to be modified in predictive codes to model deuterium and the role of these molecules in edge plasmas is detailed in [109].

2.4.1 Collisional-radiative models

Collisional-radiative (CR) models are utilised to study distribution functions of atoms and ions over their excited states. Densities of the various excited states of a specific atom or ion can be expressed as a function of a range of suitable plasma parameters, for example the electron temperature T_e, electron density n_e and ground state density n_0. The densities of these excited states can then be calculated through balance equations accounting for collisional and radiative processes. Transport processes are typically neglected from CR models.

CR models for atomic hydrogen have been studied since the early 60s [110] in order to quantify the relationship between the key plasma processes. For simple modelling of plasmas, the corona model and LTE (local thermodynamic equilibrium) model can be applied with some assumptions. The corona model assumes that within the plasma, electrons have sufficiently high kinetic energies to excite atoms and molecules. This model can be applied at low densities, where the population of the excited states can be assumed to be only populated through electron impact excitation processes from the ground state and depopulated by spontaneous emission. Collisions with other species that lead to excitation are neglected [111, 112].

Zero-dimensional collisional-radiative models are commonly utilised to provide further information about diagnostic measurements in low temperature plasmas. By combining theoretical predictions of the dominant plasma processes with experimental spectroscopy data, further information about the plasma parameters can be extracted. By correlating the population densities calculated by a collisional-radiative model with OES data, the electron density and temperature can be determined [113]. Therefore CR models are a useful tool which can provide an insight into the key processes that influence a plethora of species in low temperature plasmas.

The first hydrogen CR model was developed in 1973 by Johnson and Hinnov [114] with the aim to apply the understanding gained through theoretical predictions to diagnostic experiments. Over the past few decades a number of H CR models have been developed in order to include more reaction rates and species relevant to both fusion and non fusion plasmas [115, 116].

A LTE plasma model can be applied for high electron density, collision dominated plasmas where population distributions are governed by Boltzmann relations. The Boltzmann relation describes the ratio of the number density of a particular species, n_p, in a higher energy level, p, to the number density of a species, n_k, in a lower energy level, k, and have the form,

$$\frac{n_p}{n_k} = \frac{g_p}{g_k} \exp\left[\frac{-E_{pk}}{kT}\right] \tag{2.11}$$

where g_p and g_k are the degeneracies of the p and k state respectively.

In these plasmas, collisional processes dominate, and so the population distributions can be described using the Saha ionisation equation,

$$\frac{n_e n_{i+1}}{n_i} = \frac{2}{\lambda^3}\frac{g_{i+1}}{g_i}\exp\left[-\frac{(\epsilon_{i+1}-\epsilon_i)}{kT}\right] \tag{2.12}$$

where n_e is the electron density, n_i is the density of the atoms in the i-th ionised state, λ is the thermal de Broglie wavelength of an electron, g_i is the degeneracy of states for the i-ions and ϵ_i is the energy required to remove i electrons from an atom.

For intermediate densities, CR models are typically utilised in which the population distributions can be determined by the use of rate equations which consider both collisional and radiative processes at given temperatures and densities. The outputs of the CR model should converge to the coronal or LTE limit at low and high densities, respectively.

CR models commonly assume a Maxwellian distribution for electrons, and so use rate coefficients which depend solely on temperature. The system of differential equations is typically solved using a range of assumptions. A stationary solution can be found by fixing all temporal derivatives to zero, however the most popular solution is the Quasi-Steady State (QSS) solution. The QSS solution assumes that for all the excited states, the temporal derivatives are zero, while the atoms and molecules in the ground state and electrons relax together slowly.

The processes typically included in CR models are spontaneous transitions, electron impact processes (such as excitation, ionisation and three-body recombination), photon induced processes (such as photoexcitation, photoionisation and induced radiative recombination) and processes induced by atoms (such as excitation and charge exchange). The basic structure of a CR model is the formation of a system of coupled differential equations which include all the relevant processes to calculate the densities of excited states and have the form,

$$\frac{\mathrm{d}n_p}{\mathrm{d}t} = \sum_{q>p} A_{qp}n_q - \sum_{q<p} A_{pq}n_p + n_e\left(\sum_{q\neq p} X_{qp}n_q - \sum_{q\neq p} X_{pq}n_p + (\alpha+\beta n_e)n_+ - S_p n_p\right) \tag{2.13}$$

where n_e is the electron density, A_{qp} and A_{pq} are the transition probabilities for spontaneous emission from the states q to p and p to q respectively, X_{qp} and X_{pq} are the rate coefficients for excitation or de-excitation by electron collisions from the states q to p and p to q, α and β are the rate coefficients for radiative recombination and three-body recombination of a positive ion, and n_+ is the density of that positive ion. S_p is the

ionisation rate coefficient of the state p.

From the calculated values of the population densities, e.g population density of state p, n_p, the line emission intensity from state p to q, I_{pq} can be determined using the Einstein coefficients for the transition, A_{pq} [117–119], where,

$$I_{pq} = n_p A_{pq} \tag{2.14}$$

Therefore through the calculation of the line emission intensity using outputted population densities, it is possible to compare emission intensities from experimental emission diagnostic measurements with CR models to extract information about the key atomic and molecular processes in these plasmas. For the inclusion of molecular species within a collisional-radiative model, vibrational and rotational states become important and so the structure of the model may require important changes.

Predictive codes for modelling divertor plasmas are unsuccessful in a few vital areas and therefore further investigations into the improvement of these codes is necessary in order to control the power exhaust of tokamak divertors. Current models including EDGE2-EIRENE and SOLPS5.0 [68], used for analysing experimental data from edge plasmas in current tokamaks have been improved by international researchers. However there still exists a few shortfalls in these models for predicting plasma detachment. These areas include the link between divertor geometry and plasma detachment, the radiation from plasma species for a variety of recycling regimes, and the prediction of the plasma conditions at which detachment occurs [81]. Although there are numerous areas where these codes could be improved, there is no consensus within the fusion field about the physics that should be investigated to quantify the solutions to these problems, and a wider understanding of the range of key molecular processes is needed to allow for the development of plasma modelling codes.

The research presented in this thesis aims to provide a deeper understanding of emission from molecular species in order to contribute to the improvement of the modelling of detachment in tokamak divertors. A zero-dimensional collisional-radiative model, developed through a collaboration with Keio University and adapted for comparison with experiments at the University of Liverpool, will be described in Chapter 7. The expansion of this model will include a calculation of atomic emission intensity, the addition of a variety of molecular species and more molecular processes to fully investigate low temperature edge plasmas. Although simple 0D CR models are unable to take into account 2D and 3D effects,

with the low computational costs of 0D models they are a powerful tool for understanding the basic particle balance characteristics in low temperature plasmas.

From these models, predictions of the key processes that trigger detachment in future fusion experiments can be used to mitigate the extreme power loads on divertor plates. Through this, control of these power loads can be improved to increase confinement within tokamaks which in turn will increase the power output of future fusion reactors.

Prominent CR models include, the Atomic Data and Analysis Structure (ADAS) [116], the FLYCHK code [120], and the Yacora online CR model [121], which solve systems of equations to determine the densities of excited states and how they evolve over time. ADAS is an atomic data collection database and a collisional-radiative model which can determine the population densities of the energy levels of a variety of atoms and ions. The FLYCHK code focuses on atomic level populations and charge distributions for elements with an atomic number up to Z = 79 (Gold). The Yacora CR model solves for processes that populate and depopulate excited levels, and has 3 main-branches, a hydrogen atom CR model, a molecular H_2 CR model and a helium CR model. Since the Yacora hydrogen models are the most similar in structure and application to the 0D model developed as part of this research and includes a similar number of processes, it will be utilised to benchmark the results from the development of the Keio CR model. For hydrogen, a CR model for H and H_2 was also developed by Sawada et al [122]. Validation of these types of models is typically completed via the use of laboratory plasmas at well defined plasma conditions [123] and can provide a useful insight into trends in plasma parameters.

The Yacora model is a 0D rate balance model accessible publicly online through the webpage "Yacora on the Web" [121]. Yacora includes the following species, H_2, H, e^-, H^+, H_2^+ and H_3^+, however the model is not state resolved and so the vibrational states of H_2 are not included.

The processes included in the Yacora model are electron impact ionisation, dissociation and dissociative recombination, volume recombination and heavy particle collisions, with the input data for the reaction cross-sections taken from the Amjuel and Hydhel databases [68]. The loss of particles as a result of diffusion to the wall is included as in [124], with the probability of recombination at the chamber wall determined by a wall recombination coefficient.

2.4.2 Diagnosing atoms and molecules in low temperature plasmas

Diagnostic techniques such as spectroscopy, Langmuir probes and bolometers are often utilised to determine plasma parameters and characterise the onset of plasma detachment in low temperature regions of fusion experiments.

Until the last few years, divertor regions were typically poorly characterised by diagnostic techniques in standard tokamaks. Diagnostics for divertor plasmas have recently been improved in many devices to include specific sightlines for spatially-resolved OES and infrared measurements. Additionally, laser scattering systems have been upgraded in many machines to allow diagnosticians to monitor electron properties in low temperature regions in MAST-U [125] and ASDEX-U [126]. Detachment can be inferred by density and temperature measurements close to the divertor plates, however the exact processes that influence divertor detachment are not fully understood. By gaining a deeper understanding of the behaviour of atoms and molecules via diagnostic measurements in low temperature plasma, this thesis aims to provide an insight into the exhaust problem and the detachment solution to power handling in tokamaks.

A suite of diagnostic techniques is required to diagnose the wide range of plasma parameters found in both the core and divertor regions of tokamaks. In the high temperature core plasma, non-invasive diagnostics are utilised, however these are often ill-suited for lower temperature edge plasma regions and so appropriate techniques should be designed. A variety of electron processes dominate in edge plasmas and therefore by diagnosing electrons in low temperature plasmas, a wide range of information can be gained about the bulk plasma. Langmuir probes are the front-runner for electron diagnostic techniques in edge plasmas and are employed effectively in ICPs. However probes are typically unreliable in tokamaks due to the influence of external magnetic fields on probe collection and so alternative techniques should be utilised.

The focus of this thesis is to study the trends in atomic and molecular processes in low temperature plasmas close to divertor-like materials. In order to achieve this, optical emission spectroscopy and Langmuir probes will be utilised to diagnose the plasmas for varying discharge and sample conditions.

Optical emission spectroscopy is a non-invasive diagnostic technique used to study atomic and molecular behaviour in low temperature plasmas. Atomic and molecular interactions are key to the power exhaust region of tokamaks, and these interactions result in the creation of excited species which then relax back to their ground state and emit

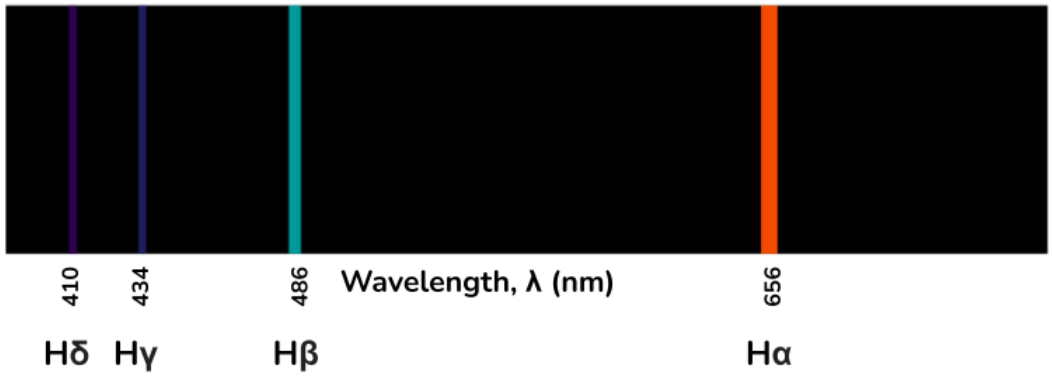

Figure 2.8: The first four Balmer emission lines of hydrogen and their corresponding wavelengths.

light. This emitted light can then be collected using a spectrometer and a detector and by analysing this light, quantitative and qualitative information about the plasma can be extracted. Due to the flexibility and simplicity of OES, it is a crucial diagnostic technique for understanding and controlling the power exhaust in fusion machines. For a detailed look into the capabilities of OES, the reader is directed to [127].

Collisions between hydrogen molecules and plasma particles in edge plasmas have a strong impact on the balance of dissociation, ionisation and recombination in divertor regions. This in turn effects the dissipation of momentum, the power exhaust and the cooling of the plasma at divertor surfaces and the emission from atoms and molecules as a result of these reactions can provide an insight into the properties of divertor plasmas.

The hydrogen Balmer series describes the spectral emission lines corresponding to electrons transitioning to the n=2 state. The wavelengths of these lines can be seen in Figure 2.8, for the first four emission lines, H_α (n=3 to 2), H_β (n=4 to 2), H_γ (n=5 to 2), and H_δ (n=6 to 2).

The Fulcher band describes the spectrum of lines associated with the emission from H_2 molecules. These molecular emission lines arise from the transition from the $d^3\Pi_u$ to $a^3\Sigma_g^+$ state. Figure 2.9 illustrates the three states that are relevant to the Fulcher transition, the upper state, $d^3\Pi_u$, the lower state, $a^3\Sigma_g^+$, and the ground state.

The molecular bands of the hydrogen spectrum correspond to a group of electronic transitions. These vibrational bands are composed of rotational lines which arise from one of three rotational branches, the P, Q and R branch. These lines can be identified

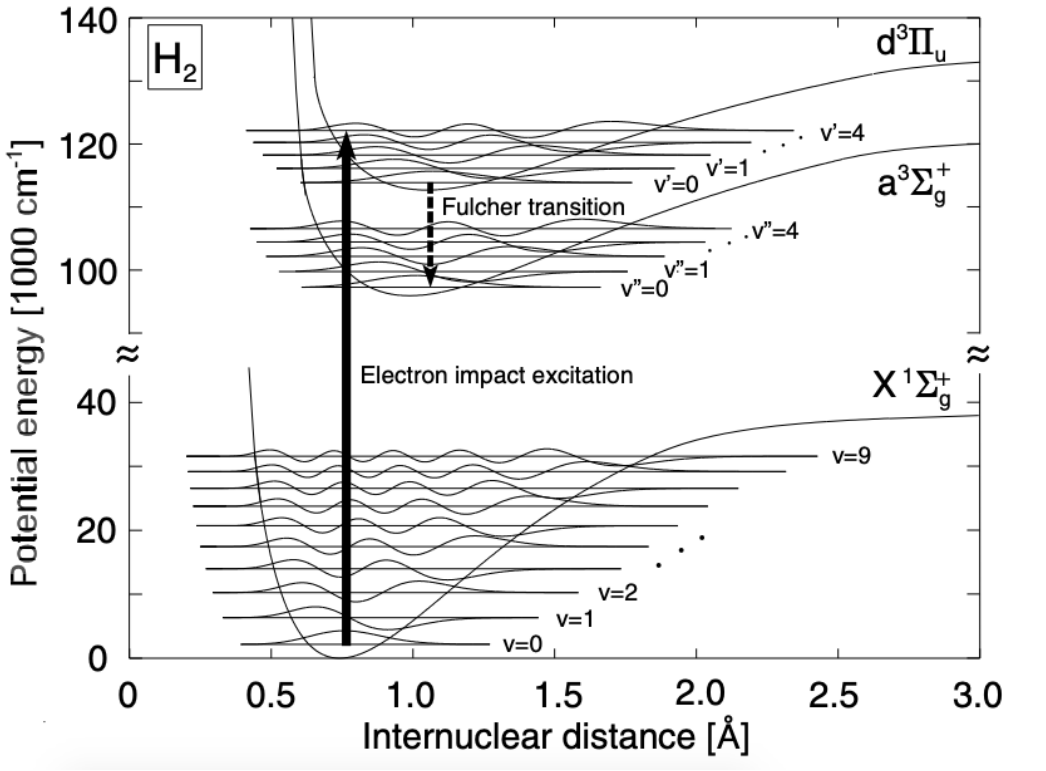

Figure 2.9: A plot of the potential curves, vibrational energy levels and wave functions for some of the states of H_2. Copied from [101].

through the use of the tables presented by Dieke [128, 129]. These branches are indicated on the hydrogen molecular spectra shown in Figure 2.10 and are a result of the rotational selection rules for the $H_2(d^3\Pi_u)$ to $a^3\Sigma_g^+$ transition. The P-branch describes the change in state in which the rotational quantum number in the lower state is one less than the upper state rotational quantum number ($\Delta J = -1$). The R-branch represents the change in rotational quantum number corresponding to $\Delta J = +1$, the rotational quantum number in the lower state is one more than the rotational quantum number in the upper state. The Q-branch, $\Delta J = 0$, signifies no change in the rotational quantum number. Due to optical selection rules, the Q-branch originates from the $d^3\Pi_u^-$ state, whereas the P- and R-branches originate from the $d^3\Pi_u^+$ state. The Q-branch is typically used to characterise the trends in molecular emission, since it is less disturbed by other emission lines than the P- and R-branches. Within each Q-branch, e.g the 0-0, 1-1 and 2-2 bands which are

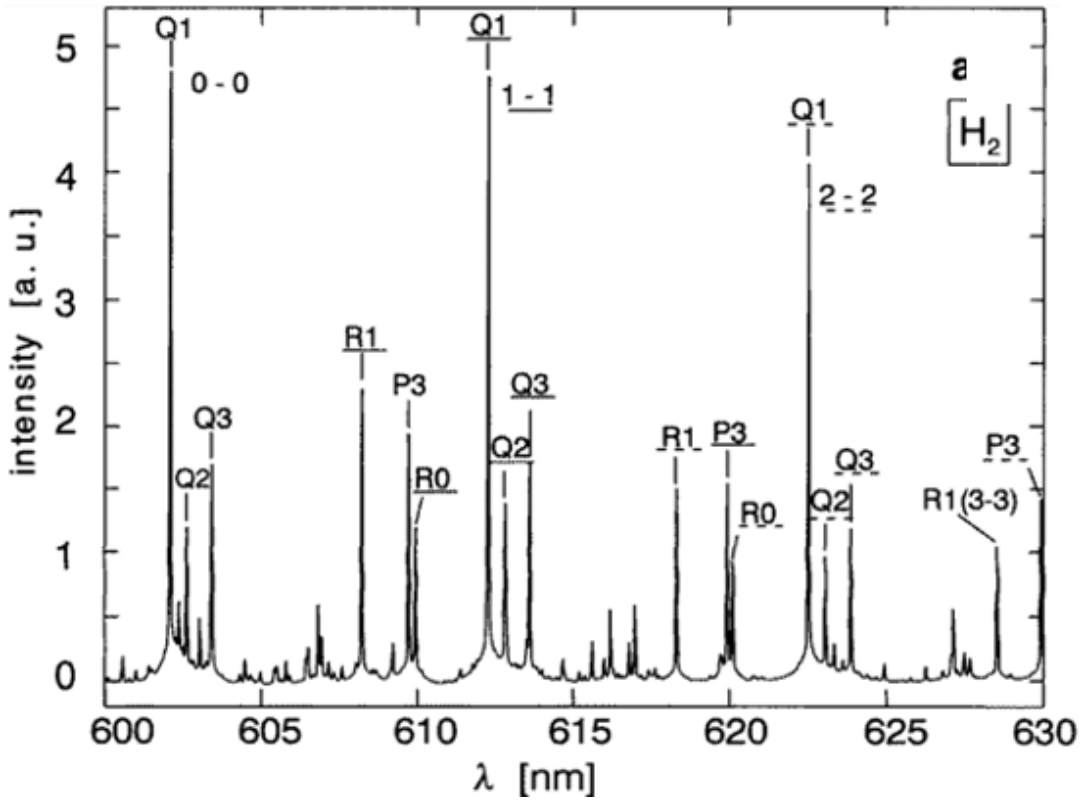

Figure 2.10: An example spectra of the Fulcher band of H_2. Indicated are an example of lines within the P-, Q- and R-branches of the vibrational transitions. Copied from [130].

related to the change in vibrational quantum number from $v'' = v' = 0$, $v'' = v' = 1$ and $v'' = v' = 2$ respectively, there are emission lines corresponding to a change in the rotational quantum number. These lines can be seen in Figure 2.10 denoted by Q1, Q2 etc. From these molecular emission bands, quantitative information can be gained about the distribution of the states and rotational temperatures can be found using Boltzmann plots. Further information about molecular emission band analysis, Boltzmann plots and rotational temperatures can be found in Chapter 3.

One disadvantage of optical emission spectroscopy is that the analysis of emission data relies on the use of accurate atomic and molecular data. For detached plasmas in divertor regions, there is a significant lack of data from spectroscopy and therefore it can be difficult to extract quantitative information about atoms and molecules in detached plasmas. There is a need to improve and develop existing models to include complex atomic and molecular

processes in order to study the behaviour of atoms and molecules in detached regions of edge plasmas in tokamaks.

Langmuir probes are a versatile diagnostic tool that consist of a biased electrode submerged in a plasma in order to measure plasma properties. From these measurements, plasma parameters can be extracted by the use of relevant probe theory. Langmuir probes can be used to monitor the onset of detachment in divertors by diagnosing particle fluxes from the SOL to the divertor plates. Further information about Langmuir probes and probe theory is discussed in Chapter 3.

Retarding field energy analysers (RFEA) can be used to measure plasma temperatures, potentials and saturation currents. Measurements of T_i in the JET SOL demonstrated that the RFA diagnostic is a powerful tool for measuring ion temperatures in low temperature plasmas.

Experiments in the NAGDIS-II linear plasma device observe a disparity between spectroscopic measurements and measurements taken using Langmuir probes [131]. Langmuir probes typically overestimate the temperature of the electrons in tokamak edge plasmas since charge distributions in divertors can introduce plasma fluctuations and resistance. Because of this uncertainty a variety of diagnostics, including the optical emission spectroscopy technique utilised in this project, are required to characterise the trends in plasma parameters within the detached plasma state.

2.5 Summary

The work presented in the four experimental chapters that make up this thesis aim to build on existing knowledge of low temperature plasmas and improve the understanding of atomic and molecular processes in tokamak divertor plasmas.

A significant amount of research has been completed to push forward the current understanding of divertor physics and detachment, however the effects of divertor surfaces on the plasmas are not fully understood and are excluded from comprehensive plasma models.

An outline of the physics and applications of inductively coupled plasma sources is included in this chapter. The use of ICPs will be the primary focus of the first two research chapters of this thesis and will be utilised to characterise the electron properties and plasma emission in low temperature plasmas under controlled conditions.

This research into low temperature laboratory plasmas will provide a basis to

understand the trends in atomic and molecular emission in tokamak divertor plasmas. Measurements in the MAST-U tokamak will build on the established research in divertor physics presented in this chapter and aim to provide a deeper understanding of divertor regions and plasma detachment.

Collisional-radiative models are a useful tool for the extraction of quantitative information from experimental measurements of low temperature plasmas. Previous research into the use of CR models to further understand key processes in low temperature plasmas is presented here to provide the motivation behind the development of a 0D collisional-radiative model in Chapter 7.

Chapter 3

Experimental Apparatus and Diagnostic Techniques

In this chapter, the experimental equipment and diagnostic apparatus utilised for optical emission spectroscopy and Langmuir probe measurements in the inductively coupled plasma at the University of Liverpool will be presented. The first section details the inductively coupled plasma rig; the second section will outline the optical emission spectroscopy diagnostic set up and analysis techniques; and the final section centres around describing the Langmuir probe measurement system and the probe theory implemented for the measurements in this thesis.

3.1 The Inductively coupled radio frequency plasma source

The experiments undertaken in this research project were collected using the University of Liverpool inductively coupled plasma discharge rig. The structure of this section is as follows; firstly a general description will be given of the chamber, vacuum system, vacuum pumps and power supplies. Secondly the bespoke sample heater for use in submerging divertor-like samples into the ICP device will be detailed, and finally a description of the diagnostic ports for emission and probe measurements will be described with reference to diagrams of the ICP rig.

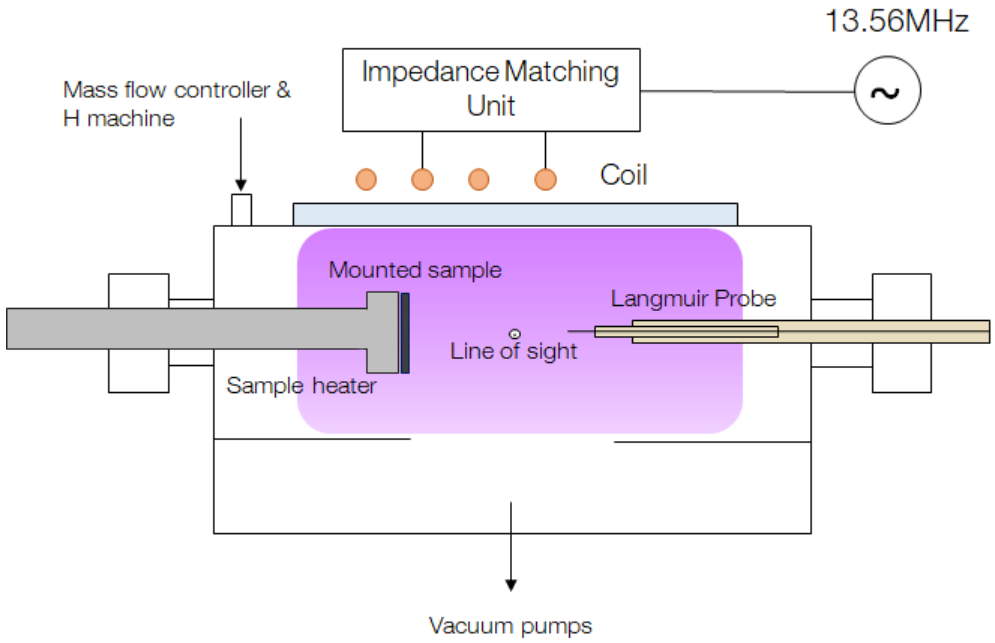

Figure 3.1: Schematic of the University of Liverpool inductively coupled plasma discharge source, highlighting the position of the RF matching unit, induction coil, and ports in relation to the centre of the chamber.

3.1.1 Discharge plasma rig set up

The University of Liverpool inductively coupled plasma (ICP) rig is comprised of a cylindrical vacuum vessel and a 10 cm diameter, 6 mm outer diameter two turn planar induction coil, separated by a quartz window. The plasma vacuum vessel is split into two halves, an upper and lower chamber, with a total height of 25 cm and a diameter of 30 cm. A schematic of the experimental apparatus can be seen in Figure 3.1. Section 2.1.1 contains a general overview of ICP sources. The aim of this section is to provide an outline of the operation of the ICP discharge source at the University of Liverpool.

The ICP discharge plasma source was chosen as a test bed for fusion edge plasmas due to the low electron temperatures measured, as found in divertor and detached divertor conditions. Detached regions in tokamaks are characterised by partially ionised plasmas with temperatures < 10 eV. These plasmas are dominated by atomic and molecular processes including recombination and ionisation, therefore by diagnosing the plasmas produced in the ICP rig, it is possible to reproduce trends close to divertor tiles in

tokamaks. By using an ICP device, a wide range of conditions can be accessed due to the E-H ICP mode transition, allowing for detailed control of the plasma parameters over a large selection of pressures and powers.

The chamber is pumped down to an average base pressure of 0.05 Pa via a combination of a backing pump (ACP 28CV) and a turbomolecular pump (HiPace 300C). The chamber pressure is measured by two 0.1 mbar range Pfeiffer baratron gauges (an upper chamber baratron and a lower baratron), a Pfeiffer Pirani gauge and a full range gauge. The full range gauge uses a cold cathode pressure gauge at pressures below 10^{-2} mbar and utilises the Pirani gauge at higher pressures.

The discharge gas used in these experiments was hydrogen, generated using deionised water through electrolysis via the hydrogen trace machine (Peak Scientific Hydrogen Trace). The hydrogen machine outputs the gas at 250 sccm, at a maximum pressure of 7.5 bar. This gas is then fed through a mass flow controller (MFC - MKS 1178A) which is used to control the gas before it then enters the ICP chamber. The gas pressure was monitored using the baratron gauges through a capacitance manometer (Pfeiffer Vacuum D-35614). To reduce pressure fluctuations in the outputted hydrogen gas, a needle valve was placed between the hydrogen machine and mass flow controller before entering the chamber. The discharge pressure was controlled by fixing the flow rate on the mass flow controller. Although the pressure of the discharge measured by the pressure gauges has an accuracy of up to $\pm 30\%$ (for the Pirani and cold cathode gauge utilised in the full range gauge), as the flow rate through the mass flow controller was constant, the pressure for different measurements should be consistent. For the experimental measurements presented in this thesis, the gas pressure was varied in the range 1-10 Pa. This pressure range was chosen to produce a wide range of measurements for different conditions that are accessible in the ICP chamber.

A RF power supply (MKS Elite 1.2kW) is utilised to supply power to the copper induction coil. This power supply can deliver a maximum of 1200 W RF power at a frequency of 13.56 MHz in continuous wave mode. The RF power is matched to the plasma in the chamber via a matching circuit. This matching unit is situated above the water-cooled copper coil as seen in Figure 3.1 and is used to manually optimise the transmitted power to the plasma. The reflected power was monitored throughout the diagnostic measurements to be kept below 5% reflected power.

The matching unit consists of two variable capacitors and a RF transformer with a turn ratio of 3:1. The transmission line is a coaxial cable with a characteristic impedance of 50

Ω. The RF coil generates an electromagnetic field in the discharge gas, which accelerates electrons and enables collisions between neutral hydrogen molecules and electrons and therefore the ignition of a plasma through electrical breakdown. The RF power range employed in these diagnostic measurements is 10-300 W. This range was utilised due to the manual matching efficiency decreasing for powers $>$ 300 W. Above 300 W, the matching unit losses increased significantly due to resistive heating, resulting in higher values of reflected power.

3.1.2 Bespoke sample heater

To study the effects of divertor-like materials on both the plasma parameters and plasma emission, a bespoke sample heater mount was designed in order to mount and submerge a variety of samples within the ICP vacuum chamber.

A one-inch diameter bespoke tungsten versatile button heater was utilised to mount samples of carbon, tungsten and nanostructured tungsten into the chamber. The heater body is made from tungsten, and the heater top plate from Shapal, suitable for use in 10^{-5} Torr vacuum. The heater body is mounted to an ISO63-K flange. The maximum temperature of the top plate of the heater is 1200C while the maximum temperature of the tungsten element is 1400C.

The position of the sample heater within the chamber, in relation to the spectroscopy line of sight and Langmuir probe position, can be seen in Figure 3.2. The sample heater is inserted into the chamber radially by 120 mm via a KF40 port and sealed using an O-ring. One inch diameter samples of carbon, tungsten and nanostructured tungsten with a thickness of 1 mm are mounted to the top plate via three tungsten clips. These sample materials were chosen for measurements in the ICP rig as carbon and tungsten are commonly used as plasma facing components in a number of international fusion machines. The sample temperature is varied from 0-1200C and the effects of the sample material, temperature and texture on the plasma emission and plasma parameters is investigated.

The nanostructured tungsten samples used in measurements presented in Chapter 5 were produced through experiments in the PISCES-A plasma linear device, with an ion flux of 1.4×10^{22} m^{-2}, ion energy of 75 eV and sample temperature of 1140 K [132]. The carbon samples used were cut from a sample of the MAST carbon divertor tiles, through a collaboration with the CCFE diagnostics team.

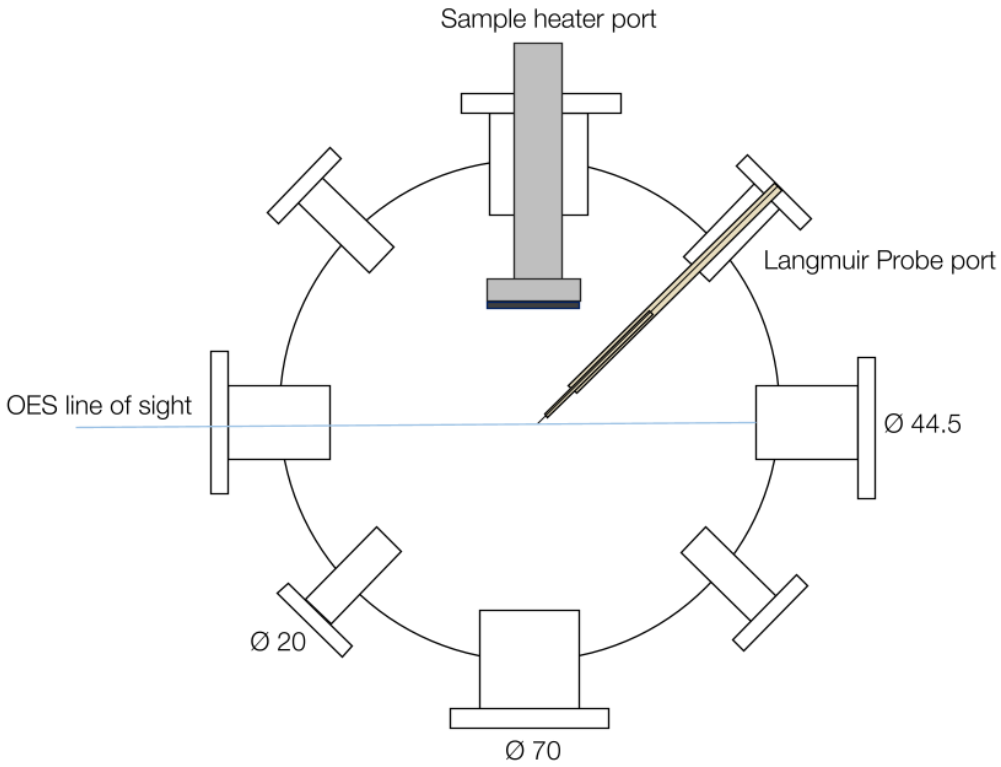

Figure 3.2: A horizontal cross-section of the ICP chamber to show the diagnostic ports, positions of the "bulk" plasma measurements and sample heater position.

3.1.3 Diagnostic measurement positions

The diagnostic ports, flanges and line of sight used for the measurements described in Chapter 4 and 5 can be seen in Figure 3.2. The diagnostic ports for the spectroscopic optical fibre and electrical probe are located in the mid-plane of the upper chamber to allow for a characterisation of the emission and plasma properties within the bulk plasma in the centre of the chamber.

In Chapter 5, measurements close to material samples are presented in order to study the effects of divertor materials on the plasma parameters and plasma emission. For this set of measurements, a Langmuir probe was designed and constructed for use in diagnosing the plasma close to the divertor-like surfaces. The construction of this probe is outlined in Section 3.3.1. The position of this sample heater probe can be seen in Figure 3.3. This "edge plasma" probe allows for a study of the effects of the sample heater on

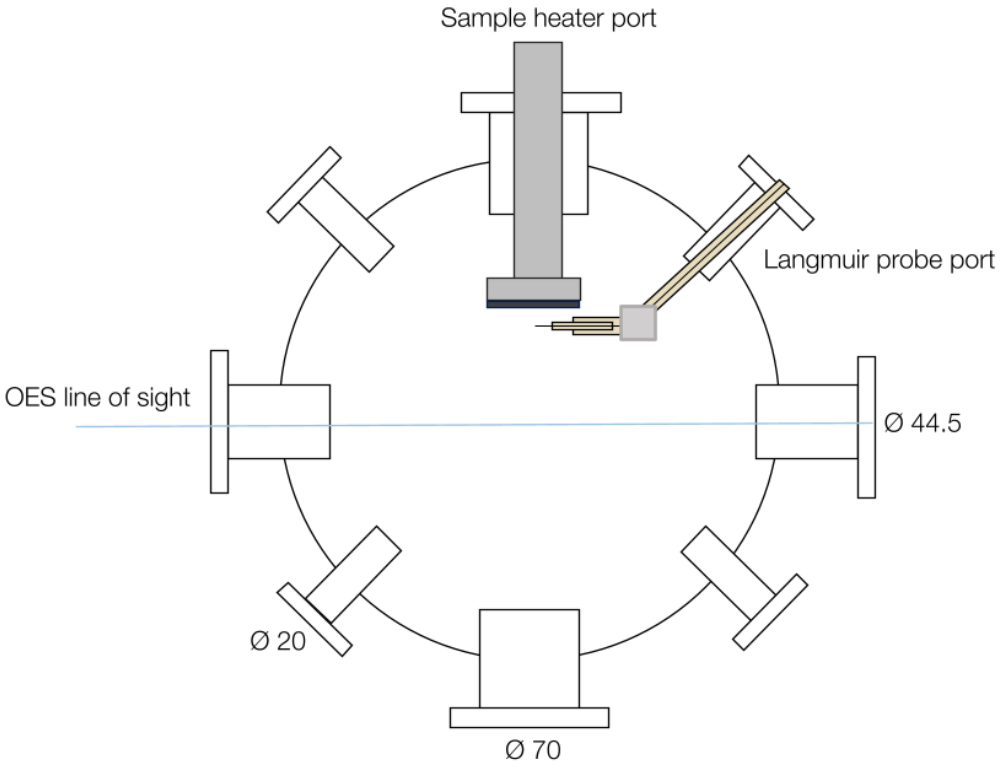

Figure 3.3: A horizontal cross-section of the ICP rig to show the diagnostic ports, measurement positions and sample heater position with the edge plasma probe.

the plasma parameters. Optical emission spectroscopy measurements were collected for varying distance from the sample in order to quantify the effects of the materials on the plasma emission. For these OES measurements, presented in Chapter 5, the line of sight was varied between four positions, which can be seen in Figure 3.4. These measurements will be discussed further in Section 3.2.

3.2 Optical emission spectroscopy

3.2.1 Experimental setup

The emission measurements in this project are collected using an automated Czerny-Turner FHR1000 spectrometer. A table summarising the spectrometer specifications can be seen

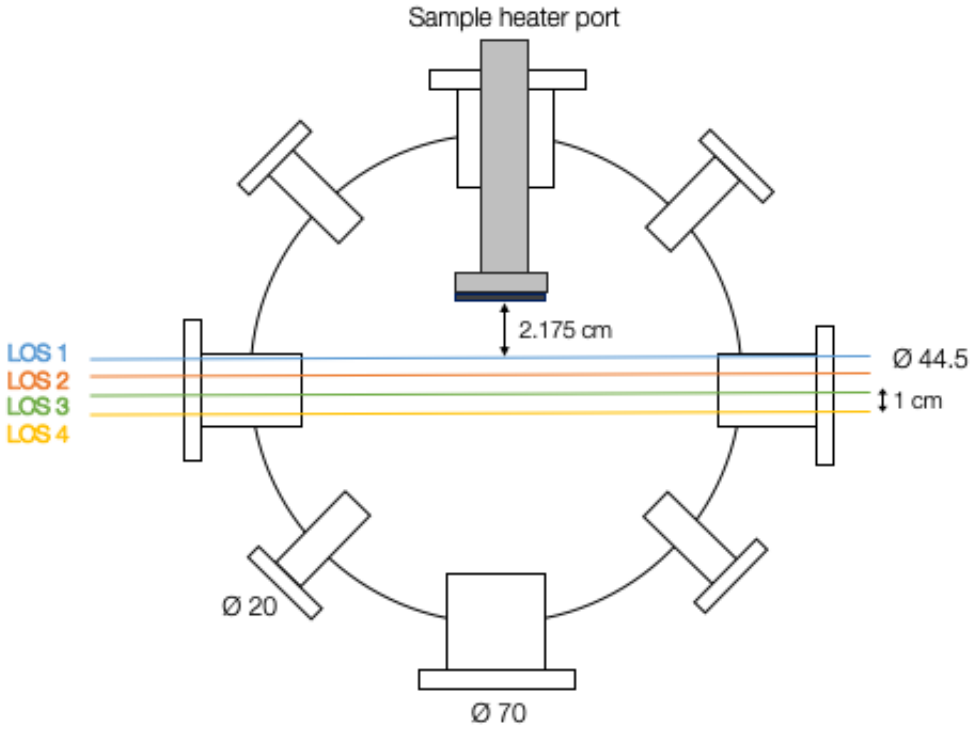

Figure 3.4: A horizontal cross-section of the ICP rig to show the four lines of sight used in emission measurements close to the material samples. LOS1, the closest line of sight to the sample, is 2.175 cm away from the sample surface, and the subsequent lines of sight are separated by 1 cm.

in Table 3.1. This spectrometer has a focal length of 1 m and spectral resolution of 0.01 nm (with 10 μm slits). The spectrometer slit width is adjustable from 0 to 7 mm with a 1200 gr/mm grating. The spectrometer is fitted with a Horiba PMT-928 photomultiplier tube which collects the light emitted from the plasma. While the detector and optical fibre are able to transmit wavelengths in the UV range, the chamber window has a transmission limit of around 400 nm, which set a lower boundary of what could be detected by the scanning spectrometer.

For fast measurements of the full hydrogen emission spectra, a secondary lower resolution spectrometer was used. This spectrometer is the Ocean Optics flame miniature spectrometer and while the resolution was significantly worse than the Horiba high-resolution spectrometer, this spectrometer could provide an overview of the emission

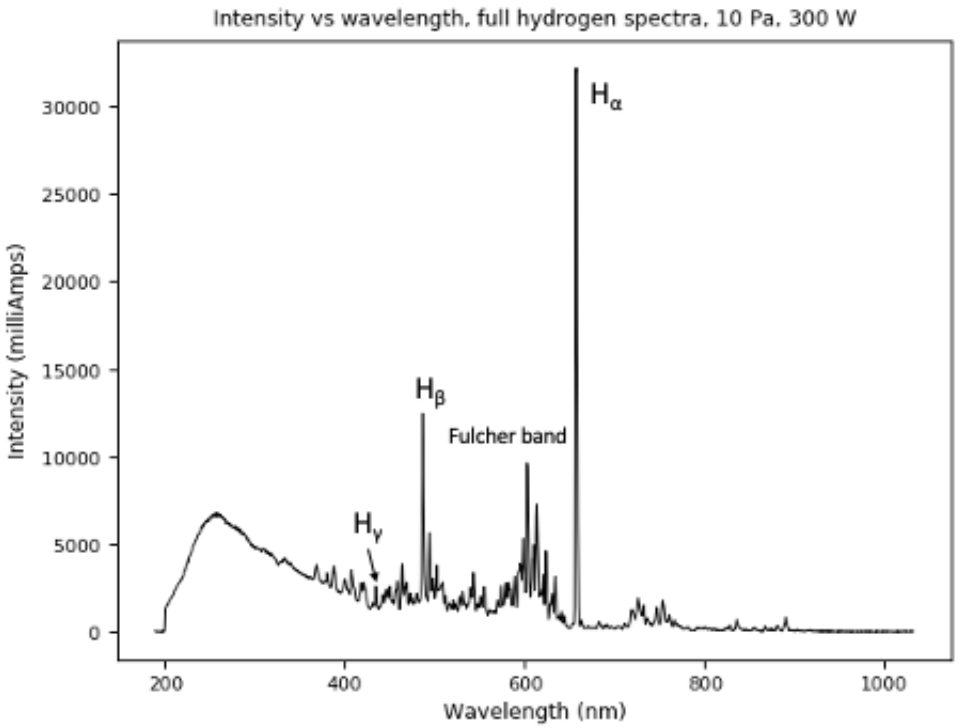

Figure 3.5: A full hydrogen spectra collected in the UoL discharge plasma rig for a discharge pressure of 10 Pa and RF input power of 300 W. The H_α, H_β, H_γ lines and Fulcher band are indicated. Collected using the Ocean Optics spectrometer.

peaks instantaneously. The specifications of this spectrometer can also be seen in Table 3.1. An example of the full hydrogen spectra taken using the Ocean Optics spectrometer can be seen in Figure 3.5. Although this was useful for observing trends in the emission and for checking the structure of the emission spectra, the analysed results presented in this thesis are taken using the high-resolution Czerny-Turner FHR1000 spectrometer.

As outlined above, the optical emission spectroscopy line of sight for measurements in Chapter 4 was positioned to intersect the centre of the chamber, shown in Figure 3.2. This was chosen to allow for a study of the trends in the emission from the bulk plasma for varying discharge pressure and RF power.

Emission measurements with varying distance from the surface of the heated samples are presented in Chapter 5. The aim of these measurements is investigate how the sample

Table 3.1: Overview of the specifications of the spectroscopic diagnostic equipment utilised in experiments in the University of Liverpool ICP discharge source.

Spectrometer (Horiba FHR1000)	Focal length	1 m
	Grating	1200 gr/mm
	Spectral dispersion	0.8 nm/mm
	Scanning range	0-1500 nm
	Spectral resolution	0.01 nm
Spectrometer (Ocean Optics flame)	Entrance slit	25 μm
	Grating	1200 gr/mm
	Scanning range	200 nm - 1.025 μm
	Spectral resolution	1.69 nm
	Integration time	1 ms - 65 s
	Pixels	2048
	Detector	Linear silicon CCD array
Photomultiplier tube	Spectral response	185-900 nm
Optical fibre (Ocean Optics - P600-2-UV-VIS)	Applicable range	UV-Vis
	Length	2 m
	Core diameter	600 μm
	Wavelength range	300 nm - 1.1 μm

temperature, material and surface of the inserted samples influence both atomic and molecular species. The lines of sight chosen for these measurements were positioned 1 cm apart starting from 2.175 cm from the sample surface and can be seen in Figure 3.4 with respect to the sample heater. These lines of sight are labelled LOS 1, LOS 2, LOS 3 and LOS 4, corresponding to the line of sight closest to the sample through to the line of sight furthest away from the material surface.

3.2.2 Data acquisition

Intensity vs wavelength measurements were acquired using the Horiba SynerJY spectrometer software. To study atomic and molecular hydrogen emission for varying conditions, scans of the hydrogen atomic Balmer series and molecular Fulcher band were completed for varying gas pressure, RF power and sample temperature, with carbon, tungsten and nanostructured tungsten samples inserted into the plasma. For the hydrogen Balmer series, wavelength scans of 430-440 nm, 480-490 nm and 650-660 nm were collected for varying discharge and sample conditions in order to allow for an investigation of the trends in the H_γ (434.1 nm), H_β (486.2 nm) and H_α (656.1 nm) lines. To study the

Fulcher band molecular emission, a wavelength scan from 580-650 nm was completed. As mentioned in Chapter 2, the Fulcher band can be typically observed in the wavelength range from 590-640 nm, and so this wavelength scan was completed to capture the full molecular band and study the effect of varying conditions on the molecular emission. These scans were averaged three times with an integration time of 0.1 s.

3.2.3 Analysis of emission data

To extract quantitative information from the collected optical emission spectra, a range of techniques can be implemented for both atomic and molecular emission. In this section, two analysis techniques will be outlined which will be implemented for the OES measurements presented in the first three experimental research chapters, Chapters 4-6.

Balmer line ratios

To study and identify the key processes in tokamak edge plasmas, the ratio of the hydrogen Balmer line intensities is used to identify specific atomic and molecular behaviour.

The ratio of Balmer line intensities can be used as an indication of the electron temperature, since the electron energies required to excite the upper levels of transitions is larger at the higher energy levels. The ratio can also be used to indicate the amount of Molecular-Assisted Recombination in a plasma and whether this is a dominant process for the emission of photons [133–135]. It has also been shown that the intensity of higher n lines increases when electron-ion recombination becomes significant.

For the measurements in this research, the ratio of lines chosen is the H_γ to H_α Balmer lines. These lines were selected as higher-n lines were not strong enough to measure in the ICP chamber and so the line could not be identified.

The intensity of the Balmer lines was calculated by integrating the area under a Gaussian function fit to each emission line. An example of a Gaussian fit to a H_α line measured in the ICP can be seen in Figure 3.6. To verify the accuracy of this method and investigate the effect of line broadening on the value of the intensity, a Python code was utilised to extract a value of the line intensity using the intensity of the peak. The values of the line intensities calculated through both the Gaussian fit and peak intensity analysis methods were found to agree within an error of 2%, and so the effects of line broadening on the values of the intensity were assumed to be minimal. The ratio of the H_γ and H_α line intensities were then taken for each measurement for varying discharge and sample

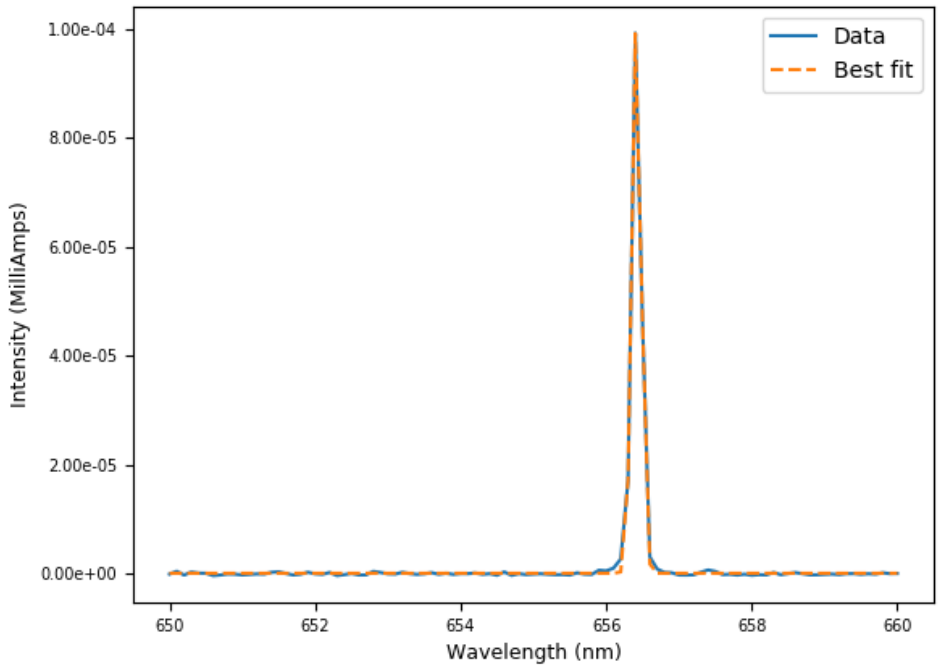

Figure 3.6: An example Gaussian fit to a H_α line collected using the Horiba FHR1000 spectrometer. The raw data and best fit are indicated.

conditions.

A background spectrum, taken with the RF power supply turned off and so no plasma in the chamber, was taken for each measurement scan. This background data was then subtracted from the corresponding measurement to correct the plasma spectra and reduce background noise.

Rotational temperature analysis

The rotational temperature, T_{rot}, is related to the molecular distribution over the rotational levels of the excited electronic-vibrational states [136], and so is a valuable parameter used to characterise the behaviour of molecules in low temperature plasmas. A Boltzmann distribution is usually assumed for the rotational distributions of the electronically excited states and therefore the rotational temperature is often interchangeable with the gas

temperature, T_g [136]. Recent studies have shown however, that for low densities, the relationship between the rotational temperature and gas temperature is more complex and so should be investigated further [136].

To determine the value of T_{rot}, the Q-branch emission lines corresponding to the Fulcher transition from the $H_2(d^3\Pi_u^-)$ state to the $(a^3\Sigma_g^+)$ state are utilised. This band of lines is chosen for two reasons. The Fulcher band has been thoroughly studied over the last century and all necessary molecular constants have been classified via experiments [128, 129, 137]. Additionally the lines that make up this band are spread out and distinct from other lines associated with irrelevant transitions in this wavelength range.

T_{rot} can be determined from the intensity of the Q-branch Fulcher band lines. If the $H_2(d^3\Pi_u^-)$ state follows a Boltzmann distribution, characterised by the rotational temperature of that state $T_{rot}^{d,v}$, then the relationship between the rotational temperature and the intensity distribution of the Fulcher band is described as [136],

$$\ln\left(\frac{\lambda^4 I_{a,v,J}^{d,v,j}}{S_{J,J}g_{as}}\right) = -\frac{hc}{kT_{rot}^{d,v}}F_v(J) + C \tag{3.1}$$

In this equation, λ is the wavelength of the transition and $I_{a,v,J}^{d,v,j}$ is the intensity of the corresponding transition. g_{as} is the nuclear spin degeneracy, which is 3 for odd values of J and 1 for even values of J.

$S_{J,J}$ is the line strength which can be calculated using the Honl-London formula,

$$S_{J,J} = 0.5(2J+1) \tag{3.2}$$

$hcF_v(J)$ is a term to denote the rotational energy of the state, where the constant h is the Planck constant and c is speed of light. The term $F_v(J)$ can be expressed as

$$F_v(J) = B_v J(J+1) \tag{3.3}$$

where B_v is the rotational constant of the $(d^3\Pi_u^-, v)$-state. For hydrogen, B_v is known to have the value 30.364 [138].

The plot of $\ln(\lambda^4 I_{a,v,J}^{d,v,j}/S_{J,J}g_{as})$ versus the rotational term $F_v(J)$ forms a Boltzmann plot. From the gradient of the Boltzmann plot, m, the rotational temperature, T_{rot} can be obtained from,

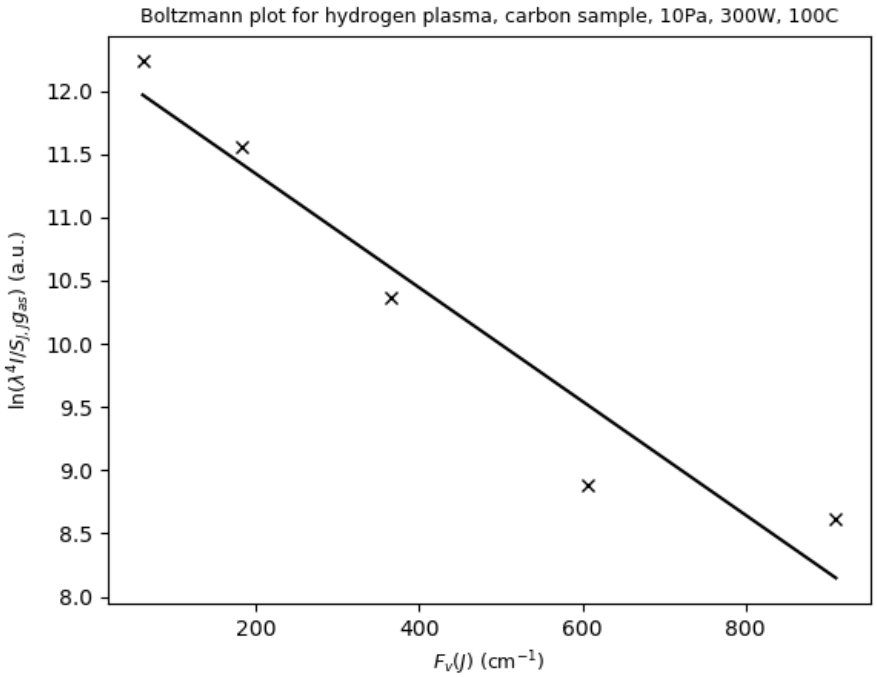

Figure 3.7: An example Boltzmann plot collected in the ICP discharge plasma at 10 Pa and 300 W using the Horiba FHR1000 spectrometer. The data points are calculated using the intensity and wavelength of the Q-branch (1-1) band with respect to rotational energy, $F_V(J)$.

$$T_{rot} = -\frac{hc}{km} \tag{3.4}$$

An example of a Boltzmann plot using Fulcher emission data with a RF power of 300 W and discharge pressure of 10 Pa in the ICP chamber can be seen in Figure 3.7.

Table 3.2: Positions of the spectral lines corresponding to the Q-branch (0-0), (1-1) and (2-2) bands of the hydrogen molecular Fulcher band. (Wavelengths in nm.)

Transition	Q1	Q2	Q3	Q4	Q5	Q6
(0-0)	601.83	602.38	603.19	604.27	605.61	607.20
(1-1)	612.18	612.72	613.54	614.62	615.96	
(2-2)	622.48	623.03	623.84	624.92	626.25	

The spectral wavelengths corresponding to the Q-branch of the ro-vibrational transitions of the Fulcher band can be seen in Table 3.2 [128, 129, 137].

If the fit to the Boltzmann plot is linear, this indicates that the rotational levels in the $H_2(d^3\Pi_u^-)$ state follow a Boltzmann distribution. For the molecular emission measurements in this thesis, the three Q-branch bands, (0-0), (1-1) and (2-2), are used to measure the rotational temperature independently. For these bands, there is a small difference in the calculated T_{rot} determined from the three Boltzmann plots with an error of less than 10%.

3.3 Langmuir probes

Langmuir probes are an invasive plasma diagnostic technique commonly used in low temperature plasmas to measure plasma parameters. This technique involves immersing an electrode, or wire, into a plasma and by monitoring the behaviour of the plasma under varying conditions, measurements of the local plasma parameters, including the electron temperature and density, T_e and n_e, the plasma potential, V_p, and floating potential, V_f, can be extracted. Langmuir probes are easy to construct and control and are a very powerful diagnostic tool which have been used to provide information about densities and temperatures in low temperature edge plasmas for almost a century [139]. Langmuir probes are very versatile, due to the simple design and installation of immersing a wire in a plasma. However they can perturb the plasma and so edge effects and perturbations should be accounted for and minimised using suitable hardware and probe theories. As probes are in direct contact with the plasma, they can ablate or melt in high temperature conditions. Hence, while probes are widely used in low temperature gas discharges, their use in tokamak plasmas is limited to the low temperature regions in divertor edge plasmas.

By sampling the current to a Langmuir probe at varying applied bias voltages, a probe IV characteristic can be constructed. Further detail to describe the ideal IV characteristic and the use of probe theories to extract plasma parameters can be found in Section 3.3.3.

3.3.1 Probe construction

As the plasma parameters extracted from Langmuir probe measurement analysis depend on the area of the probe, the stem of the probe should be insulated to reduce the surface area of the probe tip exposed to the plasma. Typically, tungsten wire is threaded through ceramic alumina tubing, leaving a short length of exposed wire to protrude from the stem

and form a probe tip. Thin ceramic tubing should be used to form the probe stem to reduce disturbance of the probe to the plasma.

A schematic of the standard Langmuir probe utilised for measurements in the centre of the chamber can be seen in Figure 3.2. This probe will be referred to as the "bulk" probe, as it is utilised to measure the plasma parameters in the plasma bulk in the centre of the ICP chamber. This probe was constructed using tungsten wire and alumina ceramic tubing of varying thicknesses and lengths. Tungsten wire with purity 99.95% and radius 0.1 mm was threaded first through alumina tubing of outer diameter 3 mm and length 40 mm. This was then inserted into alumina tubing of outer diameter 6 mm such that around 20 mm of the 3 mm tubing and 0.5 cm of the tungsten wire protruded to create a probe tip. The other end of the 3 mm tubing and the base of the 6 mm tubing was then sealed using vacuum epoxy resin (Torr seal) to form a vacuum seal and inserted into the chamber and sealed by an O-ring placed between the outer ceramic probe stem and the chamber flange. From the probe stem, a BNC cable was then connected to the tungsten wire and encased in copper tape to provide shielding from electromagnetic interference. The BNC connector then connected the probe directly to the data acquisition system. A schematic of this probe seen in Figure 3.8(a).

The probe utilised for measurements close to divertor-like surfaces, the "edge" probe, can also be seen compared to the "bulk" probe in Figure 3.8(b). The shape of this probe was designed in order to measure the plasma parameters close to the sample surface while utilising the ISO-KF 016 flange to insert the probe into the chamber, as seen in Figure 3.3. This probe measures plasma parameters 1 cm from the surface of the inserted samples.

To mirror the construction of the bulk probe, the edge probe was also constructed using tungsten wire and various lengths and thicknesses of alumina ceramic tubing. Tungsten wire with purity 99.95% and radius 0.05 mm was threaded through alumina tubing of outer diameter 3 mm and length 40 mm. This was then inserted into alumina tubing of outer diameter 6 mm and length 81 mm to form the first leg of the probe and the probe tip. The length of the tungsten probe tip was 1 cm. The non-tip end of the 6 mm tubing was then attached to a 1 cm^3 cube of PTFE to form a join for the two legs of the Langmuir probe. The second leg of the probe tip was then attached to the PTFE cube at a 135 degree angle to the first leg. Both the tubing and the PTFE cube were vacuum sealed using Torr seal and inserted through the flange and sealed using an O-ring placed between the outer ceramic probe stem and the chamber flange. From the second leg probe stem, a BNC cable is then connected to the tungsten wire, shielded with copper tape casing and

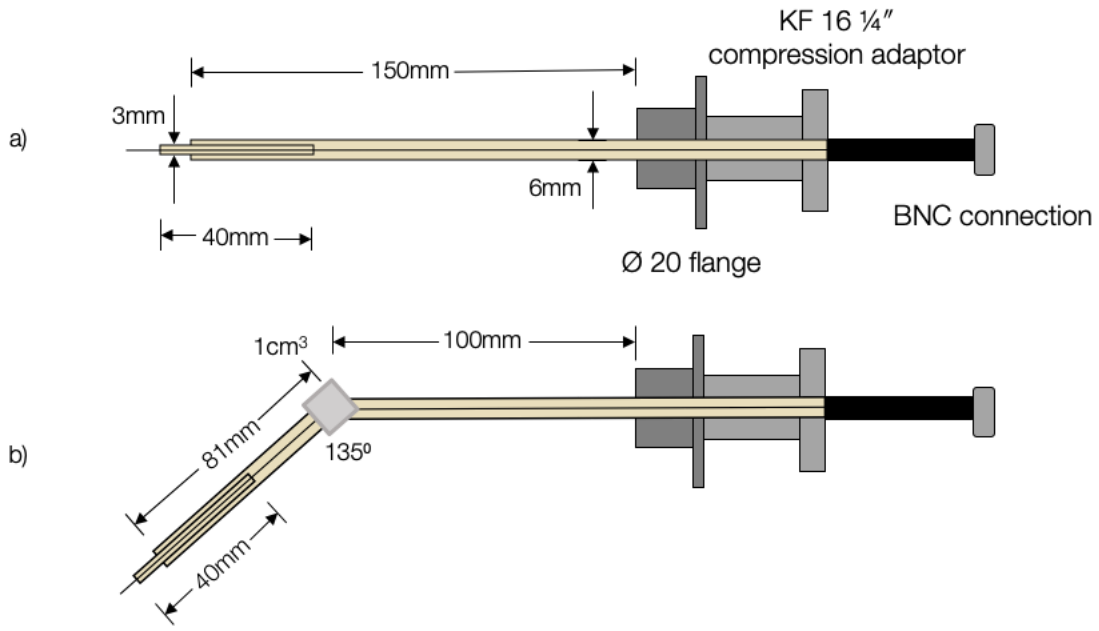

Figure 3.8: (a) The dimensions and shape of the "bulk" Langmuir probe. (b) The dimensions and shape of the "edge" Langmuir probe.

connected to the data acquisition system where the probe measurements can be obtained. The two probes utilised for the measurements in this thesis were constructed without RF compensation. As RF oscillations are expected to be very small in ICP discharges and electromagnetic fields are shielded within the ICP skin depth, it was decided that RF compensation was not necessary for these experiments.

3.3.2 Data acquisition

A schematic of the Langmuir probe ramp generator circuit is shown in Figure 3.9. To generate a current-voltage probe characteristic, a sawtooth voltage waveform was applied to the probe and the resulting current was recorded. The current in the circuit was determined using a differential amplifier (AD8479) through the measurement of the voltage drop across a 68.3 Ω sense resistor, both of which can be seen in Figure 3.9. The value of this sense resistor was chosen as the voltage drop across the sense resistor is required to be small compared to the voltage drop across the probe sheath. When the probe is collecting ions

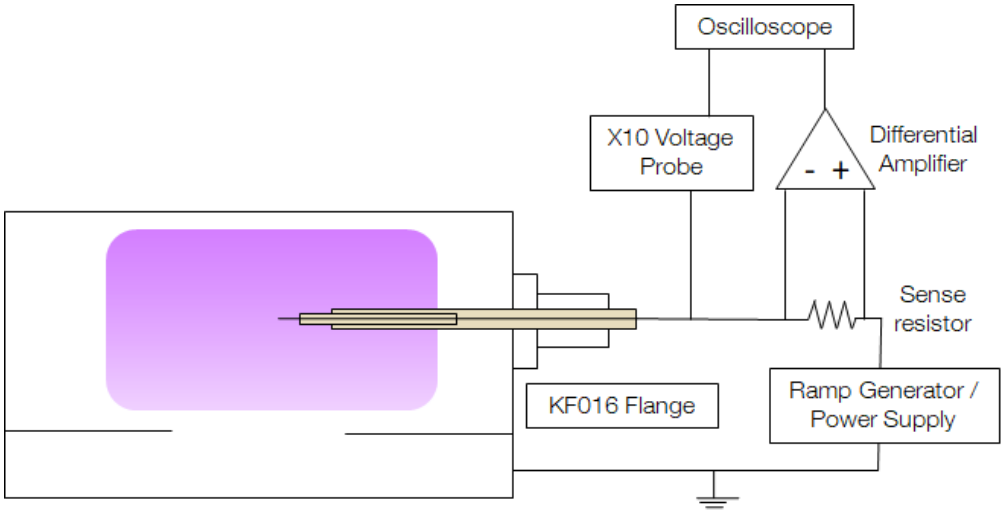

Figure 3.9: A schematic of the Langmuir probe ramp circuit utilised to bias the probe in diagnostic measurements. The circuit is comprised of a ramp generator used to supply a sawtooth waveform to the probe, and both a voltage probe and differential amplifier in order to measure the current and voltage simultaneously.

there is a high sheath impedance and so a large sense resistor should be used. However in the electron collection region, a small sense resistor should be used as the sheath impedance is low. To obtain a sweep across the full IV curve, a compromise should be met between these two regimes, and so for n_e values of 10^{15}-10^{17} m^{-3}, a 68.3 Ω resistor was chosen.

The bias voltage applied to the probe was measured using a Tektronix P6139A ×10 voltage probe at the base of the Langmuir probe stem. The voltage bias ramp was displayed on a Tektronix DPO3034 oscilloscope and the measured signal on the oscilloscope was compiled of 100k data points and averaged by the oscilloscope 512 times. The waveforms were triggered by the sawtooth voltage waveform generated by the ramp generator, which can be seen in Figure 3.9. The current and voltage waveform data was then transferred to a personal computer for analysis in Python. By matching the bias voltage with the corresponding current waveform on the time axis, these IV characteristics were constructed using a Python analysis code, with resolutions of 0.01 V and 0.1 μA, and plasma parameters could then be extracted. The DC offset and peak-to-peak voltage of the sawtooth waveform could be adjusted via the ramp generator for a specific bias voltage range. The range -120

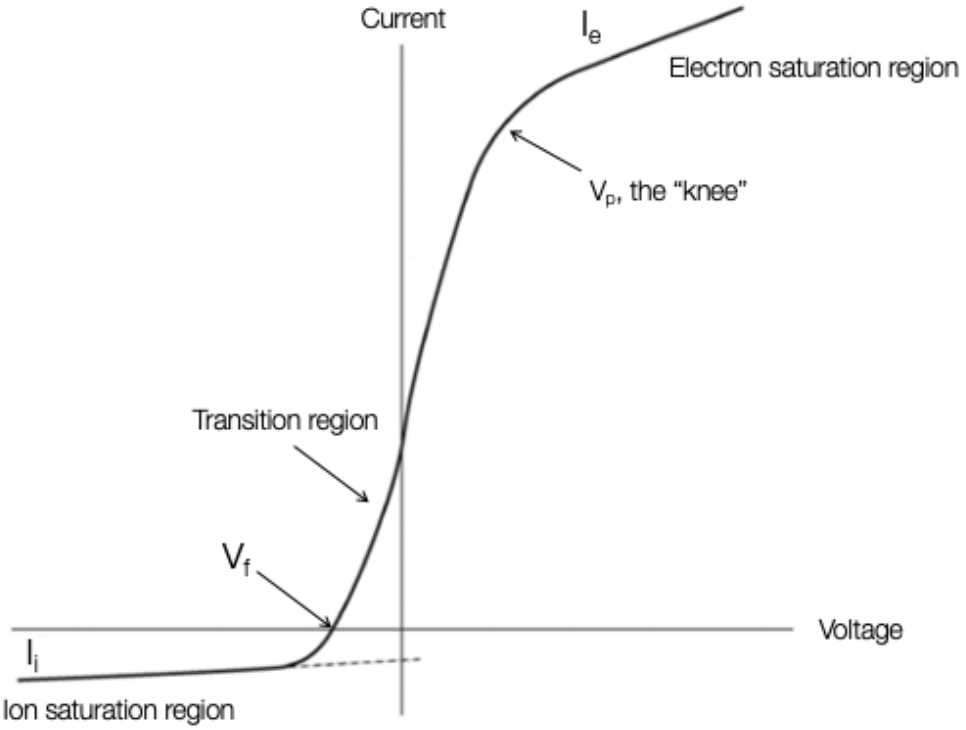

Figure 3.10: An ideal IV characteristic indicating the electron and ion saturation regions, the transition region and the plasma and floating potentials. Adapted from [140].

to 30 V was chosen to allow for a full collection of the ion saturation region while limiting the electron saturation region to prevent damage to the electrical probes.

3.3.3 Implementing probe theory and extracting plasma parameters

Despite the simple implementation and control of Langmuir probes for diagnosing plasmas, it can be difficult to extract reliable and accurate information from Langmuir probe data about local plasma parameters. A range of Langmuir probe theories have been formulated using various assumptions to allow for more precise analysis under specific plasma conditions.

An ideal IV probe characteristic can be seen in Figure 3.10. A typical Langmuir probe characteristic has a number of key features, including the ion saturation region, transition region and electron saturation region, the floating potential, V_f, and the plasma potential V_p. The ion saturation region defines the region in which the net current collected by the

probe is negative. The floating potential can be found when the net current to the probe is zero and the IV characteristic intersects the x-axis. The region for increasing bias voltage between the floating potential and plasma potential is the transition region in which the probe shifts from collecting mainly ions to collecting electrons as the bias voltage begins to repel ions from the probe.

The plasma potential marks the boundary between the transition region and electron saturation region and can be identified by the "knee" in the IV curve. The value of the plasma potential can be found through three methods. V_p can be found from the maximum of the first derivative of the IV characteristic, the intersection of the x-axis in the second derivative, or through the intersection of a linear fit to the electron saturation region and the end of the transition region. This knee is only well defined in unmagnetised discharges at low pressure. Radio frequency waves can introduce oscillations in the plasma potential which cause a "rounding" of the knee and distort the shape of the characteristic. This can result in difficulties in accurately determining the plasma potential.

When the bias voltage increases to above the plasma potential, the electron current is expected to stay constant as the electrons in the sheath fall into the probe collection region. However in real plasmas, both the electron and ion currents may never saturate as the large bias voltage causes the surrounding sheath to expand. This in turn increases the surface area of the probe for collection and so the currents never fully saturate. The grounded chamber walls of the inductively coupled plasma discharge source act as a reference for the probe bias in these measurements.

The floating potential is typically less than the plasma potential and they are both different from ground due to the increased electron mobility compared with ions. At the floating potential, the electrons reach the probe sooner than the positive ions resulting in a negative potential with respect to ground. A positive ion sheath then forms around the probe and the negative potential is sustained. At the plasma potential, the electrons are more mobile and so there is an increased loss of electrons to the grounded chamber walls. Above the plasma potential, the electrons are not repelled from the probe and so the electron current saturates.

The current collected by the probe in the electron region with a Maxwellian temperature distribution is given by,

$$I_e = I_{es} \exp\left(\frac{e(V_p - V)}{kT_e}\right) \tag{3.5}$$

Where the electron saturation current, I_{es} is described by,

$$I_{es} = en_e A_p \sqrt{\frac{kT_e}{2\pi m}} \tag{3.6}$$

Here A_p is the probe surface area, k is the Boltzmann constant and n_e is the electron density.

Probe collection theories typically use the electron temperature to calculate the ion density, and so this is usually calculated first. When the probe current is plotted against the bias voltage on a semi-logarithmic plot, the electron temperature can be found from the inverse of the gradient of the linear region.

The electron density can be found by substituting the value of the current at the plasma potential for I_{sat_e} in Equation 3.6. However since the exponential nature of the transition region can result in large errors to the values of the current in this region, it is more accurate to calculate both electron and ion densities through established ion collection theories.

The ion density, n_i can be found from the probe characteristic. Due to the reduced ion mobility in contrast to electrons, the ion current region is considered to be more stable and so, with some assumptions, plasma parameters can be extracted more easily from this region.

The orbital motion-limited (OML) probe theory, developed by Langmuir and Mott-Smith [139], describes the condition in which all particles which are able to reach a cylindrical probe are collected by the probe. For an ion trajectory, if the point of closest approach is less than the radius of the probe, the ion will be collected by the probe. The geometry of a cylindrical probe is the most simple and therefore is the easiest to implement accurate probe theory for.

Using the conservation of energy and angular momentum, the following expression can be formulated,

$$\frac{1}{2}m(v_\phi^2 + v_r^2) = \frac{1}{2}m(v_\phi'^2 + v_r'^2) - e(V_p - V) \tag{3.7}$$

and

$$av_\phi' = sv_\phi \tag{3.8}$$

where m is the mass of the collected species, a is the radius of the probe, s is the radius of the sheath, $-v_r$ and v_ϕ are the radial and azimuthal initial velocities respectively and

$-v_r'$ and v_ϕ' are the velocities at the probe radius.

Combining Equations 3.7 3.8 gives,

$$v_r'^2 = v_r^2 + v_\phi^2 + \frac{2e(V_p - V)}{m} - \frac{s^2}{a^2} v_\phi^2 \tag{3.9}$$

By setting $v_r'^2$ equal to zero, Equation 3.9 becomes,

$$v_{\phi 0} = \left(\frac{v_r^2 + 2e(V_p - V)/m}{s^2/a^2 - 1} \right)^{\frac{1}{2}} \tag{3.10}$$

The saturation current can be determined through integration of the radial ion flux over the energy distribution function at the edge of the sheath [59], which gives the saturation current collected by the probe, I, as:

$$I = -2\pi s d n_s e \int_{-\infty}^{0} v_r \mathrm{d}v_r \int_{-v_{\phi 0}}^{v_{\phi 0}} f(v_r, v_\phi) \mathrm{d}v_\phi \tag{3.11}$$

It is assumed that the energy distribution is an isotropic Maxwellian with the form,

$$f = \frac{m}{2\pi e T} \exp\left[-\frac{m(v_r^2 + v_\phi^2)}{2eT} \right] \tag{3.12}$$

where T is the temperature of the collected species at the edge of the sheath.

To simplify the integral of this function, assumptions can be made for large probe bias voltages. At large bias voltages, the sheath size should be much bigger than the radius of the probe, which leads to the first assumption,

$$\frac{a}{s} \ll 1 \tag{3.13}$$

The next two assumptions made are for the radial and azimuthal velocities,

$$v_r^2 \ll \frac{e(V_p - V)}{m} \tag{3.14}$$

and

$$v_{\phi 0}^2 \ll \frac{eT}{m} \tag{3.15}$$

By combining these assumptions with Equation 3.10, one can obtain,

$$v_{\phi 0} = \frac{a}{s}\left(\frac{2e(Vp - V)}{m}\right)^{\frac{1}{2}} \tag{3.16}$$

Using Equations 3.16, 3.11 and 3.12, the saturation current is found to be

$$I = 2adn_s e\left(\frac{2e(Vp - V)}{m}\right)^{\frac{1}{2}} \tag{3.17}$$

Therefore this saturation current (of either ions or electrons) is independent of the species temperature, T, and so a plot of I^2 against V should be linear. The square of the plasma density, n_s^2 can then be found from the gradient of the linear fit to this plot. By rearranging Equation 3.17, the plasma density is formulated as,

$$n_s^2 = \frac{m}{8e^3a^2d^2}\frac{\mathrm{d}I^2}{\mathrm{d}V} \tag{3.18}$$

OML theory is typically utilised in low density plasmas with two assumptions. The first assumption is that no ion collisions occur within the sheath, i.e that the mean free path for collisions with neutrals and ions is much larger than the thickness of the sheath. An increase in collisions leads to smaller sheath sizes [141], which impacts the validity of this assumption and can lead to an overestimation of the plasma density.

The second assumption of OML is that there is no absorption radius around the probe, and so the electric field is sufficiently strong such that ions cannot escape and are collected by the probe. In most plasmas there is a defined absorption radius and so OML is often not applicable. However OML is considered to be an applicable approach when the ratio of probe radius, R_p to the Debye length λ_D is less than three [142].

$$R_p/\lambda_D < 3 \tag{3.19}$$

For values of this ratio above three, OML is still a useful theory and can provide accurate density values in conditions when it does not satisfy the above assumptions [143]. OML typically produces results that are much simpler to interpret compared with other ion collection theories such as La Framboise and ABR and so for these reasons was utilised in the measurements of the plasma parameters presented in Chapters 4 and 5.

Electron Energy Distribution Functions

The Electron Energy Distribution Function (EEDF) is a useful plasma property that can be found from probe characteristics. EEDFs can provide useful insight into the energy distribution of electrons within a plasma and whether the distribution has a Maxwellian, bi-Maxwellian or Druyvesteyn shape.

The determination of the nature of the distribution function is important for ICP discharges. At low discharge pressures, stochastic heating can dominate and result in higher electron temperatures. If the degree of stochastic heating increases, this can result in a bi-Maxwellian energy distribution with two electron temperatures, however if the electrons are in thermodynamic equilibrium, the distribution function follows a Maxwellian shape. For the distribution to be Maxwellian, the plasma should be strongly ionised and so electron-electron collisions can then push the distribution towards a Maxwellian shape. For weakly ionised plasmas, inelastic collisions of electrons with atoms and molecules can result in a reduction in the EEDF at higher electron energies. In this case, the Druyvesteyn function is most applicable to describe the shape of the EEDF.

The energy distribution function of an isotropic distribution of electrons can be found by using the second derivative of the IV characteristic by the Druyvesteyn formula [144],

$$f_E^D(E) = \frac{2(2m_eE)^{\frac{1}{2}}}{e^3A_p} \cdot \frac{d^2I_e}{dV^2} \tag{3.20}$$

The Druyvesteyn method is very powerful as it allows for an evaluation of the EEDF regardless of the convex probe shape. Unlike other methods, this method also does not make any assumptions on the ratio of the radius of the probe to the Debye length and can be applied to any isotropic electron distribution.

The density of electrons, n_e, can then be calculated by integrating the distribution (Equation 3.20) over all the electron energies,

$$n_e = \int_0^\infty f_E^D(E)\mathrm{d}E \tag{3.21}$$

The EEDF is a powerful tool which can offer information about the population of electrons in plasmas. However since the EEDF is related to the second derivative of the IV curve, it is inherently noisy and smoothing filters are usually required before the information can be utilised quantitatively. A Savitzky-Golay smoothing function filter with a second order polynomial was applied to the raw IV data to reduce noise before

the calculation of the EEDF using the second derivative of the curve, however the level of noise was significantly large despite filtering efforts. So while the EEDF can provide useful information on the plasma characteristics, even with the implementation of a smoothing filter, the large levels of noise in the data resulted in no meaningful quantitative information about the energy distribution able to be extracted from the probe data. Improvements to the hardware should be made in future research to extract useful EEDF information.

3.4 Summary

In this chapter, the experimental set up of the inductively coupled plasma discharge source at the University of Liverpool and the key diagnostic techniques utilised in this thesis were introduced. This set up is employed for the collection of measurements in the ICP discharge rig which will be presented in Chapters 4 and 5. The design and configuration of the Liverpool ICP was outlined, alongside the diagnostic theory used to extract information about the plasma for varying conditions from both OES and Langmuir probe measurements. A bespoke sample heater will be utilised for measurements presented in Chapter 5, in order to study the effects of samples on the local plasma parameters and emission, and the set up of these measurements was also outlined in this chapter.

Optical emission spectroscopy can provide useful information about the behaviour of atoms and molecules through analysis of both the hydrogen Balmer emission lines and the Fulcher band. The atomic and molecular emission will be analysed using both line intensity ratios and Boltzmann plots to extract quantitative information from these measurements, and these techniques were presented in Section 3.2.3. The line of sight will be varied in order to observe the line-averaged emission at a range of positions in the chamber, to enable a study of the trends in emission with material samples inserted into the plasma. Emission measurements will be collected close to the surface of these samples and in the bulk plasma in the centre of the chamber in order to quantify the effects of the samples on the atomic and molecular processes.

Langmuir probes are conventionally utilised to measure densities and temperatures in low temperatures plasmas. A description of the probe construction and data acquisition methods were presented here alongside the ion collection theory implemented for plasma parameter measurements in this thesis. Two probes will be utilised in the measurements in Chapter 4 and 5 in order to characterise the bulk plasma properties and the parameters close to divertor-like samples for varying plasma and sample conditions.

Chapter 4

Characterisation of a Low Temperature Hydrogen Plasma in an Inductively Coupled Plasma Discharge Source

4.1 Introduction

The overall aim of this research is to understand the general mechanisms of the low temperature plasmas that exist within divertors, specifically close to divertor surfaces. The research presented in this chapter aims to characterise the plasma parameter regimes available in the hydrogen ICP discharge source at the University of Liverpool for a range of plasma conditions. ICP discharges can provide a good vehicle for accessing divertor plasma relevant conditions in a laboratory discharge environment. While a significant amount of research has been completed to characterise the general mechanisms and properties of ICP discharges, mainly focusing on the technological applications of ICPs outlined in Chapter 2, the research presented in this thesis requires detailed knowledge of the conditions in this particular discharge. Measurements in the absence of the divertor-like surface detailed in this chapter will provide a reference for later measurements that include these novel surfaces.

The objective for the research in this chapter is the characterisation of a hydrogen

ICP discharge which will provide a reference for measurements of plasma emission and plasma parameters close to divertor-like surfaces presented in the next chapter. Optical emission spectroscopy and Langmuir probes were utilised to obtain plasma emission and plasma parameter data for varying discharge conditions and these measurements were then analysed to quantify key atomic and molecular processes for trends in plasma parameters.

Through the research presented in this chapter, both the emission and plasma parameters in the ICP discharge plasma were characterised for varying RF power and discharge pressure. These results show the positive dependence of the electron density on both the RF power and gas pressure, due to increased collisionality and ionisation. The electron temperature decreases for increasing power and pressure, due to both the E-H ICP transition and the increase in collision frequency in these conditions. The atomic and molecular emission is shown to vary more significantly with increasing power, since there are more electrons available for excitation, and is only weakly dependent on the gas pressure. This work provides a basis on which experiments shown in Chapter 5 close to divertor-like surfaces will build on.

The ICP discharge rig and diagnostic equipment are described in detail in Chapter 3.

The structure of the chapter is as follows. The first section will summarise the range of conditions available within the ICP rig for varying discharge pressure and RF power, alongside the diagnostic techniques utilised for this research. The second section presents the results of electron property measurements from Langmuir probes positioned in the centre of the chamber to characterise the range of properties of the bulk plasma. Measurements of plasma emission for varying discharge conditions will be presented in the third section, which will provide more information about the most important atomic and molecular processes and the trends in the both the Balmer atomic emission and Fulcher molecular emission for varying discharge conditions. In the final section, a comparison of the results of these measurements with published research in ICPs will be discussed.

4.2 Range of measurements

Optical emission spectroscopy and Langmuir probe diagnostics have been utilised to investigate a hydrogen plasma using the UoL inductively coupled plasma discharge rig. Trends in the plasma emission from spectroscopy, and plasma parameters from Langmuir probes, can be used to infer key atomic and molecular processes in low temperature edge plasmas.

A summary of the diagnostic research previously completed using ICPs will be presented later in this chapter in Section 4.3.3, with a comparison of the typical plasma parameters in literature with the results presented in Section 4.3.1.

The measurements of atomic and molecular emission plasma parameters presented in this chapter for an initial characterisation of the ICP device were collected for gas pressures in the range 1 to 10 Pa, whilst the RF input power was varied from 10 to 300 W. The Langmuir probe and line of sight were positioned in the centre of the ICP chamber to allow for an investigation of the bulk plasma properties.

The measurements presented in this chapter are an average of multiple data sets collected over five consecutive days for the same plasma conditions. Multiple measurements were completed to allow for an investigation into the reproducibility of the ICP discharge plasma and to calculate the standard errors for each data set.

4.3 Characterisation of electron properties

This section contains electron property measurements made over the full range of conditions of the ICP discharge. The results were obtained using the Langmuir probe apparatus described in Section 3.3, made in the centre of the plasma chamber, in the arrangement shown in Figure 3.2. Section 4.3.1 contains the results of these experiments and Section 4.3.2 contains an interpretation of the data with reference to the known understanding of ICP discharges. In Section 4.3.3, a comparison of these measurements will be made with published diagnostic ICP results and the final section outlines the set of three distinct regimes of plasma conditions that can be identified from these electron property measurements.

4.3.1 Electron properties for varying pressure and power

Two sets of measurements are presented here in order to characterise the electron properties of the discharge. The first set consists of measurements for pressures ranging from 1 Pa to 10 Pa, made at a constant power of 100 W. The second set consists of measurements for powers in the range 10-300 W, made at a constant pressure of 10 Pa. Additional measurements were made at other combinations of pressure and power, but these are not presented here as the two sets of measurements outlined in this chapter are sufficient for a characterisation of the discharge.

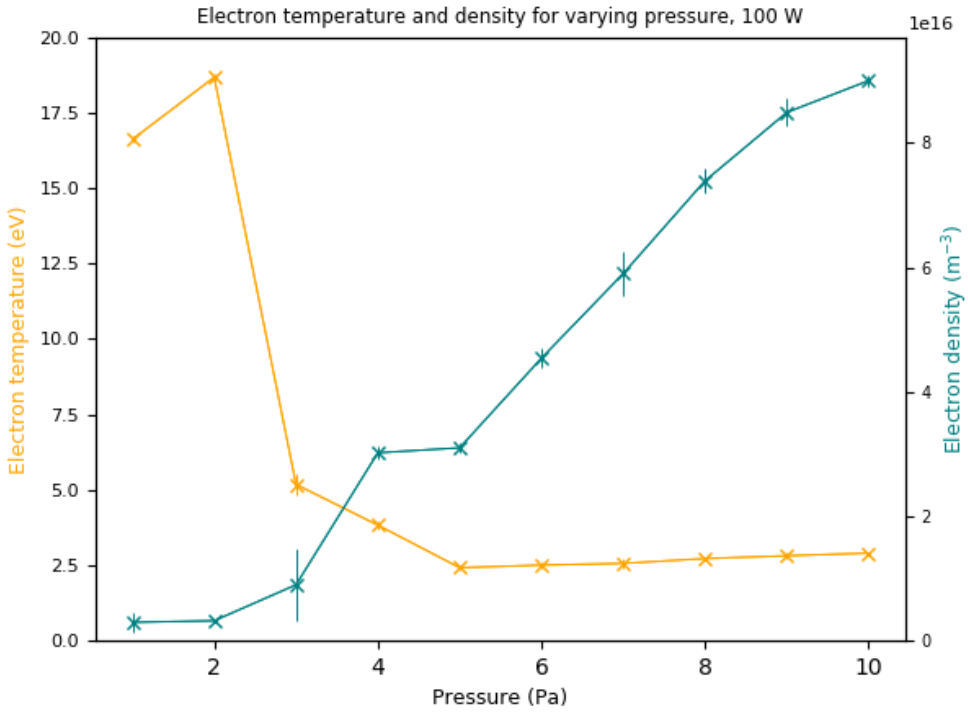

Figure 4.1: Electron temperature and electron density for varying discharge pressure at a constant power of 100 W collected using a Langmuir probe in the centre of the chamber.

A plot of the electron temperature and density for varying pressure at a constant power of 100 W can be seen in Figure 4.1. The electron temperature measurements show very high temperatures at the lowest pressures. There is then a sharp drop to lower and more constant temperatures in the 2-3 eV range at higher pressures. Over the same pressure range, the electron density increases almost linearly, changing by an order of magnitude and reaching a value of nearly 10^{17} m^{-3} at the highest pressure of 10 Pa.

Figure 4.2 shows the power dependence of the electron properties, measured for powers in the range of 10 W to 300 W, at a constant pressure of 10 Pa. The electron temperature dependence shows two regimes, with a moderate temperature of 5 eV at the lowest power and a nearly constant value of around 3 eV for higher powers. For this range of power, it can be seen that the electron density increases almost linearly, reaching a value of around 2.5×10^{17} m^{-3} for the maximum power of 300 W.

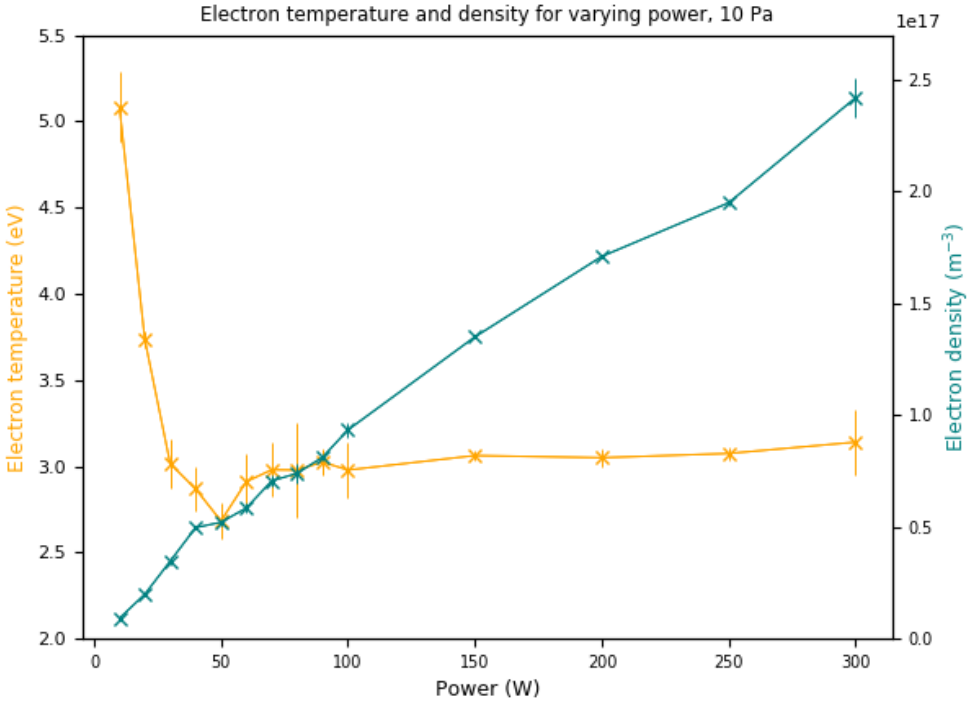

Figure 4.2: Electron temperature and electron density for varying RF power at a constant pressure of 10 Pa collected using a Langmuir probe in the centre of the chamber.

4.3.2 Interpretation of electron property measurements

The trends shown in Figures 4.1 and 4.2 are typical for ICP discharges, and have been observed by other researchers using similar discharge geometries [145, 146]. Because of this, the mechanisms that lead to these trends are reasonably well-understood.

The observed pressure dependence is attributed almost solely to the change in electron collisions as the background density of neutral molecules increases. At low gas densities, the mean free path for both elastic and inelastic electron collision is long, and the electrons can gain significant energy from the discharge electric fields before colliding with any background species. This leads to a high average electron energy, which is reflected in the high value of T_e observed for the lowest pressures. However, although the average electron energy is high, the low gas density means there are few collisions and hence little ionisation, which results in the low electron densities observed at these pressures.

At higher gas densities, the electron mean free paths are still long enough for the electrons to gain energy between collisions, but the increased gas density means significantly more collisions will occur. This leads to both higher electron densities and more thermalisation of the electron population.

The power dependence, measured at the higher pressure of 10 Pa, is characterised by a linear increase of density with power and a small change of T_e over this range. The change in density is attributed simply to the power increase, with the higher power leading to more ionisation and more electrons. A second effect will be the change of power coupling mechanisms over this range, with the low power plasmas being predominantly capacitively coupled and higher power conditions predominantly inductively coupled. Inductive coupling is known to be more efficient, and hence this change also contributes to the general increase of electron density with power.

The dependence of T_e on power is also attributed to the change of power coupling mechanism. For lower power conditions, coupling occurs by electron heating via capacitive sheaths, and the associated high sheath electric fields lead to higher average electron energies. For the higher power conditions, the electron heating will predominantly be by the smaller and more widely distributed inductive fields, and average electron energies will be lower.

There is one further point worth noting from these results. The lowest pressure conditions have electron collision lengths that are significantly larger than the chamber dimensions, meaning that electrons can traverse the chamber without any collisions. Figure 4.3 shows the mean free path of the electrons for varying discharge pressure. This figure shows that at low pressures, the mean free path is much larger than the diameter of the chamber, at around 0.3 m, and so there are essentially no collisions within the chamber. This lack of collisionality is likely to result in EEDFs that are distinctly non-Maxwellian, with significant numbers of high energy electrons, and little of the collisionality required to generate a bulk T_e. As seen in Figure 4.3, for increasing pressure, the mean free path decreases almost exponentially. This results in higher collisionality at higher pressures, leading to a lower bulk electron temperature. This increase in collisional processes results in increased rates of ionisation and so the density of charge carriers increases.

As noted earlier, these trends are in agreement with diagnostic studies in published research, with increasing electron density and decreasing electron temperature for increasing pressure [147]. These similarities will be discussed further in Section 4.3.3.

Error bars are included to highlight the uncertainties in the electron property

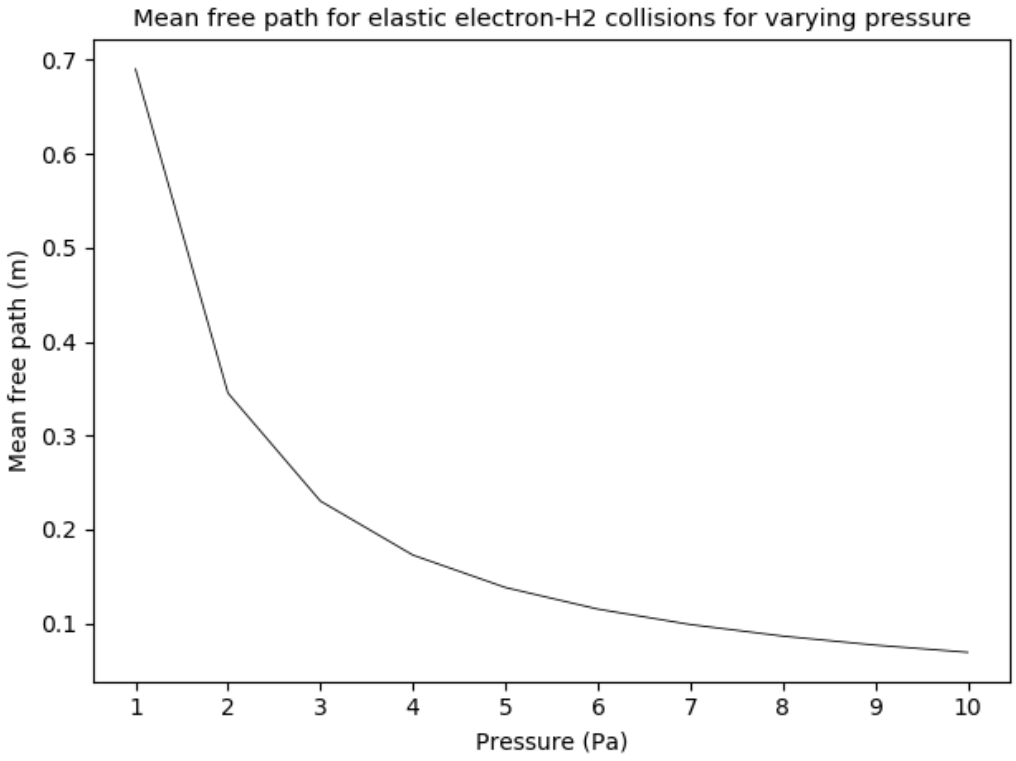

Figure 4.3: Mean free path for elastic electron-hydrogen molecule collisions for varying pressure at 500 K. Cross-sections used in mean free path calculations taken from [152].

measurements for varying power and pressure. These uncertainties are taken from standard error measurements for data collected on five consecutive days at the same discharge conditions and are typically less than 20% for both the T_e and n_e data sets.

4.3.3 Comparison with published ICP research

Langmuir probes are used in a plethora of research studies to provide a reliable characterisation of ICP discharges [147–151]. Typical values of electron temperatures and densities in literature in ICP discharge sources for varying plasma conditions are in the range 1 - 7 eV and 10^{15} - 10^{18} m^{-3} respectively [153]. The probe measurements presented in Section 4.3.1 agree with published results and values of T_e and n_e follow characteristic trends for varying discharge pressure and RF power.

Figure 4.4 shows a plot of both the electron temperature and electron density

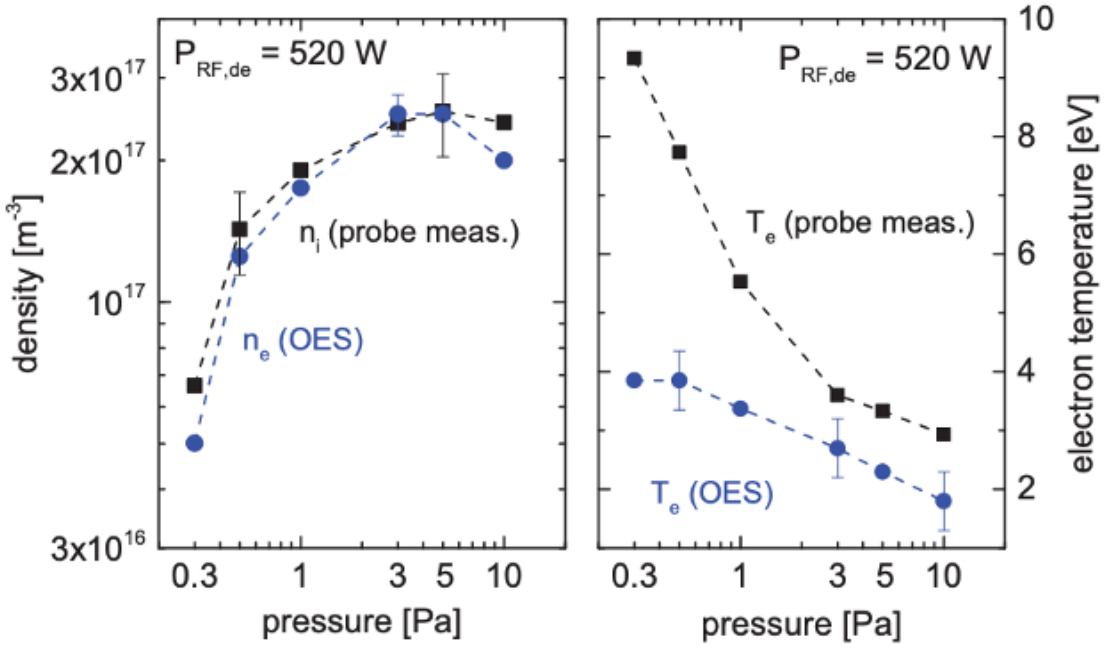

Figure 4.4: A plot of electron density and electron temperature for varying discharge pressure at a constant input power of 520 W. Taken from [154].

measurements for varying pressure taken from [154]. The trends in the plasma parameters show an increase in density and decrease in electron temperature for increasing discharge pressure, mirroring the trends presented in Section 4.3.1.

The results presented in Figure 4.4 are collected at higher powers than that are achievable in the UoL ICP discharge plasma, however the trends for increasing pressure mirror those found in the UoL ICP rig. At these higher powers, inductive coupling will be dominant, and so the power coupling to the electrons in the bulk plasma is much more efficient. The results presented in this chapter indicate that the E- to H-mode transition occurs at around 100 W for a constant discharge pressure of 10 Pa in the UoL ICP rig. To investigate trends in the electron parameters at higher powers, issues with overheating in the RF matching unit should be solved so the plasma discharge can run consistently.

4.3.4 Conclusions about available regimes

The main motivation for using the ICP discharge to study plasmas in contact with divertor-like surfaces is the range of plasma conditions that can be generated. With this in mind, it is worth examining the pressure and power dependences to identify the conditions available for testing.

By varying the gas pressure and fixing the RF power, three key plasma regimes were identified that are accessible in the ICP discharge source. These regimes will be utilised in measurements close to samples in Chapter 5 and are indicated on the plot of electron properties vs pressure in Figure 4.5 and characterise the range of conditions available in the hydrogen ICP plasma. The data in Figure 4.5 is copied from Figure 4.1 in order to highlight the three regimes accessible in the ICP device over the full pressure range.

1. Low n_e, high T_e

The first regime, for low pressures from 1 to 3 Pa, is a low electron density, high electron temperature regime. For these plasma parameters, there will be low H_2 densities, and a large number of high energy electrons with low collision frequencies due to the lower densities.

2. Intermediate densities and temperatures

At gas pressures of 4 to 6 Pa, there exists an intermediate regime characterised by intermediate electron temperatures and densities. This regime will be discussed in further detail in the next section, as plasma emission is shown to peak in this regime.

3. High n_e, low T_e

For higher gas pressures above 6 Pa, there will be a high density of electrons, a high density of molecular hydrogen, and a much lower electron temperature, signifying that there are now significantly fewer high energy electrons than in the first regime.

These three regimes provide a basis to the parameters achievable in the ICP hydrogen plasma discharge, and will be referred to when discussing the experimental research completed in the University of Liverpool ICP rig.

By varying the RF power, this opens up a sub-regime characterised by an unchanging EEDF (and therefore T_e), and varying electron density with few high energy electrons

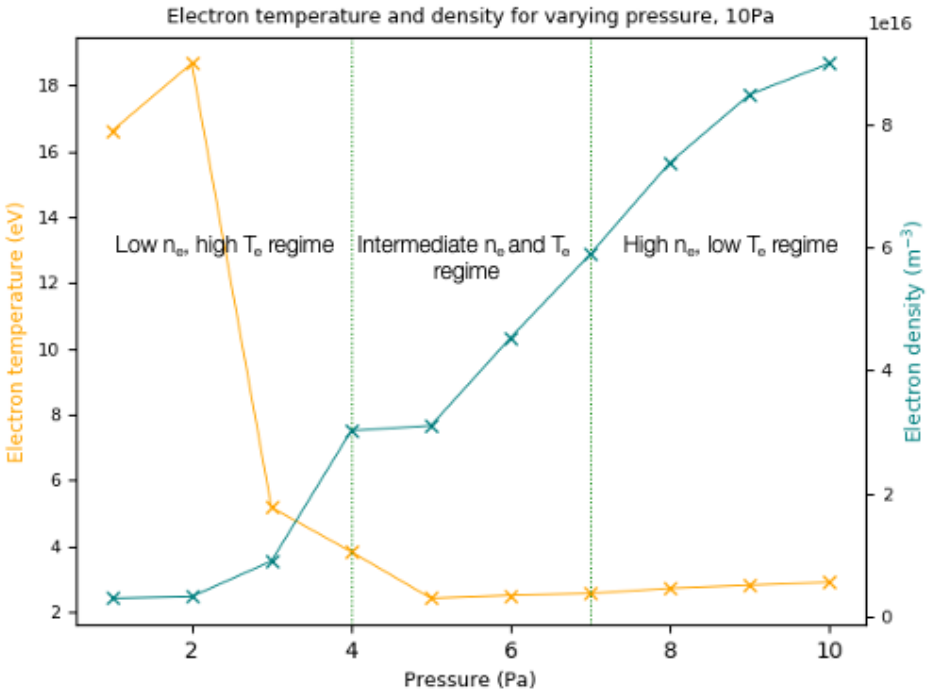

Figure 4.5: Electron temperature and density for varying pressure at a constant power of 100 W. A copy of Figure 4.1 to highlight the three available regimes, (i) low pressure below 4 Pa (ii) intermediate pressures between 4 - 7 Pa and (iii) high pressures above 7 Pa.

available for electron-molecule or electron-electron interactions. Research on the effects of varying the discharge pressure and RF power on the plasma emission will be outlined in the subsequent sections, with an extension of this research aiming to study the effects of varying the plasma and material conditions on the plasma emission and plasma parameters close to a divertor-like sample presented in Chapter 5.

4.4 Measurements of atomic and molecular emission

This section contains measurements of both atomic and molecular emission collected over the full range of conditions of the ICP discharge. The results were obtained using the high-resolution spectroscopy apparatus described in Section 3.2, using the line of sight through the centre of the plasma chamber, in the arrangement shown in Figure 3.2. Section

4.4.1 contains the results of the atomic and molecular emission measurements with both the Balmer line emission intensities and the Fulcher band line emission intensities presented. Ratios of the H_γ/H_α lines for varying pressure and power will be presented in Section 4.4.2. In Section 4.4.3 calculations of the rotational temperature for varying discharge pressure and power will be presented to provide further information about the key characteristics of the ICP discharge, with the final section summarising the information that is useful from the analysis of these emission measurements.

4.4.1 Emission results for varying pressure and power

The objective of this section is to outline the trends in the line intensities of the first three hydrogen Balmer lines and key lines in the Fulcher band for two sets of conditions. As in Section 4.3.1, the first set consists of measurements for pressures ranging from 1 Pa to 10 Pa at a constant power of 100 W. The second set of measurements presented in this section corresponds to powers in the range 10-300 W, collected at a constant pressure of 10 Pa. A range of additional emission measurements were made at other combinations of pressure and power within these ranges, but the two sets of measurements presented here provide a thorough insight into the trends in emission for varying discharge conditions.

A plot of the H_α, H_β and H_γ emission for varying pressure at a constant power of 100 W can be seen in Figure 4.6. These emission measurements show a slight increase in intensity for all three lines for increasing pressure from 1 Pa until a peak at pressures around 4 Pa. These measurements at low pressure correspond to the first regime outlined in Section 4.3.4. The Balmer line intensities then remain roughly constant from 4 to 7 Pa, corresponding to the second regime, until they slowly decrease in intensity from 7 to 10 Pa, in the third regime with high electron density and low electron temperature.

Figure 4.7 shows a plot of the intensity of the H_α, H_β and H_γ lines for varying power at a constant discharge pressure of 10 Pa. There is shown to be a sixfold increase in the intensity of the three Balmer emission lines for increasing RF power from 10 W to 300 W, with a larger increase in intensity for increasing power above 100 W. Figure 4.8 shows a Fulcher band spectra and the band structure of the molecular emission in the ICP discharge source. This spectra was collected in the centre of the ICP chamber at a constant pressure of 10 Pa and a RF power of 300 W. This spectra will be compared to measurements of the Fulcher band close to different samples in Chapter 5 in order to study the effects of the materials on the vibrational states.

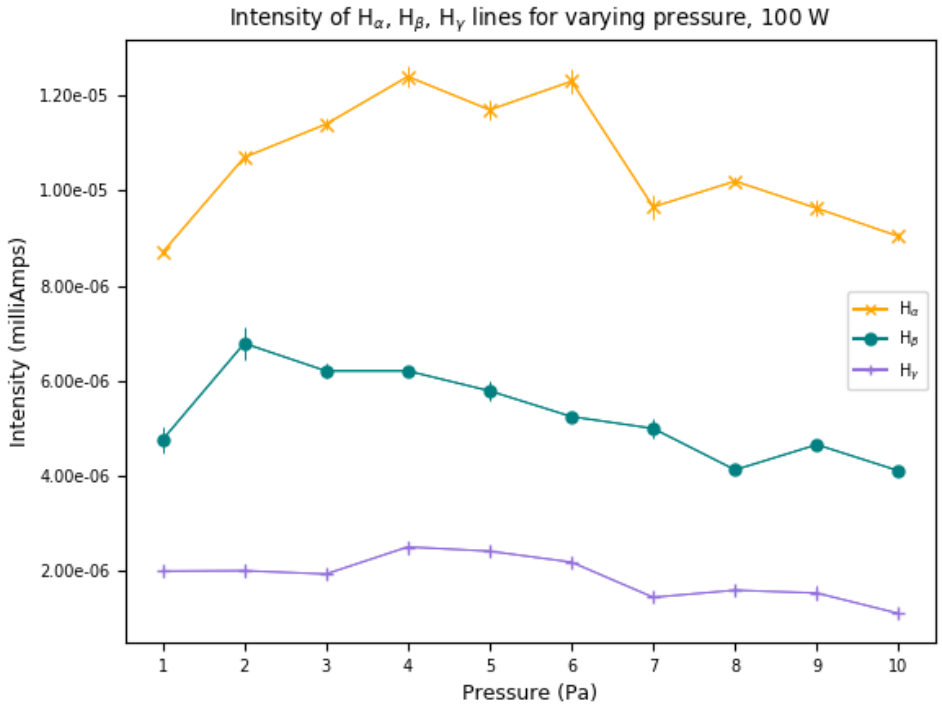

Figure 4.6: H_α, H_β and H_γ line intensity for varying discharge pressure for a fixed power of 100 W.

A plot of the Fulcher band Q1 (0-0), (1-1) and (2-2) line emission for varying pressure collected at a constant power of 100 W can be seen in Figure 4.9. The emission intensity of the three molecular lines has a weak dependence on pressure but is shown to decrease for increasing discharge pressure. The 1-1 line is shown to decrease most significantly from 3.5×10^{-6} mA at 1 Pa, to 1.8×10^{-6} mA, while the other two lines also decrease over this pressure range from around 2.5×10^{-6} mA at 1 Pa, to 1.3×10^{-6} mA. The unit of measurement (mA) for these values comes from the photomultiplier current measured by the spectrometer detector.

Figure 4.10 shows a plot of the Fulcher band Q1 (0-0), (1-1) and (2-2) line emission for varying RF power at a constant discharge pressure of 10 Pa. The emission of all three lines in the Fulcher band increases almost exponentially for increasing power by more than an order of magnitude from 10 W to 300 W.

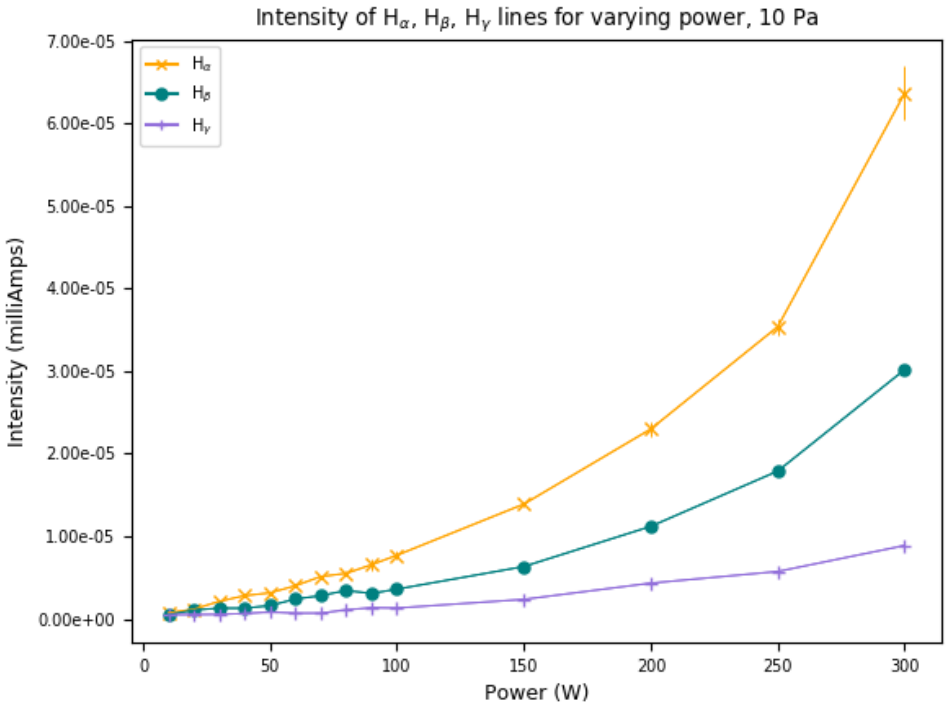

Figure 4.7: H_α, H_β and H_γ line intensity for varying RF power at a fixed pressure of 10 Pa.

4.4.2 Analysis of Balmer line emission for varying discharge conditions

In this section, further analysis of the atomic Balmer line emission will be presented. As discussed in Section 3.2.3, the ratio of the intensities of the H_γ/H_α lines is a useful tool to gain a deep understanding of the behaviour of atoms and molecules in a plasma. The results in this section will highlight the trends in the H_γ/H_α ratio for varying gas pressure and RF power in order to characterise the emission in the ICP discharge. These trends will then be interpreted further in Section 4.4.4.

The ratio of the H_γ to H_α line intensities for increasing pressure can be seen in Figure 4.11 for fixed RF power of 100 W. This ratio is shown to decrease for increasing discharge pressures almost linearly from 1 Pa to 10 Pa, from a ratio of the two Balmer lines of 0.23 at low pressures to 0.12 at a discharge pressure of 10 Pa.

In Figure 4.12, a plot of the ratio of H_γ to H_α line intensities for increasing RF power

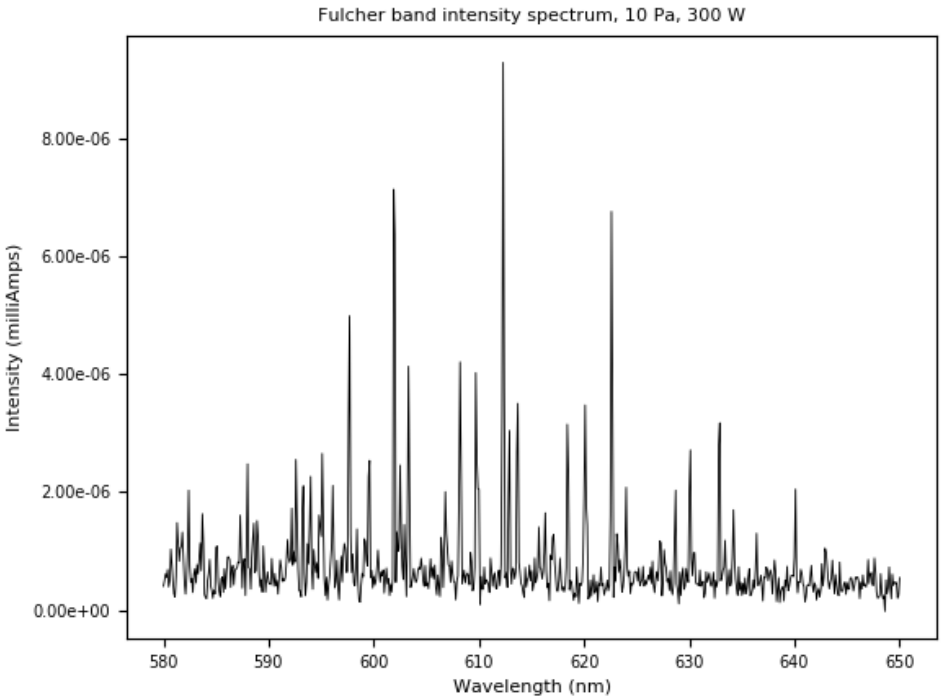

Figure 4.8: Fulcher band spectra Collected in the centre of the ICP chamber at a constant pressure of 10 Pa and power of 300 W.

and fixed gas pressure of 10 Pa is presented. The H_γ/H_α ratio is also shown to decrease for increasing RF power at a constant pressure of 10 Pa. At lower powers this ratio is high, however at an input power of around 50 W this ratio decreases from 0.7 to around 0.2 and remains almost constant at 0.2 for increasing powers from 50 W to 300 W.

4.4.3 Analysis of Fulcher band emission for varying discharge conditions

The aim of this section is to present rotational temperature analysis of the Fulcher emission through the use of Boltzmann plots. This technique is described in Section 3.2.3 and provide a means of quantitative analysis to extract information about the behaviour of molecules in low temperature plasmas. The results in this section will present the trends in the rotational temperature, T_{rot}, for varying pressure and power and will then be interpreted further in Section 4.4.4.

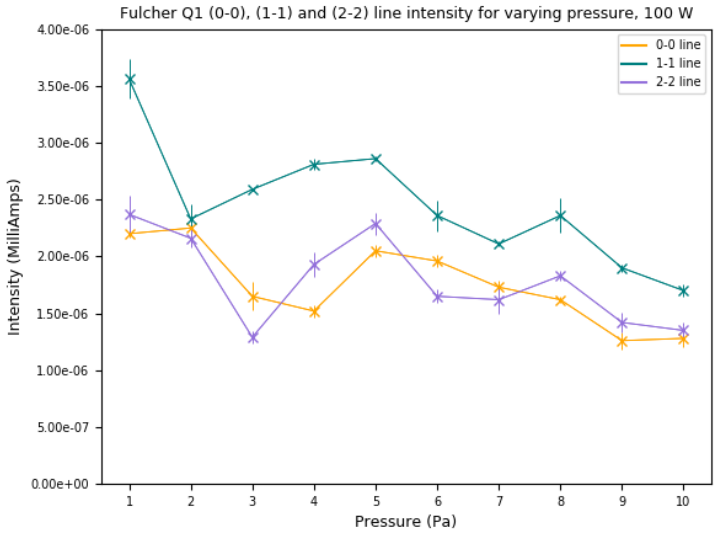

Figure 4.9: Fulcher band Q1 (0-0), (1-1) and (2-2) line intensity for varying pressure at a fixed RF power of 100 W.

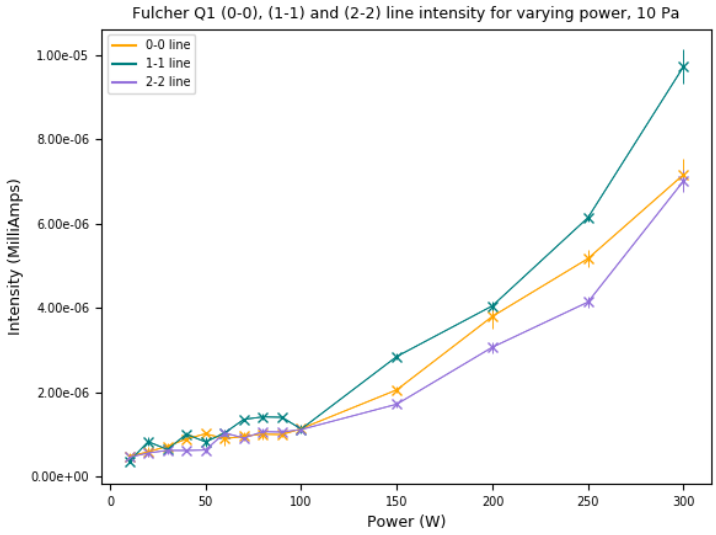

Figure 4.10: Fulcher band Q1 (0-0), (1-1) and (2-2) line intensity for varying power at a discharge pressure of 10 Pa.

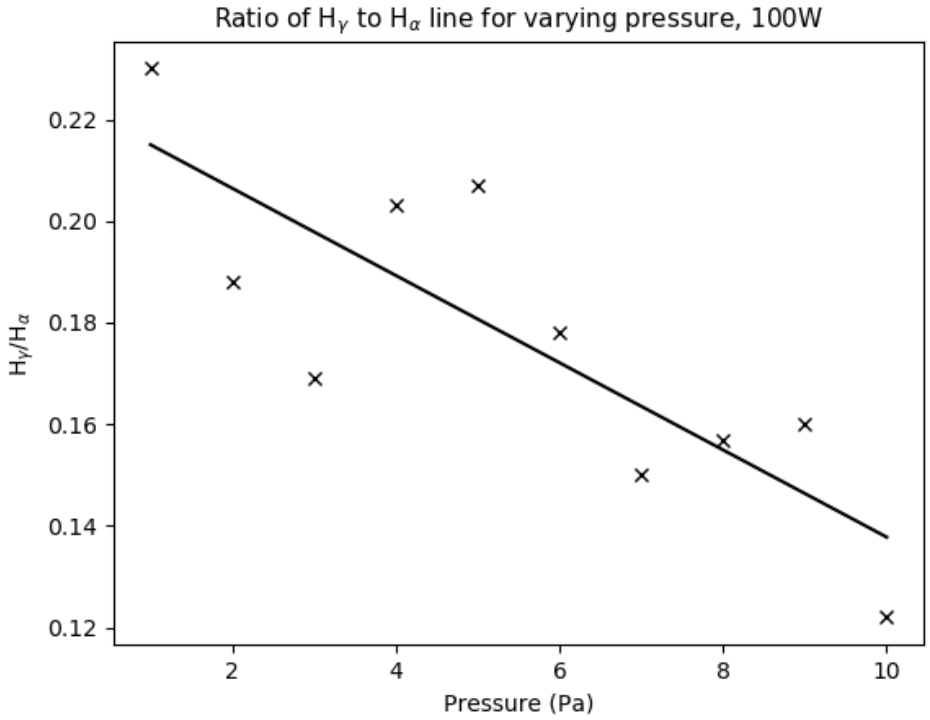

Figure 4.11: The ratio of the H_γ to H_α line intensities for varying pressure at a constant RF power of 100 W.

As in previous sections in this chapter, this section is separated into two sets of measurements. The first of which consists of Boltzmann plots and the resulting rotational temperatures for pressures ranging from 1 Pa to 10 Pa at a constant power of 100 W. The second set of measurements are collected for powers in the range 10-300 W, collected at a constant pressure of 10 Pa.

Rotational temperatures for values of increasing pressure 1 Pa, 5 Pa and 10 Pa at a fixed RF power of 100 W can be seen in Figure 4.13. At both 1 and 10 Pa, in the first and third regimes outlined in Section 4.3.4 respectively, the rotational temperature were found to both be around 600 K. In the intermediate regime with a discharge pressure of 5 Pa, the rotational temperature was significantly lower at around 250 K.

In Figure 4.14, the rotational temperature calculated for RF input powers of 10, 50, 100 and 300 W with a fixed discharge pressure of 10 Pa can be seen. For increasing RF

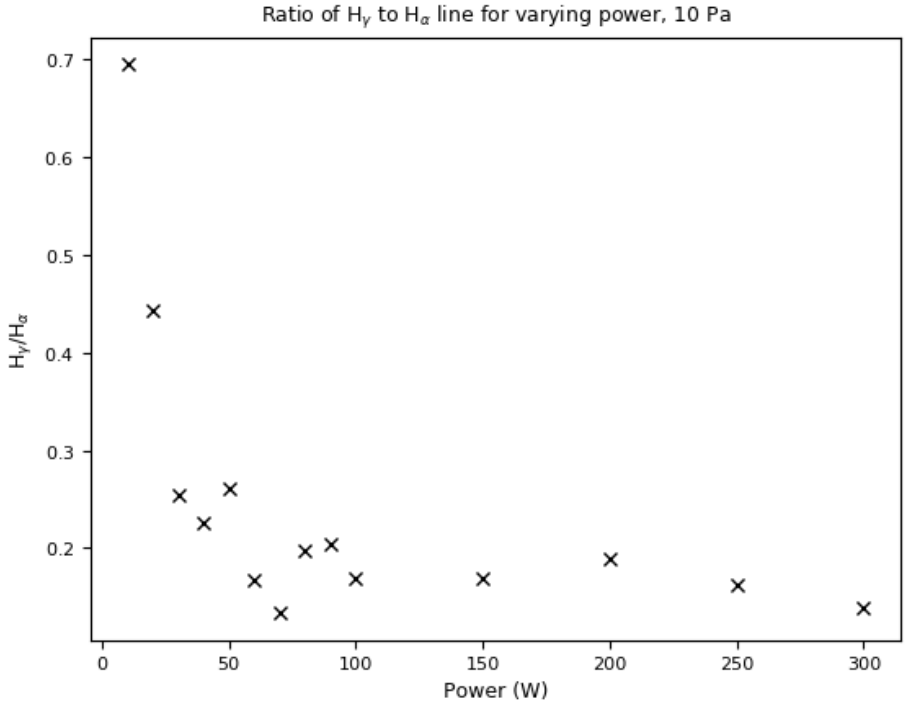

Figure 4.12: The ratio of H_γ to H_α line intensities for varying power at a constant pressure of 10 Pa.

power, the rotational temperature decreases from 736.98 K at 10 W to 562.91 K at 300 W, with an almost linear decrease in temperature for varying power.

4.4.4 Interpretation of atomic and molecular emission measurements

The trends for both the atomic and molecular emission measurements shown in Figures 4.6-4.14 are mirrored in published research for ICP hydrogen discharges.

To interpret the emission measurements shown in Section 4.4.1, the frequency of collisions will be an important tool. The general expression for the collision frequency, f_{coll}, is related to the density of electrons, n_e, and hydrogen gas density, n_{H_2}, via the following expression,

$$f_{coll} \propto n_{H_2} n_e \int_{E_{threshold}}^{\infty} f(EEDF, \sigma)\mathrm{dE} \tag{4.1}$$

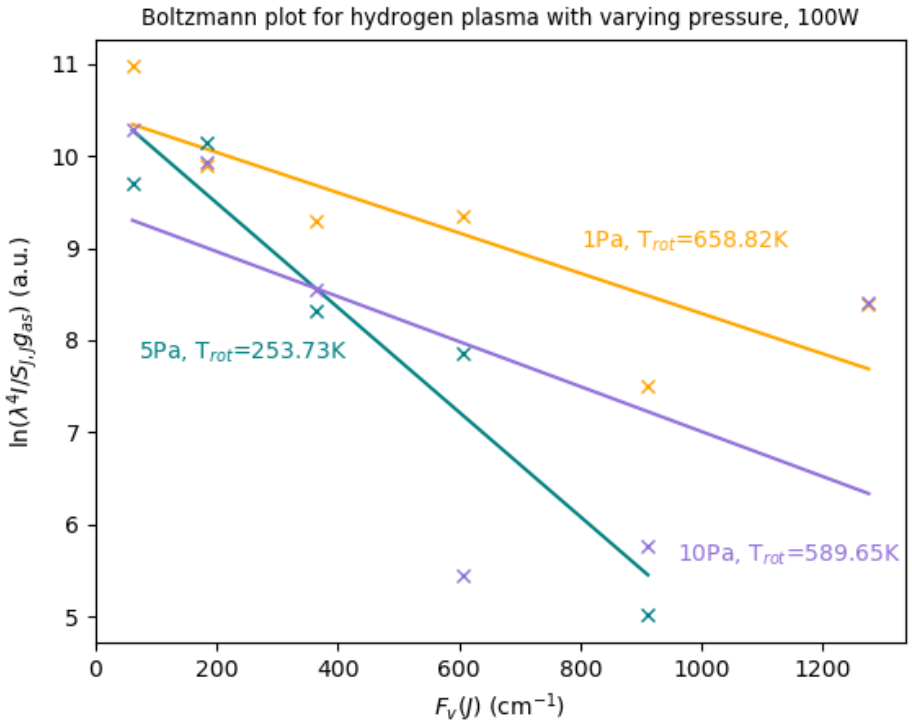

Figure 4.13: Boltzmann plot and rotational temperatures for 1, 5 and 10 Pa at a constant power of 100 W calculated using the Q-branch (0-0) band.

where σ is the cross-section of the collision, and E is the electron energy.

The increase in intensity of all three Balmer lines for varying pressure from 1 Pa to 4 Pa is a consequence of higher collision frequencies for increasing pressure (as n_{H_2} increases in Equation 4.1), coupled with high energy electrons which result in increased excitation of hydrogen atoms, leading to higher rates of Balmer line emission.

The intensity of the Balmer lines is effectively constant for increasing pressures from 4 to 7 Pa, before a decrease in emission intensity occurs above 7 Pa. The decrease in intensity from 7 to 10 Pa indicates there is less excitation of hydrogen atoms at higher pressures. Although there are more particles in the chamber available for collisions, the electron temperature is much lower, and so the electrons do not have sufficient energy to dissociate and the available free electrons do not have the required energy to excite hydrogen. Therefore at higher pressures, the Balmer line intensity is similar in intensity to

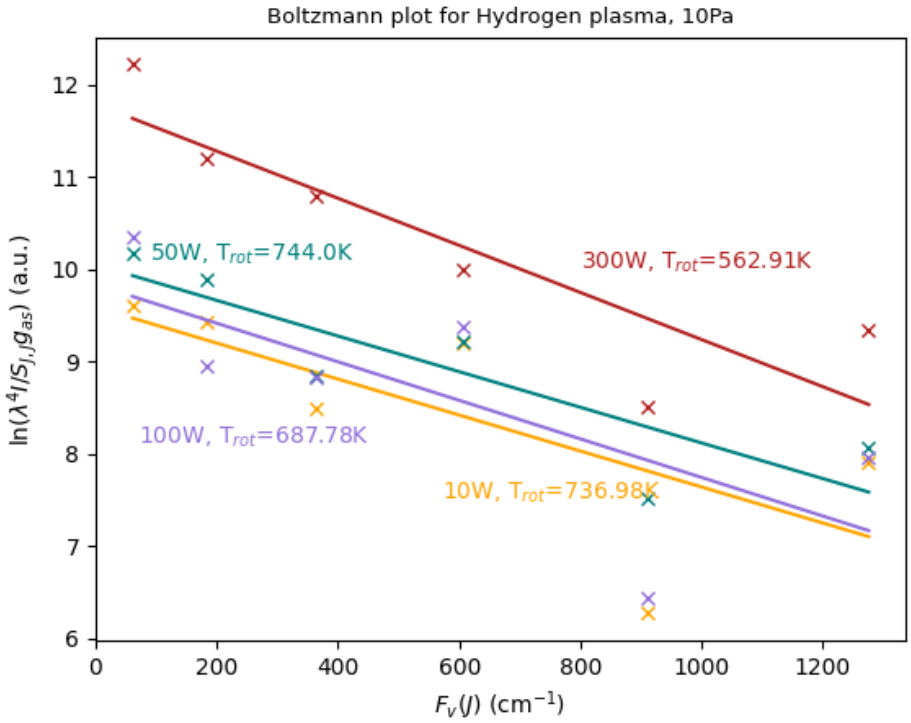

Figure 4.14: Boltzmann plot and rotational temperatures for 10, 50, 100 and 300 W at a constant pressure of 10 Pa calculated using the Q-branch (0-0) band.

the values measured at low temperatures, and less than the peak intensity at intermediate pressures between 4 Pa and 7 Pa. This trend in the Balmer emission for increasing discharge pressure may also be attributed to the change in spatial distribution of the plasma in the ICP chamber. At low pressures, the plasma will fill the chamber, however as the pressure increases, the plasma will become more dense in the region closest to the coil. As the emission measurements presented in this chapter are collected using a line of sight through the centre of the chamber, these results may not be indicative of the brightest region at higher pressures and so the decrease in atomic emission after 7 Pa may correspond to this effect.

The power dependence of the Balmer intensities is related to the increased density of electrons that are available to excite hydrogen atoms. Despite the electrons having less energy at higher powers, the increased electron density is enough to strongly impact the

intensity of the Balmer lines series resulting in an almost exponential relationship between the line intensities and RF power.

Additionally, the transition to inductive coupling of the RF power will have an effect on the trends in emission. In the inductive coupling mode, power is absorbed over a much larger volume throughout the plasma than in the capacitive coupling mode, where the RF power is absorbed close to the sheaths. For higher powers at constant pressure there will be an increase in electrons resulting in an increase in excitation of excited atoms, alongside increased emission over a larger volume of the plasma, therefore more emission observed along the chord. These two effects of the inductive power coupling can combine to give the increase in emission in H-mode observed in Figure 4.7.

The emission intensity for the Fulcher band Q1 (0-0), (1-1) and (2-2) lines is shown to have a strong dependence on the input power, however varies significantly less for increasing discharge pressure. The power dependence can be explained by the increase in electron-molecule collisions resulting in an increase in molecular excitation and therefore molecular emission. All three lines increase relatively equally with respect to input RF power, implying the increased emission is due to ionisation of electrons and increased collisions between electrons and molecules. For increasing pressure, the Fulcher lines decrease in intensity. As the plasma constituents have less energy at higher pressure, the electrons do not have sufficient energy to excite the H_2 molecules, resulting in this measured decrease in emission. In a low temperature ICP discharge, the mean free path for Coulomb collisions will be relatively long, on the order of the diameter of the chamber, and so electron-molecule collisions dominate. Therefore molecular excitation will be proportional to the density of electrons in the chamber.

Further analysis presented in Section 4.4.2 and 4.4.3 provides information about the behaviour of atoms and molecules in the ICP discharge plasma. For increasing discharge pressure, the ratio of the H_γ/H_α emission lines decreases, indicating a decrease in the rate of electron-ion recombination. This is also related to the decrease in electron temperature for increasing gas pressure, since at higher pressures the electrons do not have sufficient energy to excite the hydrogen atoms to the higher-n states, and therefore the H_γ/H_α ratio will decrease. The excited hydrogen atoms that are created through electron-ion recombination result in the higher-n lines increasing in strength relative to the H_α line.

The H_γ/H_α ratio does not decay linearly for increasing powers. At low powers the ratio is high, however above 50 W the line ratio is much lower and remains constant for increasing RF power. In this range, recombination emission is known to dominate over

excitation emission implying recombination as the dominant process. Alongside the change in molecular reactions, the trend in Figure 4.12, is also partially due to the change in T_e with varying power, as the electron temperature drops significantly at 50 W, shown in Figure 4.2. After 50 W, the electron temperature remains roughly constant, and so this trend is also mirrored in the ratio of the H_γ/H_α lines, since there is a constant electron energy available for excitation over this range.

As shown in Figure 4.13, at low and high pressures the value of the rotational temperature is around 600 K. However at intermediate pressures around 5 Pa, the rotational temperature calculated using the Boltzmann plot technique is found to be significantly reduced, at around 250 K. This mirrors the relationship between the Balmer emission and discharge pressure as seen in Figure 4.6 and discussed in Section 4.4.1. At lower pressures, the Balmer intensity is low, gradually increasing with increasing pressure until around 5 Pa, before decreasing again at higher discharge pressures. This decrease in the rotational temperatures for increasing pressure may be due to the higher rate of collisions of energetic species, transferring their kinetic energy e.g through H_2^+/H^+ collisions with H_2. As the rotational temperature is calculated using measured absolute intensities of the Fulcher band lines, the spatial distribution of the plasma will also impact the value of rotational temperatures at higher pressures. As previously mentioned, at higher pressures the plasma will be most dense closer to the induction coil, and so will be brightest in the upper half of the chamber. As the line of sight for these measurements is through the centre of the chamber, the rotational temperatures calculated from these results may not be representative of the bulk plasma temperature.

The rotational temperatures are observed to decrease with increasing input power, as shown in Figure 4.14. This decrease in T_{rot} for increasing power corresponds to the transition from the capacitive to the inductive power coupling mode in the ICP chamber. In the capacitive coupling mode, there is an increase in the number of higher energy electrons and ions in the plasma sheath region, and so a higher density of energetic species, resulting in a higher value of T_{rot}. This then decreases into the H-mode of the ICP where inductive heating dominates and the average energy of the charged species is lower.

4.5 Summary

In this chapter, a characterisation of the inductively coupled discharge plasma at the University of Liverpool was presented. These measurements provide a clean slate on which

measurements close to divertor-like samples will build on in Chapter 5, in order to identify trends in plasma emission and electron properties for varying sample material.

To enable a study of plasma parameters, Langmuir probes were utilised to characterise the plasma for varying discharge pressure and RF power. These results show an increase in electron density from 1×10^{16} to 1×10^{17} m^{-3} from 1-10 Pa at a constant power of 100 W and from 1×10^{16} to 2.5×10^{17} m^{-3} from 0-300 W at a constant pressure of 10 Pa. These trends are credited to an increased number of collisions for increasing pressure and power leading to more ionisation. The electron temperature is shown to decrease from around 20 to 2 eV from 1-10 Pa at a constant RF power of 100 W and from 5 to 2 eV for 10-300 W at a constant pressure of 10 Pa. These trends are also attributed to increasing collisionality in the ICP plasma for increasing power and pressure, resulting in lower average values of T_e. This work is consistent with published research in the field and mirrors typical trends in inductively coupled plasmas.

Further information about the behaviour of atoms and molecules in the ICP was gained through measurements of the atomic and molecular emission using optical emission spectroscopy. These measurements show a sixfold increase in the Balmer intensities from 10-300 W at constant pressure due to a higher number of collisions, leading to increased excitation of hydrogen atoms. The Q1 lines of the molecular Fulcher band are shown to decrease for increasing pressure, as the vibrational states of H_2 become more evenly distributed. The Q1 lines are also shown to increase linearly with increasing RF power due to higher densities of electrons available to excite hydrogen molecules.

Analysis of the Fulcher band emission shows a decrease in the rotational temperature for increasing power by almost 200 K over the full power range utilised. This trend corresponds to the transition from capacitively coupled mode where, due to the larger sheaths, the charged species have more energy and therefore can transfer energy to hydrogen molecules, increasing the rotational temperatures, to the inductively coupled mode. At higher powers, inductive coupling dominates, the sheaths are much smaller and so although there are more charged particles, they do not have as much energy as in the lower power E-mode, resulting in a decreased rotational temperature.

The ratio of the H_γ to H_α Balmer lines decreases linearly with increasing discharge pressure, corresponding to the lower temperatures measured at high pressures, resulting in less energetic species available to excite hydrogen to higher-n states. The rotational temperatures measured for increasing pressure increase to a peak at 5 Pa and then decrease for increasing pressure above 5 Pa. This may be due to the spatial distribution of the

plasma at higher pressures and should be investigated further in future studies.

The work outlined in this chapter will form a reference for measurements close to sample surface in the next chapter. These results allow for the distinction between the effects of changing plasma conditions and varying surface materials and temperatures on the plasma emission to be made.

Chapter 5

A Study of Low Temperature Plasma Conditions Close to Divertor-like Materials

5.1 Introduction

Plasma-material interactions play an important role in the successful operation of the power exhaust in fusion machines, however the interplay of edge plasmas and material surfaces are yet to be fully understood. Having characterised the hydrogen plasma parameters and emission in the University of Liverpool ICP discharge source for a range of plasma conditions in Chapter 4, the measurements presented in this chapter aim to study the effects of divertor-like material surfaces on these plasmas.

The main objective of the research presented in this chapter is to draw conclusions on the effects of three different material samples submerged in a low temperature plasma on the plasma parameters and plasma emission close to these surfaces. By utilising diagnostic techniques, the key atomic and molecular processes and trends in plasma parameters will be quantified for both varying plasma and material conditions. The ICP discharge rig and experimental set up outlined in Chapter 3 will be utilised for the measurements in this chapter. Optical emission spectroscopy and Langmuir probes will be utilised to obtain plasma emission and plasma parameter data close to samples of carbon, tungsten and nanostructured tungsten which will be submerged in the ICP chamber via a bespoke sample

heater described in Section 3.1.2.

Typical plasma parameter and plasma emission measurements in the ICP discharge source were presented in Chapter 4. From the characterisation of the ICP discharge, trends in the plasma parameters and plasma emission were detailed for varying discharge pressure and RF power. The electron temperature was shown to vary between 1-18 eV with electron densities in the range 10^{15}-10^{17} m^{-3}. The trends in the atomic and molecular emission were outlined and further analysis completed to study trends in line ratios and rotational temperatures.

The measurements in this chapter are an extension of the results outlined in Chapter 4, and this chapter is structured as follows. In Section 5.2 an outline of the experimental set up for specific measurements close to sample surfaces alongside the range of conditions utilised for the measurements in this chapter will be given. In Section 5.3, electron property measurements collected using a Langmuir probe close to the sample surfaces will be presented for varying pressure, power and sample temperature. Measurements of the atomic and molecular emission for varying discharge and sample conditions will then be presented in Section 5.4, which will provide further information about the effects of the divertor samples on the atoms and molecules in the plasma. In the final section, conclusions on the key atomic and molecular behaviour and trends in the plasma parameters close to the samples will be discussed.

The work in this chapter highlights the strong influence of carbon on the plasma emission, specifically affecting the vibrational distribution of the molecular Fulcher band. The two tungsten samples are observed to have little effect on both the plasma parameters and emission, only influencing the electron properties at high sample temperatures and specific discharge conditions. This research provides useful information on the behaviour of low temperature plasmas close to material surfaces relevant to fusion divertor regions.

5.2 Range of conditions utilised

For the measurements that make up the bulk of this chapter, optical emission spectroscopy and Langmuir probes have been utilised to investigate plasma conditions close to three different samples.

Measurements were collected for varying discharge conditions for gas pressures in the range 1 Pa to 10 Pa and RF input powers from 10 W to 300 W, as in Chapter 4, and material conditions for various sample materials, temperatures and texture. Three samples

Table 5.1: A description of the key properties of the three materials utilised in measurements close to divertor-like samples.

Material	Material properties
Tungsten	Metallic surface similar physically to the stainless steel and aluminium surfaces of the ICP chamber. High melting point and low sputtering yield.
Nanostructured tungsten	Same material properties as smooth tungsten, however has completely different surface topology, and likely has different surface reactivity due to the massively increased surface area of material exposed to the plasma.
Carbon	Different to the metallic surfaces in both reactivity and surface conditions. Carbon reacts easily with hydrogen so can generate hydrocarbon compounds that may be present as long-lived impurities in the discharge volume. Carbon has a high sublimation temperature and low Z.

were used in this investigation, carbon, tungsten and nanostructured tungsten which were inserted into the ICP chamber via the bespoke sample heater. The sample temperature was then varied from 0 to 1200C in order to investigate the influence of sample temperature on the atoms and molecules in the ICP discharge rig. A summary of the samples used in this research can be seen in Table 5.1, which highlights the key properties of each material.

To study the trends in plasma emission and parameters close to the samples, the "edge" Langmuir probe and line of sight closest to the sample were utilised. Figure 5.1 shows the orientation of the edge probe which can measure local plasma parameters 1 cm from the sample surface. The trends in plasma parameters using this probe will be highlighted in Section 5.3. The perpendicular distance from the line of sight parallel to the sample surface was varied to investigate the effects of the heated sample on the atomic and molecular emission. Four different positions were utilised which will be described in Section 5.4 alongside the results from these measurements.

The OES and probe measurements presented throughout this chapter are taken from an average of five complete data sets collected for the same plasma conditions. Repeat measurements were collected in order to ensure the reproducibility of the conditions in the ICP discharge plasma and calculate errors in the diagnostic techniques. Errors were estimated by calculating standard deviations in the measured values of T_e, n_e and absolute intensities of the Balmer series from five repeat data sets. The magnitude of the uncertainties in the measurements in this chapter were similar to those measured in

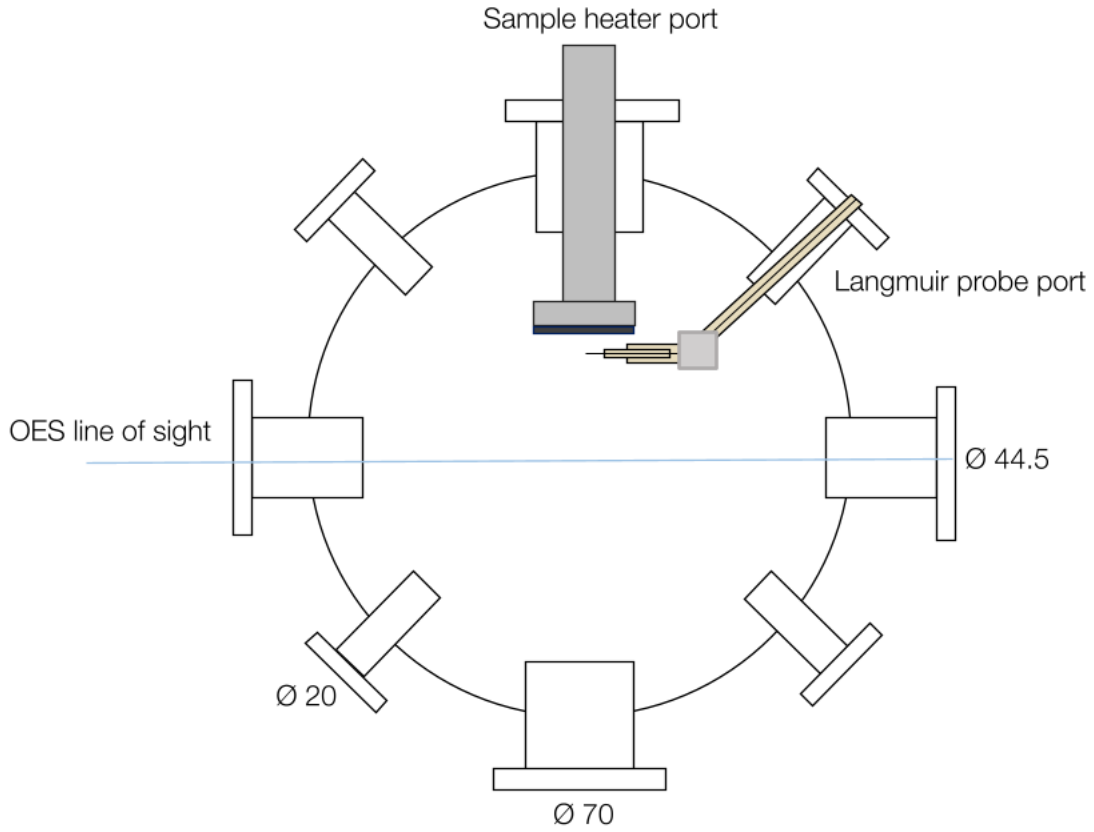

Figure 5.1: A repeat of Figure 3.3 to show the horizontal cross-section of the ICP rig to highlight the diagnostic ports, measurement positions and sample heater position with the edge plasma probe.

Chapter 4 for similar conditions. Due to this, error bars are not included in the figures in this chapter for varying pressure and power. However error bars are included in figures of the electron property and emission measurements for varying sample temperature and highlight the higher uncertainties in the measurements for increasing sample temperature compared with varying discharge pressure and power.

Measurements of plasma emission and plasma parameters were also collected with the sample heater submerged in the plasma but with no sample on the sample heater. As these measurements yielded similar results to the measurements presented in Chapter 4 with no sample heater, it was concluded that the presence of the sample heater in the chamber

did not have any significant effect on the plasma conditions. Therefore the focus of this chapter will be to investigate the effects of the different sample materials on the plasma emission and plasma parameters.

5.3 Measurements of electron properties

This section contains electron property measurements collected over the full range of conditions of the ICP discharge. The results were obtained using the Langmuir probe apparatus outlined in Section 3.3, both in the centre and edge of the plasma chamber close to divertor-like surfaces, in the positions shown in Figure 3.2 and 3.3. Section 5.3.1 contains the results of the measurements for each sample, while Section 5.3.2 contains an interpretation of these measurements with respect to the known understanding of ICP discharges, with reference to the characterisation of the discharge plasma completed in Chapter 4.

5.3.1 Electron properties for varying power, pressure and sample temperature

Three sets of measurements are presented here in order to study the trends in the electron properties at the edge of the chamber close to varying material surfaces. The first set consists of probe measurements for pressures ranging from 1-10 Pa, made at a constant power of 100 W and fixed sample temperature of 100C. The second set consists of measurements for RF powers in the range 10-300 W, made at a constant pressure of 10 Pa and sample temperature of 100C. The final set of results in this section consists of measurements collected at varying sample temperature from 100-1200C, with a constant gas pressure of 10 Pa and RF power of 100 W. These three sets of measurements were then completed three times, with a carbon, tungsten and nanostructured tungsten sample submerged in the plasma. Additional measurements were made at other combinations of pressure, power and sample temperature. However, these are not shown in this chapter as they do not add any additional information or insight about the effects of the surfaces on plasma conditions.

Electron property measurements can be seen for all three samples inserted in the plasma, with the probe in the centre of the chamber. Measurements in the centre of the plasma were collected in order to investigate the effects of the materials on the

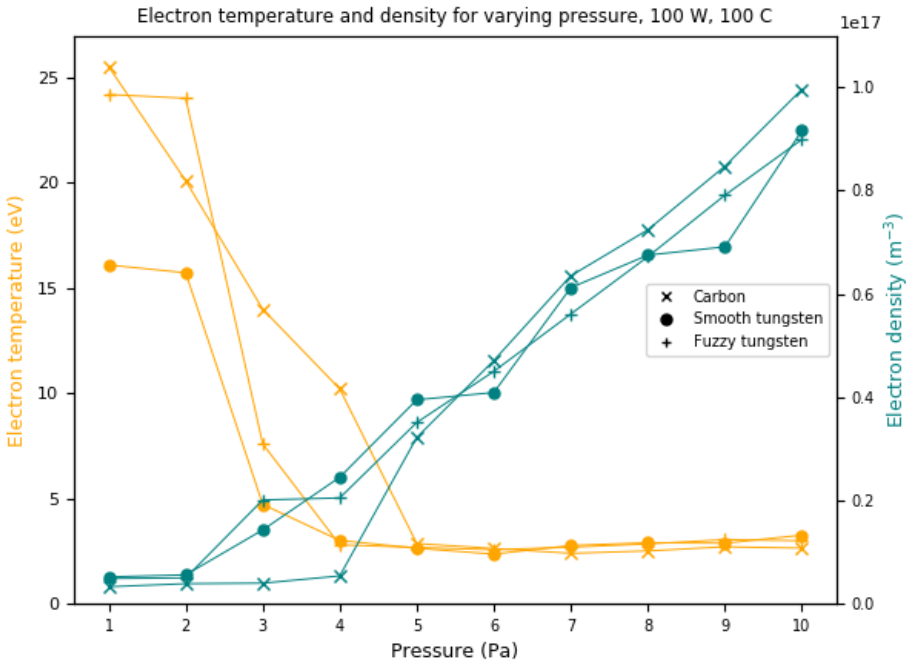

Figure 5.2: Electron temperature and density measurements for varying pressure with carbon, tungsten and nanostructured tungsten samples inserted into the plasma at a constant power of 100 W and sample temperature of 100C. Measured in the centre of the chamber using the "bulk" Langmuir probe.

bulk plasma parameters. Figure 5.2 shows electron temperatures and electron densities measured for varying pressure with each of the three samples inserted into the plasma. These measurements were collected for varying pressure in the range 1 - 10 Pa, at a constant power of 100 W and sample temperature of 100C. As in Figure 4.1, the electron temperature measurements are largest at low temperatures. The high values of T_e at low pressure conditions determined by the Langmuir probe are not believed to be an accurate reflection of the true plasma temperature. Discharges at these low pressures are associated with extremely long collisional path lengths, longer than the chamber dimensions, and hence the EEDF is likely to be non-Maxwellian with high average energy electrons, rather than a collisionally-generated EEDF with a true T_e. As the pressure increases, there is a sudden drop to lower, constant temperatures in the 2-3 eV range above 4 Pa. These trends are very similar for all three samples and mirror the observed trends in the no-sample case

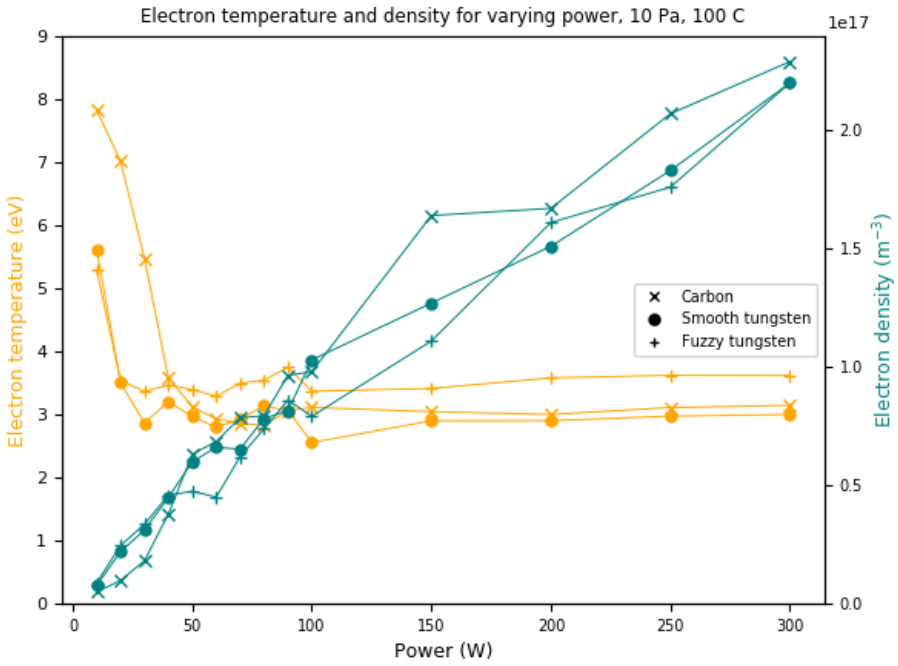

Figure 5.3: Electron temperature and density measurements for varying power with carbon, tungsten and nanostructured tungsten samples inserted into the plasma at a constant pressure of 10 Pa and sample temperature of 100C. Measured in the centre of the chamber using the "bulk" Langmuir probe.

as shown in Figure 4.1. Over this same pressure range, the electron density is shown to have a positive, almost linear relationship with increasing pressure. The electron densities are low at low pressure, and increase tenfold from 1 Pa to 10 Pa. The trends in the electron density for increasing pressure for all three samples are similar, with the carbon sample measurements yielding slightly lower electron densities than the other two samples at low pressures and slightly higher values above 5 Pa. These results are also very similar to electron density measurements for varying pressure without the sample heater, as seen in Figure 4.1.

Figure 5.3 shows the power dependence of the electron properties with the three samples, measured for powers in the range of 10 W to 300 W, at constant pressure of 10 Pa and sample temperature 100C. The electron temperature dependence shows two regimes, as in Figure 4.2. For lower powers the electrons are shown to have moderate temperature

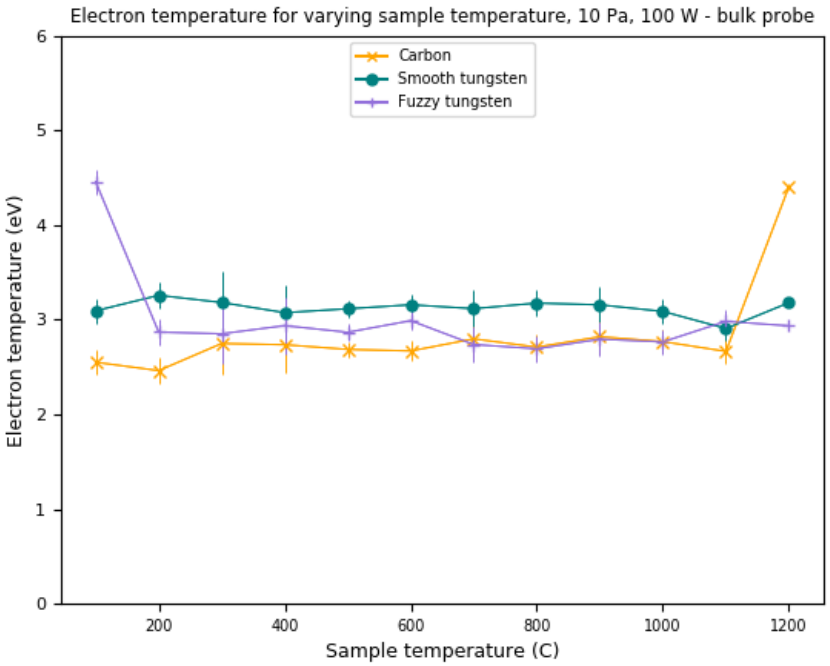

Figure 5.4: Electron temperature measurements for varying sample temperature with carbon, tungsten and nanostructured tungsten samples inserted into the plasma at a constant pressure of 10 Pa and RF power of 100 W. Measured in the centre of the chamber using the "bulk" Langmuir probe.

between 6-8 eV, with T_e measurements with the carbon sample inserted in the chamber yielding the highest values. Above an input power of 50 W, the electron temperatures for all three samples have an almost constant value of around 2-3.5 eV. These measurements follow a similar trend to electron temperature measurements collected without the sample heater seen in Figure 4.2 and there are no significant differences in the results for the three different samples. For increasing power, the electron density measurements increase linearly from 2×10^{16} to 2.5×10^{17} m^{-3}. This linear trend is also observed in the electron density measurements shown in Figure 4.2. An interpretation of these trends will be presented in Section 5.3.2.

In Figure 5.4, the relationship between electron temperature and sample temperature for all three samples immersed in the ICP discharge plasma can be seen. The plots of electron temperature and density have been separated to more clearly display these results

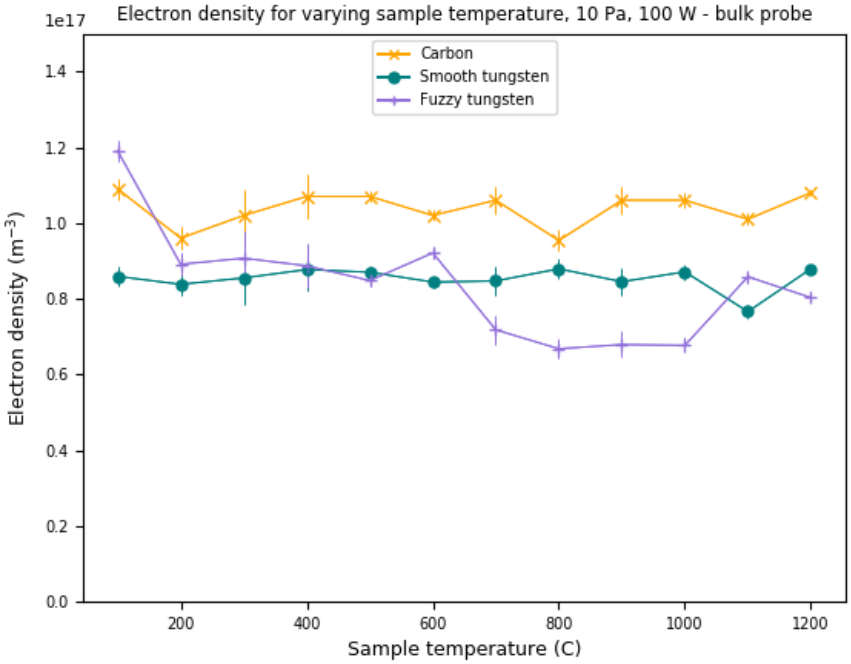

Figure 5.5: Electron density measurements for varying sample temperature with carbon, tungsten and nanostructured tungsten samples inserted into the plasma at a constant pressure of 10 Pa and RF power of 100 W. Measured in the centre of the chamber using the "bulk" Langmuir probe.

for varying sample material. These measurements were collected for temperatures in the range 100-1200C, at a constant pressure of 10 Pa and RF power of 100 W in the centre of the chamber using the "bulk" probe positioned as in Figure 3.2. These measurements show a similar trend in T_e for increasing sample temperature for all three samples.

The electron temperatures measured with the three different divertor samples remains constant at around 3 eV, with a slight spike in temperature at high sample temperatures with the carbon sample, and at low sample temperatures with the smooth tungsten sample. The relationship between electron density in the centre of the discharge chamber and sample temperature can be seen in Figure 5.5. There trends in n_e for increasing sample temperature for all three samples are similar. For increasing sample temperature, the electron density remains roughly constant, with only a slight decrease in the electron density observed in the case where the nanostructured tungsten sample is inserted in the

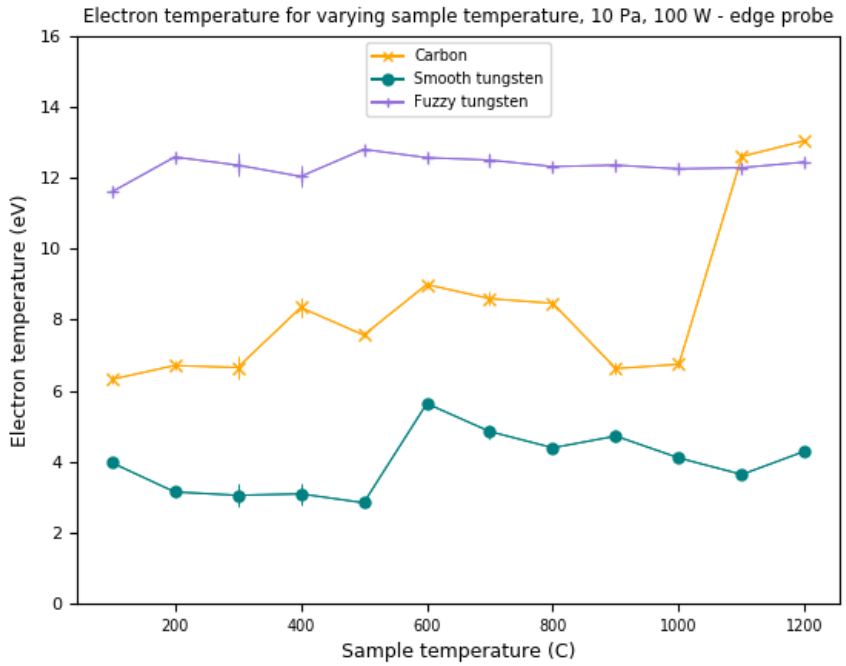

Figure 5.6: Electron temperature measurements for varying sample temperature with carbon, tungsten and nanostructured tungsten samples inserted into the plasma at a constant pressure of 10 Pa and RF power of 100 W. Measured close to the surface of the sample using the "edge" Langmuir probe.

ICP chamber.

To further investigate the relationship between plasma parameters and sample temperature, Langmuir probe measurements close to the surface of the three samples were collected. The "edge" Langmuir probe detailed in Section 3.3.1 was utilised to measure the electron temperature and electron density for increasing sample temperature in the range 100-1200C at a constant gas pressure of 10 Pa and RF power of 100 W. The results from these measurements for electron temperature and electron density can be seen in Figures 5.6 and 5.7 respectively. For increasing sample temperature, the measurements of electron temperature for both tungsten samples remain almost constant. The smooth sample yields a much lower electron temperature than for the nanostructured tungsten measurement, with values of T_e at 4 eV and 12 eV respectively. The carbon sample yields a distinctly different trend for increasing sample temperature, with a relatively

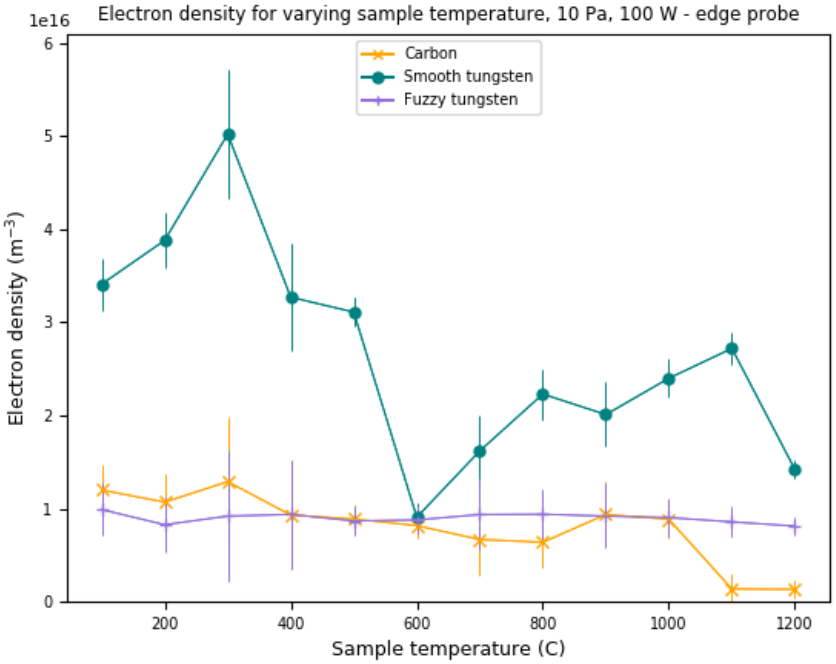

Figure 5.7: Electron density measurements for varying sample temperature with carbon, tungsten and nanostructured tungsten samples inserted into the plasma at a constant pressure of 10 Pa and RF power of 100 W. Measured close to the surface of the sample using the "edge" Langmuir probe.

constant electron temperature of around 7 eV for sample temperatures of 100C to 1000C, however for measurements taken at 1100C and 1200C the electron temperature increases significantly to around 13 eV. The electron density measurements collected with the carbon and fuzzy tungsten samples immersed in the plasma show are unchanged for increasing sample temperature. However with the smooth tungsten sample, the electron density decreases from around $4 - 5 \times 10^{16}$ m^{-3} at 100C to around 1×10^{16} m^{-3} at 1200C.

5.3.2 Interpretation of trends in plasma parameters close to samples

The trends presented in Section 5.3.1 highlight the electron property dependence on pressure, power and sample temperature in the presence of three different samples relevant to tokamak divertors.

For increasing discharge pressure, similar trends are observed to those presented in Section 4.3.1. As outlined previously, the trends for increasing pressure are attributed to the increase in electron collisions with background neutral particles. There is no notable difference in the electron properties for varying sample material over this pressure range. As these measurements for varying pressure and power were collected using the bulk probe in the centre of the chamber, these results indicate that the composition of the material sample does not impact the bulk plasma parameters significantly.

The power dependence, measured at the higher pressure of 10 Pa and sample temperature of 100C, is characterised by an increase in the electron density and a small reduction in the electron temperature over the range of powers utilised. The change in density is attributed to an increased rate of ionisation at higher powers, along with the transition to the inductively coupled power mode. These trends were described in Section 4.3.2, and similar trends are observed here. The relationship between T_e and input power is also linked to this change of power coupling mechanism as described in Section 4.3.2.

Measurements for increasing sample temperature were collected using both the "bulk" probe, in the centre of the chamber, and the "edge" probe, close to the sample surfaces. The results from these measurements indicate that the change in surface material and temperature has minimal impact on the electron density in the centre of the chamber. The measurements with increasing sample temperature show a slight decrease in n_e with the smooth tungsten sample, whereas n_e remains constant in the presence of carbon and nanostructured tungsten. This may be due to the differences in plasma chemistry and surface morphology and further investigation is required to quantify this effect.

For the measurements of electron temperature shown in Figure 5.6, only the carbon sample is shown to influence the measured value of T_e for increasing sample temperature. This increase in measured T_e, may reflect a change in collisionality close to the surface at higher sample temperatures as opposed to a higher bulk electron temperature. As the temperature of the sample increases, the gas density will decrease close to the sample. This decrease in density results in a decrease in the collisional frequency, and in turn yields a higher electron temperature measured by the probe. This sudden increase in the electron temperature occurs at 1100C, which may be the limit at which the sample temperature increases above the temperature the sample is heated to through contact with the plasma. This trend is also likely to occur with the tungsten samples inserted in the plasma, but the temperature of the sample heater may need to be increased above 1200C to see this dependence.

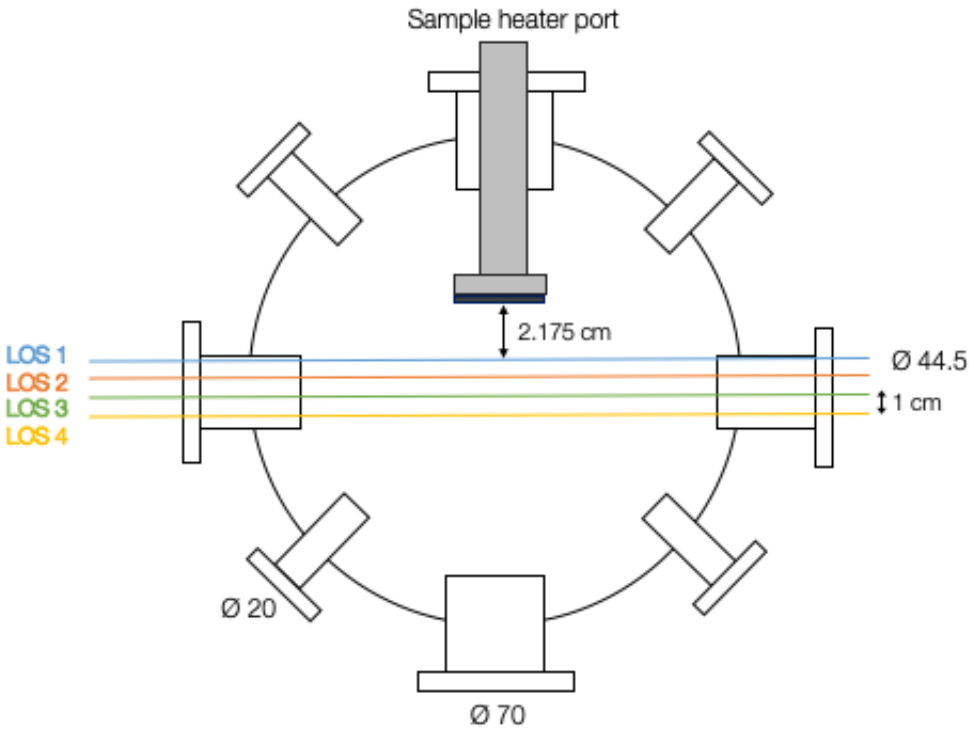

Figure 5.8: A repeat of Figure 3.4 to show the horizontal cross-section of the ICP rig and highlight the four lines of sight used in emission measurements close to the material sample. LOS1, the closest line of sight to the sample, is 2.175 cm away from the sample surface, and the subsequent lines of sight are separated by 1 cm.

5.4 Measurements of atomic and molecular emission close to sample surfaces

This section contains measurements of both atomic and molecular emission collected over the full range of conditions of the ICP discharge. The results presented here were obtained using the high resolution spectroscopy apparatus described in Section 3.2, with the closest line of sight parallel to the sample, "LOS1", used to collect emission data as seen in Figure 5.8. In Section 5.4.1 the results from atomic and molecular emission measurements will be described with both the trends in the Balmer line emission intensities and the Fulcher band line emission intensities for varying pressure, power and sample temperature presented. Further analysis of these emission measurements will be described in the

subsequent sections, with the ratios of the H_γ/H_α lines presented in Section 5.4.2 and calculations of rotational temperatures in Section 5.4.3 for varying discharge and material conditions. An interpretation of this analysis will be given in Section 5.4.4 with the key takeaways from this research summarised in Section 5.5.

5.4.1 Emission results close to material surfaces for varying pressure, power and sample temperature

The objective of this section is to outline observed trends in the line intensities of the first three hydrogen Balmer lines and key lines in the Fulcher band across three sets of conditions. To mirror the results presented in Section 5.3.1, the first set of measurements consists of results for varying pressure in the range 1-10 Pa at a constant power of 100 W and constant sample temperature of 100C. The second set of measurements presented in this section corresponds to powers in the range 10-300 W, collected at a constant pressure of 10 Pa and fixed sample temperature of 100C and the third set of measurements at varying sample temperature at a constant pressure of 10 Pa and RF power of 100 W. A range of additional emission measurements were made at other combinations of pressure, power and sample temperature within these ranges, but the measurements presented in the subsequent sections are sufficient to provide insight into the trends in emission across these three sets of conditions. The plots of these measurements are separated to highlight the trends for each sample clearly.

Figures 5.9, 5.10 and 5.11 show measurements of the H_α, H_β and H_γ emission for varying pressure at a constant power of 100 W and sample temperature of 100C with a carbon, tungsten and nanostructured tungsten sample respectively. Figure 5.12 shows the H_α Balmer line emission for varying pressure for each sample, so a clearer comparison can be made for the effects of varying the sample material on the emission. For the two tungsten samples, increasing the pressure has little effect on all three Balmer lines and the emission intensities are roughly constant for pressures in the range 1-10 Pa, as shown in Figure 5.10 and Figure 5.11. Figure 5.9 shows a trend of decreasing Balmer emission intensity for increasing pressure with the carbon sample, with the intensities of all three Balmer lines decreasing by a factor of 2 over the pressure range utilised. These trends are highlighted in Figure 5.12 where the H_α emission varies for increasing pressure solely in the presence of the carbon sample.

In Figures 5.13, 5.14 and 5.15 measurements of the H_α, H_β and H_γ emission for varying

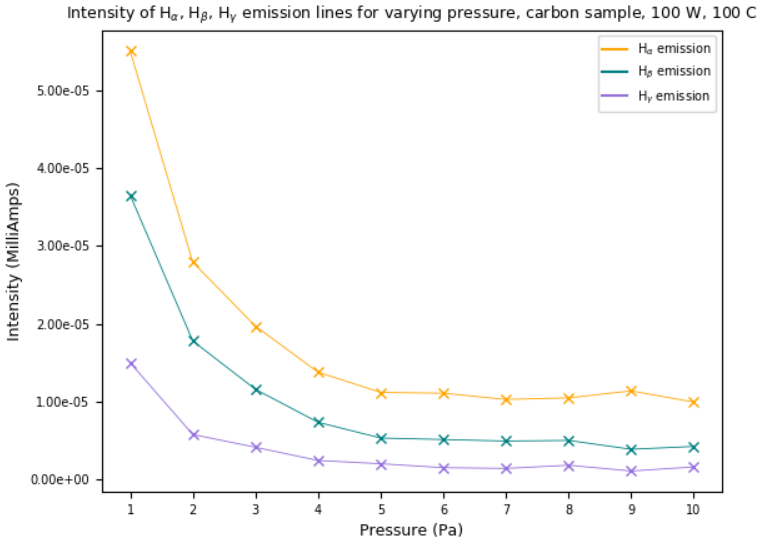

Figure 5.9: H_α, H_β and H_γ line intensities for varying pressure with a carbon sample inserted into the plasma at a constant power of 100 W and sample temperature of 100C using LOS1, the line of sight closest to the sample.

RF power at a constant pressure of 10 Pa and sample temperature of 100C with a carbon, tungsten and nanostructured tungsten sample, are presented.

For all three samples, the increase in input power increases the intensity of the three Balmer lines. This trend mirrors the relationship between atomic intensity and input power observed in Section 4.4.1 without the sample heater. Figure 5.16 highlights the trends in the H_α emission lines for all three samples and highlights that the trends in the atomic emission for varying power are independent of sample material.

For varying sample temperature, Figures 5.17, 5.18 and 5.19 show measurements of the H_α, H_β and H_γ emission close to the surfaces of the three different samples. The pressure is held constant at 10 Pa and the sample temperature fixed at 100C. At higher sample temperatures, the three Balmer lines increase significantly with the carbon sample. Figure 5.17 shows a spike in the emission intensity for the H_α, H_β and H_γ lines at 800C, then a constant emission intensity from 900-1200C.

The measurements collected close to the two tungsten samples shown in Figure 5.18 and 5.19 show no change in the emission for increasing sample temperature.

However the results shown in Figure 5.20 indicate higher levels of emission with the

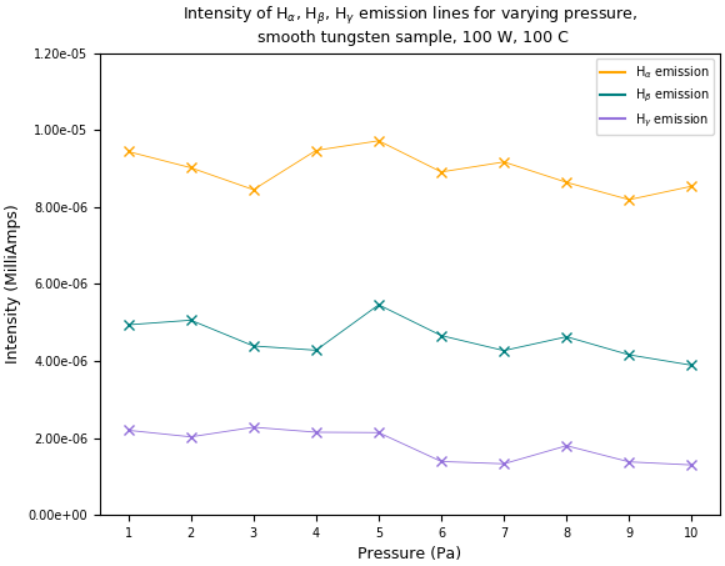

Figure 5.10: H_α, H_β and H_γ line intensities for varying pressure with a tungsten sample inserted into the plasma at a constant power of 100 W and sample temperature 100C using LOS1, the line of sight closest to the sample.

nanostructured tungsten sample compared to the smooth sample. The measurements presented in this chapter will be analysed further in the following two sections, with an interpretation of the key processes behind the trends for varying discharge and sample conditions outlined in Section 5.4.4.

Measurements of the Balmer series emission intensities were also collected for varying sample temperature utilising the four lines of sight, LOS1, LOS2, LOS3 and LOS4, shown in Figure 3.4. These lines of sight are 1 cm apart and allow for an investigation into the spatial distribution of the emission intensity throughout the region close to the sample heater. Using this data, heat maps were then plotted for each set of measurements in order to investigate the effects of the material surface on the emission at different positions in the ICP chamber. These measurements were collected at sample temperatures of 0, 300, 600, 900 and 1200C at all four lines of sight for the three different material samples. The RF power was fixed at 100 W and the gas pressure at 10 Pa in these measurements.

In Figure 5.21, the H_α intensity with a sample of carbon inserted in the plasma at different lines of sight for varying sample temperatures can be seen. The trends in emission show the peak emission intensity at high sample temperatures close to the carbon sample.

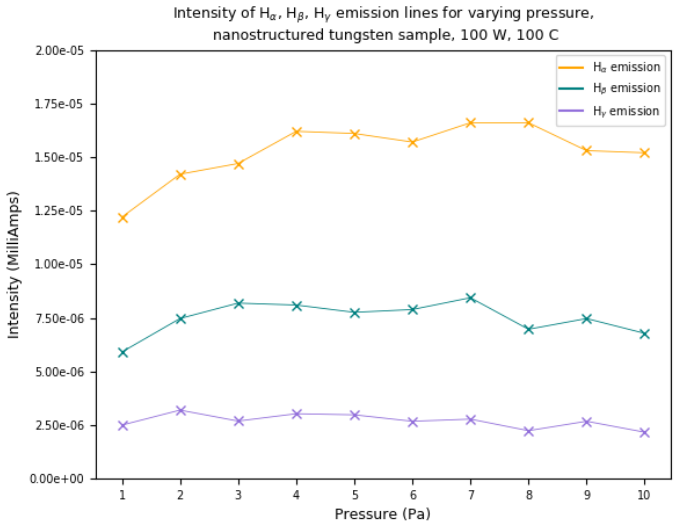

Figure 5.11: H_α, H_β and H_γ line intensities for varying pressure with a nanostructured tungsten sample inserted into the plasma at a constant power of 100 W and sample temperature 100C using LOS1, the line of sight closest to the sample.

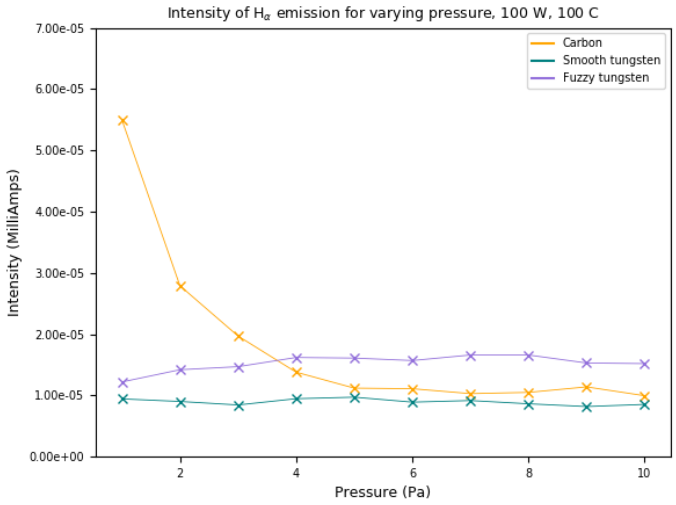

Figure 5.12: H_α line intensity for varying pressure with carbon, tungsten and nanostructured tungsten samples inserted into the plasma at a constant power of 100 W and sample temperature 100C using LOS1, the line of sight closest to the sample.

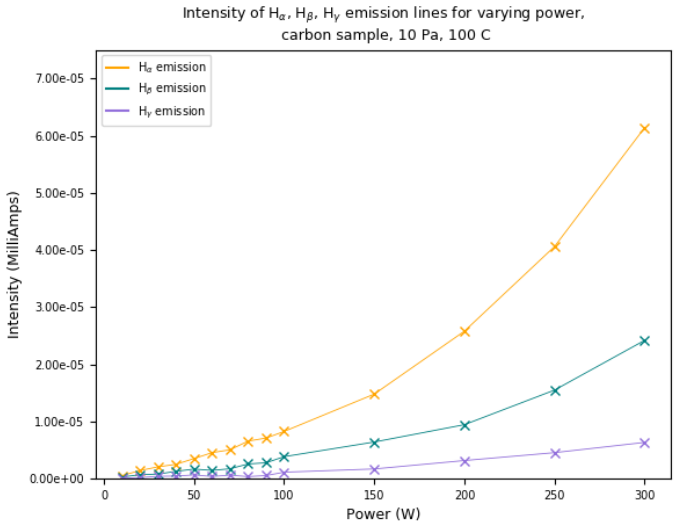

Figure 5.13: H_α, H_β and H_γ line intensities for varying power with a carbon sample inserted into the plasma at a constant pressure of 10 Pa and sample temperature 100C using LOS1, the line of sight closest to the sample.

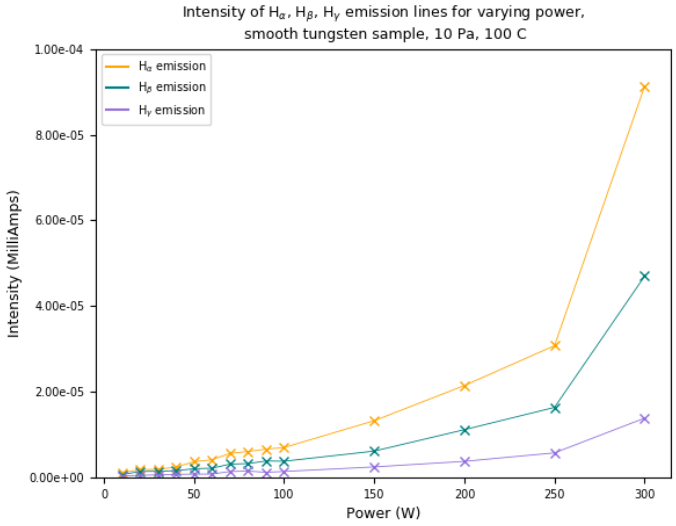

Figure 5.14: H_α, H_β and H_γ line intensities for varying power with a smooth tungsten sample inserted into the plasma at a constant pressure of 10 Pa and sample temperature 100C using LOS1, the line of sight closest to the sample.

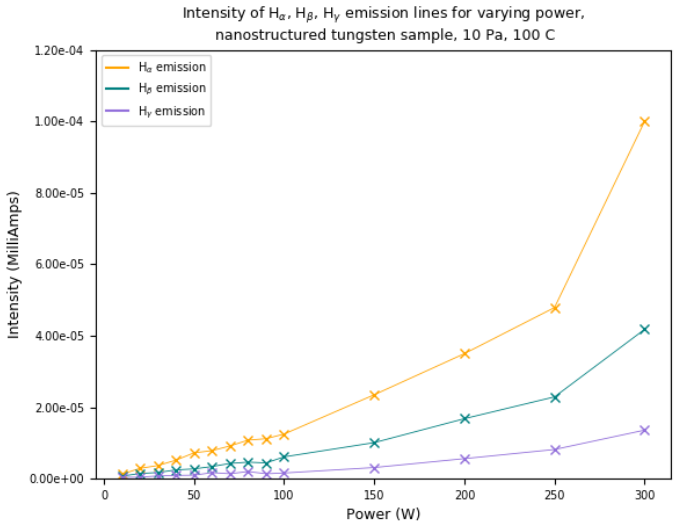

Figure 5.15: H_α, H_β and H_γ line intensities for varying power with a nanostructured tungsten sample inserted into the plasma at a constant pressure of 10 Pa and sample temperature 100C using LOS1, the line of sight closest to the sample.

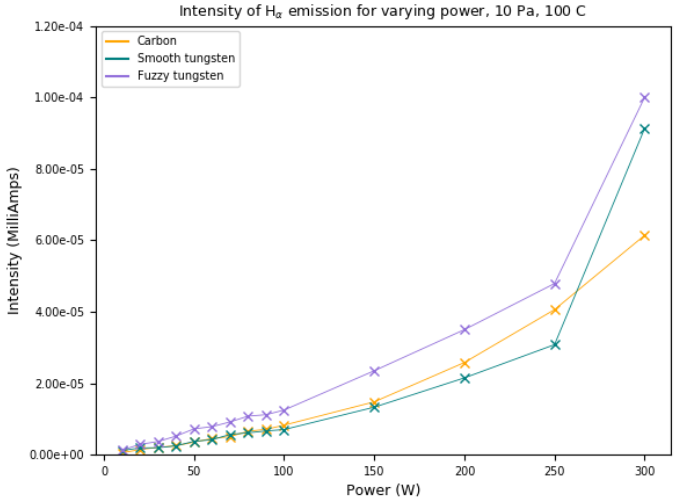

Figure 5.16: H_α line intensity for varying power with carbon, tungsten and nanostructured tungsten samples inserted into the plasma at a constant pressure of 10 Pa and sample temperature 100C using LOS1, the line of sight closest to the sample.

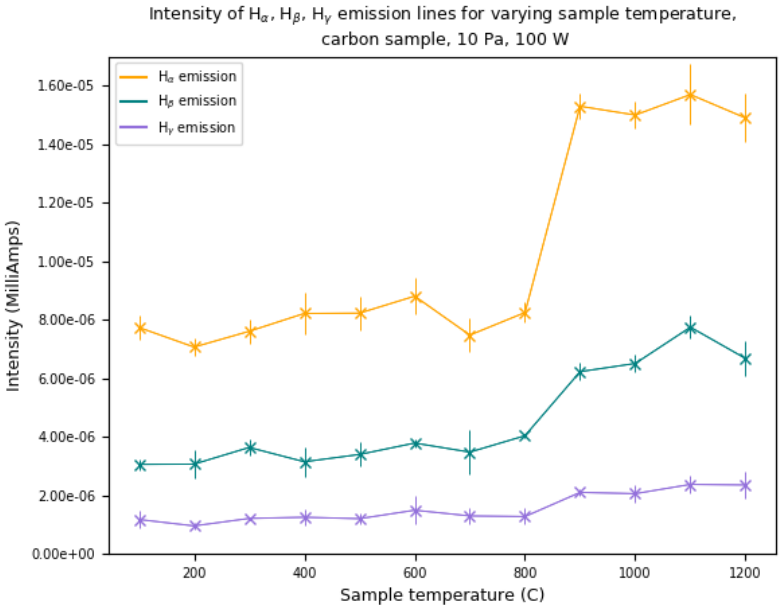

Figure 5.17: H_α, H_β and H_γ line intensities for varying sample temperature with a carbon sample inserted into the plasma at a constant pressure of 10 Pa and RF power of 100W using LOS1, the line of sight closest to the sample.

Figure 5.22 shows the H_α intensity at varying lines of sight close to a sample of smooth tungsten. The value of the line intensity increases for increasing distance from the sample, peaking at 5.175 cm from the sample at 0C. The emission collected using the line of sight closest to the sample, LOS1, shows no significant change in intensity for increasing sample temperature.

In the presence of a nanostructured tungsten sample, the H_α emission, shown in Figure 5.23, increases slightly with decreasing distance to the sample, with the highest emission intensity 3.175 cm from the sample. These trends in emission across the chamber for varying sample temperature will be analysed further with conclusions presented in Section 5.4.4.

Molecular emission measurements were collected in the presence of the three divertor samples using the line of sight closest to the sample, LOS1. Figures 5.24, 5.25 and 5.26 show the full Fulcher band spectrum, from 580-650 nm, with the carbon, tungsten and nanostructured tungsten samples inserted into the plasma respectively.

The trends in the Q1 lines are highlighted using a dashed trend line, and are similar

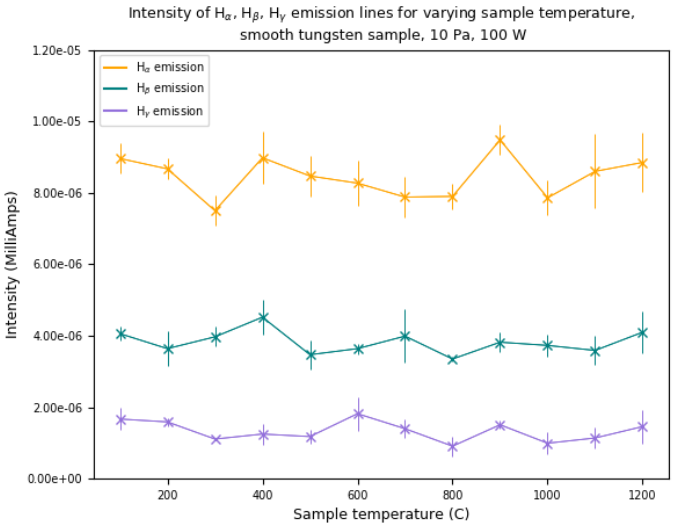

Figure 5.18: H_α, H_β and H_γ line intensities for varying sample temperature with a smooth tungsten sample inserted into the plasma at a constant pressure of 10 Pa and RF power of 100W using LOS1, the line of sight closest to the sample.

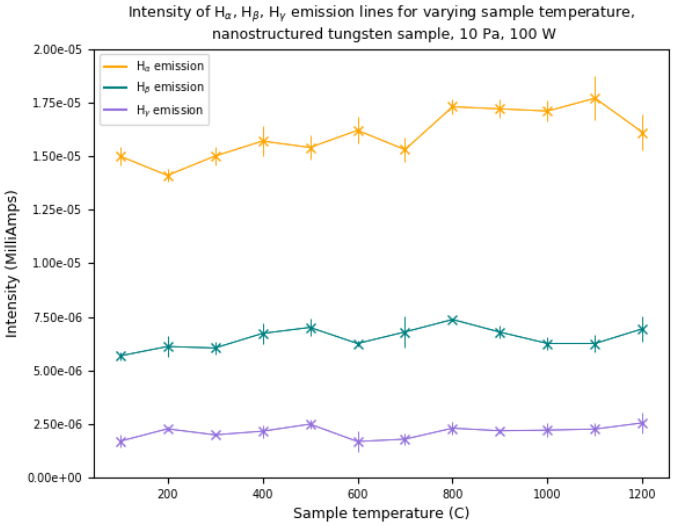

Figure 5.19: H_α, H_β and H_γ line intensities for varying sample temperature with a nanostructured tungsten sample inserted into the plasma at a constant pressure of 10 Pa and RF power of 100W using LOS1, the line of sight closest to the sample.

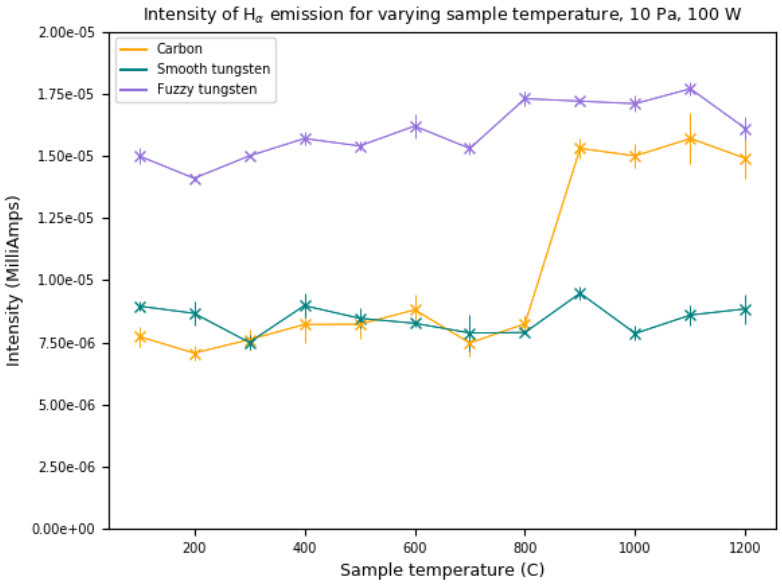

Figure 5.20: H_α line intensity for varying sample temperature with carbon, tungsten and nanostructured tungsten samples inserted into the plasma at a constant pressure of 10 Pa and RF power of 100 W using LOS1, the line of sight closest to the sample.

for both the smooth and nanostructured tungsten samples, with the (1-1) line observed to be the most intense, followed by the (0-0) and the (2-2).

These trends in the Fulcher emission mirror the trend shown without the sample, seen in Figure 4.8. However the molecular lines with the nanostructured tungsten sample are almost three times stronger than the measurements of emission with the smooth tungsten sample.

Figure 5.24 shows the Fulcher band spectrum with a sample of carbon on the sample heater.

The trends in the three Q1 lines are significantly different than for the tungsten samples and are highlighted using a dashed trend line. Unlike Figure 5.25 and 5.26, the spectra measured in the presence of a carbon sample shown in Figure 5.24 indicates the most intense line is the (0-0) line, then decreasing in intensity for the (1-1) and (2-2) lines.

To investigate the effects of the carbon and tungsten samples on the hydrogen emission, Figures 5.27 and 5.28 present the full hydrogen spectrum collected in the presence of the carbon and tungsten samples respectively. The carbon and tungsten emission lines

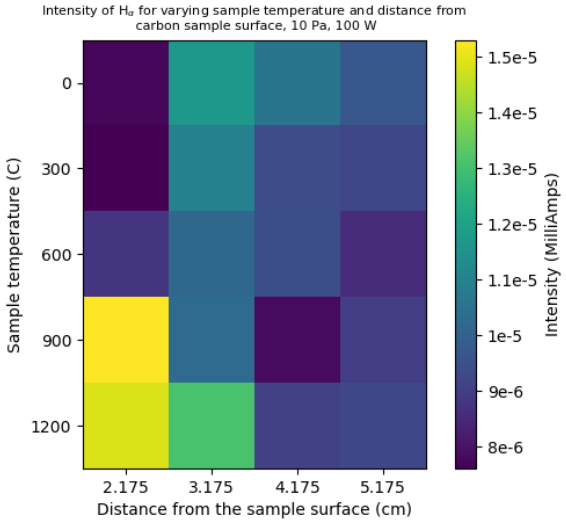

Figure 5.21: Heat map of the H_α intensity for varying line of sight and sample temperature with a carbon sample inserted in the plasma. The gas pressure is fixed at 10 Pa and RF power at 100 W.

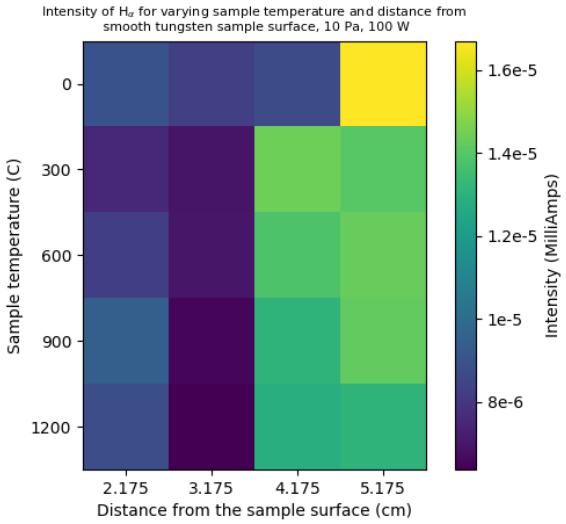

Figure 5.22: Heat map of the H_α intensity for varying line of sight and sample temperature with a smooth sample inserted in the plasma. The gas pressure is fixed at 10 Pa and RF power at 100 W.

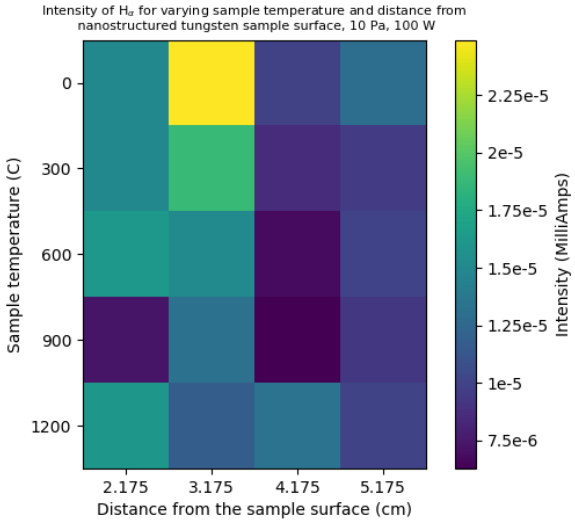

Figure 5.23: Heat map of the H_α intensity for varying line of sight and sample temperature with a nanostructured sample inserted in the plasma. The gas pressure is fixed at 10 Pa and RF power at 100 W.

(taken from the NIST database [119]) are superimposed on the spectrum to highlight any contributions to the spectra from these strong lines of C and W. From these plots it is clear that there is no significant contribution to the emission spectra from carbon and tungsten excitation and any trends in the emission are purely from hydrogen atomic and molecular processes.

5.4.2 Analysis of Balmer line emission for varying discharge and material conditions

The objective of this section is to present further analysis of the Balmer line emission measurements. The trends in the H_γ/H_α lines across the three sets of conditions outlined above and with three different material samples will be presented here. The results in this section aim to highlight the trends in the H_γ/H_α ratio for varying gas pressure, RF power and sample temperature and will the be interpreted further in Section 5.4.4.

The ratio of the H_γ to H_α line intensities for increasing pressure can be seen in Figure 5.29 for a fixed RF power of 100 W and sample temperature of 100C. This ratio is shown to decrease for increasing discharge pressures for all three samples, mirroring trends observed

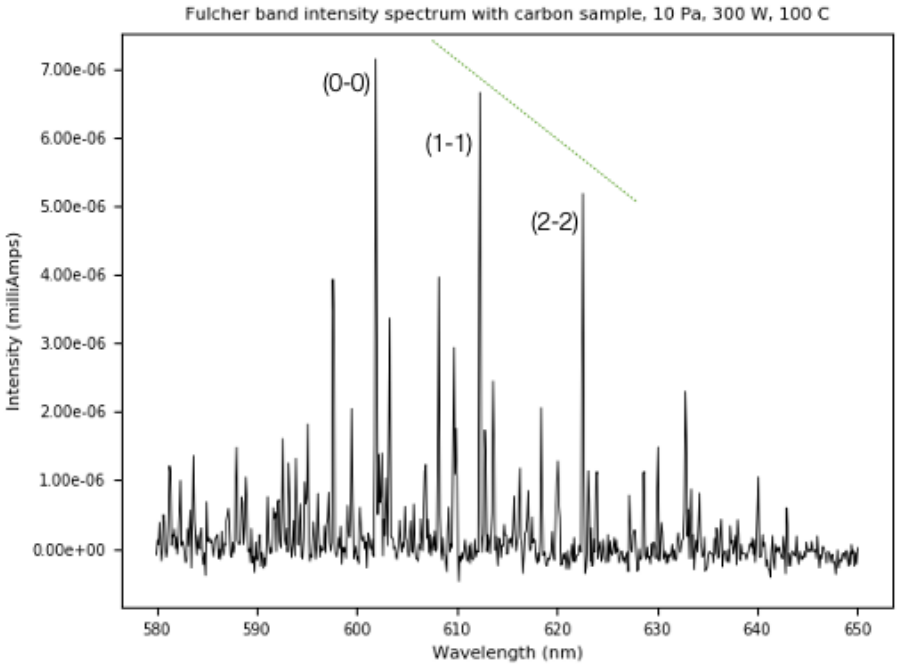

Figure 5.24: Fulcher band spectra in the presence of the carbon sample using LOS1, the line of sight closest to the sample. Collected at a constant pressure of 10 Pa, power of 300 W and sample temperature of 100C.

in Section 4.4.2. There are no significant differences in the ratio for varying sample material.

Figure 5.30 shows a plot of the ratio of H_γ to H_α line intensities for varying RF power with all three divertor-like samples. The RF power was varied from 10-300 W, with a fixed gas pressure of 10 Pa and sample temperature of 100C.

The ratio for all three samples is very similar, with only slightly higher values of the ratio for the smooth tungsten sample. The trends in the ratio for increasing RF power mirror the trends measured without the sample heater in Figure 4.12. The ratio for all three samples decreases steadily until around 50 W at which point the ratios flatten out and remain constant for increasing RF power up to 300 W.

In Figure 5.31, the relationship between the H_γ to H_α ratio and the temperature of the sample can be seen. Measurements with all three samples were collected for sample temperatures in the range 100-1200C. The RF power was fixed at 100 W and the gas pressure at 10 Pa. The ratio remains roughly constant for all three samples at varying

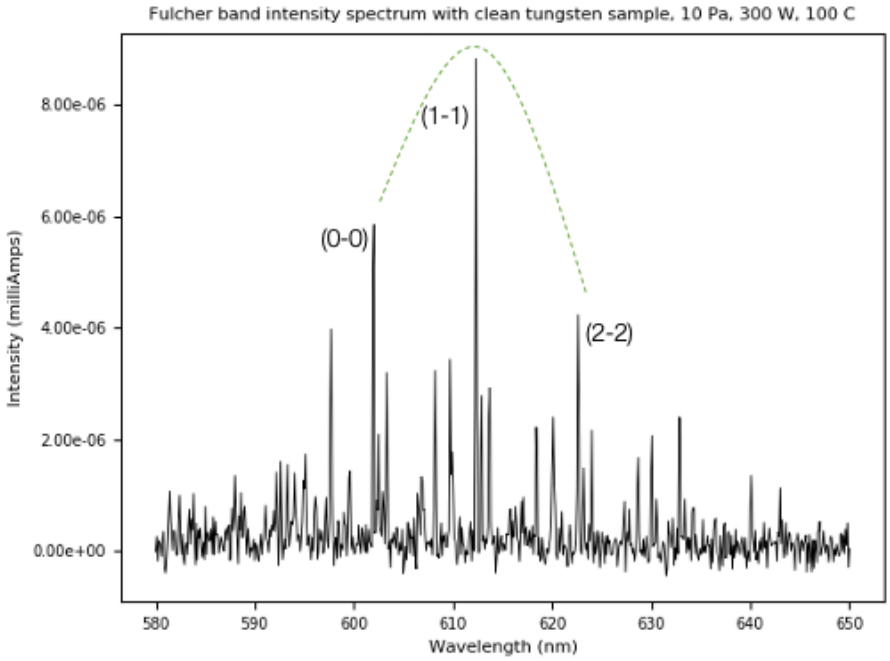

Figure 5.25: Fulcher band spectra in the presence of the smooth tungsten sample using LOS1, the line of sight closest to the sample. Collected at a constant pressure of 10 Pa, power of 300 W and sample temperature of 100C.

sample temperatures, with no significant differences between the differing samples.

5.4.3 Analysis of Fulcher band emission for varying discharge and material conditions

Rotational temperatures were calculated for varying sample material through the use of Boltzmann plots. This technique is described in Section 3.2.3 and utilised in Section 4.4.3. The calculation of rotational temperatures provides a method of quantitative analysis to extract information about the behaviour of molecules in low temperature plasmas. The aim of this section is to outline the trends in the rotational temperature, T_{rot}, at constant pressure, power and sample temperature for the three samples submerged in the plasma.

Figure 5.32 shows the Boltzmann plots and subsequent rotational temperatures measured in the ICP plasma in the presence of carbon, smooth tungsten and nanostructured tungsten samples. The Fulcher band emission measurements which are

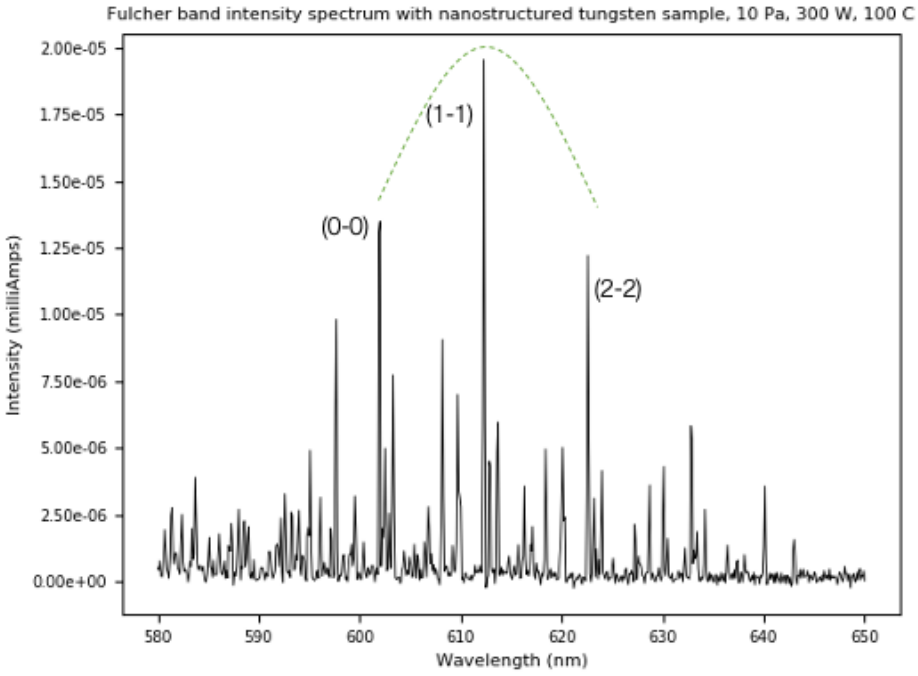

Figure 5.26: Fulcher band spectra in the presence of the nanostructured tungsten sample using LOS1, the line of sight closest to the sample. Collected at a constant pressure of 10 Pa, power of 300 W and sample temperature of 100C.

used to calculate these temperatures were collected at a discharge pressure of 10 Pa, RF power of 300 W and sample temperature of 1000C. These measurements indicate that the rotational temperature is independent of sample material, since the calculated temperatures were found to be around 550 K for all three samples. These temperatures are also similar to the rotational temperature measured for the 300 W ICP plasma without the sample heater shown in Figure 4.14 at 562.91 K.

5.4.4 Interpretation of emission measurements close to the samples

The trends for both the atomic and molecular emission measurements shown in Figures 5.9-5.32 will be discussed in this section in order to quantify the influence of material surfaces on low temperature plasmas.

The trends in the Balmer line intensities for varying pressure with the two tungsten samples mirror trends seen in Figure 4.6. There is a slight increase in intensity of all

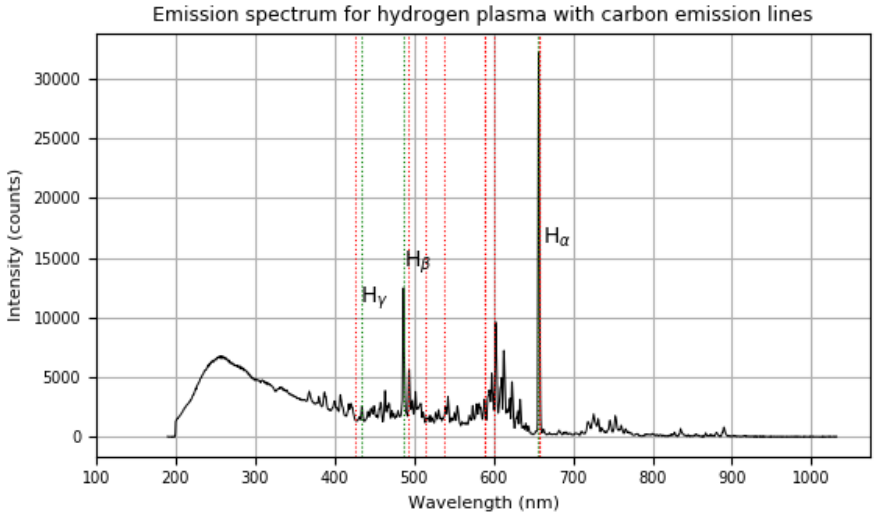

Figure 5.27: Hydrogen spectra in the presence of the carbon sample using LOS1, the line of sight closest to the sample. Collected at a constant pressure of 10 Pa, power of 300 W and sample temperature of 100C. Carbon emission lines are emphasised with the red dashed lines.

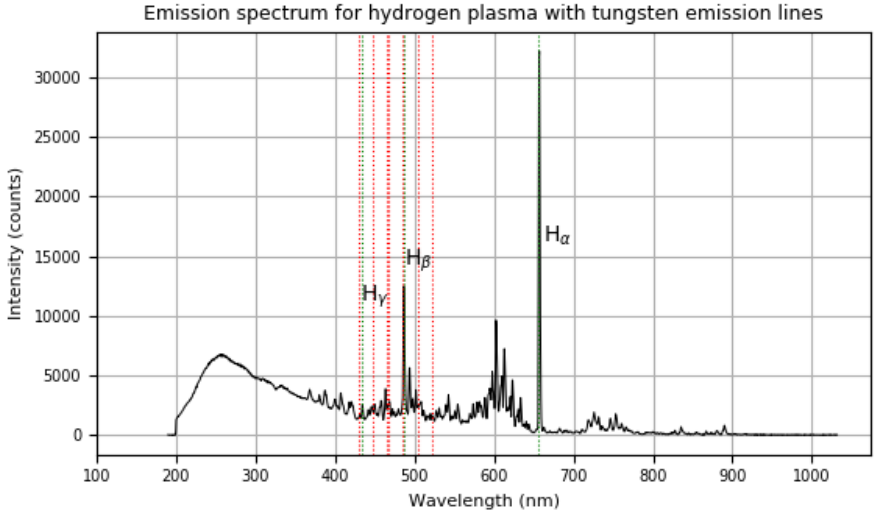

Figure 5.28: Hydrogen spectra in the presence of the smooth tungsten sample using LOS1, the line of sight closest to the sample. Collected at a constant pressure of 10 Pa, power of 300 W and sample temperature of 100C. Tungsten emission lines are emphasised with the red dashed lines.

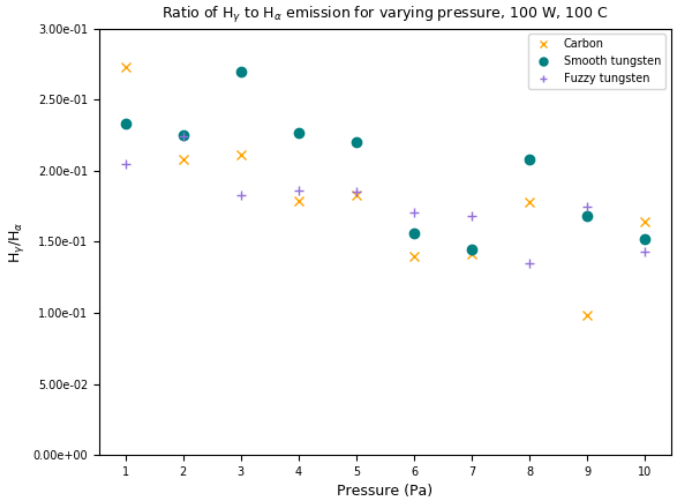

Figure 5.29: The ratio of the H_γ to H_α line intensities with all three samples for varying gas pressure at a constant RF power of 100 W and sample temperature of 100C.

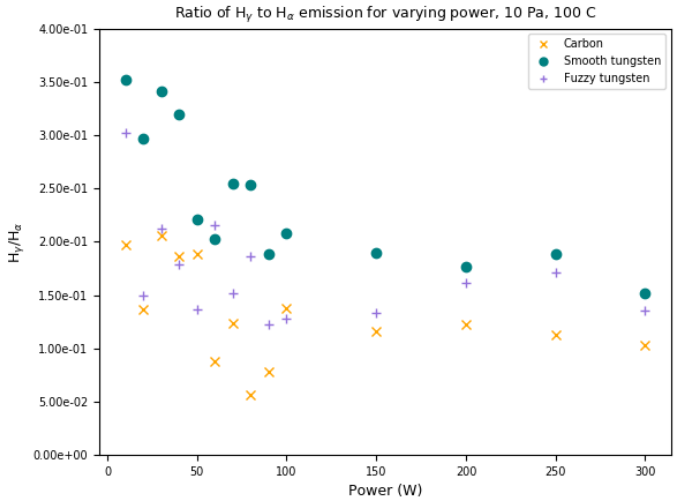

Figure 5.30: The ratio of the H_γ to H_α line intensities with all three samples for varying RF power at a constant pressure of 10 Pa and sample temperature of 100C.

three Balmer lines for varying pressure with a peak at around 4-5 Pa, attributed to the higher collision frequencies at increasing pressure, along with a significant number of high

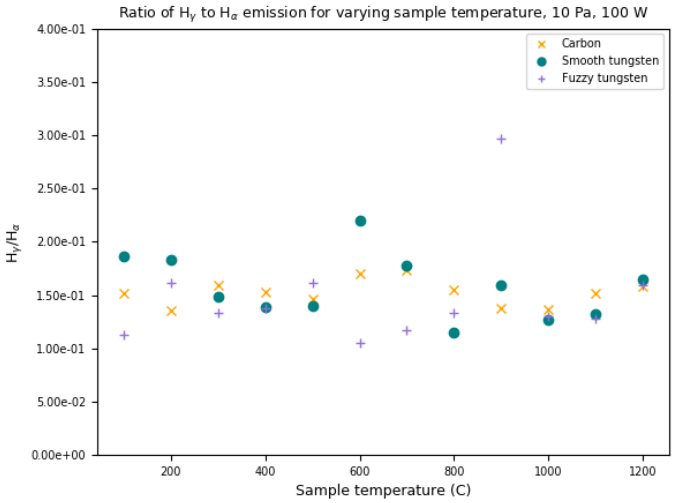

Figure 5.31: The ratio of the H_γ to H_α line intensities with all three samples for varying sample temperature at a constant pressure of 10 Pa and RF power of 100 W.

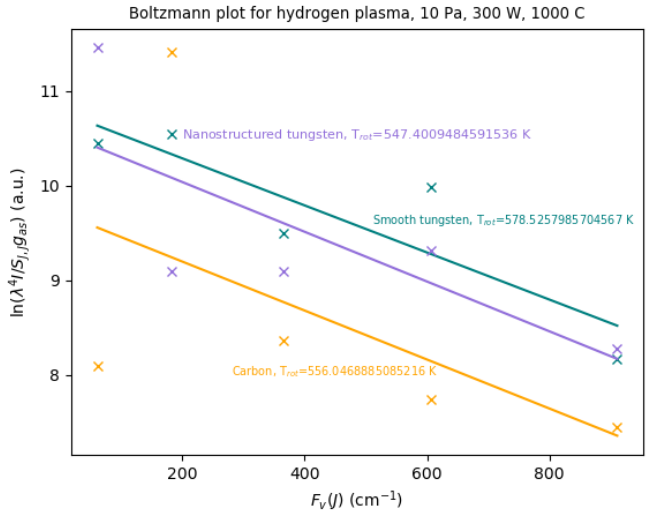

Figure 5.32: Boltzmann plot and rotational temperatures at constant pressure of 10 Pa, power of 300 W and sample temperature 1000C in the presence of a carbon, smooth tungsten and nanostructured tungsten sample. Boltzmann plot calculated using the Q-branch (1-1) band.

energy electrons at this pressure range. These two factors result in increased excitation of hydrogen atoms, leading to higher rates of Balmer line emission. The tungsten samples do not influence these trends in emission significantly, however the carbon sample has a notable effect on the emission intensities of all three Balmer lines. At low temperatures the Balmer emission is shown to be high in the presence of the carbon sample, then decreasing for increasing pressure. This reflects the relationship between electron temperature and pressure shown in Figure 5.2. At around 5 Pa, the emission intensity is shown to decrease and remain constant with increasing pressure, which mirrors the constant electron temperature measured over this pressure range.

The power dependence of the Balmer intensities is independent of the inserted sample. The trends seen in Section 5.4.1 are also seen in Section 4.4.1 for increasing RF power. The increased density of electrons at higher powers leads to increased rates of excitation of hydrogen atoms, resulting in higher emission intensities.

For varying sample temperature, carbon is shown to have the most significant effect on the Balmer emission. The measured Balmer line intensities double after 800C with the carbon sample, however are almost constant for increasing sample temperature with both of the tungsten samples. This trend is mirrored in electron property measurements near the surface, where the electron temperature is roughly constant at around 6 eV until a spike at 1100C to around 12 eV in the presence of the carbon sample shown in Figure 5.6. As there is an increased number of high energy electrons at higher sample temperatures, this results in an increased rate of excitation leading to higher atomic emission intensities. Intensity is higher in the presence of the fuzzy tungsten compared to the smooth tungsten sample. Further research to investigate the processes influencing this trend is required. The heat map for the smooth tungsten measurement implies the presence of the smooth tungsten sample suppresses atomic emission. This correlates to the lower electron temperatures observed close to the the smooth tungsten sample, as seen in Figure 5.6, and therefore less excitation of the atomic hydrogen. The Fulcher band emission for the Q1 (0-0), (1-1) and (2-2) lines are strongly dependent on the sample material, for constant pressure, RF power and sample temperature. The two tungsten samples yield similar trends in the line intensities as those seen in Chapter 4 without the sample heater, indicating the tungsten material has little effect on the molecular states. However the carbon sample results in an increase intensity of the Q1 (0-0) line. One possible explanation for this result is the formation of hydrocarbons which then penetrate into the plasma and dissociate to vibrationally excited hydrogen molecules. In addition, the interaction of hydrocarbons

with hydrogen molecules may occur, influencing the Fulcher band emission.

Further analysis presented in Section 5.4.2 and 5.4.3 provides information about the behaviour of atoms and molecules in the presence of the samples. For increasing discharge pressure, the ratio of the H_γ/H_α emission lines decreases as in Section 4.4.2 and this trend is similar for all three samples. This indicates higher rates of electron-ion recombination at lower pressures, independent of the sample material.

The H_γ/H_α ratio decays for all three samples over the range of RF powers. At low powers the ratio is high, however above 50 W the line ratio is roughly constant, a trend which can also be seen in Figure 4.12. This is relatively independent of sample material, however calculations of the ratio with the smooth tungsten sample are the highest of the three samples. This may be due to the lower electron temperatures and reduced emission close to the smooth tungsten sample, discussed in Section 5.3.1 and 5.4. Further research into the physical processes behind these trends is required.

There is no significant difference in the H_γ/H_α ratio for all three samples with varying sample temperature. These ratios are shown to stay relatively constant for increasing sample temperature indicating there is no change in the rate of excitation to higher-n states in the plasma close to the samples at higher sample temperatures.

5.5 Summary

The measurements presented in this chapter aim to detail the trends in atomic and molecular emission close to different material samples for varying discharge and surface conditions. This is important as key divertor processes are not currently fully understood and predictive modelling codes lack information about plasma-surface interactions.

Electron property measurements for increasing gas pressure and RF power mirror trends discussed in the previous chapter and indicate the electron parameters are not significantly affected by varying sample material.

For increasing sample temperature, measurements using the edge probe, close to the samples, show a sudden increase in electron temperature with the carbon sample above 1000C. This is concluded to be linked to the increase in the temperature of the sample from the sample heater above the temperature that the sample is heated to by the plasma. Electron temperatures are also seen to be higher in the presence of the nanostructured tungsten sample compared with the smooth tungsten sample.

Measurements of atomic and molecular emission show similar trends for the three

different samples for varying pressure and power. For increasing RF power, all three Balmer lines increase in the presence of all three samples. These trends agree with measurements presented in Chapter 4 without the sample heater.

For varying pressure there is seen to be no real change in the presence of the tungsten samples and the emission measurements follow similar trends as seen without the sample heater in the previous chapter. It is concluded that the presence of metallic surfaces inserted into the plasma has little effect on the plasma emission. However at low pressures, the Balmer line intensities are significantly higher with the carbon sample, before decreasing steadily and flattening out above 5 Pa. At lower pressures, although the density of electrons is reduced, the electrons have significantly more energy. With larger sheaths and higher energy electrons, there will be an increased rate of bombardment of the carbon sample. These interactions may effect how atoms and molecules are recycled from the carbon surface. Since carbon is more reactive than tungsten, and the interaction of hydrogen and carbon molecules is complex, better modelling of these interactions would allow for these trends to be studied further.

For varying sample temperature, an increase in Balmer intensity can be seen with the carbon sample above 800C. This result mirrors trends in the electron temperatures measured with the carbon sample for increasing sample temperature. The higher electron temperatures result in higher rates of excitation, however the relationship between sample material and electron temperature should be studied further to explain these trends. The emission is also shown to be higher with the nanostructured tungsten sample compared to the smooth tungsten sample, which is also attributed to the higher electron temperatures in the presence of the fuzzy tungsten sample. From emission measurements collected at varying lines of sight in the presence of a smooth tungsten sample, the emission intensity is shown to peak furthest from the sample surface.

Fulcher band emission measurements were presented in order to quantify the effects of the sample material on the vibrational bands. These investigations clearly show that the vibrational population of hydrogen molecules is affected by different material surfaces. This may be due to the recycling of hydrogen atoms on the carbon surface which leads to hydrogen molecules in excited vibrational ground states however the atomic and molecular processes influencing these populations are not currently understood. Due to this, detailed investigations on the dependence of vibrational populations on substrate material and temperature should be completed in order to provide further information about the most important processes.

From the trends in the measurements presented in this chapter, it is clear that the plasma is affected by the carbon sample more significantly than by the two tungsten samples. The nanostructured surface of the fuzzy tungsten influences the plasma emission under certain conditions, but has no notable effect on the broader plasma properties. The smooth tungsten sample does not seem to have a strong impact on both the plasma parameters or emission, even at substantially enhanced surface temperatures.

The results presented in this chapter open up avenues for further investigation to fully understand the trends in atomic and molecular processes. The use of fusion codes with synthetic diagnostics would be very useful to further understand how the Fulcher band changes for varying sample material.

Chapter 6

Emission Measurements in the MAST-U Divertor

6.1 Introduction

The aim of the research described in this chapter is to identify the degree to which optical emission data from the MAST-U tokamak divertor could be used to provide information about plasma properties and detachment. One of the main aims of the first MAST-U experimental campaign was to investigate the effects of alternative divertor configurations on power exhaust. This involved the use of measurements of atomic and molecular emission to gain an understanding of the processes that impact the onset and control of divertor detachment. The diagnostic measurements collected through this campaign demonstrated a tenfold reduction in the flux of power to the carbon divertor plates [39].

The data in this chapter was collected as part of the 2021 MAST-U experimental campaign through a collaborative research project with the MAST-U diagnostics team. This research focused on analysing emission measurements, of the same type that was measured from the ICP in previous chapters, in order to understand how emission data can be used to control and optimise divertor detachment.

The objectives of the spectroscopy diagnostic measurements presented in this chapter are twofold. The first aim was to investigate the processes behind the evolution of detachment, from the onset of detachment close to divertor surfaces, to the expansion of the detached region towards the X-point through the divertor. The second aim was to observe how the magnetic configuration within the divertor impacts the evolution of

the detachment front, and the advantages of utilising advanced divertor configurations to improve the power handling in fusion machines.

Through this work, the emission profiles for varying divertor conditions and configurations were analysed in order to highlight key atomic and molecular processes throughout the evolution of the shots. In the Super-X divertor, it was observed that the molecular Fulcher band retreats to the entrance of the divertor, indicating a much colder region close to the divertor plates with high rates of recombination. This was verified through calculations of the rotational temperature, which is much lower in the Super-X divertor than in the conventional divertor configuration. Conversely, in the conventional divertor, the measured rotational temperatures are much higher and the plasma does not extend fully into the divertor leg. This work provides a basis on which future diagnostic studies in divertors can build upon in order to quantify the extent to which material surfaces influence the behaviour of atoms and molecules in low temperature fusion plasmas.

The structure of this chapter is as follows. In Section 6.2, the experimental set up and range of measurements utilised to collect the emission data will be detailed along with a description of the plasma conditions for each of the shot numbers studied in this chapter. Following this, both qualitative trends in the deuterium atomic and molecular emission, and carbon-deuterium bands along with quantitative analysis of the molecular Fulcher bands to extract rotational temperatures will be discussed in Section 6.3. Conclusions on the analysis of these measurements will then inform trends in the emission for varying plasma conditions and divertor configurations, allowing for an investigation into the behaviour of atoms and molecules in the MAST-U divertor.

6.2 Range of measurements and experimental set up

In this section, the experimental set up will be outlined along with a description of the different plasma configurations that were studied in the shots analysed for this chapter. Data from nine different MAST-U shots was examined, with each shot corresponding to different plasma conditions and configurations. Six shots were utilised for the quantitative study of trends in emission profiles discussed in Section 6.3.1, and three shots with high resolution Fulcher band data were utilised to calculate the rotational temperatures and study the trends in T_{rot} for varying divertor configuration, presented in Section 6.3.2. Table 6.1 outlines the divertor configuration and conditions of each shot used in this chapter.

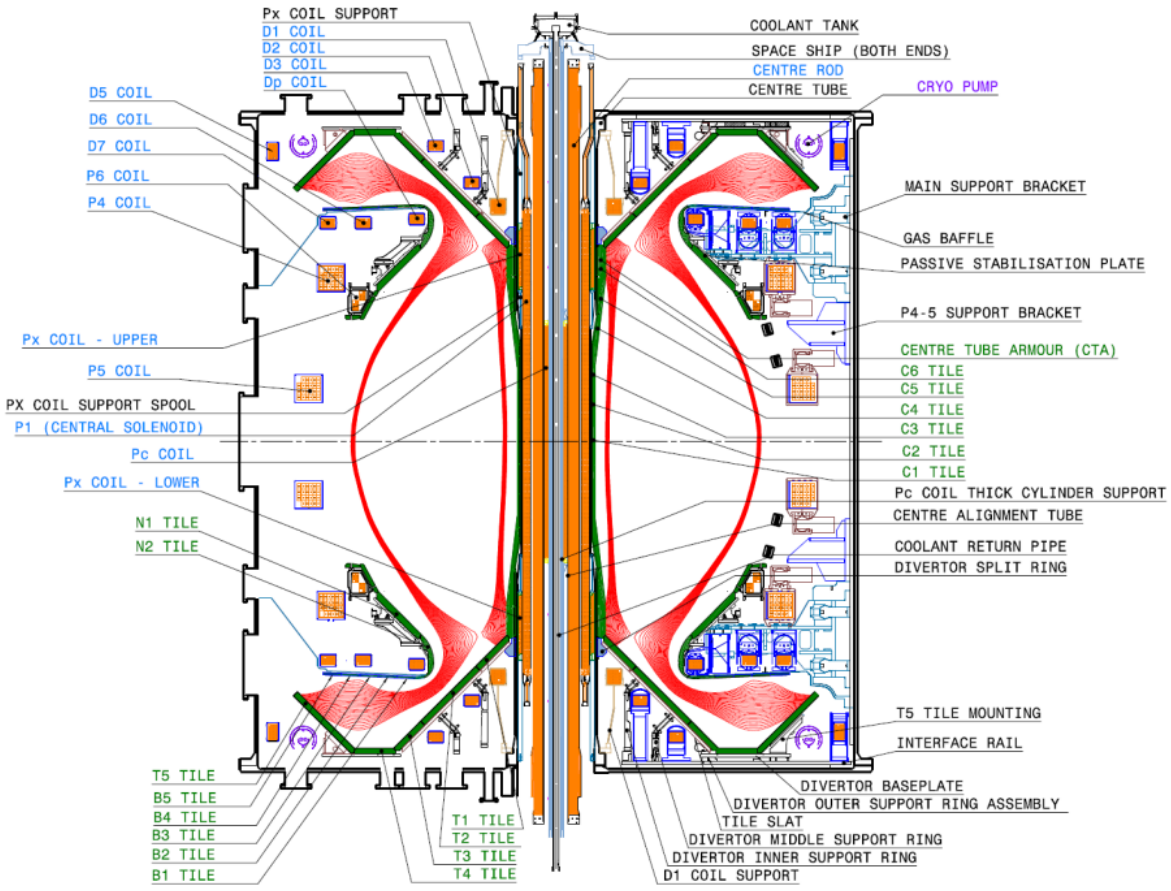

Figure 6.1: A detailed schematic of the MAST-U tokamak with annotations highlighting the divertor tiles, poloidal coils and structure of the machine. Copied from [155]

A detailed schematic of the MAST-U tokamak can be seen in Figure 6.1 which details the vessel structure, poloidal field coil configuration and divertor tile arrangement.

A wide range of diagnostic techniques are implemented in order to characterise both the core and divertor regions of the MAST-U machine. The main plasma properties measured in MAST-U include electron temperatures and densities, optical, X-ray and VUV emission, neutron fluxes, heat fluxes, radiated power and neutral pressure, among others. The focus of this chapter will be on optical emission measurements collected in the MAST-U divertor.

To measure the emission through the entire divertor region, the MAST-U spectroscopy system is comprised of four spectrometers. The two spectrometers utilised for the

Table 6.1: Description of the MAST-U shot numbers utilised in this research.

Shot number	Divertor configuration	Conditions
45243	Super-X	Development Super-X discharge
45247	Conventional	Density ramp discharge
45371	Super-X	Low levels of divertor fuelling
45372	Super-X	Repeat of 45371
45376	Super-X	Repeat of 45371
45377	Super-X	Repeat of 45371
45068 - high res FB	Conventional	Development conventional discharge
45244 - high res FB	Super-X	Repeat of 45243
45248 - high res FB	Conventional	Disruption with PFC occurs

measurements in this chapter are the (i) Divertor Monitoring Spectrometer - York (DMS-York), and the (ii) Divertor Monitoring Spectrometer - CCFE (DMS-CCFE) systems. The SPEX-B spectroscopy system is a single line of sight through the midplane with the aim of monitoring oxygen impurities, while the DIBS spectrometer monitors the upper divertor with 26 lines of sight. These two spectrometers will not be utilised in this chapter.

The DMS system is comprised of forty lines of sight through the divertor region. Twenty of which are used by the DMS-York spectrometer and twenty by the DMS-CCFE spectrometer. The combined forty lines of sight set up through the MAST-U divertor can be seen in Figure 6.2. The two DMS systems utilise alternating lines of sight to scan across the divertor from the entrance of the divertor to the divertor tiles, with the first fibre corresponding to the line of sight closest to the target and the last line of sight looking through the divertor entrance. The labels V1 and V2 seen in Figure 6.2 indicate the forty fibres used by the DMS spectrometers. These lines are then utilised by the DMS-CCFE and -York spectrometers to study trends in the emission across the divertor region. Emission measurements are collected at a frequency of 75 Hz which can then be smear corrected and resampled in the post processing of the data.

These spectrometers are configured to measure the molecular Fulcher band, the D_α, D_γ and D_δ lines, and the carbon-deuterium CD band. From measurements of the CD band spectra, carbon flux profiles across the divertor can be derived.

The DMS-York spectrometer is set up to observe the $n = 5$ and $n = 6$ Balmer lines, alongside the CD band (around 431 nm). It utilises a 1200 l/mm grating centred at 422

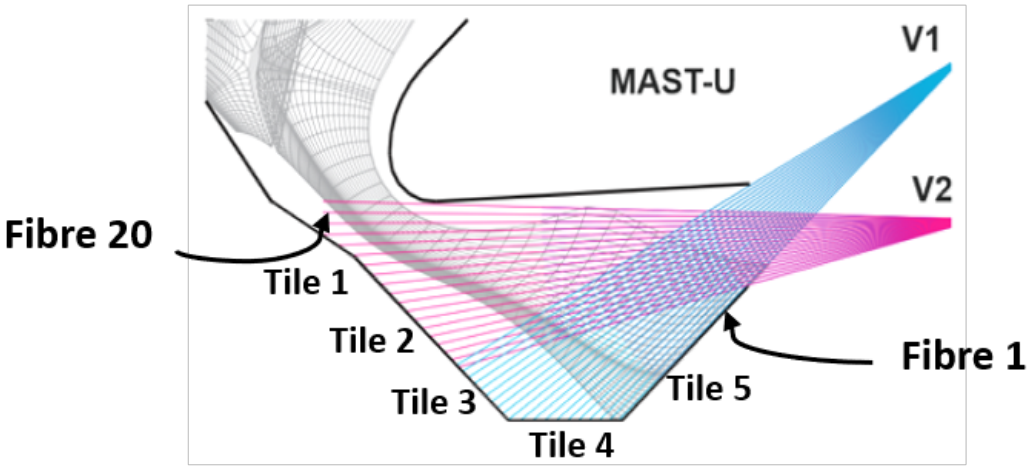

Figure 6.2: A schematic of the line of sight configuration through the MAST-U divertor region connected to the DMS system. Fibre 1 is close to the divertor surface at tile 5, and fibre 20 approaches the entrance of the divertor. Fibre 13 intersects tiles 2 and 3. Taken from the MAST Users page.

nm. The DMS-CCFE system uses a shortpass filter at 625 nm to facilitate the observation of the D_α emission line and a section of the Fulcher band simultaneously and utilises a 300 l/m grating centred at 635 nm.

The DMS-CCFE system collects data for the Fulcher band in the wavelength range from 596-614 nm. The majority of shots in this experiment collected low resolution Fulcher data for which the band structure cannot be analysed but the brightness of the molecular band can be tracked across the divertor. However for three shot numbers, indicated in Table 6.1, high resolution Fulcher emission data was collected using the DMS-York spectrometer which will be presented in Section 6.3.2.

For the low resolution Fulcher band, D_α line, n=6/5 ratio and carbon-deuterium CD band data, the intensity of the emission was plotted for varying fibre through the divertor region and time throughout the shot. The results of these measurements are presented in Section 6.3.1, with further analysis of the high resolution Fulcher data given in Section 6.3.2.

Emission measurements were collected in both the conventional divertor configuration, where the exhaust is directed to tiles 2 and 3, closer to the X-point, and the Super-X divertor configuration, where the exhaust is directed much further into the divertor towards

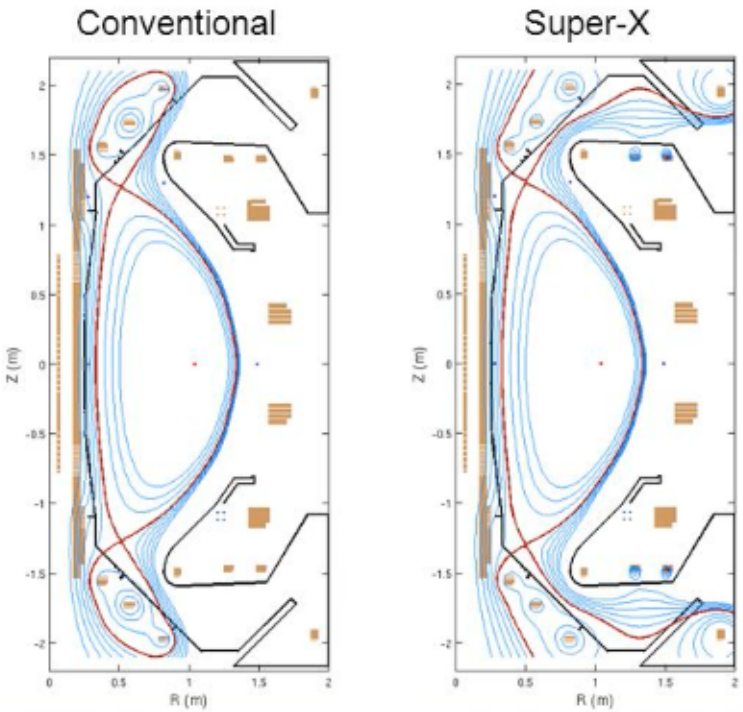

Figure 6.3: A comparison of the conventional and Super-X divertor configurations utilised in the MAST-U tokamak divertor. The magnetic field lines can be seen to extend further into the leg of the Super-X divertor when compared with the conventional configuration. Taken from the MAST Users page.

tile 5. These configurations are shown in Figure 6.3. The effects of varying divertor configurations and plasma conditions will be highlighted in Section 6.3.3.

6.3 Atomic and molecular emission in the MAST-U divertor

This section contains atomic and molecular emission measurements collected for varying conditions in the MAST-U divertor. The results were obtained using the DMS-CCFE and DMS-York spectrometers described in Section 6.2 made across the entire divertor in the arrangement shown in Figure 6.2. Section 6.3.1 contains the results of the four emission profiles for varying line of sight and time. Section 6.3.2 presents further analysis of the high resolution Fulcher band data to extract rotational temperatures utilising Boltzmann plots and Section 4.3.2 contains an interpretation of these measurements for varying divertor

configuration and conditions. The units of intensity in these figures is photon/m^2/s.

6.3.1 Emission measurements for varying divertor conditions and configurations

This section aims to present the trends in emission intensity for the six different shots corresponding to different plasma conditions and divertor configurations, as seen in Table 6.1. The trends in the D_α emission, Fulcher band emission, CD band emission and ratio of the n=6/5 intensity will be detailed.

Figure 6.4 shows a heat map plot from emission data for a single shot. 6.4(a) shows the D_α emission for each fibre as a function of time, 6.4(b) shows the Fulcher band emission evolution throughout the shot, 6.4(c) shows the CD band emission throughout the divertor and 6.4(d) shows the ratio of the n=6 to n=5 lines. The data is shown plotted with fibre number on the horizontal axis, where fibre 20 collects data at the divertor entrance and fibre 1 collects data along a chord inside the divertor, furthest from the entrance.

The data in Figure 6.4 is from shot number 45243, in the Super-X divertor configuration. The D_α emission approaches the tile located at the most interior part of the extended divertor, labelled tile 5 in Figure 6.2, at around 400 ms and then pulls off the target at 750 ms before returning back to the target around 800 ms. The Fulcher emission approaches tile 5 after 400 ms before moving towards the entrance of the divertor at around 620 ms. The CD band emission follows the trends of the Fulcher band profile, with strong emission near the target from 400 to 600 ms before moving towards the divertor entrance.

The ratio of the n=6/5 lines is high at the beginning of the shot, but decreases steadily from 200 ms throughout the evolution of the shot. The ratio is then high close to tile 5 at around 780 ms before decreasing after 800 ms.

In Figure 6.5, the emission intensities measured in shot number 45247 are presented. Shot 45247 is a density ramp discharge utilising the conventional divertor configuration. Figure 6.5(a) corresponds to the D_α line emission and shows strong atomic emission on tiles 2 and 3 at around 800 ms. The Fulcher band emission shown in Figure 6.5(b) indicates strong molecular emission at the target, located around the midpoint of the divertor leg, from 400 ms, before pulling away from the target and approaching the entrance of the divertor at around 580 ms. Figure 6.5(c) shows the carbon-deuterium CD band emission throughout the divertor region.

The CD band tracks the Fulcher emission, with strong emission close to the divertor

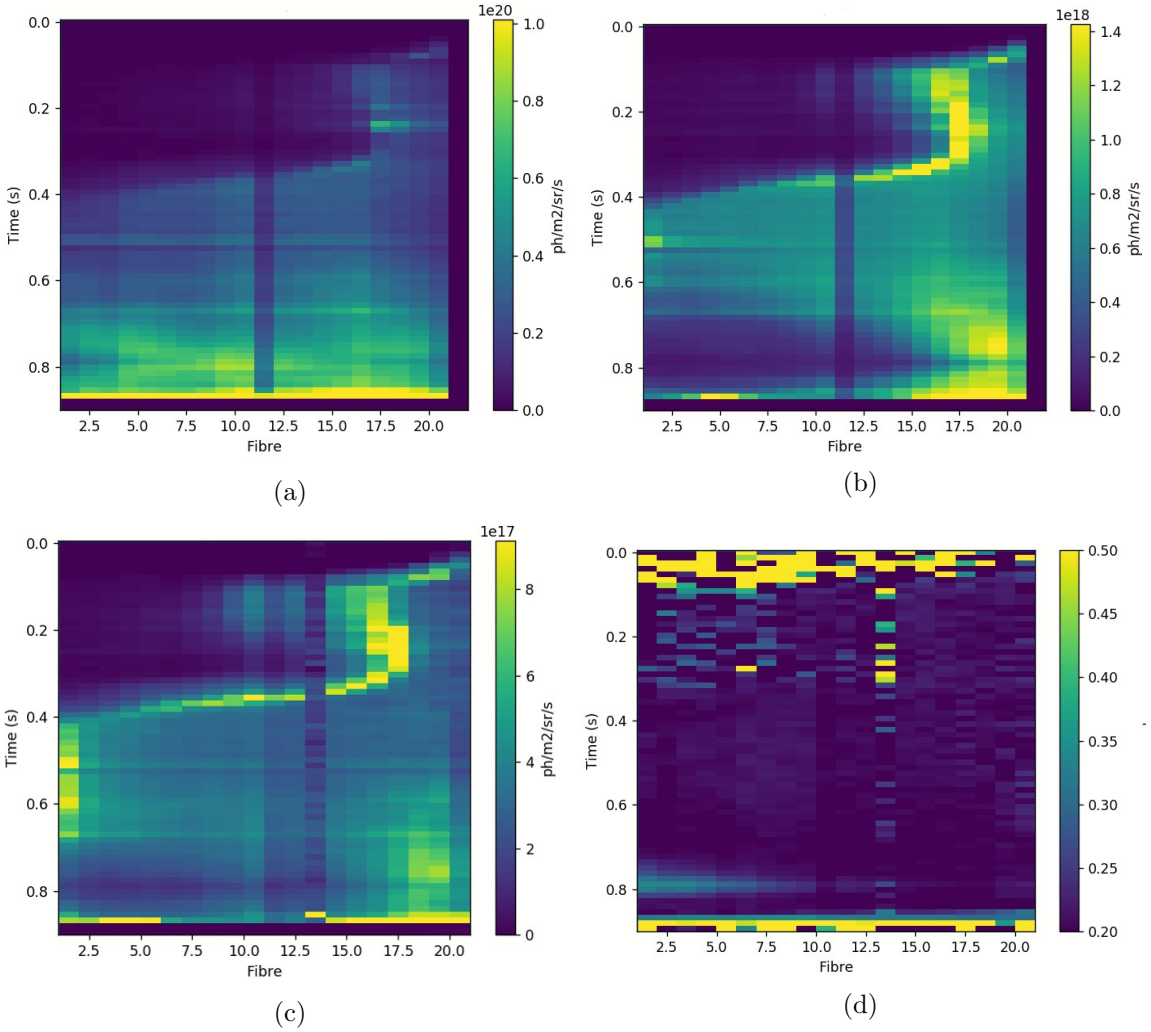

Figure 6.4: Emission data for each fibre as a function of time for shot number 45243. (a) shows the D_α emission profile, (b) shows the Fulcher band profile, (c) corresponds to the CD band emission and (d) to the n=6/5 Balmer line ratio.

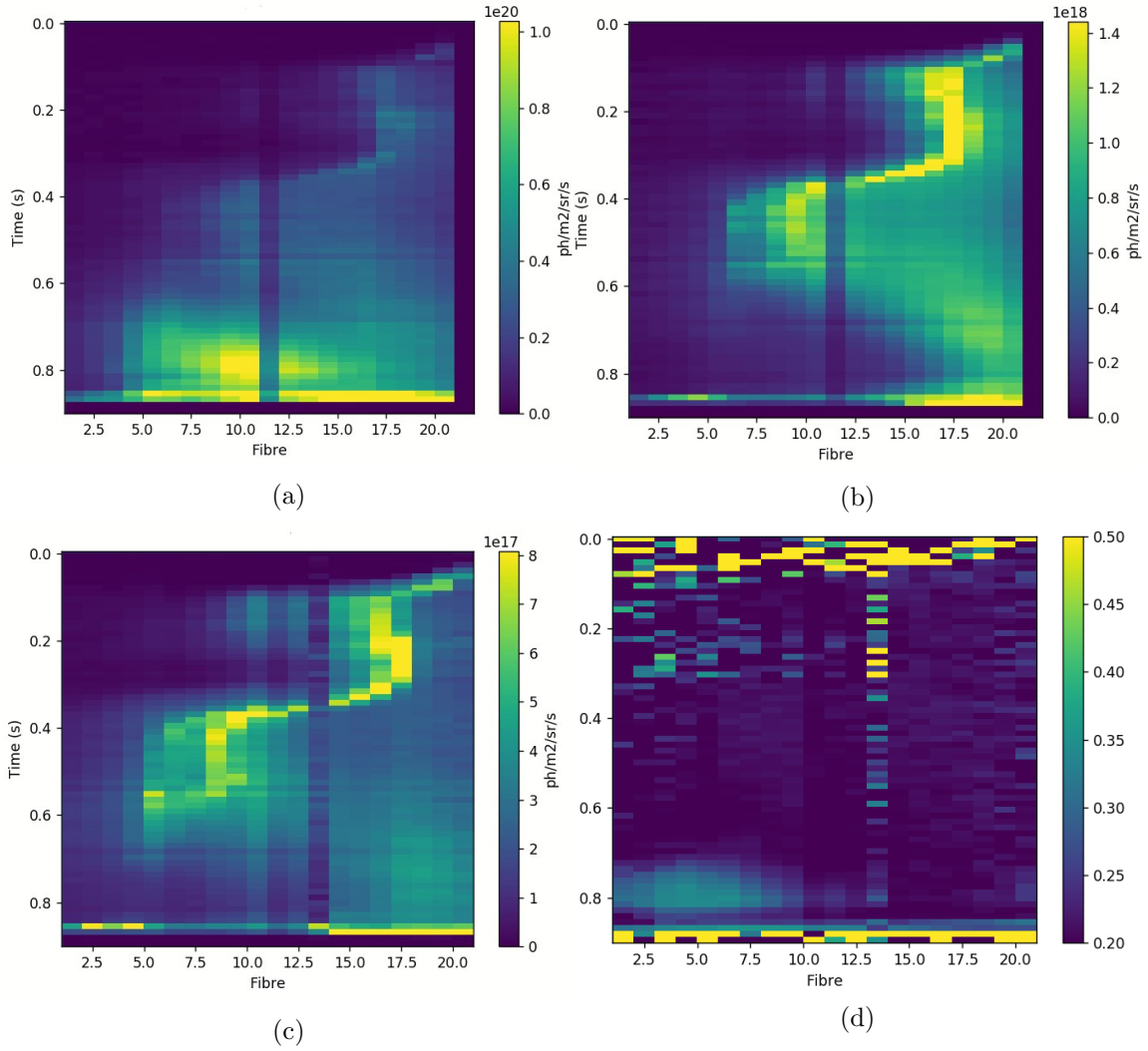

Figure 6.5: Emission data for each fibre as a function of time for shot number 45247. (a) shows the D_α emission profile, (b) shows the Fulcher band profile, (c) corresponds to the CD band emission and (d) to the n=6/5 Balmer line ratio.

target between 400 ms and 600 ms. This band then moves towards the divertor entrance after 600 ms. The ratio of the n=6 to n=5 emission lines, shown in Figure 6.5(d), is large around tiles 2 and 3, in the middle of the divertor, from the beginning of the shot until 600 ms, but decreases significantly from 600 ms onwards. This ratio is then strong further in the divertor from 650 ms to around 800 ms.

The emission intensities measured in shot number 45371 can be seen in Figure 6.6. Shot 45371 is a Super-X divertor configuration discharge with lower divertor fueling. The D_α emission line profile shown in Figure 6.6(a) indicates a movement of the D_α line towards the surface of tile 5, furthest into the divertor leg, at around 500 ms. The D_α emission then pulls away from the divertor target at 600 ms and approaches the entrance of the divertor at 700 ms.

Figure 6.6(b) shows the Fulcher band emission evolution throughout this shot. The Fulcher band emission moves towards the target after 400 ms, before then moving back completely towards the divertor entrance close to 600 ms. The CD band emission in Figure 6.6(c) shows similar trends as for the Fulcher band in Figure 6.6(b), approaching the divertor tile furthest into the divertor leg around 400 ms, before pulling back from the target around 600 ms and approaching the entrance to the divertor. This strong reduction in Fulcher and CD band emission close to the divertor tile and movement towards the X-point is a clear indication of divertor detachment. The ratio of the n=6 to n=5 lines can be seen in Figure 6.6(d). This ratio is large throughout the divertor region from 600 ms onwards. These trends will be discussed further in Section 6.3.3.

Figure 6.7 shows a heat map of the emission profiles collected in shot 45372. Shot 45372 is a repeat of shot 45371 without lower divertor fuelling. The D_α emission shown in Figure 6.7(a) moves towards the furthest tile in the divertor leg, tile 5, at 400 ms and then remains strong throughout the rest of the shot. Figure 6.7(b) shows the Fulcher band emission throughout the shot. The Fulcher band approaches tile 5 at 420 ms, before retreating slightly towards the divertor entrance around 800 ms. This reduction in the Fulcher band is much less than with the divertor fuelling shown in Figure 6.6, showing that divertor fuelling has a significant impact on the evolution and degree of detachment in the divertor. The carbon-deuterium CD band emission in Figure 6.7(c), like the Fulcher band, approaches tile 5, furthest in the divertor leg, at around 400 ms, but stays peaked close to the target throughout the rest of the shot only reducing slightly around 750 ms. The n=6 to n=5 ratio seen in Figure 6.7(d) is very low throughout the shot with only a slight increase in this ratio throughout the divertor region after 800 ms.

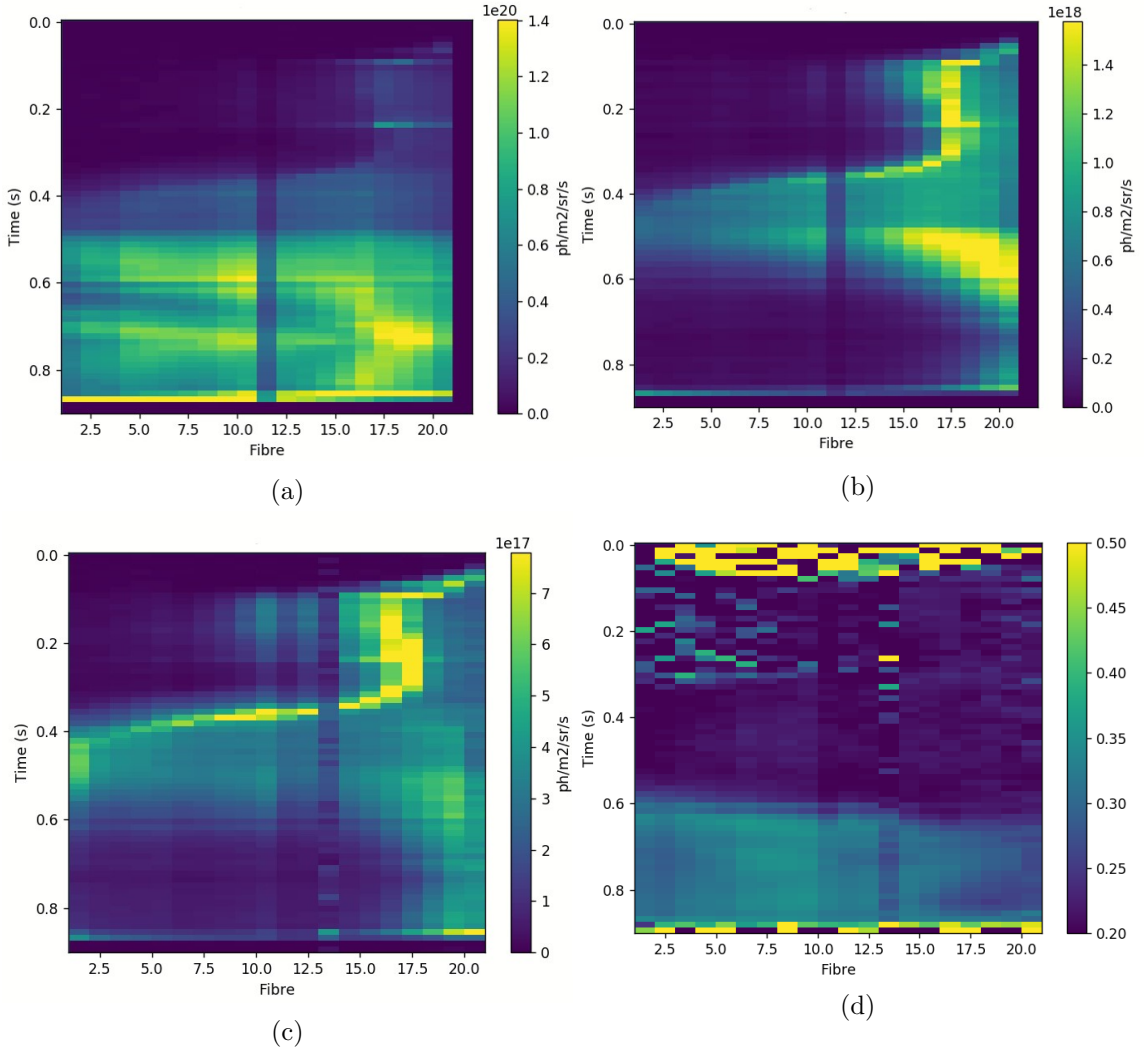

Figure 6.6: Emission data for each fibre as a function of time for shot number 45371. (a) shows the D_α emission profile, (b) shows the Fulcher band profile, (c) corresponds to the CD band emission and (d) to the n=6/5 Balmer line ratio.

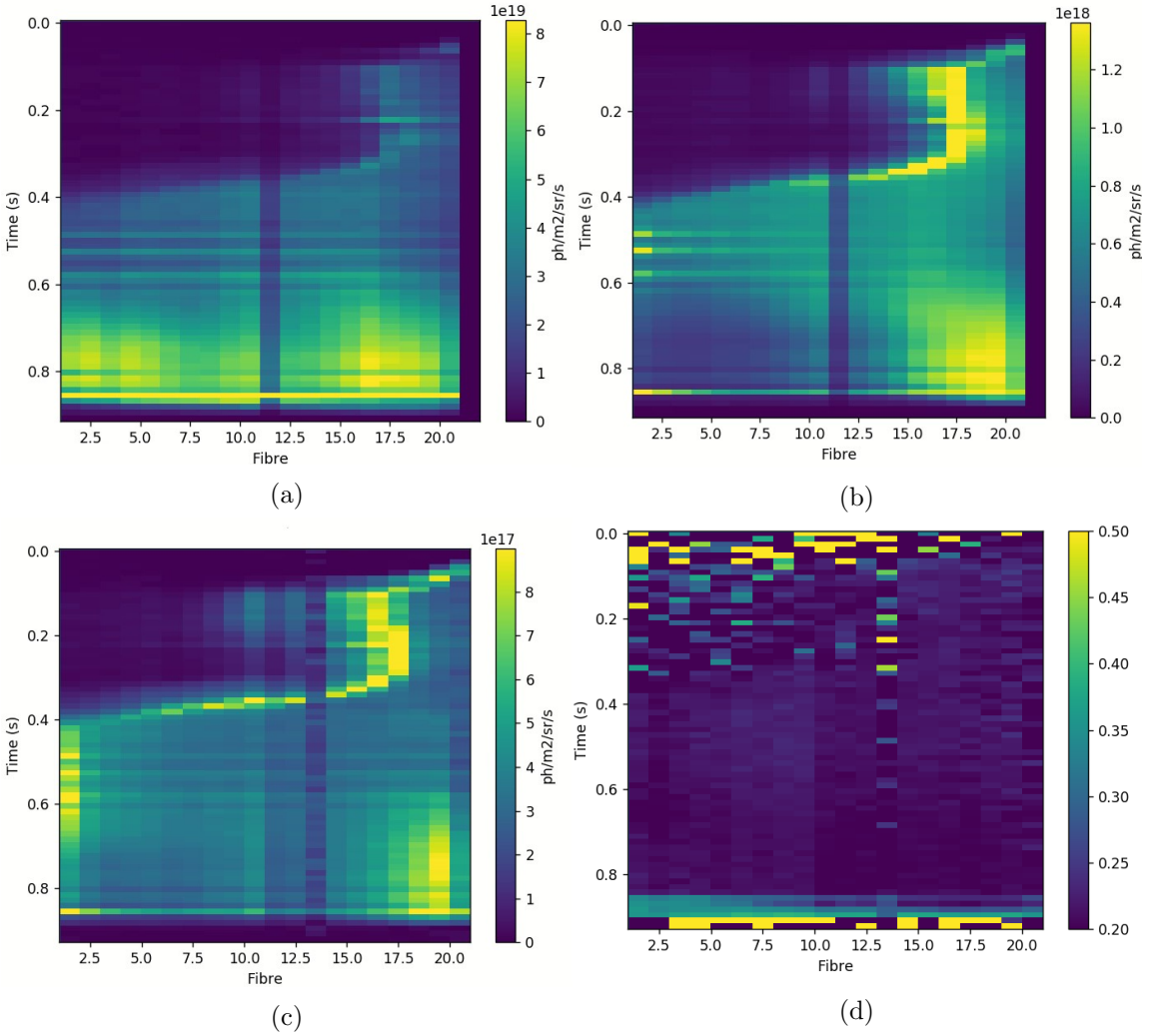

Figure 6.7: Emission data for each fibre as a function of time for shot number 45372. (a) shows the D_α emission profile, (b) shows the Fulcher band profile, (c) corresponds to the CD band emission and (d) to the n=6/5 Balmer line ratio.

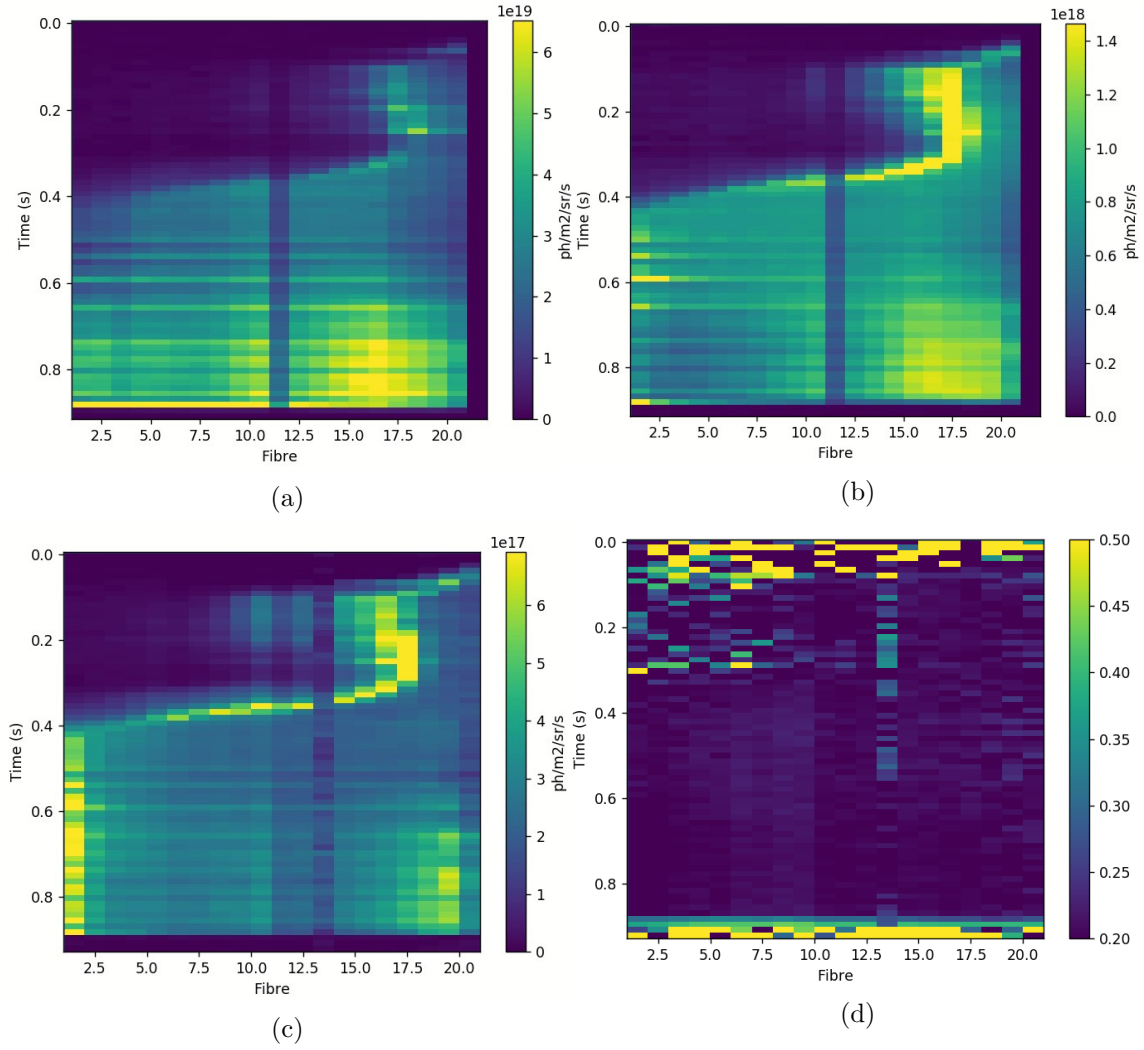

Figure 6.8: Emission data for each fibre as a function of time for shot number 45376. (a) shows the D_α emission profile, (b) shows the Fulcher band profile, (c) corresponds to the CD band emission and (d) to the n=6/5 Balmer line ratio.

The emission profiles shown in Figure 6.8 correspond to measurements collected in shot 45376, a repeat of the discharge in shot 45371. The emission measurements presented in Figures 6.8(a)-(d) mirror the trends seen in Figures 6.7(a)-(d). The D_α emission moves towards the furthest tile in the divertor leg, tile 5, at 400 ms before remaining relatively constant throughout the shot. The Fulcher band emission shown in Figure 6.8(b) moves towards tile 5 at 420 ms, but unlike in shot 45372 does not then retreat towards the divertor entrance and is constant throughout the divertor region. The CD band emission in Figure 6.8(c), also approaches tile 5 at around 400 ms and stays peaked within the leg of the divertor throughout the rest of the shot. The n=6 to n=5 ratio seen in Figure 6.8(d) is again low throughout the shot with a slight increase around tile 2, closer to the divertor entrance, until a reduction in the ratio at 600 ms.

The final set of measurements from this campaign utilised in this chapter are collected from shot 45377, also a repeat Super-X discharge with increased divertor fuelling. Figure 6.9 shows the evolution of the emission over this shot. The D_α emission shown in Figure 6.9(a) approaches the divertor target at 400 ms, but unlike Figure 6.8(a) does not fully extend into the divertor leg. The D_α emission remains fairly constant throughout the shot from the divertor entrance to around tile 4. Similarly, the Fulcher band emission moves close to the target after 400 ms, but is slightly weaker than the Fulcher emission recorded in shot 45376. The Fulcher band then moves up the divertor region towards the entrance of the divertor with a peak close to the divertor entrance at around 800 ms. The CD band shown in Figure 6.9(c) also follows the Fulcher band trends, with a movement of the band emission towards tile 5 further in the divertor leg around 400 ms and an almost constant peak across the full divertor for the rest of the shot. The Balmer line ratio of the n=6/5 lines shown in Figure 6.9(d) is weak throughout the evolution of the shot and decreases to almost zero after 300 ms with a slight increase throughout the divertor region after 850 ms.

There are clear differences between the emission profiles in the conventional divertor configuration and Super-X divertor configuration. In the conventional divertor, the atomic and molecular emission does not appear further into the divertor leg, instead approaches tiles 2 and 3, in the middle of the divertor region. Whereas, the emission is shown to approach tile 5, further into the divertor leg, in the Super-X divertor configuration, before typically moving back towards the entrance of the divertor. This movement of the emission profiles towards the divertor entrance is shown to be more distinct in the presence of increased divertor fuelling. The variations in the emission in the two divertor configurations

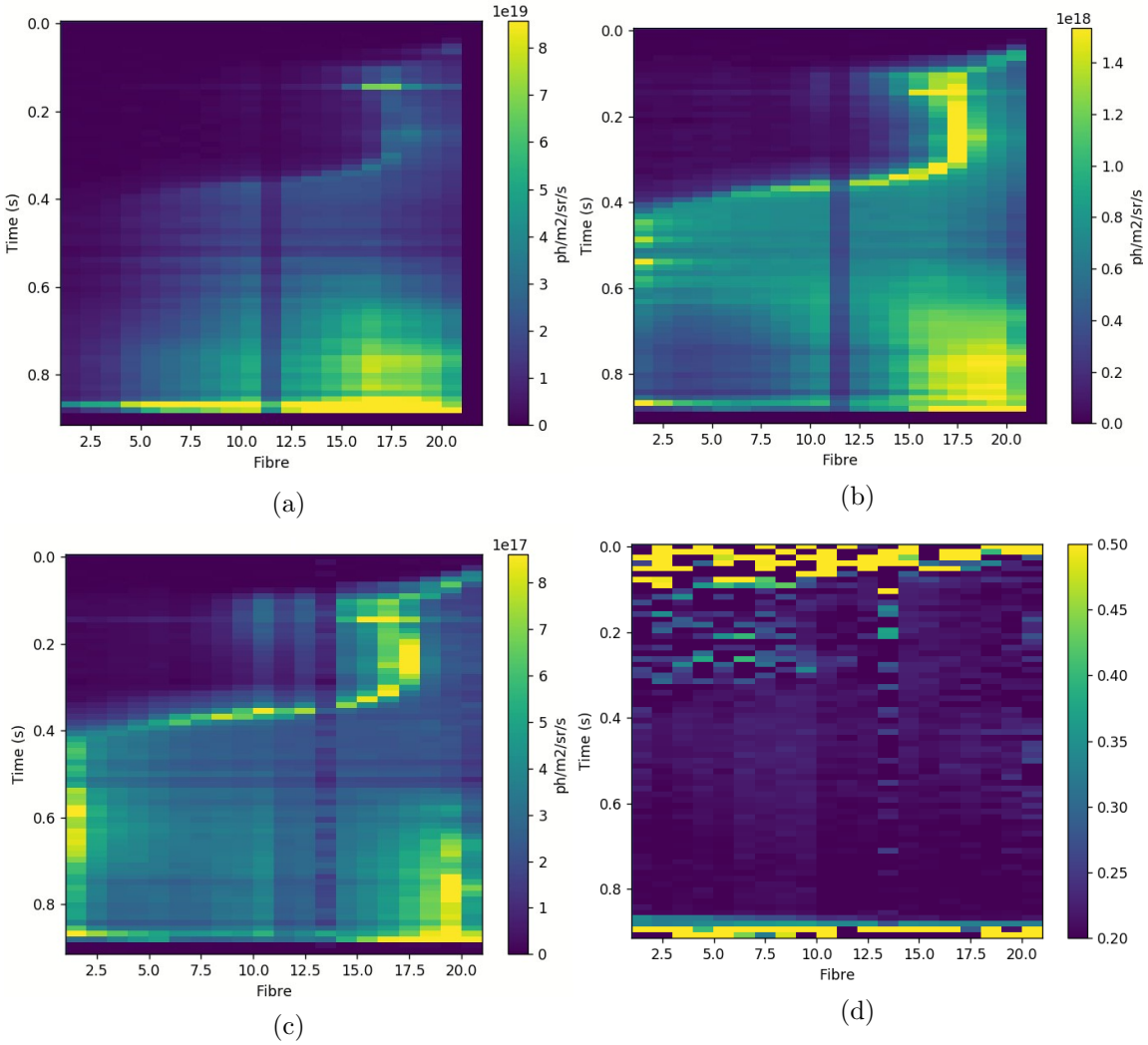

Figure 6.9: Emission data for each fibre as a function of time for shot number 45377. (a) shows the D_α emission profile, (b) shows the Fulcher band profile, (c) corresponds to the CD band emission and (d) to the n=6/5 Balmer line ratio.

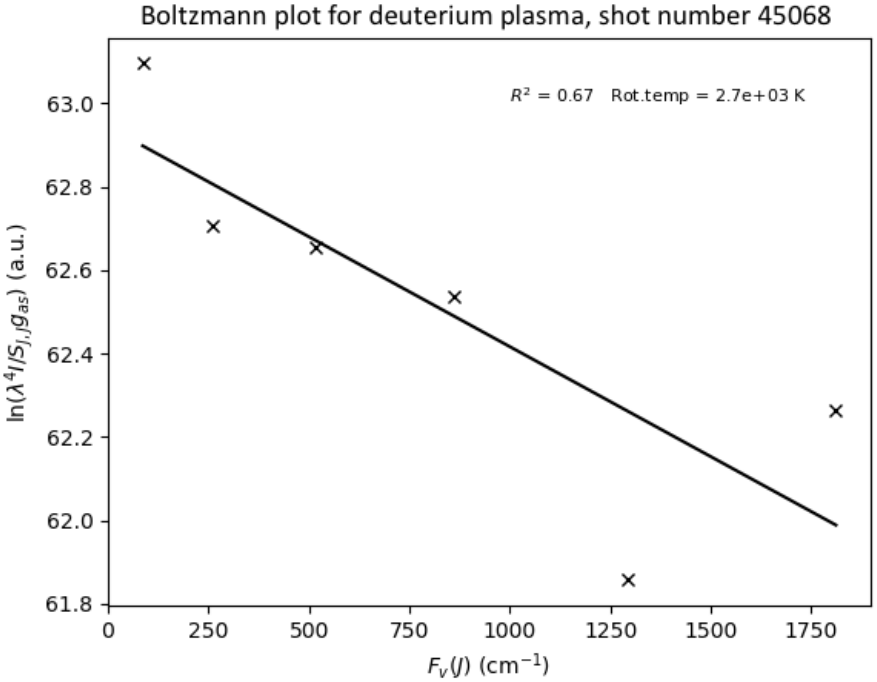

Figure 6.10: Boltzmann plot and rotational temperature calculated using the (0-0) Q-branch lines of the high resolution Fulcher band measured in shot 45068 with a conventional divertor configuration.

will be discussed further in Section 6.3.3.

6.3.2 Analysis of Fulcher band emission for varying divertor conditions

In this section, trends in the rotational temperatures in different divertor configurations will be presented. The rotational temperatures discussed in this section were calculated using the Boltzmann plot method outlined in Section 3.2.3 for high resolution Fulcher band data collected in three different shots. The divertor conditions and configurations of these three shots, 45068, 45244 and 45258 are described in Table 6.1.

There were three successful shots in which high resolution Fulcher band emission data was collected using the DMS spectrometers, and so line identification of these bands was possible. Through the Boltzmann plot technique, the lines corresponding to the (0-0) Q-branch of the Fulcher band were identified and rotational temperatures calculated from

the intensities of these lines.

Figure 6.10 shows a Boltzmann plot for shot 45086. Shot 45068 is a development discharge with a conventional divertor configuration which included the collection of high resolution Fulcher band data in the lower divertor. Each data point represents a Q-branch line in the (0-0) band, e.g Q1, Q2, etc, outlined in Section 2.4. The calculation of the factor $\ln(\lambda^4 I^{d,v,j}_{a,v,J}/S_{J,J}g_{as})$ for each Q-branch line is then plotted against $F_v(J)$, where $hcF_v(J)$ is the rotational energy. From the line fitted to these data points, the rotational temperature can then be found. The Boltzmann plot of the Fulcher band measured in shot 45068 yields a rotational temperature of 2700 K.

In Figure 6.11, a Boltzmann plot calculated utilising the high resolution Fulcher band emission data collected in shot 45244 can be seen. Shot 45244 is a repeat of shot 45243, a discharge in the Super-X divertor configuration, discussed in the previous section and shown in Figure 6.4. The high resolution Fulcher band data collected in the lower Super-X divertor is utilised to calculate a rotational temperature of 1400 K, significantly lower than the value of T_{rot} calculated for shot 45068. Further interpretation of these results will be discussed in Section 6.3.3.

A Boltzmann plot for shot 45248 is presented in Figure 6.12. Shot 45248 is a density ramp discharge employing the conventional divertor configuration. However early in this shot the plasma was observed to interact with the wall resulting in a disruption. Due to this, the Fulcher band emission data was collected over a much shorter time period than in previous shots. The rotational temperature calculated for this shot was estimated to be 1600 K. This value is much lower than the rotational temperature calculated for shot 45068, at 2700 K, also in the conventional divertor configuration, and is closer to the value of T_{rot} calculated in the Super-X configuration in shot 45244. This value may be an anomaly due to the disruption in the shot, but will be discussed further in the next section.

6.3.3 Interpretation of emission measurements

Qualitative trends in emission

The trends seen in Figures 6.4-6.9 show distinct differences in the emission profiles between conventional and Super-X divertor configurations. These trends will be highlighted in a subsequent section. In this section, an interpretation of the emission profiles in relation to the atomic and molecular indicators of the line emission will be outlined.

In shot 45243, the higher ratio of the n=6 to n=5 lines close to the target indicates

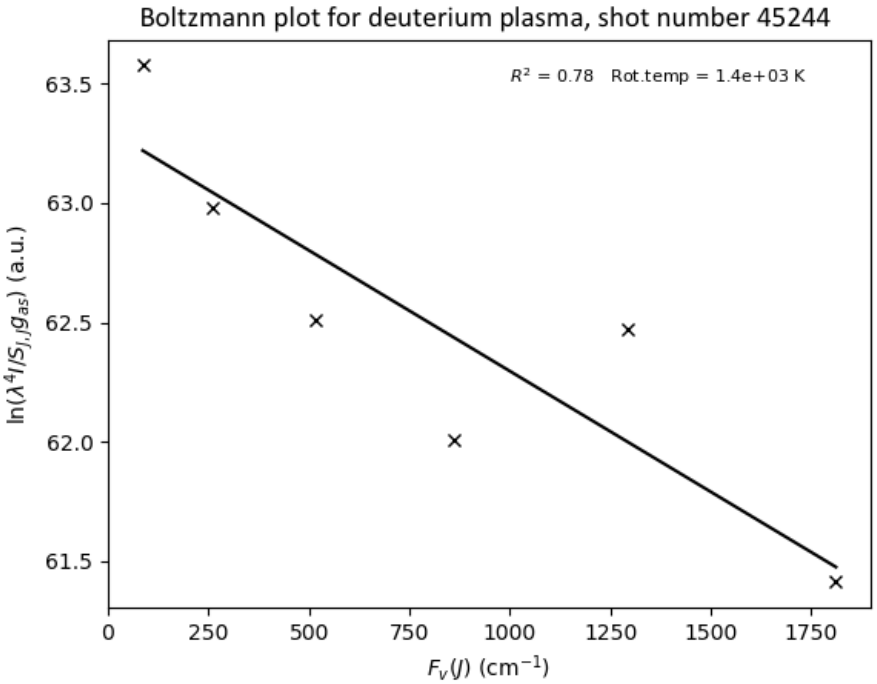

Figure 6.11: Boltzmann plot and rotational temperature calculated using the (0-0) Q-branch lines of the high resolution Fulcher band measured in shot 45244 with a Super-X divertor configuration.

the presence of electron-ion recombination around 780 ms, however these signs of EIR disappear after 800 ms. The D_α emission profile approaches the target at around 400 ms and then broadens throughout the entire divertor. This broadening of the D_α profile is observed around the onset of detachment [133], and can lead to increased radiation in the SOL from the carbon divertor tiles. The carbon-deuterium band can be observed to pull back towards the divertor entrance at around 750 ms, potentially increasing the radiation in the SOL.

In shot 45247, the D_α, Fulcher band and CD profiles do not reach tile 5 (fibre 0), furthest into the divertor leg and so the strike point drifts to tile 4, further up into the divertor region. The D_α emission moves towards the target at around 400 ms, but pulls away from the target at around 650 ms. There is also strong D_α emission on tile 3 at 800 ms. The increased ratio of the n=6 to n=5 lines around 750 ms indicates electron-ion

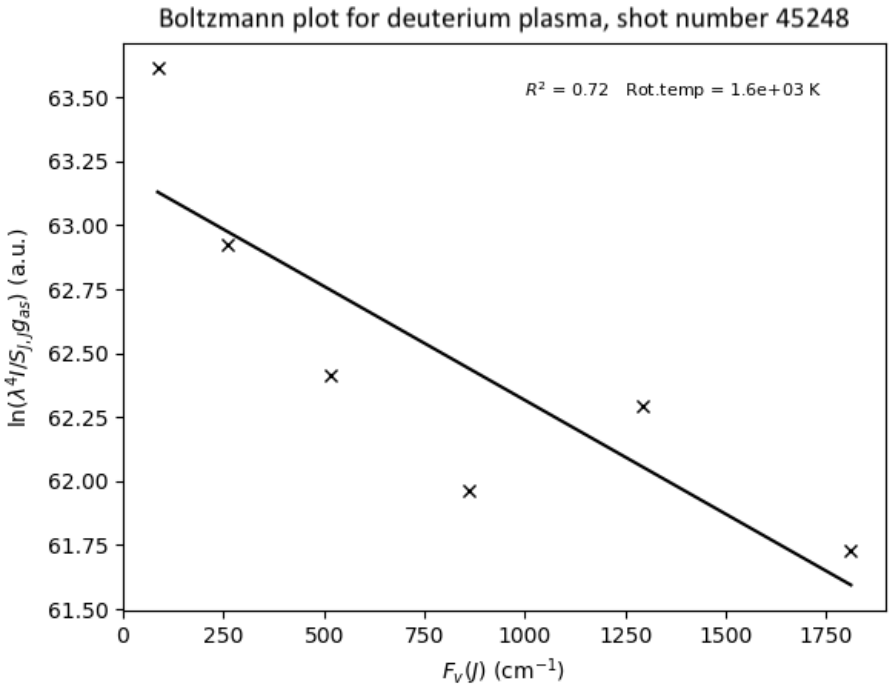

Figure 6.12: Boltzmann plot and rotational temperature calculated using the (0-0) Q-branch lines of the high resolution Fulcher band measured in shot 45248 with a conventional divertor configuration.

recombination (EIR) close to tile 5 in the divertor leg. As the n=6 to 5 ratio decreases close to tile 3, the increase in D_α emission implies strong molecular-activated recombination around the middle of the divertor. The Fulcher emission pulls away from tile 4 around 600 ms and retreats to the entrance of the divertor. The Fulcher emission is known to track the ionisation region, as a significant amount of energy is required to excite molecules to higher vibrational states, therefore there is an increased rate of ionisation close to the divertor entrance from 800 ms onwards where the Fulcher emission is seen to be high.

The evolution from an attached plasma to the onset of detachment can be inferred by the sudden retreat of the Fulcher band from the divertor tile to the divertor entrance, as seen at around 580 ms in Figure 6.6. This indicates a significant reduction in temperature within the divertor around this time in the shot since temperatures are seen to be too low for electron impact dissociation. As the Fulcher band tracks the hottest region in the

divertor, Figure 6.6(b) indicates a sudden decrease in temperature close to the divertor tiles at 580 ms. The increased n=6/5 ratio at around 630 ms also indicates a reduction in temperature across the divertor since this ratio is indicative of increased ion-electron recombination, which is known to be a dominant process at low temperatures < 5 eV. As strong IER can be seen throughout the divertor towards the end of the shot, the evolution of divertor detachment can be inferred since temperatures are low enough for detachment to occur. These trends are replicated in shot 45372, 45376 and 45377 in the Super-X divertor, however it is clear that the additional divertor fuelling in shot 45371 increases the degree of detachment and suppresses impurity radiation transport throughout the divertor. Without divertor fuelling, the Fulcher band intensity, shown in Figures 6.7(b), 6.8(b) and 6.9(b), does not retreat to the divertor entrance as drastically as seen in Figure 6.6(b), and so temperatures close to the target are not reduced as significantly as in the fuelling case.

Quantitative trends in rotational temperatures

As previously discussed, detached divertor plasmas conditions are markedly cooler than for attached plasmas. The Super-X divertor is shown to influence the evolution of detachment and result in higher degrees of detachment, resulting in reduced temperatures close to divertor materials. The trends in the rotational temperatures outlined in Section 6.3.2 highlight this relationship for varying divertor configuration, since the measured rotational temperature in shot 45068, a conventional divertor discharge, was 2700 K, almost double the value of T_{rot} measured in the Super-X configuration for shot 45244 at 1400 K. These trends are not surprising, as numerous models predict similar temperatures in alternative divertor configurations, however these results validate these hypotheses and the use of OES to analyse detachment. The lower rotational temperature measured for shot 45248 is excluded from quantitative analysis as the uncertainty in this measurement is unknown. As there was a significant disruption early on in the shot, the results from this shot are not indicative of the emission measured in similar plasmas.

Conventional vs Super-X divertor

The effects of alternative divertor configurations on the onset of detachment is a key research focus of the MAST-U experimental campaign. Emission measurements for a variety of shots both in the conventional and Super-X divertor configuration were collected to enable an analysis of the effects of the magnetic geometry on the ionisation and

recombination regions in the divertor.

There are significant differences in the emission profiles seen in Figure 6.5, for the conventional divertor, and Figure 6.6, for the Super-X divertor. In the conventional divertor, the D_α and Fulcher emission approach tile 4, close to the divertor leg, at around 400 ms, but do not extend to tile 5 further into the divertor leg. The emission is centred on tiles 2, 3, and 4, indicating high levels of recombination and ionisation close to these targets. The Fulcher emission indicates strong ionisation close to the divertor entrance at the beginning of the shot, moving towards the strike point at around 400 ms. Under attached conditions, the Balmer emission intensity and the impurity line emission are known to peak close to the strike points. as mirrored in the D_α profile shown in Figure 6.5(a).

In the Super-X divertor, shown in shot 45371, there is a clear evolution from the attached to detached plasma regime, with a sudden drop in Fulcher emission close to the tile furthest in the divertor leg. The n=6/5 ratio is much brighter in the Super-X divertor, implying increased rates of volume recombination across the whole divertor region. Volume recombination is known to be an important process required for detachment, as highlighted in Section 2.

As outlined in Section 6.3.2, the rotational temperature is estimated to be significantly higher in the conventional, attached divertor discharge. For shot 45068, the rotational temperature was found to be 2700 K, almost double the value of the rotational temperature calculated for shot 45244 in the Super-X configuration of 1400 K. The conventional divertor discharge for shot 45248, shows a slightly reduced rotational temperature than for similar conditions measured in shot 45068. However this discharge was disrupted early in the shot and so the uncertainties of this value are likely to be high and so this doesn't represent the bulk divertor temperature.

6.4 Summary

The control of the tokamak power exhaust is an important research topic and divertor detachment will be key to the successful operation of future fusion devices. The research presented in this chapter aims to characterise the trends in the emission profiles for varying plasma conditions and divertor configuration. Through the analysis of these emission profiles, key differences are shown between the conventional and Super-X divertor, including increased volume recombination in the Super-X configuration and lower

rotational temperatures. Strong electron-ion recombination regions are indicated by large values of the n=6/5 ratio, the broadening of the D_α profile across the divertor indicates the onset of detachment and the Fulcher band tracks the ionisation region. Through these emission measurements the processes that influence the onset and evolution of divertor detachment can be monitored.

Divertor fuelling is shown to increase the degree of detachment in the Super-X divertor, observed through the decreased ionisation close to the divertor surfaces. The recycling of molecules from the divertor surfaces will influence the intensity of the emission and so the temperature of the divertor surface will also have an effect on the emission profiles.

These results demonstrate the power of using emission measurements to monitor divertor detachment in tokamaks. The detachment front can be seen clearly in the emission profiles and the change of detachment conditions is reflected in routine emission measurements. An improved understanding of the underlying emission mechanisms is needed to fully utilise the information provided by these measurements. This understanding is one of the goals of modelling studies, including the sophisticated multiphysics models of fusion edge plasmas, such as SOLPS and EIRENE, as well as the purely emission models such as those presented in Chapter 7.

Chapter 7

The Development of a Zero-Dimensional Collisional-Radiative Model

Understanding atoms and molecules is key to diagnosing low temperature plasmas. To extract information about the atomic and molecular processes in tokamak edge plasmas from diagnostic measurements, collisional-radiative models are a useful tool.

This chapter summarises the research completed through a collaborative research project at Keio University, Tokyo. This work centres on the study of a zero-dimensional collisional-radiative model (0D CR model) for hydrogen plasmas and the development and adaption of this model for purposes relevant to emission measurements at the University of Liverpool. The main aims of the project will be outlined in Section 7.1, with the structure of the model outlined in Section 7.2. Section 7.3 then describes the areas of development and methodology used to expand the model. Results from benchmarking with a range of results from the Yacora 0D CR model [121] will be outlined in Section 7.4, and comparisons with experimental data will be detailed in Section 7.5 before conclusions on the key results and validity of the model are outlined.

Collisional-radiative (CR) models are used to study the population distributions of ions and atoms as a function of various plasma parameters, such as electron temperature and ion density, over their excited states. Through these models, detailed information about the collisional and radiative processes within plasmas can be studied and by comparing with

experimental data, these models can allow for a deeper analysis of the trends in emission within the low temperature divertor regions of tokamaks. A Maxwellian distribution for the electrons is commonly assumed for use in CR models and the population distribution is then obtained by rate equations that employ a balance of collisional and radiative properties [157]. Basic CR models are used to describe the collisional excitation processes that compete with the radiative decay of atoms and molecules in plasmas, and have the form,

$$\frac{\partial n(p)}{\partial t} + \nabla \cdot (n(p) w_p) = \Big(\frac{\partial n(p)}{\partial t}\Big)_{c,r} \tag{7.1}$$

The CR model developed throughout this collaborative research project is a simple 0D model and so is unable to take profile effects into account unlike 2D and 3D codes of SOL/divertor plasmas such as SOLPS and EIRENE [68, 69]. However since the computational costs of 0D models are significantly lower, they are considered to be more practical for understanding the basic particle balance characteristics and plasma densities in tokamaks. Through this work, an improved, more capable collisional-radiative model was developed and benchmarked with results from an established 0D CR model. The benchmarking highlights the ability of this model to replicate established trends in atomic emission and allows for a wider understanding of the most important processes that influence the behaviour of atoms and molecules in low temperature plasmas.

7.1 Research aims

The main objectives of this project were the development and adaption of a 0D CR model to include species and reactions relevant to low temperatures found in tokamak divertors. The original CR model source code, centred on the analysis of Tsubotani et al [158], was studied to understand the structure of the model and processes previously added to the code. From this, three aims were formulated in order to expand the model and alter the code to enable a comparison of the outputted results to experimental emission data.

To extend and develop the existing model, the three main objectives were as follows.

1. Molecular species and reactions

The first aim involved the inclusion of H_3 species and an additional nine reactions to the 0D model to allow for an improved understanding of the key atomic and molecular

processes in low temperature plasmas.

2. Atomic emission output

The second objective centred upon modifying the code to allow for a prediction of atomic emission intensity to be outputted. As optical emission spectroscopy is a key diagnostic technique utilised in low temperature plasmas, this step would allow for direct comparisons of experimental studies with the computational model.

3. Wall recycling

The third goal of this project was to include a simple wall recycling model to enable the effects of wall recycling on the population densities and provide information about plasma-wall interaction processes.

These aims will be detailed further in Section 7.3, alongside the results of these areas of development.

7.2 Model structure

The original 0D collisional-radiative model is written using the Fortran programming language with the aim of studying the dynamic behaviour of divertor detachment and the impacts of Molecular-Assisted Recombination on the evolution of detachment [158]. Values of initial electron temperature, T_e, and electron density n_e are inputted, along with particle confinement times and gas temperatures. The outputs of the code are the densities of the hydrogen atom, H_2, H_2^- and H_2^+ molecules, with the inclusion of H_3 and H_3^+ molecules completed through this work, reaction rates for all reactions, and the intensities and wavelengths of the atomic Balmer lines.

A flowchart outlining the structure of the code can be seen in Figure 7.1.

7.3 Development of the collisional-radiative model

As outlined in Section 7.1, the main objective of this research was to extend the 0D CR model for a comparison with experimental emission measurements. This centred on three main areas of development to adapt the model to allow for a comparison with low temperature plasmas.

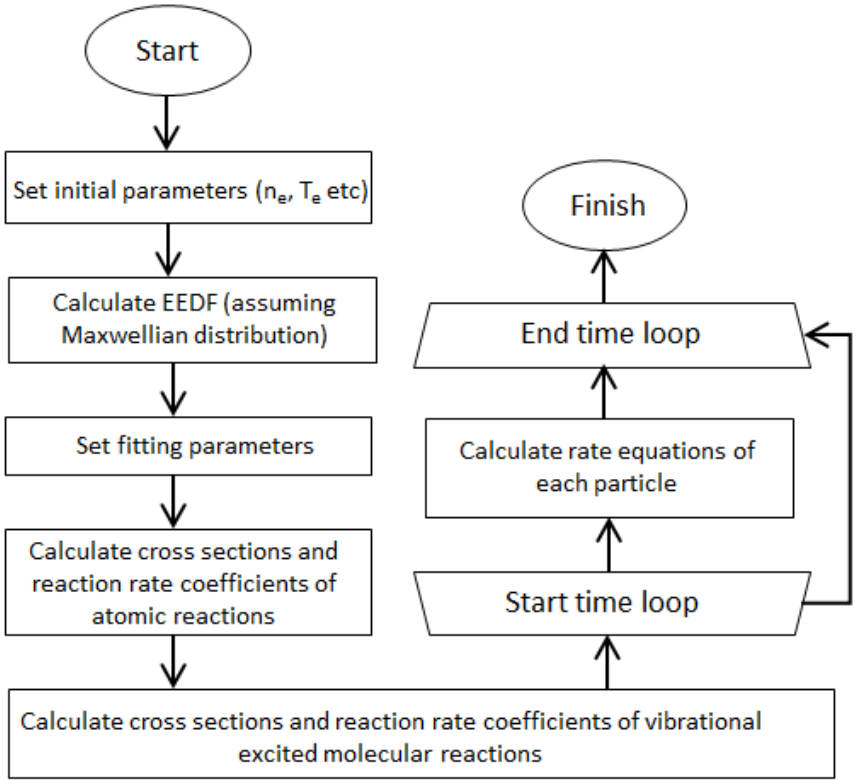

Figure 7.1: Flowchart highlighting the structure of the model in order to calculate the rate equations for each species.

7.3.1 The inclusion of molecular species

The first area of development was the inclusion of additional molecular reactions relevant to low temperature plasmas and the addition of H_3 and H_3^+ ions to the model. The addition of these species was important since H_3 is known to play an important role in ionising and recombining plasmas in tokamak divertors [159].

The Keio CR model originally included sixteen atomic and molecular reactions, including excitation, ionisation, dissociative attachment, mutual neutralisation, among others which can be seen in Table 7.1. Through this research, an additional nine molecular reactions were added to the model alongside the inclusion of reactions with H_3 molecules and H_3^+ ions.

The nine reactions added to the model can be seen in Table 7.2. Reaction rates and

Table 7.1: Reactions for hydrogen atoms and molecules previously added to the 0D collisional-radiative model.

No.	Reaction Name	Reaction	Rate Coefficient
1	Vibrational excitation/de-excitation	$e + H_2(X^1\Sigma_g^+;\nu) \rightarrow H_2^- \rightarrow e + H_2(X^1\Sigma_g^+;\nu')$ $e + H_2(X^1\Sigma_g^+;\nu) \rightarrow e + H_2(B^1\Sigma_u^+, C^1\Pi_u)$ $\rightarrow e + H_2(X^1\Sigma_g^+;\nu')$	$R_{eV}(\nu \rightarrow \nu')$ $R_{EV}(\nu \rightarrow \nu')$
2	Ion conversion	$H_2(\nu) + H^+ \rightarrow H_2^+ + H(1s)$	$R_{IC}(\nu)$
3	Dissociative attachment	$H_2(\nu) + e \rightarrow H^- + H(1s)$	$R_{DA}(\nu)$
4	Dissociative recombination	$H_2^+ + e \rightarrow H(1s) + H(n)$	R_{DR}
5	Mutual neutralisation	$H^- + H^+ \rightarrow H(n = 2, 3) + H(1s)$	R_{MN}
6	H_2 dissociation	$H_2(\nu) + e \rightarrow H_2(b^3\Sigma_u^+) + e \rightarrow e + H(1s) + H(1s)$	$R_{FC}(\nu)$
7	Electron detachment/H^- loss	$H^- + e \rightarrow H(1s) + e + e$	R_{ED}
8	H_2^+ dissociation	$H_2^+ + e \rightarrow H^+ + H(1s) + e$	R_{DE}
9	H_2 ionisation	$H_2(\nu) + e \rightarrow H_2^+ + 2e$	$R_{MI}(\nu)$
10	Dissociative ionisation	$H_2(\nu) + e \rightarrow H_2^+(B^2\Sigma_u^+) + 2e \rightarrow H^+ + H(1s) + 2e$ $H_2(\nu) + e \rightarrow H_2^+(X^2\Sigma_g^+) + 2e \rightarrow H^+ + H(1s) + 2e$	$R_{DI}(\nu)$
11	H excitation	$H(p) + e \rightarrow H(q) + e \quad (p < q)$	$C(p, q)$
12	H de-excitation	$H(p) + e \rightarrow H(q) + e \quad (p > q)$	$F(p, q)$
13	H ionisation	$H(p) + e \rightarrow H^+ + 2e$	$S(p)$
14	Three-body recombination	$H^+ + e + e \rightarrow H(p) + e$	$R_{TBR}(p)$
15	Radiative recombination	$H^+ + e \rightarrow H(p) + h\nu$	$R_{RR}(p)$
16	Spontaneous emission	$H(q) \rightarrow H(p) + h\nu$	$A(p, q)$

cross-sections were calculated using the Hydhel database [160] for each reaction and the density of both the H_3 and H_3^+ ions could then be calculated. The inclusion of a number of molecular reactions for different species in the model was completed to allow for a more thorough comparison with the experimental spectroscopy study at the University of Liverpool in which molecular species are a focus. As molecular reactions are particularly important in detached divertor regimes [161], the inclusion of molecules in the model increases the applicability of the model to future studies of divertor plasmas.

The rates for the added molecular reactions were plotted alongside the preexisting reactions rates. A plot of the loss rates for H_3^+, as an example of the evolution of the

Table 7.2: Reactions for hydrogen atoms and molecules that were added to the 0D collisional-radiative model through the development of the code.

No.	Reaction Name	Reaction	Rate Coefficient
1	Dissociative excitation (H_2)	$H_2(\nu) + e \rightarrow H(1s) + H(2s) + e$	$R_{H2DE}(\nu)$
2	Direct impact dissociation	$H_3^+ + e \rightarrow 3H(n=1)$	R_{H3pDID}
3	Dissociative excitation (H_3)	$H_3^+ + e \rightarrow 2H(n=1) + H^+ + e$	R_{H3pDE}
4	Dissociative proton transfer	$H_3^+ + H_2(\nu) \rightarrow 2H_2(\nu) + H^+$	$R_{H3pDPT}(\nu)$
5	Mutual neutralisation	$H^- + H_3^+ \rightarrow H + H_3$	R_{H3pMN}
6	Dissociative mutual neutralisation	$H^- + H_3^+ \rightarrow H_2(\nu) + H + H$	$R_{H3pDMN}(\nu)$
7	H_3^+ formation	$H_2^+ + H_2(\nu) \rightarrow H_3^+ + H$	$R_{H3pF}(\nu)$
8	Proton transfer	$\underline{H_3^+}(\nu_3) + H_2(\nu_0) \rightarrow \underline{H_2}(\nu_0') + H_3^+(\nu_3')$	$R_{H3pH2PT}(\nu)$
9	Dissociative electron capture & Fast H_2 production	$\underline{H_3^+} + H_2(\nu) \rightarrow \underline{H} + \underline{H_2}(\nu) + H_2^+$	$R_{H3FHP}(\nu)$

reaction rates over time, is shown in Figure 7.2. The evolution of the density of the species included in the model over time can be seen in Figure 7.3 below. The time is set to ensure convergence of the model.

The densities of the H_2 vibrational states can also be calculated through the model, and Figure 7.4 shows the evolution of the first 12 states over time until the model converges.

7.3.2 Emission intensity calculation

Another key focus for the development of this model was the inclusion of a calculation for the atomic line emission for the hydrogen Balmer series. This would then allow for a comparison between theoretical line intensities calculated by the model with experimental emission data. Through this comparison, further information about the key atomic and molecular processes at specific densities and temperatures can be identified.

To calculate the intensity of the emission in the model, Einstein coefficients for specific transitions and absolute densities should be known. Einstein coefficients, the transition rates per unit time for emission, are used to describe the emission of photons via electronic transitions in atoms. The Einstein A coefficients, (A_{21}), describe spontaneous emission for hydrogen transitions to the $n = 2$ state (the Balmer series) and a density and population solution was incorporated into the model to output the values for the emission intensity

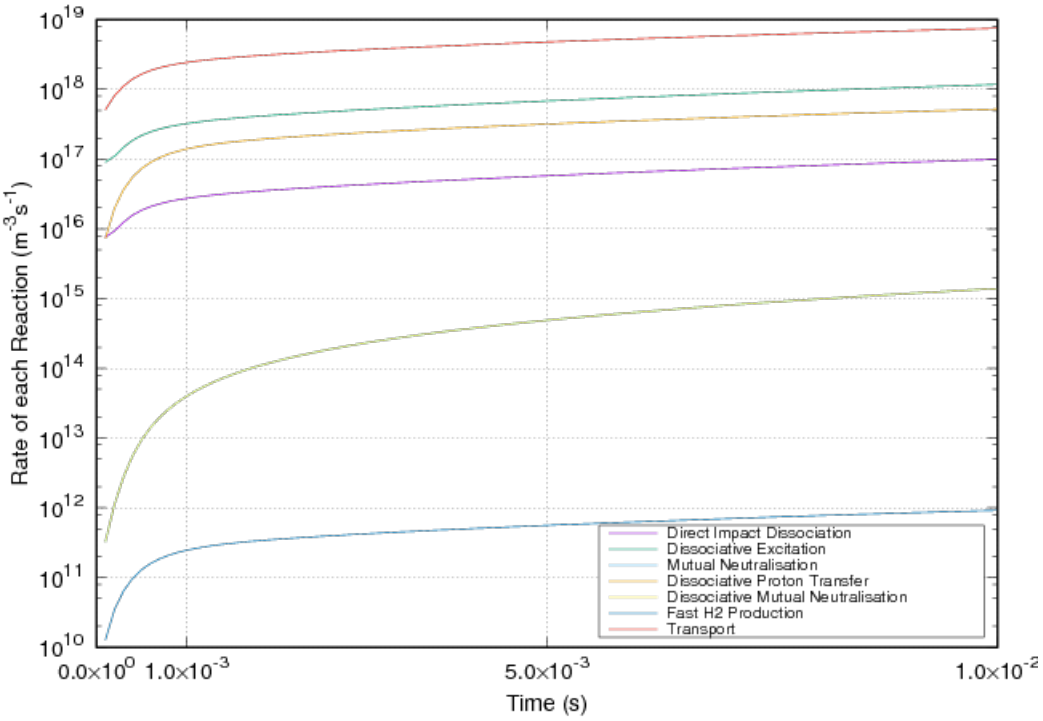

Figure 7.2: The development of the reaction rates for the loss reactions of H_3^+ over time.

using the following formula,

$$\epsilon_{pk} = A_{pk} n_H(p) \tag{7.2}$$

for every H_0 state, where ϵ_{pk} is the line emission intensity from atomic hydrogen from level p to level k, A_{pk} is the Einstein A coefficient transition probability from level p to level k and $n_H(p)$ is the population density of atomic hydrogen in the electronically excited state, p. Figure 7.5 shows an example of an emission intensity vs wavelength plot outputted by the CR model. The intensity is plotted on a log-scale so that the intensities of the higher-n Balmer lines can be seen clearly.

The inclusion of the emission intensity calculation in the CR model allows for a comparison with emission measurements in the ICP discharge source. A comparison of the outputted emission line ratios and those observed in experimental measurements will be detailed in Section 7.5.

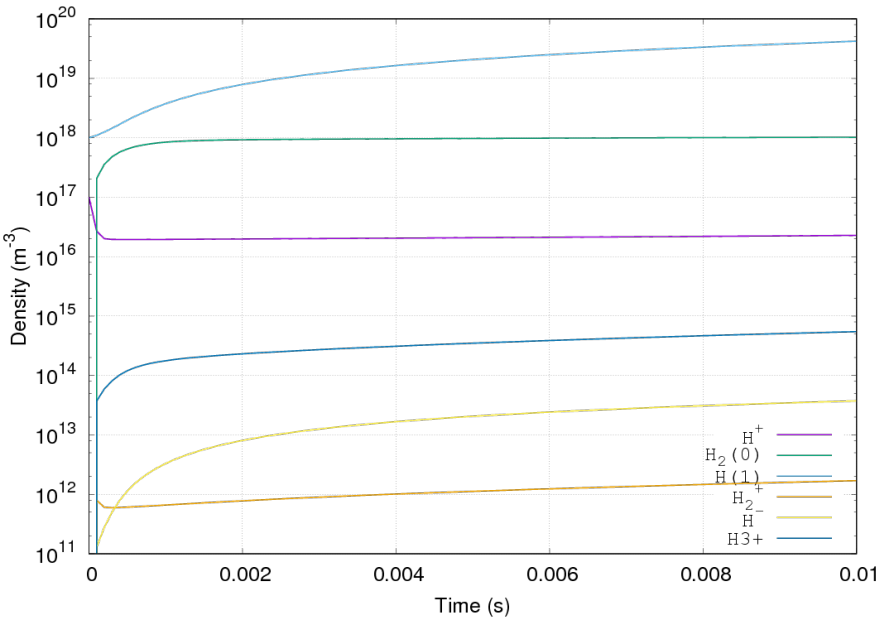

Figure 7.3: Densities of all the species included in the model over time until steady-state convergence.

7.3.3 Wall recycling coefficient

Initially the sole source of neutrals in the 0D model originated from a background neutral density corresponding to the density of neutrals through gas puffing in a divertor. A simple plasma wall recycling model was added to the model to implement a recycling yield to add a source of neutrals and provide information about key plasma-wall interaction processes. A recycling coefficient, R, was defined and calculated for H atoms and H_2 molecules in the ground state. No time dependence was required for the recycling coefficient since tokamak divertor plates are assumed to be saturated. This recycling flux term was added to the rate equations to include the effect of wall recycling on the population densities.

The loss of particles is necessary to prevent the particle density from increasing indefinitely, therefore a pumping effect was incorporated into the recycling coefficient to provide a sink of particles. The structure of the wall will impact the vibrational molecular state of the recycled particle, with effects on the reflection coefficient resulting from differences in material structures and temperatures and this should be investigated in future work.

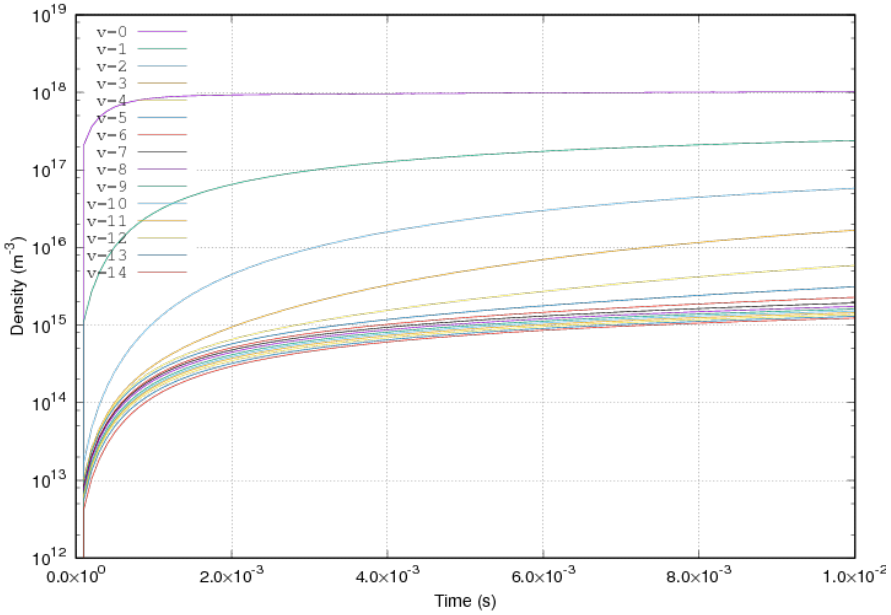

Figure 7.4: The density of the H_2 vibrational species, v=0-12, over time.

The particle reflection coefficient, R_N, is calculated using the following equation formulated in [162],

$$R_N = \left[(1 + 3.2116\epsilon_L^{0.34334})^{1.5} + (1.3288\epsilon_L^{1.5})^{1.5}\right]^{-\frac{1}{1.5}} \tag{7.3}$$

where ϵ_L is equal to

$$\epsilon_L = 32.55\frac{m_2}{m_1 + m_2} + \frac{1}{z_1 z_2 \left(z_1^{2/3} + z_2^{2/3}\right)^{1/2}} E_H \tag{7.4}$$

and E_H is the incident energy.

Using this reflection coefficient, the recycling rates Γ_{H_0}, for hydrogen atoms, and Γ_{H_2}, for H_2 molecules in the ground state were formulated as

$$\Gamma_{H_0} = R_N\left(\frac{n_i}{\tau_i} + \frac{n_H}{\tau_H}\right) \tag{7.5}$$

$$\Gamma_{H_2} = \frac{(1 - R_N)}{2}\left(\frac{n_i}{\tau_i} + \frac{n_H}{\tau_H}\right) \tag{7.6}$$

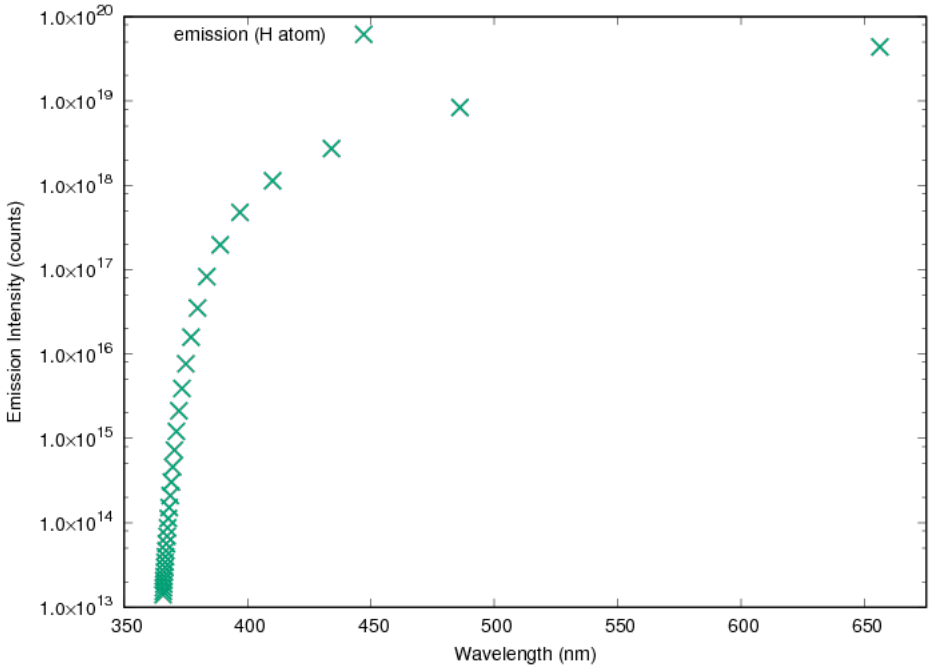

Figure 7.5: Emission intensity against wavelength plot for the Balmer series outputted by the CR model with the intensity plotted on a log scale.

These rates were then included in the CR model to provide a source of reflected particles. Further research into the impact of wall materials and conditions, such as purity, roughness, defects, wall temperature and degree of excitation angle of incidence with respect to the surface normal on the reflection coefficient should be completed in order to improve the accuracy of the recycling rate equations.

7.4 Benchmarking with the Yacora CR model

In order to verify the trends in emission outputted by the improved CR model, benchmarking with the Yacora model was completed. An outline of the Yacora 0D model can be found in Section 2.4.1 where the structure and composition of the model are detailed. The Yacora model has been designed with a user-friendly interface to encourage collaboration and has had considerable validation in low pressure gas discharges. The atomic hydrogen branch of the Yacora model includes twelve reactions for H, H^+, H^-, H_2, H_2^+ and H_3^+. H_3 molecules and the vibrational states of H_2 are not included.

Additionally, the CR model outputs the intensities of the Balmer series, and although this can be calculated from the population densities outputted by Yacora, this is not currently a feature of the Yacora model.

The Keio CR model benefits from an increased number of species and reactions, to more accurately model the low temperature plasma constituents, and a prediction of emission intensity to allow for an easy comparison with emission measurements.

To benchmark the 0D CR model with the Yacora 'on the web' model, identical input parameters were used and the resulting population densities compared. The Keio CR model calculates the absolute intensities for the Balmer line series using the calculated population densities, however the Yacora model does not. To compare the corresponding absolute intensity for the Keio and Yacora models, the H_α and H_γ lines outputted by the Keio CR model were compared with the emission intensity calculated as in Section 7.3.2 for the corresponding population densities outputted by Yacora. The ratio of these Balmer lines was then compared for varying input electron density and can be seen in Figure 7.6.

Figure 7.6 shows good agreement between the outputted line intensities for the CR model and Yacora. The trends in the H_γ/H_α ratio for varying density are roughly constant for both the CR model and Yacora data. The outputted line ratios from the CR model agree with the Yacora line ratios within 20% and so demonstrates the ability of the improved CR model to predict established trends from published work in the field.

7.5 Comparison with experimental data

After benchmarking with the Yacora model, the CR model was then compared with experimental measurements in the ICP discharge plasma presented in Chapter 4 to allow for an interpretation of ICP discharge measurements.

The ratio of the H_γ and H_α emission lines from experimental measurements and the CR model were compared to enable a validation of the model with experimental measurements. Figure 7.7 shows these ratios from both the Keio CR model and from experimental results for varying values of electron density.

At higher electron densities above 1×10^{17} m^{-3}, the experimental ratio and the ratio given by the CR model agree within 30%. Below 5×10^{16} m^{-3} the CR model fails to predict the experimental emission intensities. It can be concluded that the model predicts the intensity of the Balmer emission accurately at higher electron densities, but is not valid for lower electron densities. At low electron densities, the dominant power coupling

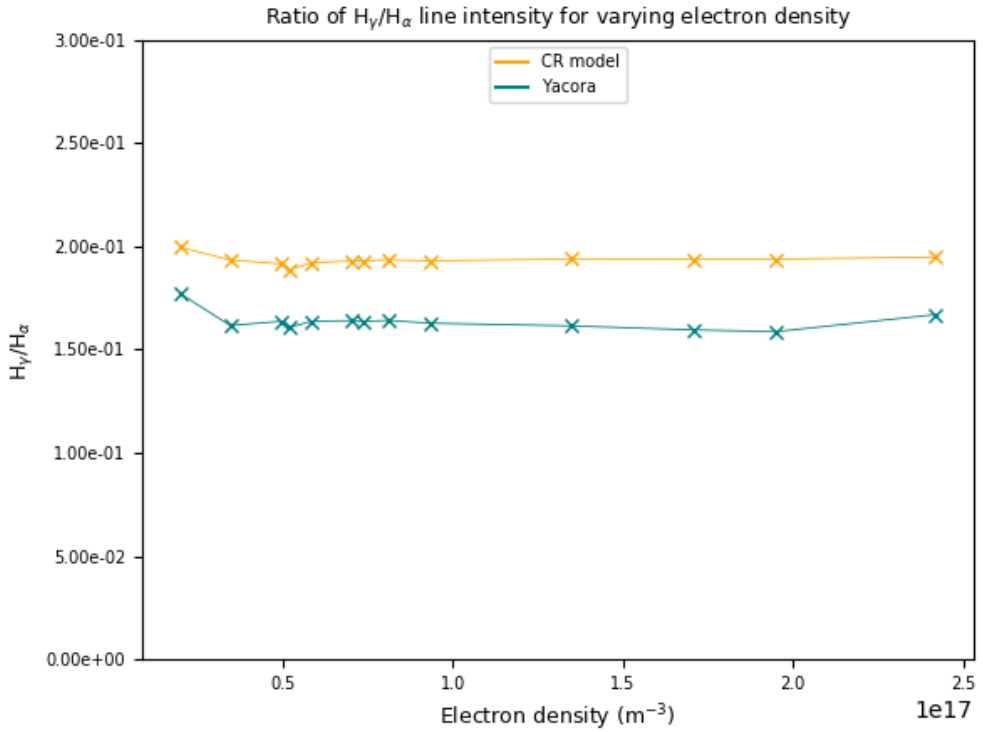

Figure 7.6: Benchmarking of the ratio of the H_γ to H_α intensities for varying electron density outputted by the Keio CR 0D model and the Yacora 0D model.

mode in the ICP discharge plasma will be capacitive. The high plasma potential sheaths and non-Maxwellian distributions in capactively coupled plasmas do not agree with the assumptions in the CR model and so the model will not be able to accurately predict the experimental trends at low n_e conditions in the ICP chamber.

7.6 Summary

In this chapter, the development of a 0D collisional-radiative model for use in extracting information on the key atomic and molecular processes in low temperature plasmas was described.

Nine additional molecular processes were added to the model including those for the species H_3 and H_3^+. The inclusion of these molecular species enabled a wider picture of

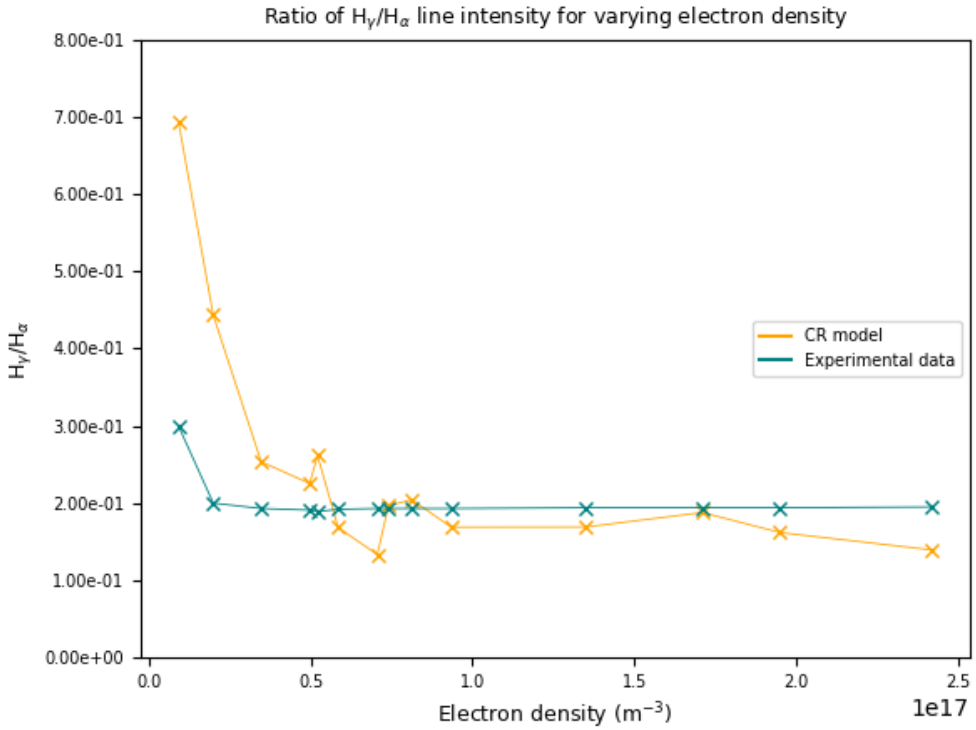

Figure 7.7: Comparison of the ratio of the experimental H_γ to H_α intensities for varying electron density with the outputted CR model ratio.

the processes in low temperature plasmas to be created.

A wall recycling model was formulated to allow for the effects of plasma-wall interactions and the recycling of molecules to be studied. Through this recycling model the recycling of H atoms and ground state H_2 molecules were included, however the vibrational states of H_2 are not yet added to the recycling model. The next step in expanding this wall model would be to incorporate the recycling of H_2 vibrational states and to research how this recycling coefficient is influenced by the surface texture and temperature of the wall. The TRIM database could then be utilised to adjust the recycling coefficient to include vibrational states of molecules.

The final aim of this research was to include a prediction of the atomic line emission calculated from the population densities. It was then possible to plot the Balmer series line intensities against wavelength for various input parameters. These intensities outputted

from the model can then be used in plasma parameter analysis by comparing results from the model for known input parameters with intensity vs wavelength plots from experimental emission data.

Benchmarking with the 0D Yacora model showed good agreement for the ratio of the H_γ/H_α emission lines calculated from population densities outputted by both models. Comparison of the improved CR model with measurements from the Liverpool ICP source also showed that the emission predicted by the model agreed with the experimental results for conditions where the model assumptions are reasonably satisified. From these results, it is clear that the CR model can be utilised effectively to provide information on the key processes in low temperature plasmas.

From the development of this collisional-radiative model, a more detailed picture can be made about the key atomic and molecular processes in low temperature plasmas. The research in this chapter shows the value of 0D collisional-radiative models in understanding plasma behaviour. While a complete understanding of divertor detachment requires a more sophisticated approach, of the type employed in the SOLPS and EIRENE fusion codes, a 0D model can help identify the key processes that must go into those models.

To further improve this type of 0D CR model, it is necessary to include a larger number of molecular processes, so that molecular emission can also be modelled accurately. Such a model might be useful for interpreting some of the results of Chapter 5, where the Fulcher band emission was observed to depend strongly on plasma-surface interactions.

Chapter 8

Conclusions and Future Work

8.1 Conclusions

An understanding of the key atomic and molecular processes in the low temperature divertor regions of fusion machines is vital for the success of fusion as a source of clean energy for the future. This thesis focuses on studies related to low temperature plasmas in the power exhaust region, or divertor, of tokamak devices. A specific focus was placed on the behaviour of atoms and molecules in both low temperature laboratory plasmas and edge plasmas in fusion machines. The behaviour of atoms and molecules influence detachment in tokamak divertors, an important process to reduce the power fluxes on divertor surfaces in future fusion devices to below material limits.

Extensive studies highlight the capabilities of detachment in reducing the huge heat loads on divertor materials, however this process is not currently understood. Fully detached plasmas require plasma recombination close to the divertor surfaces, which results in increased emission through the excited neutral particles created in this process. Therefore optical emission spectroscopy can provide useful information to quantify divertor detachment.

Research using inductively coupled plasmas can also contribute to the field of low temperature fusion plasmas as similar electron temperatures to those found in divertors can be replicated. Through the use of ICPs, a study of the key atomic and molecular processes can be completed in controlled conditions with improved diagnostic access.

Chapters 1-3 of this thesis explain the aims, background and context of the research, as well as describing the equipment and measurement techniques. The original research

in this thesis is presented in the next four chapters. The main outcomes of those chapters can be summarised as follows.

In Chapter 4, a characterisation of the inductively coupled discharge plasma at the University of Liverpool was presented in order to quantify the trends in both electron properties and plasma emission for varying discharge conditions. It was found that electron property measurements mirror trends in published literature and show increasing electron densities and decreasing electron temperatures for both increased discharge pressure and RF power. These trends are attributed to the changes in collisionality and the transition from capacitive to inductive coupling in the ICP discharge.

Emission measurements showed that intensities of atomic and molecular emission are higher for increased RF input power, as the increased rates of ionisation lead to a higher number of collisions of neutrals with charged species. The Q1 lines of the molecular Fulcher band are shown to decrease for increasing pressure, as the vibrational states of H_2 become more evenly distributed. Rotational temperatures calculated using the Fulcher band emission lines show that the gas temperature is highest when the discharge is predominantly capacitively coupled, and is reduced for conditions when inductive coupling was dominant.

In Chapter 5, trends in plasma properties and atomic and molecular emission close to different material samples for varying discharge and surface conditions were detailed, building on the measurements presented in Chapter 4.

Electron parameters are shown to be relatively unaffected by varying sample material. For increasing sample temperature, measurements close to the divertor samples highlight the effects of the carbon sample on the electron temperature, with a peak at high sample temperatures above 1000C. Electron temperatures are also seen to be higher in the presence of the nanostructured tungsten sample compared with the smooth tungsten sample, although the reasons for this require further investigation.

Measurements of atomic and molecular emission show similar trends for the three different samples for varying pressure and power. For increasing RF power, all three Balmer lines increase in the presence of all three samples. These trends agree with measurements presented in Chapter 4 without the sample heater. There is shown to be no real change in the presence of the tungsten samples on the plasma emission, and the trends are similar to those seen without the sample heater. These results imply that the presence of metallic surfaces has little effect on the plasma emission. The carbon sample however, does seem to effect both the atomic and molecular emission for increasing sample temperature. One

explanation for these observed trends is due to electron bombardment of the carbon sample at low pressures, and therefore a variety of hydrogen and carbon reactions influencing the excitation of hydrogen atoms and molecules. These interactions may effect how atoms and molecules are recycled from the carbon surface, however this relationship is complex and should be studied further in future work. Investigation into the influence of the sample material and texture on the molecular emission clearly show that the vibrational population of hydrogen molecules can be affected by different material surfaces.

Fulcher band measurements show distinctly different distributions in the presence of a carbon sample compared with the two tungsten samples. The measurements with the tungsten samples mirror trends in the molecular band structure without the sample heater so are shown to have little effect on the H_2 vibrational distribution. From these trends, it is clear that the plasma is affected by the carbon sample more significantly than by the tungsten samples. The nanostructured tungsten sample has no noteworthy effect on the plasma properties, however the plasma emission is affected at certain plasma and sample conditions. The smooth tungsten sample does not seem to have a strong impact on both the plasma parameters or emission, even at substantially enhanced surface temperatures.

In Chapter 6, measurements of emission in the MAST-U divertor are presented. Through the trends in the emission profiles, atomic and molecular processes are seen to dominate at specific regions in the divertor and at specific times throughout the shot. D_α, Fulcher band and carbon-deuterium band emission was studied, along with the ratio of the Balmer n=6/5 lines, to quantify the key differences between the conventional and Super-X divertor configurations. Through trends in these profiles, key regions of recombination and ionisation can be observed and from these regions, the onset of divertor detachment can be studied. The rotational temperatures are significantly reduced in the Super-X configuration and the ionisation region can be seen to retreat towards the entrance of the divertor. Increased fuelling in the divertor is also shown to drastically increase the degree of detachment in the Super-X divertor. These results demonstrate the power of emission measurements to monitor the onset and evolution of divertor detachment in tokamaks. A deeper understanding of the underlying emission mechanisms observed through these measurements is required to fully characterise the key processes throughout the divertor region.

In the final research chapter, Chapter 7, the improvements made to a 0D collisional-radiative model were outlined. Additional species and molecular processes were added to the model to enable a more accurate prediction of the key processes dominating

in low temperature plasmas. A wall recycling model was formulated to allow for the effects of plasma-wall interactions and recycling of molecules to be included and the prediction of the hydrogen atomic emission intensity using calculated population densities was added.

Benchmarking with the 0D Yacora model shows good agreement for the ratio of the H_γ/H_α emission lines outputted by both CR models. Emission results collected using the ICP discharge plasma were compared with the CR model and also showed good agreement for conditions where the model assumptions are reasonably satisified. These results highlight the ability of the improved CR model to provide information on the key processes in low temperature plasmas.

8.2 Suggestions for future work

A few suggestions to motivate future work related to the research presented in this thesis are discussed here.

Issues with overheating in the University of Liverpool ICP RF matching unit should be resolved to allow for an investigation of the trends in the plasma emission and parameters at higher powers in the ICP inductive mode. Additionally, improved signal-to-noise in the Langmuir probe measurements would allow for an investigation into the electron energy distribution functions which would provide a deeper understanding of the key processes in low temperature plasmas and how they influence plasma emission.

To understand the mechanisms that influence plasma detachment in the MAST-U divertor, improved predictive models to quantify the plasma-wall interactions would be desirable. Modelling of molecular emission compared to experimental Fulcher band data collected in the MAST-U divertor would allow for an improved understanding of the key processes in tokamak divertors. The understanding gained through this work would enable the use of the Fulcher band to reliably estimate molecular density to be quantified.

Combining the 0D collisional-radiative model with a 2D plasma edge code would offer the possibility to study the atomic and molecular processes that influence detachment across the whole divertor and highlight specific regions. The model could also be expanded further to increase it's capabilities. One area for expansion of the model would be the inclusion of more molecular processes, including those for H_3^- and D, species relevant to fusion plasmas, to give a clearer picture of the key processes in the divertor region in tokamaks. Through the use of a recycling coefficient added to the CR model, the recycling of H atoms and ground state H_2 molecules were added, however the vibrational states

of H_2 are not currently included in the recycling model. The next step in expanding this wall model would be to incorporate the recycling of H_2 vibrational states and study how recycling of particles is affected by the surface texture and temperature of the wall. The main motivation for including emission prediction in this model was to allow for a comparison between the CR model and experimental emission data. By including an output of emission, an analysis of how the emission depends on the plasma parameters can be made. Throughout the work at Keio University, an output of the Balmer series line emission was included. However, since molecular processes influence the power exhaust in tokamaks, emission from molecules should also be included in future research. This will require more research into the Einstein coefficients for molecular transitions and an appropriate formula for predicting the emission in this case and would enable an interpretation of the results presented in Chapter 5, where the Fulcher band emission was observed to depend strongly on plasma-surface interactions.

8.3 Outlook

The work presented in this thesis has laid some important foundations on which future research can build upon to develop the understanding of low temperature plasmas. By fully understanding the behaviour of atoms and molecules in exhaust regions of tokamaks, magnetic confinement fusion grows increasingly more viable.

Diagnostic techniques for atoms and molecules in low temperature plasmas provide an insight into the key processes in tokamak edge plasmas. Through the results from measurements presented in this thesis, an improved knowledge of the processes that influence divertor detachment can be inferred.

Materials used for plasma-facing components in tokamaks can influence the plasma conditions and impact the onset of detachment. Therefore it is important to study the interactions between plasmas and surfaces in order to control the handling of power in divertor regions.

The research presented here on the behaviour of atoms and molecules in low temperature plasmas close to divertor-like materials should form a useful contribution to the field, with the hope that this work will provide a step towards the success of commercial fusion energy and a green energy future.

References

[1] International Energy Agency. (2017). *World Energy Outlook 2017*. [Online]. Available: https://www.iea.org/reports/world-energy-outlook-2017

[2] Diffen. (2015). *Nuclear Fission and Fusion* [Online]. Available: https://www.diffen.com/difference/NuclearFissionvsNuclearFusion

[3] University of York. *Fusion on Earth* [Online]. Available: https://www.york.ac.uk/physics/public-and-schools/nuclear-masterclass-student-course/module-3-fusion-student-course/

[4] I. Friedman, "Deuterium content of natural waters and other substances", *Geochimica et Cosmochimica Acta*, 4, 1–2, 89-103, Aug 1953

[5] R. J. Pearson, A. B. Antoniazzi and W. J. Nuttall, "Tritium supply and use: a key issue for the development of nuclear fusion energy", *Fusion Engineering and Design*, 136, 1140-1148, Nov 2018

[6] J. Ongena and G. Van Oost, "Energy for Future Centuries: Prospects for Fusion Power as a Future Energy Source", *Fusion Science and Technology*, 61, 3-16, Aug 2012

[7] I. Langmuir, "Oscillations in Ionized Gases", *Proceedings of the National Academy of Sciences*, 14, 8, 627–637, 1928

[8] F. F. Chen, "Introduction to Plasma Physics and Controlled Fusion", Third edition. Switzerland, Springer, 2018

[9] K. Miyamoto, "Plasma Physics and Controlled Nuclear Fusion", First edition. Tokyo, Springer, 2004

[10] M. Goossens, "An Introduction to Plasma Astrophysics and Magnetohydrodynamics", 15-58, Dordrecht, Springer, 2003

[11] A. de Castro, C. Moynihan, S. Stemmley, M. Szott, and D. N. Ruzica, "Lithium, a path to make fusion energy affordable", *Physics of Plasmas*, 28, 2021

[12] M. Keilhacker, A. Gibson, C. Gormezano, P. J. Lomas, P. R. Thomas, M. L. Watkins, P. Andrew, B. Balet, D. Borba, C. D. Challis, I. Coffey, G. A. Cottrell, H. P. L. De Esch, N. Deliyanakis, A. Fasoli, C. W. Gowers, H. Y. Guo, G. T. A. Huysmans, T. T. C. Jones, W. Kerner, R. W. T. König, M. J. Loughlin, A. Maas, F. B. Marcus, M. F. F. Nave, F. G. Rimini, G. J. Sadler, S. E. Sharapov, G. Sips, P. Smeulders, F. X. Söldner, A. Taroni, B. J. D. Tubbing, M. G. von Hellermann, D. J. Ward and JET Team, "High fusion performance from deuterium - tritium plasmas in JET", *Nuclear Fusion*, 39, 2, p.209–234, 1999

[13] R. Pitts, R. Buttery and S. Pinches, "Fusion: the way ahead", *Physics World*, 2006

[14] J. W. Berkery, G. Xia, S. A. Sabbagh, J. M. Bialek, Z. R. Wang, C. J. Ham, A. Thornton and Y. Q. Liu, "Projected Global Stability of High Beta MAST-U Spherical Tokamak Plasmas", *Plasma Physics and Controlled Fusion*, 62, 8, Aug 2020

[15] EuroFusion. (2008). *50 years of tokamaks*, [Online]. Accessible: https://www.euro-fusion.org/newsletter/50-years-of-tokamaks/

[16] Y. Xu, "A general comparison between tokamak and stellarator plasmas", *Matter and Radiation at Extremes*, 1, 4, p.192-200, Jul 2016

[17] CCFE. (2012). *Fusion energy: Achieving fusion power* [Online]. Accessible: http://www.ccfe.ac.uk/Fusionpower.aspx

[18] HB11 Energy. (2021) *HB11 Energy* [Online]. Accessible: https://hb11.energy/

[19] TAE Technologies. (2021) *TAE Technologies* [Online]. Accessible: https://tae.com/

[20] General Fusion. (2021) *General Fusion* [Online]. Accessible: https://generalfusion.com/

[21] Fusion Industry Association. (2021) *The global fusion industry in 2021* [Online]. Accessible: https://www.fusionindustryassociation.org/about-fusion-industry

[22] Lawrence Livermore National Laboratory (2014) *Inertial Confinement Fusion: How to Make a Star* [Online]. Accessible: https://lasers.llnl.gov/science/icf

[23] A. W. Morris, and the MAST U team, "MAST Upgrade Divertor Facility: A test bed for novel divertor solutions", Jun 2017

[24] C. Theiler, "Basic Investigation of Turbulent Structures and Blobs of Relevance for Magnetic Fusion Plasmas", Ph.D. dissertation, EPFL, 2011

[25] V. Philipps, J. Roth and A. Loarte, "Key Issues in Plasma-Wall Interactions for ITER: A European Approach", 3, 01-46, 2014

[26] H. Bolt, V. Barabash, G. Federici, J. Linke, A. Loarte, J. Roth and K. Sato, "Plasma facing and high heat flux materials – needs for ITER and beyond", *Journal of Nuclear Materials* 307–311, 43–52, 2002

[27] A. Loarte, "Effects of divertor geometry on tokamak plasmas", *Plasma Phys. Control. Fusion*, 43, 2001

[28] D. Ryutov, R. H. Cohen, T. D. Rognlien and M. V. Umansky, "A snowflake divertor: a possible solution to the power exhaust problem for tokamaks", *Plasma Phys. Control. Fusion*, 54, 2012

[29] E. Havlíčková, W. Fundamenski, M. Wischmeier, G. Fishpool and A. W. Morris, "Investigation of conventional and Super-X divertor configurations of MAST Upgrade using scrape-off layer plasma simulation", *Plasma Physics and Controlled Fusion*, 56, 7, 2014

[30] X. Bonnin, R. A. Pitts, V. Komarov, F. Escourbiac, M. Merola, L. Bo, L. Wei, L. Pan and A. S. Kukushkina, "ITER divertor plasma response to time-dependent impurity injection", *Nuclear Materials and Energy*, 12, 1100-1105, 2017

[31] A. Kallenbach, M. Bernert, R. Dux, L. Casali, T. Eich, L. Giannone, A. Herrmann, R. McDermott, A. Mlynek, H. W. Müller, F. Reimold1, J. Schweinzer, M. Sertoli, G. Tardini, W. Treutterer, E. Viezzer, R. Wenninger, M. Wischmeier and the ASDEX Upgrade Team, "Impurity seeding for tokamak power exhaust: from present devices via ITER to DEMO", *Plasma Phys. Control. Fusion*, 55, 2013

[32] H. V. Willett, K. J. Gibson and P. K. Browning, "The role of plasma instabilities in the onset of detachment in the York Linear Plasma Device", *43rd EPS Conference on Plasma Physics*, 2016

[33] R. Perillo, R. Chandra, G. R. A. Akkermans, I. G. J. Classen, S. Q. Korving, and Magnum-PSI Team, "Investigating the effect of different impurities on plasma detachment in linear plasma machine Magnum-PSI", *Physics of Plasmas*, 26, 2019

[34] A. E. Costley, "Towards a compact spherical tokamak fusion pilot plant", *Phil. Trans. R. Soc.*, 377, 2019

[35] CCFE. (2019) *MAST Upgrade Research Plan* [Online]. Available: https://ccfe.ukaea.uk/research/mast-upgrade/

[36] J. Wesson, "The Science of JET", *JET Joint Undertaking, Abingdon*, 2000

[37] T. Oku, "Carbon/Carbon Composites and Their Properties", *Carbon Alloys*, Pages 523-544, 2003

[38] IAEA, "The upgrade to the Mega Amp Spherical Tokamak", ICC/P5-06, 2010

[39] United Kingdom Atomic Energy Authority. (2021) *First results from UK experiment point to a solution to one of fusion's hottest problems* [Online]. Accessible: https://ccfe.ukaea.uk/first-results-from-uk-experiment-point-to-a-solution-to-one-of-fusions-hottest-problems/

[40] M. E. Koepke, "Interrelationship between Lab, Space, Astrophysical, Magnetic Fusion, and Inertial Fusion Plasma Experiments", *atoms*, 2019

[41] N. Ohno, "Plasma detachment in linear devices", *Plasma Physics and Controlled Fusion*, 59, 3, 2017

[42] Y. Hirooka, R. W. Conn, T. Sketchley, W. K. Leung, G. Chevalier, R. Doerner, J. Elverum, D. M. Goebel, G. Gunner, M. Khandagle, B. Labombard, R. Lehmer, P. Luong, Y. Ra, L. Schmitz, and G. Tynan, "A new plasma-surface interactions research facility: PISCES-B and first materials erosion experiments on bulk-boronized graphite", *Journal of Vacuum Science Technology* 8, 1790, 1990

[43] Y. Nakashima, H. Takeda, K. Ichimura, K. Hosoi, K. Oki, M. Sakamoto, M. Hirata, M. Ichimura, R. Ikezoe, T. Imai, M. Iwamoto, Y. Hosoda, I. Katanuma, T. Kariya, S. Kigure, J. Kohagura, R. Minami, T. Numakura, S. Takahashi, M. Yoshikawa, N. Asakura, M. Fukumoto, A. Hatayama, Y. Hirooka, S. Kado, H. Kubo, S. Masuzaki, H. Matsuura, S. Nagata, N. Nishino, N. Ohno, A. Sagara, T. Shikama, M. Shoji, A. Tonegawa and Y. Ueda, "Progress of divertor simulation research toward the realization of detached plasma using a large tandem mirror device", *Journal of Nuclear Materials*, 463, 537-540, Aug 2015

[44] Y. Hayashi, K. Ješko, H. J. van der Meiden, J. W. M. Vernimmen, T. W. Morgan, N. Ohno, S. Kajita, M. Yoshikawa and S. Masuzaki, "Plasma detachment study of high density helium plasmas in the Pilot-PSI device", *Nucl. Fusion*, 56, 126006, 2016

[45] T. Schenkel, A. Persaud, H. Wang, P. A. Seidl, R. MacFadyen, C. Nelson, W. L. Waldron, J. L. Vay, G. Deblonde, B. Wen, Y. M. Chiang, B. P. MacLeod and Q. Ji, "Investigation of light ion fusion reactions with plasma discharges", *J. Appl. Phys.* 126, 203302, 2019

[46] M. J. Barnes, "A Pulsed RF Discharge for a Caesium Free H Ion Source", Ph.D. dissertation, Dept. Elect. Eng., University of Liverpool, Liverpool, Sept 2018

[47] Lawrence Livermore National Laboratory (2021) *Plasma Physics* [Online]. Accessible: https://lasers.llnl.gov/science/understanding-the-universe/plasma-physics

[48] T. Okumura, "Inductively Coupled Plasma Sources and Applications", *Physics Research International*, 2010, 2011

[49] G. G. Lister and M. Cox, "Modelling of inductively coupled discharges with internal and external coils", *Plasma Sources Sci. Technol.*, 167, 1992

[50] J. W Denneman, "Determination of electromagnetic properties of low-pressure electrodeless inductive discharges", *J. Phys. D: Appl. Phys.*, 23, 293, 1990

[51] J. Hopwood, "Review of inductively coupled plasmas for plasma processing", *Plasma Sources Sci. Technol.*, 1, 109, 1992

[52] J. Yoo, G. Yu and J. Yi, "Large-area multicrystalline silicon solar cell fabrication using reactive ion etching (RIE)", *Solar Energy Materials and Solar Cells*, 95, 1, 2011

[53] M. Aceto, O. Abollino, M. C. Bruzzoniti, E. Mentasti, C. Sarzanini and M. Malandrino, "Determination of metals in wine with atomic spectroscopy (flame-AAS, GF-AAS and ICP-AES); a review", Food Additives and Contaminants, 19, 2, 2002

[54] B. Heinemann, U. Fantz, W. Kraus, L. Schiesko, C. Wimmer, D. Wünderlich, F. Bonomo, M. Fröschle, R. Nocentini and R. Riedl, "Towards large and powerful radio frequency driven negative ion sources for fusion", *New Journal of Physics*, 19, 2017

[55] U. Fantz, P. Franzen and D. Wünderlich, "Development of negative hydrogen ion sources for fusion: Experiments and modelling", *Chemical Physics*, 398, 2012

[56] R. Maurizio, U. Fantz, F. Bonomo and G. Serianni, "Characterisation of the properties of a negative hydrogen ion beam by several beam diagnostic techniques", Nucl. Fusion, 56, 2016

[57] M. Bandyopadhyay, "Studies of an inductively coupled negative hydrogen ion radio frequency source through simulations and experiments", Ph.D. dissertation, IPP Garching, 2004

[58] V. I. Kolobov and D. J. Economou, "The anomalous skin effect in gas discharge plasmas", *Plasma Sources Sci. Technol.*, 6, 1997

[59] M. A. Lieberman and A. J. Lichtenberg, *Principles of Plasma Discharges and Materials Processing*, Wiley, New York, 1994

[60] E. S. Weibel, "Anomalous Skin Effect in a Plasma", *Phys Fluids*, 10, 741, 1967

[61] M. M. Turner, "Collisionless electron heating in an inductively coupled discharge", *Phys Rev Lett*, 71, 1844, 1993

[62] A. Piel, *Plasma Physics An Introduction to Laboratory, Space and Fusion Plasmas*, Second edition, Springer, Switzerland, 2017

[63] KTH. (2021). *Fusion Plasma Physics Essentials* [Online]. Accessible: https://www.kth.se/ee/fpp/introduction-to-fusi/fusion-plasma-physics-essentials-1.30839

[64] P. C. Stangeby, *The Plasma Boundary of Magnetic Fusion Devices*, The Plasma Boundary of Magnetic Fusion Devices, Institute of Physics Publishing, Bristol, 2000

[65] M. Keilhacker, "JET Deuterium-Tritium Results and their Implications", *JET Joint Undertaking Abingdon*, 1999

[66] ITER. (2022). *JET makes history again* [Online]. Accessible: https://www.iter.org/newsline/-/3722

[67] G. Federici, C. H. Skinner, J. N. Brooks, J. P. Coad, C. Grisolia, A. A. Haasz, A. Hassanein, V. Philipps, C. S. Pitcher, J. Roth, W. R. Wampler and D. G. Whyte, "Plasma-material interactions in current tokamaks and their implications for next step fusion reactors", *Nucl. Fusion*, 41, 1967, 2001

[68] D. Reiter, M. Baelmans and P. Borner, "The Eirene and B2-Eirene codes", *Fusion Science and Technology*, 47, 2005

[69] S. Wiesen and W. R Dekeyser, "The new SOLPS-ITER code package", *Journal of Nuclear Materials*, Oct 2014

[70] E. Havlíčková, M. Wischmeier and G. Fishpool, "Modelling the Effect of the Super-X Divertor in MAST Upgrade on Transition to Detachment and Distribution of Volumetric Power Losses", *Contributions to Plasma Physics*, 54, 4-6, 2014

[71] E. Havlíčková, J. Harrison, B. Lipschultz, G. Fishpool, A. Kirk, A. Thornton, M. Wischmeier, S. Elmore and S. Allan, "SOLPS Analysis of the MAST-U Divertor with the Effect of Heating Power and Pumping on the Access to Detachment in the Super-X Configuration", *Plasma Physics and Controlled Fusion*, 57, 11, 2015

[72] EuroFusion. (2018). *The road to fusion electricity* [Online]. Accessible: https://www.euro-fusion.org/eurofusion/roadmap/

[73] U. Fantz, "Atomic and Molecular Emission Spectroscopy in Low Temperature Plasmas Containing Hydrogen and Deuterium, *Max-Planck-Institut fuer Plasmaphysik IPP Report*, 10/21, 2002

[74] U. Fantz, B. Heger and D. Wünderlich, "Using the radiation of hydrogen molecules for electron temperature diagnostics of divertor plasmas", *Plasma Phys. Control. Fusion*, 43, 907, 2001

[75] A. G. McLean, "Understanding Plasma Divertor Detachment in Fusion Power Reactors", *Lawrence Livermore National Lab*, Nov 2019

[76] J. R. Harrison, C. Theiler, O. Février, H. de Oliviera, R. Maurizio, K. Verhaegh, A. Perek, A. Karpushov, B. Lipschultz, B. P. Duval, X. Feng, S. Henderson, B. Labit, B. Linehan, A. Merle, H. Reimerdes, U. Sheikh, C. K. Tsui, W. A. J. Vijvers, C. Wüthrich, the TCV team and the EUROfusion MST1 team, "Progress toward divertor detachment on TCV within H-mode operating parameters", *Plasma Phys. Control. Fusion*, 61 065024, 2019

[77] K. Verhaegh, B. Lipschultz, B. P. Duval, O. Février, A. Fil, C. Theiler, M. Wensing, C. Bowman, D. S. Gahle, J. R. Harrison, B. Labit, C. Marini, R. Maurizio, H. de Oliveira, H. Reimerdes, U. Sheikh, C. K. Tsui, N. Vianello, W. A. J. Vijvers, the TCV team and the EUROfusion MST1 team, "An improved understanding of the roles of atomic processes and power balance in divertor target ion current loss during detachment", *Nucl. Fusion*, 59, 126038, 2019

[78] U. Fantz, "Optical emission measurements of H2 and D2 molecules in the divertor region of ASDEX Upgrade", *Journal of Nuclear Materials*, 266-269, 490-494, 1999

[79] S. Krasheninnikov, A. S. Kukushkin, and A. A. Pshenov, "Divertor Plasma Detachment", *Physics of Plasmas*, 23, 055602, 2016

[80] G. F. Matthews, "Plasma detachment from divertor targets and limiters", *Journal of Nuclear Materials*, 220–222, p.104-116, Apr 1995

[81] M. Wischmeier, M. Groth, S. Wiesen, S. Potzel, L. Aho-Mantila, D. P. Coster, R. Dux, C. Fuchs, A. Kallenbach, H. W. Müller, D. Reiter, A. Scarabosio and the ASDEX Upgrade team, "Assessment of edge modeling in support of ITER", *Journal of Nuclear Materials*, 415, 1, Aug 2011

[82] M. Wischmeier, M. Groth, A. Kallenbach, A. V. Chankin, D. P. Coster, R. Dux, A. Herrmann, H. W. Müller, R. Pugno, D. Reiter, A. Scarabosio, J. G. Watkins, DIII-D team and ASDEX Upgrade team, "Current understanding of divertor detachment: Experiments and modelling", *Journal of Nuclear Materials*, 390, 1, Jun, 2009

[83] F. Reimold, M. Wischmeier, M. Bernert, S. Potzel, A. Kallenbach, H. W. Müller, B. Sieglin, U. Stroth and the ASDEX Upgrade Team, "Divertor studies in nitrogen induced completely detached H-modes in full tungsten ASDEX Upgrade", *Nucl. Fusion*, 55, 3, 2015

[84] A. Loarte, R. D. Monk, J. R. Martín-Solís, D. J. Campbell, A. V. Chankin, S. Clement, S. J. Davies, J. Ehrenberg, S. K. Erents, H. Y. Guo, P. J. Harbour, L. D. Horton, L. C. Ingesson, H. Jäckel, J. Lingertat, C. G. Lowry, C. F. Maggi, G. F. Matthews, K. McCormick, D. P. O'Brien, R. Reichle, G. Saibene, R. J. Smith, M. F. Stamp, D. Stork and G. C. Vlases, "Plasma detachment in JET Mark I divertor experiments", *Nucl. Fusion*, 38, 331, 1998

[85] J. Neuhauser, M. Alexander, G. Becker, H. S. Bosch, K. Buchl, D. Coster, R. Dux, A. Field, S. Fiedler, Ch. Fuchs, O. Gehre, O. Gruber, G. Haas, A. Herrmann, S. Hirsch, A. Kallenbach, M. Kaufmann, K. Lackner, G. Lieder, K. F. Mast, V. Mertens, H. Murmann, B. Napiontek, R. Neu, F. Ryter, H. Salzmann, R. Schneider, J. Schweinzer, M. Sokoll, K. H. Steuer, J. Stober, W. Suttrop, M. Weinlich, U. Wenzel, H. P. Zehrfeld, H. Zohm, M. Albrecht, K. Asmussen, K. Behler, K. Behringer, M. Bessenrodt-Weberpals, M. Brambilla, A. Carlson, R. Chodura, L. Cupido, H. J. DeBlank, S. De Pena Hempel, S. Deschka, C. Dorn, R. Drube, W. Engelhardt, H. U. Fahrbach, H. U. Feist, G. Fieg, G. Fussmann, C. Garcia-Rosales, J. Gernhardt, W. Herrmann, P. Ignacz, B. Juttner, W. Junker, T. Kass, W. Koppendorfer, H. Kollotzek, K. Krieger, B. Kurzan, P. Lang, R. Lang, M. Laux, M. E. Manso, M. Maraschek, P. McCarthy, D. Meisel, R. Merkel, D. Naujoks, G. Neu, M. Niethammer, J. M. Noterdaeme, G. Pautasso, C. S. Pitcher, W. Poschenrieder, G. Raupp, H. Rohr, J. Roth, W. Sandmann, H. B. Schilling, M. Schittenhelm, H. Schneider, W. Schneider, K. Schonmann, G. Schramm, U. Seidel, F. Serra, A. Silva, E. Speth, A. Stabler, B. Streibl, W. Treutterer, M. Troppmann, M. Ulrich, P. Varela, O. Vollmer, H. Wedler, F. Wesner, W. P. West, R. Wunderlich, D. Zasche and T. Zehetbauer, "The compatibility of high confinement times and complete divertor detachment in ASDEX-Upgrade", *Plasma Phys. Control. Fusion*, **37**, 1995

[86] M. Kotschenreuther, P. M. Valanju, S. M. Mahajan and J. C. Wiley, "On heat loading, novel divertors, and fusion reactors", *Physics of Plasmas*, 14, 072502, 2007

[87] W. Stacey, "Detachment and divertor temperature and density redistribution", *Physics of Plasmas*, 8, 2, 2001

[88] S. Togo, T. Takizuka, M. Nakamura, K. Hoshino, K. Ibano, T. L. Lang and Y. Ogawa, "Simulation Study of Detached Plasmas by Using One-Dimensional SOL-Divertor

Fluid Code with Virtual Divertor Model", *Contributions to Plasma Physics*, 56, 6, 2016

[89] N. Wolf, "Effect of divertor geometry on plasma detachment in DIII-D", *Journal of Nuclear Materials*, 266–269, 739-741, 1999

[90] U. Samm, *Plasma Wall Interaction: Status and Data Needs*, Nuclear Fusion Research, p.3-28, Springer Series in Chemical Physics, Berlin, 2005

[91] J. Roth, *Review and Status of Physical Sputtering and Chemical Erosion of Plasma Facing Materials*, Nuclear Fusion Research, p.203-224, Springer Series in Chemical Physics, Berlin, 2005

[92] R. Behrisch and D. E. Post, *Physics of Plasma–Wall Interactions in Controlled Fusion*, Plenum Press, New York, 1986

[93] P. Goranson, G. Barnes, J. Chrzanowski, P. Heitzenroeder, B. Nelson, C. Neumeyer and J. Ping, "Design of the plasma facing components for the National Spherical Tokamak Experiment", *18th IEEE/NPSS Symposium on Fusion Engineering*, 1999

[94] J. Heirbaut (2012) *How to Line a Thermonuclear Reactor* [Online]. Accessible: https://www.science.org/content/article/how-line-thermonuclear-reactor

[95] R. Dux, "Tungsten as first wall material in ASDEX Upgrade", *IAEA fusion energy conference*, 2007

[96] M. Gilbert and J. Sublet, "Neutron-induced transmutation effects in W and W-alloys in a fusion environment", *Nucl. Fusion*, 51, 4, 2011.

[97] A. Loarte, B. Lipschultz, A. S. Kukushkin, G. F. Matthews, P. C. Stangeby, N. Asakura, G. F. Counsell, G. Federici, A. Kallenbach, K. Krieger, A. Mahdavi, V. Philipps, D. Reiter, J. Roth, J. Strachan, D. Whyte, R. Doerner, T. Eich, W. Fundamenski, A. Herrmann, M. Fenstermacher, P. Ghendrih, M. Groth, A. Kirschner, S. Konoshima, B. LaBombard, P. Lang, A. W. Leonard, P. Monier-Garbet, R. Neu, H. Pacher, B. Pegourie, R. A. Pitts, S. Takamura, J. Terry, E. Tsitrone and the ITPA Scrape-off Layer and Divertor Physics Topical Group, "ITER physics basis. Chapter 4: Power and particle control", *Nucl. Fusion*, 47, 6, p.203–263, 2007

[98] J. Robertson, "Diamond-like amorphous carbon. Review of Deposition methods, properties, and applications", *Mat. Sci. Eng. Reports*, 37, 129, 2002

[99] S. Silva, *Properties of Amorphous Carbon*, EMIS Datareviews Series, 29, 2003

[100] C. Wu, *Hydrogen Recycling at Plasma Facing Materials*, Springer Netherlands, NATO Science Series, 2000

[101] D. Reiter and R. Clark, *Nuclear Fusion Research - Understanding Plasma Surface Interactions*, Springer Science and Business Media, 5, 127, 2006

[102] P. Fiflis, N. Connolly and D. N. Ruzic, "Experimental mechanistic investigation of the nanostructuring of tungsten with low energy helium plasmas", *Journal of Nuclear Materials*, 482, p.201–209, 2016

[103] T. J. Petty, M. J. Baldwin, M. I. Hasan, R. P. Doerner and J. W. Bradley, "Tungsten 'fuzz' growth re-examined: the dependence on ion fluence in non-erosive and erosive helium plasma", *Nucl. Fusion*, 55, 9, Sep 2015

[104] G. M. Wright, D. Brunner, M. J. Baldwin, R. P. Doerner, B. Labombard, B. Lipschultz, J. L. Terry and D. G. Whyte, "Tungsten nano-tendril growth in the Alcator C-Mod divertor", *Nucl. Fusion*, 52, 2012

[105] D. Reiter, Chr. May, M. Baelmans and P. Börner, "Non linear effects on neutral gas transport in divertors", *Journal of Nuclear Materials*, 241-243, 1, p.342-348, Feb 1997

[106] C. Guillemaut, R. A. Pitts, J. Bucalossi, G. Corrigan, A. S. Kukushkin, D. Harting, A. Huber, M. Wischmeier, G. Arnoux, S. Brezinsek, S. Devaux, J. Flanagan, M. Groth, S. Jachmich, U. Kruezi, S. Marsen, J. Strachan, S. Wiesen and JET EFDA contributors, "EDGE2D-EIRENE modelling of divertor detachment in JET high triangularity L-mode plasmas in carbon and Be/W environment", *Journal of Nuclear Materials*, 438, Jul 2013

[107] C. Guillemaut, R. A. Pitts, A. S. Kukushkin, J. P. Gunn, J. Bucalossi, G. Arnoux, P. Belo, S. Brezinsek, M. Brix, G. Corrigan, S. Devaux, J. Flanagan, M. Groth, D. Harting, A. Huber, S. Jachmich, U. Kruezi, M. Lehnen, C. Marchetto, S. Marsen, A. G. Meigs, O. Meyer, M. Stamp, J. D. Strachan, S. Wiesen, M. Wischmeier and JET EFDA Contributors, "Influence of atomic physics on EDGE2D-EIRENE simulations

of JET divertor detachment with carbon and beryllium/tungsten plasma-facing components", *Nucl. Fusion*, 54, 9, Sept 2014

[108] K. Verhaegh, "The role of plasma-molecule interactions on power and particle balance during detachment on the TCV tokamak", *Nucl. Fusion*, 61, 10, May 2021

[109] A. Pospieszczyk, S. Brezinsek, P. Mertens and G. Sergienko, "The Role of Hydrogen Atoms and Molecules in the Plasma Boundary", *Contrib. Plasma Phys.*, 42, 663, 2002

[110] D. R. Bates, A. E. Kingston and R. W. P. McWhirter, "Recombination between electrons and atomic ions, I. Optically thin plasmas", *Proceedings of the Royal Society A*, 267, 1330, May 1962

[111] K. Behringer and U. Fantz, "Some Basic Physics Results for Plasma Spectroscopy and Modelling", *Contrib. Plasma Phys.*, 39, 411, 1999

[112] R. W. McWhirter, *Spectral Intensities, In: R. H. Huddlestone and S. L. Leonard, Eds., Plasma Diagnostic Techniques*, Academic, New York, pp. 165-217, 1965

[113] U. Fantz, "Basics of plasma spectroscopy", *Plasma Sources Sci. Technol.*, 15, 2006

[114] L. C. Johnson, E. Hinnov, "Ionization, recombination, and population of excited levels in hydrogen plasmas", J. Quant. Spectrosc. Radiat. Transfer, 13, 1973

[115] K. Sawada, K. Eriguchi and T. Fujimoto, "Hydrogen-atom spectroscopy of the ionizing plasma containing molecular hydrogen: Line intensities and ionization rate", *J. Appl. Phys.*, 73, 1993

[116] ADAS. (2020). *Atomic Data and Analysis Structure* [Online]. Accessible: https://www.adas.ac.uk/index.php

[117] R. C. Hilborn, "Einstein coefficients, cross sections, f values, dipole moments, and all that", *American Journal of Physics*, 50, 11, 1982

[118] L. C. Johnson, "Approximations for collisional and radiative transition rates in atomic hydrogen", *Astrophysics J.*, 174, 227-36, 1972

[119] NIST. (2013). *Handbook of Basic Atomic Spectroscopic Data* [Online]. Accessible: https://www.nist.gov/pml/handbook-basic-atomic-spectroscopic-data

[120] Atomic Molecular Data Services. (2022). *FLYCHK: Generalized Model of Atomic Processes In Plasmas* [Online]. Accessible: https://www-amdis.iaea.org/FLYCHK/

[121] D. Wünderlich, M. Giacomin, R. Ritz and U. Fantz, "Yacora on the Web: Online collisional radiative models for plasmas containing H, H2 or He", *J. Quant. Spectrosc. Radiat. Transfer*, 240, 106695, 2020

[122] K. Sawada and T. Fujimoto, "Effective ionization and dissociation rate coefficients of molecular hydrogen in plasma, J. Appl. Phys., 78, 2913, 1995

[123] B. Heger, Ph.D. dissertation, University of Augsburg, 2002

[124] W. Moller, "Plasma and surface modeling of the deposition of hydrogenated carbon films from low-pressure methane plasmas", *Appl Phys a*, 56, 527-546, 1993

[125] J. G. Clark, M. D. Bowden and R. Scannell, "Low temperature Thomson scattering on MAST-U", *The Review of scientific instruments*, 92, 4, Apr 2021

[126] J. Terry and M. Reinke, "Diagnostic tools for studying divertor detachment: bolometry, spectroscopy, and thermography for surface heat-flux", *Plasma Physics and Controlled Fusion*, 59, 4, 2017

[127] A. Thorne, U Litzen and S. Johansson, *Spectrophysics: Principles and Applications*, Springer, New York, 1999

[128] G. H. Dieke and R. W. Blue, "The Fulcher Bands of HD and D2", *Phys. Rev.*, 47, 2611, 1935

[129] H. M. Crosswhite, *The Hydrogen Molecule Wavelength Tables of Gerhard Heinrich Dieke*, Wiley–Interscience, New York, 1972

[130] U. Fantz and B. Heger, "Spectroscopic diagnostics of the vibrational population in the ground state of and molecules", *Plasma Phys. Control. Fusion*, 40 2023, 1998

[131] N. Ohno, N. Tanaka, N. Ezumi, D. Nishijima and S. Takamura, "Influence of Plasma Resistance and Fluctuation on Probe Characteristics in Detached Recombining Plasmas", *Contrib. Plasma Phys.*, 41, 5, 2001

[132] T. J. Petty, A. Khan, T.Heil and J. W. Bradley, "Fuzzy tungsten in a magnetron sputtering device", *Journal of Nuclear Materials*, 480, p.374-385, 2016

[133] J. R. Harrison, W. A. J. Vijvers, C. Theiler, B. P. Duval, S. Elmore, B. Labit, B. Lipschultz, S. H. M. van Limpt, S. W. Lisgo, C. K. Tsuic, H. Reimerdes, U.Sheikh, K. H. A. Verhaegh, M. Wischmeier and the MST and TCV Teams, "Detachment evolution on the TCV tokamak", *Nuclear Materials and Energy*, 12, p.1071-1076, Aug 2017

[134] G. M. McCracken, M. F. Stamp, R. D. Monk, A. G. Meigs, J. Lingertat, R. Prentice, A. Starling, R. J. Smith and A. Tabasso, "Evidence for volume recombination in JET detached divertor plasmas", *Nucl. Fusion*, 38 619, 1998

[135] S. Potzel, M. Wischmeier, M. Bernert, R. Dux, H. W. Müller, A. Scarabosio and the ASDEX Upgrade Team, "A new experimental classification of divertor detachment in ASDEX Upgrade", *Nucl. Fusion*, 54, 2014

[136] Z. Qing, D. K. Otorbaev, G. J. H. Brussaard, M. C. M. van de Sanden, and D. C. Schram, "Diagnostics of the magnetized low-pressure hydrogen plasma jet: Molecular regime", *J. Appl. Phys.*, 80, 1312 (1996)

[137] O. W. Richardson, *Molecular Hydrogen and its Spectrum*, Yale University Press, New Haven, 1934

[138] K. P. Huber and G. Herzberg, *Molecular structure and molecular spectra*, Springer 1979

[139] H. M. Mott-Smith and I. Langmuir, "The Theory of Collectors in Gaseous Discharges", *Phys. Rev.*, 28, 727, Oct 1926

[140] F. Magnus and J. Gudmundsson, "Digital smoothing of the Langmuir probe I-V characteristic", *Review of Scientific Instruments*, 79, 7, 2008

[141] T. E. Sheridan and J. Goree "Collisional plasma sheath model", *Physics of Fluids B: Plasma Physics*, 3, 2796, 1991

[142] I. D. Sudi and R. Claude Woods, "A study of the accuracy of various Langmuir probe theories", *J. Appl. Phys.*, 76, 4488, 1994

[143] F. F. Chen, "Langmuir probes in RF plasma: Surprising validity of OML theory", *Plasma Sources Sci. Technol.*, 18, 2009

[144] M. J. Druyvesteyn, "Der Niedervoltbogen", *Zeitschrift fur Physik*, 64, 781, 1930

[145] J Krištof, A Annušová, M Anguš, P. Veis, X Yang, T Angot, P. Roubin and G.Cartry, "Diagnostics of low-pressure hydrogen discharge created in a 13.56 MHz RF plasma reactor", *Physica Scripta, IOP Publishing*, 91, 7, 2016

[146] P. Scheubert, U. Fantz, P. Awakowicz, and H. Paulin, "Experimental and theoretical characterization of an inductively coupled plasma source", *Journal of Applied Physics*, 90, 587, 2001

[147] J. Y. Son, M. S. Kim, H. W. Lee, J. S. Yu and K. H. Kwon, "Surface Modification of Polypropylene Separators in Lithium-Ion Batteries Using Inductively Coupled Plasma Treatment", *J. Nanosci.Nanotechno.*, 14, 2014

[148] M. Y. Naz, S. Shukrullah, A. Ghaffar and N. U. Rehman, "Development of simple designs of multitip probe diagnostic systems for RF plasma characterization", *Scientific World Journal*, 1, 2014

[149] A. Mishra, S. Lee and G. Y. Yeom, "Plasma dynamics in a discharge produced by a pulsed dual frequency inductively coupled plasma source", *J. Vac. Sci. Technol.*, 32, 6, 2014

[150] F. Jan, A. W. Khan, A. Saeed and M. Zakaullah, "Comparative Study of Plasma Parameters in Magnetic Pole Enhanced Inductively Coupled Argon Plasmas", *Plasma Sci. Technol.*, 4, 329-334, 2013

[151] M. Nisha, K. J. Saji, R. S. Ajimsha, N. V. Joshy, and M. K. Jayaraj, "Characterization of radio frequency plasma using Langmuir probe and optical emission spectroscopy", *J. Appl. Phys.*, 99, 2006

[152] J. S. Yoon, M. Y. Song, J. M. Han, S. H. Hwang, W. S. Chang, and B. J. Lee, "Cross Sections for Electron Collisions with Hydrogen Molecules", *J. Phys. Chem. Ref. Data*, 37, 913, 2008

[153] W. Ni, G. Song and D. Liu, "Langmuir probe measurements of an RF driven high-density inductively coupled argon plasma", *IOP Conf. Ser.: Earth Environ. Sci.*, 242, 2019

[154] D. Rauner, S. Mattei, S. Briefi, U. Fantz, A. Hatayama, J. Lettry, K. Nishida, and M. Q. Tran, "Investigation of the RF efficiency of inductively coupled hydrogen plasmas at 1 MHz", *AIP Conference Proceedings*, 1869, 2017

[155] R. Martin, "MAST Upgrade – Construction status and early research plans", IAEA Report, 2014

[156] B. Mihaljcic, " Studies of detached recombining plasmas in the UMIST Linear System". Ph.D dissertation, University of Manchester, 2004

[157] G. Tallents, *An Introduction to the Atomic and Radiation Physics of Plasmas*, Chapter 12 Cambridge University Press, 2018

[158] Y. Tsubotani, "Analysis of Molecular Activated Recombination in Detached Divertor Plasmas", *12th International Conference on Open Magnetic Systems for Plasma Confinement*, 2018

[159] U. Fantz and D. Wünderlich, "Relevance of Molecules in Ionizing and Recombining Plasmas in the Divertor and in Negative Ion Sources for Fusion", IAEA Presentation [Online], Dec 2014. Available: https://www-amdis.iaea.org/meetings/AMPMI14/Presentations/AMPMI-2014-12-16-Talk-Fantz-MolecularProcesses-2by4.pdf

[160] R. K. Janev, W. D. Langer, K. Evans, Jr. and D. E. Post, Jr., *Elementary Processes in Hydrogen-Helium Plasmas*, Springer, 1987

[161] S. Kado, S. Kajita, Y. Iida, B. Xiao, T. Shikama, D. Yamasaki, T. Oishi and S. Tanaka, "Experimental Study of the Atomic and Molecular Processes Related to Plasma Detachment in Steady-State Divertor Simulator MAP-II", *Plasma Science and Technology*, 6, 2451, 2004

[162] T. Shibata, *Transport processes of plasma in a negative hydrogen ion source - Study on spatial non-uniformity*, Ph.D dissertation, Keio University, Japan, 2013